University of Windsor

Scholarship at UWindsor

Electronic Theses and Dissertations

Theses, Dissertations, and Major Papers

2010

Multi-objective Optimization of Tube Hydroforming Using Hybrid Global and Local Search

Honggang An
University of Windsor

Follow this and additional works at: https://scholar.uwindsor.ca/etd

MULTI-OBJECTIVE OPTIMIZATION OF TUBE HYDROFORMING USING

HYBRID GLOBAL AND LOCAL SEARCH

by

Honggang An

A Dissertation

Submitted to the Faculty of Graduate Studies

through Mechanical, Automotive and Materials Engineering

in Partial Fulfillment of the Requirements for

the Degree of Doctor of Philosophy at the

University of Windsor

Windsor, Ontario, Canada
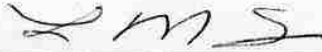
2010

Multi-objective Optimization of Tube Hydroforming Using

Hybrid Global and Local search

by

Honggang An

APPROVED BY:

_____

L. M. Smith, External Examiner
Oakland University, USA

_____

W. Altenhof
Department of Mechanical, Automotive & Materials Engineering

_____

N. Zamani
Department of Mechanical, Automotive & Materials Engineering

_____

F. Ghrib
Department of Civil & Environmental Engineering

_____

J. Johrendt, Co-Advisor
Department of Mechanical, Automotive & Materials Engineering

_____

D. E. Green, Advisor
Department of Mechanical, Automotive & Materials Engineering

_____

Dr. M. Mirhassani, Chair of Defense
Department of Electrical Engineering

11 August 2010

Declaration of Co-Authorship / Previous Publication

I. Co-Authorship Declaration

I hereby declare that this dissertation does not incorporate material that is result of joint research. In all cases, the key ideas, primary contributions, experiment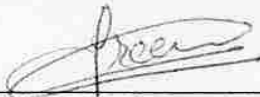al designs, data analysis and interpretation, were performed by the author, and Dr. D. E. Green and Dr. J. Johrendt as advisors.

I certify that, with the above qualification, this dissertation, and the research to which it refers, is the product of my own work.

II. Declaration of Previous Publication

This dissertation reflects the content of 5 original papers that have been previously published/submitted for publication in peer reviewed journals and conferences, as follows:

Dissertation Chapter	Publication title/full citation	Publication status
Chapter 4	H. An, D.E. Green, J. Johrendt, Multi-objective optimization and sensitivity analysis of tube hydroforming simulations, *Int. J. Advanced Manufacturing Technology,* DOI:10.1007/s00170-009-2505-x (2010)	*Published*
Chapter 5	H. An, D.E. Green, J. Johrendt, Optimal load path design for tube hydroforming using hybrid constrained MOGA and local search, *Advanced Engineering Informatics*	*Submitted*
Chapter 5	An, H., Green, D.E., and Johrendt J. A global optimization of load path design for tube hydroforming applications using MOGA, *IDDRG*, June, Golden, CO, USA, p307-318 (2009)	*Published*
Chapter 5	Honggang An, Green, D.E., Johrendt J. and K. Hertell, Inverse Analysis in Hydroforming of a Refrigerator Door Handle Using MOGA, Accepted by *NUMIFORM2010*, Pohang, Korea. June 2010.	*Published*
Chapter 6	An, H., Green, D.E., and Johrendt J. Optimization of tube hydroforming using pulsating internal pressure, *Proceedings of Materials Science & Technology (MS&T)*, October 25-29, 2009, Pittsburgh, Pennsylvania, USA, p2321-2332 (2009)	*Published*

I certify that I have obtained written permission from the copyright owner(s) to include the above published material(s) in my dissertation. I certify that the above material describes work completed during my registration as graduate student at the University of Windsor.

I declare that, to the best of my knowledge, my dissertation does not infringe upon anyone's copyright nor violate any proprietary rights and that any ideas, techniques, quotations, or any other material from the work of other people included in my dissertation, published or otherwise, are fully acknowledged in accordance with the standard referencing practices. Furthermore, to the extent that I have included copyrighted material that surpasses the bounds of fair dealing within the meaning of the Canada Copyright Act, I certify that I have obtained a written permission from the copyright owner(s) to include such material(s) in my dissertation.

I declare that this is a true copy of my dissertation, including any final revisions, as approved by my dissertation committee and the Graduate Studies office, and that this dissertation has not been submitted for a higher degree to any other university or institution.

ABSTRACT

An investigation of non-linear multi-objective optimization is conducted in order to define a set of process parameters (i.e. load paths) for defect-free tube hydroforming. A generalized forming severity indicator that combines both the conventional forming limit diagram (FLD) and the forming limit stress diagram (FLSD) was adopted to detect excessive thinning, necking/splitting and wrinkling in the numerical simulation of formed parts.

In order to rapidly explore and capture the Pareto frontier for multiple objectives, two optimization strategies were developed: normal boundary intersection (NBI) and multi-objective genetic algorithm (MOGA) based on the concept of "dominated solutions". The NBI method produced a uniformly distributed set of solutions. For the MOGA method, a stochastic Kriging model was used as a surrogate model. Furthermore, the constraint-handling technique was improved, Kriging model updating was automated and a hybrid global-local search was implemented in order to rapidly explore the Pareto frontier.

Both piece-wise linear and pulsating pressure paths were investigated for several case studies, including straight tube, pre-bent tube and industrial tube hydroforming. For straight tube hydroforming, the optimal load path was obtained using the NBI method and it showed a smaller corner radius compared to that predicted by the commercial program LS-OPT4.0. Moreover, the hybrid method coupling global search (MOGA) and local search (sequential quadratic programming: SQP) was applied for straight tube hydroforming, and the results showed a significant improvement in terms of the stress safety margin and reduced local thinning. For a commercial refrigerator door handle, the MOGA method was utilized to inversely analyze the loading path and the calculated path correlated well with the production path. For a hydroformed T-shaped tubular part, the amplitude and frequency of the pulsating pressure were optimized with MOGA. Thinning was reduced by 25% compared with experimental results.

A multi-stage (prebent) tube hydroforming simulation was performed and it indicated that the reduction in formability due to bending can be largely compensated by end feeding the tube during hydroforming. The loading path optimized by MOGA showed that the expansion into the corner of the hydroforming die increased by 16.7% compared to the maximum expansion obtained during experimental trials.

DEDICATION

To

My family and

my wife, Carol

ACKNOWLEDGEMENTS

TABLE OF CONTENTS

LIST OF TABLES

LIST OF FIGURES

LIST OF ABBREVIATIONS

ANN   Artificial Neural Networks

ANOVA   Analysis of variance

ASA   Adaptive simulated annealing

CFE   Corner fill expansions

CHIM   Convex Hull of Individual Minima

CLR   Centerline radius

COF   Coefficient of friction

CV   Constraint violation

DM   Decision maker

DACE   Design and analysis of computer experiments

DOE   Design of experiments

EAs   Evolutionary algorithms

EMO   Evolutionary multi-objective optimization

EO   Evolutionary optimization

FE   Finite element

FEA   Finite element analysis

FLC   Forming limit curve

FLD   Forming limit diagram

FLSC   Forming limit stress curve

FLSD   Forming limit stress diagram

GA   Genetic Algorithm

H-MOGA   Hybrid MOGA

iff   if and only if

LHS   Latin hypercube sampling

LHD   Latin hypercube design

LVDT   Linear variable differential transformers

MB   Medium boost

MOP   Multi-objective optimization problem

MOGA   Multi-objective genetic algorithm

MOEA   Multi-objective evolutionary algorithms

MOP   Multi-objective optimization problem

NBI   Normal boundary intersection

NSGA-II   Non-dominated sorting genetic algorithm

NBI   Normal-boundary intersection

OA   Orthogonal array

PWD   Process window diagram

PRESS   Prediction error sum of squares

RSM   Response surface methodology

R/D ratio   Ratio of the CLR of the bend to the tube outer diameter

S/N   Signal-to-noise ratio

SRSM   Sequential response surface method   or sequential with domain
             reduction

SQP   Sequential quadratic programming

THF   Tube hydroforming

NOMENCLATURE

σ_1, σ_2 true principal major and minor stresses

$\varepsilon_1, \varepsilon_2$ true principal major and minor strains

σ_f as-received stress limit on the Forming Limit Stress Curve (FLSC) for a given value of σ_2

σ_1^{max} maximum principal stress in element

d_f distance in stress space from a point to the FLSC for fracture measurement

d_w distance in stress space from a point to the FLSC for wrinkling measurement

d_{th} distance in strain space from a point to the FLC for measurement of thinning

Obj_f/f_1 objective of fracture

Obj_w/f_2 objective of wrinkling

Obj_th/f_3 objective of severe thinning

Obj_r/f_4 objective of corner radius

P_c calibration pressure

P_y yield pressure

P_b bursting pressure

σ_{UTS} ultimate tensile stress

R_C corner radius

t wall thickness

$F(x)$ the vector of objective functions

$h(x)$ equality constraints

$g(x)$ inequality constraints

x^L and x^U the lower and upper bounds for the decision variables

$\bar{\beta}$ regression coefficients

Chapter 1: Introduction and Problem Statement

In the automotive industry, the hydroforming process has drawn the attention of designers because tubular hydroformed structures have a greater stiffness-to-weight ratio. Parts are formed with an evolution of internal pressure and end-feed displacement by applying compressive forces to the ends of the tube (commonly known as end feed); this combination defines the loading path. Although a variety of hydroforming processes have been proposed to produce automotive parts, the determination of the optimum loading path remains a challenge with regard to maximizing formability and minimizing manufacturing costs. The objective of this work is to obtain the optimum loading path for tubular hydroforming that will generate a quality part using multi-objective optimization methods.

1.1   Introduction

1.1.1   Tube hydroforming and its advantages

Tube hydroforming (THF) is a metal forming process that involves the use of high fluid pressures to deform metal into shapes that otherwise would have been unobtainable using conventional manufacturing processes. Tube hydroforming technology can be traced back to the forming of a T-shaped tube in 1940 (Dohmann and Hartl, 1996). Between 1950 and 1970, researchers in the United States, United Kingdom and Japan developed related patents and application products. After 1970, researchers in Germany studied tube hydroforming and applied it to produce structural parts for automobiles. Since the early 1980's, tube hydroforming has been increasingly used in the automotive and aerospace industries, manufacturing of household appliances, and other applications.

Tube hydroforming offers several advantages over conventional manufacturing via stamping and welding, such as part consolidation, weight reduction, improved structural stiffness, reduced tooling costs due to fewer parts, fewer secondary operations, tighter dimensional tolerances and reduced distortion due to springback and reduced scrap, since

trimming of excess material can be completely eliminated in THF (Dohmann and Hartl, 1996).

As the number and variety of parts produced by THF technology increased dramatically in the automotive industry over the last two decades, problems related to practical production conditions required further research and development. One of the most significant areas of research has been the determination of loading path.

1.1.2 Tube failure in THF

The success of a THF process is, however, dependent on a number of parameters such as the loading path, lubrication conditions, and material formability (Aue-U-Lan et al., 2004). A suitable combination of all these variables is vital to avoid part failure. Most failure modes in THF can be classified as wrinkling or buckling, bursting, or severe thinning. These types of failures are caused by either excessive internal pressure or excessive axial end feed during the forming process.

1.1.3 Evaluation of forming severity in THF: FLD and FLSD

The severity of the hydroforming process increases with the deformation of the tube. In order to ensure a robust manufacturing process, it is necessary to measure its severity relative to known process limits.

A number of in-process methods have been proposed to measure the deformation of the tube, such as the use of linear variable differential transformers (LVDTs) and charge coupled device (CCD) image sensors. In most situations, however, the forming severity has been evaluated through circle grid analysis, which consists of electrochemically etching a pattern of circles onto the surface of the undeformed tube, and measuring the deformation of individual circles after the part has been hydroformed (past-process).

In spite of the fact that tube deformation can be detected, the determination of the forming severity is not straightforward using circle grid analysis. A deformed circle is manually or automatically measured at a critical location, and the corresponding surface strains are compared to a forming limit diagram (FLD). The FLD provides information

about how much a specific metal can be deformed before necking occurs. However, it has been found that the traditional FLD does not reliably predict necking in situations with nonlinear strain paths such as pre-forming, pre-bending, and crushing followed by hydroforming (Ghosh and Laukonis, 1976; Graf and Hosford, 1994; Stoughton, 2000). Therefore, the FLD is not a reliable failure criterion for tube hydroforming applications. One way to overcome this limitation is to use the forming limit stress diagram (FLSD) since it has been shown to be nearly insensitive to strain path effects. Furthermore, the stress-based failure criterion appears to be applicable to complex forming processes such as multi-stage forming and hydroforming.

Asnafi (1999) identified process limits for wrinkling, fracture, yielding, and sealing, and sketched a THF process window where the safe working range is dependent on the combination of the axial compressive force and internal pressure (Fig. 1.1).

Chu and Xu (2004a, 2004b) formulated a theoretical process window for predicting forming limits induced by buckling, wrinkling, and bursting of free-expansion THF. An
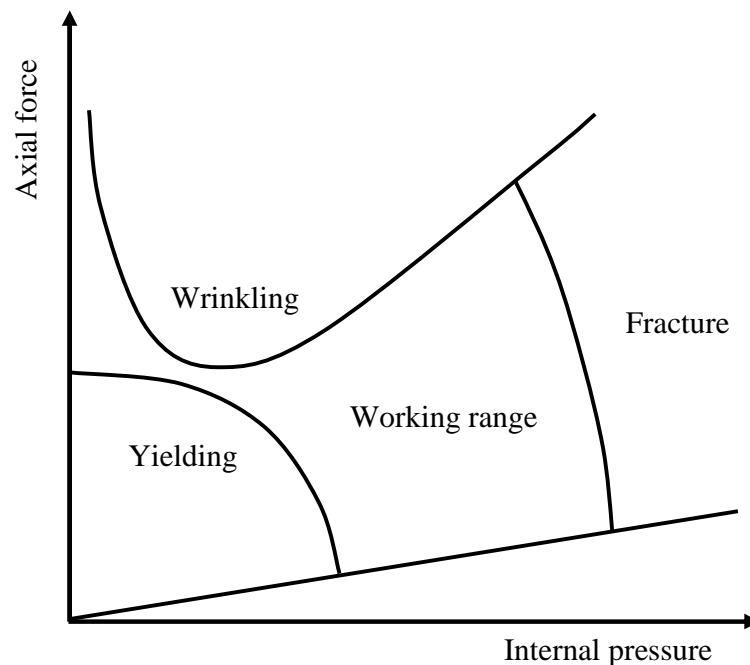
Fig. 1.1 Example of THF process window (Adapted from Asnafi, 1999)

optimal loading path was also proposed in the process window diagram (PWD) with an attempt to define the ideal forming process. However, an assumption of a proportional loading path was adopted. Since using a piece-wise linear combination of strain paths might enable the process to achieve a larger expansion ratio for the THF process, such a curved loading path will result in translating the boundary of the process window. The path dependency of the PWD was not discussed in their paper. Moreover, the window for an industrial part may be very small due to multi-stage forming and is difficult to determine.

1.1.4   Multi-objective optimization

Engineering design, by its very nature, is non-linear and multi-objective, often requiring tradeoffs between disparate and conflicting objectives. For instance, for typical hydroformed components, there are competing objectives; there is a need to reduce the risk of necking/fracture and wrinkling, minimize thinning, while achieving a specified geometry and maintaining a reasonably uniform thickness distribution throughout the part. This constitutes a problem of multiple objectives.

To solve problems with multiple objectives, it is common practice to reduce the problem to a single objective, even though there may exist different conflicting goals (e.g., maximizing formability and minimizing thinning) for the optimization task. As a result, multiple goals are often redefined as a weighted sum objective function, to provide an equivalent cost or a profit value, thereby artificially reducing the number of apparently conflicting goals into a single objective. However, the correlation between objectives is usually rather complex and dependent on the alternatives available. Moreover, the different objectives are typically conflicting, so it is difficult to aggregate them into one synthetic objective function (where the objective function is used to calculate the objective value). As a consequence, it may be very difficult to combine different objectives into a single goal function a priori, that is, before alternatives are known.

One way of defining optimality in a more precise way is via the concept of "dominated solutions". A point or solution b for hydroforming problem (green dot) is called "dominated" by another point a (red dot) when all objective values of a are smaller (Deb et al., 2002) (Fig. 1.2). The set of non-dominated points is called the "Pareto front" or "Pareto solutions", and represents a set of optimal solutions. It may be comparatively easier to choose among a given set of alternatives if appropriate decision support is available for the decision maker (DM). Hence, the main purpose of multi-objective problems is to find such non-dominated points.
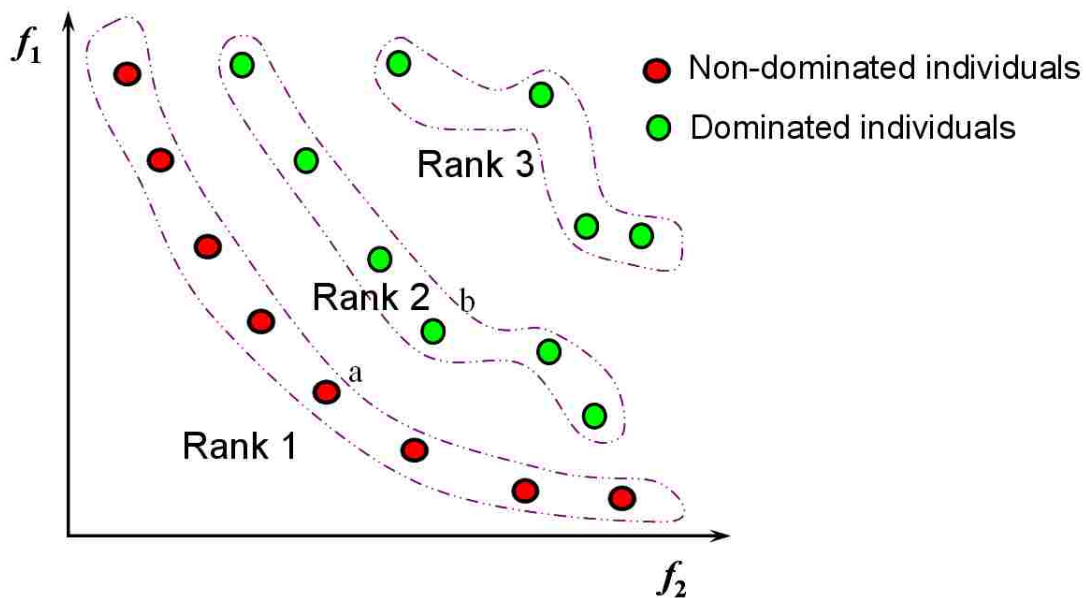
Fig. 1.2: Pareto set for multi-objective optimization with two objectives (Minimizing)

Ingarao et al. (2009) pointed out that two main phases should be developed in metal forming optimization in order to reach an optimal solution: the modelling phase and the computation phase. In the modelling phase the proper design variables to be optimized must be selected, and a correct formulation of the objective function must also be developed. Moreover, in most metal forming optimization problems the analytical linkage between the design variables and the objective function is not available.

Through numerical simulation, finite element analysis can assist in setting up the link between design variables and the objective function, and therefore be employed to find an

acceptable load path. The cost of the complete series of simulations, however may be expensive. To save computation time, a widely accepted practice is to build an inexpensive approximation model to replace the time-consuming simulation problem, and to optimize the surrogate model instead of the original finite element simulations.

Recently, the Kriging method, or design and analysis of computer experiments (DACE) (Sacks et al., 1989), which originated from the field of spatial statistics, has attracted attention in the area of metal forming (Stander et al., 2007; Lee and Kang, 2007). This model predicts the value of the unknown point using stochastic processes. Sample points are interpolated with the Gaussian random function to estimate the trend of the stochastic processes. However, the Kriging model is not a suitable method for data sets which have anomalous pits or spikes, or abrupt changes such as breaklines, and it is a much more complex method to use compared to the response surface methodology.

1.2   Problem statement

Currently, the development of THF processes is greatly delayed by long lead times, which result from many iterations of either trial-and-error based finite element (FE) simulations or expensive changes to prototype tooling. Moreover, the hydroformability of tubular parts is affected by a large number of parameters such as material properties, tube geometry, complex die-tube interface phenomena, and process parameters (i.e. loading paths). Consequently, more powerful design tools are needed to help engineers design better products and robust processes and to reduce lead time and cost. As a result, the goals of the proposed work are to:

1. Determine a forming severity indicator for hydroformed tubular parts and establish a general form of objective functions for THF;

2. Investigate two optimization strategies for solving multi-objective optimization problems: normal boundary intersection (NBI) and multi-objective genetic algorithm (MOGA);

3. Seek to reduce the computational expense of multi-objective optimization by focusing on efficient methods for obtaining rich Pareto sets; a method that employs design of

experiments (e.g. central composite designs, Latin hypercubes) and surrogate approximations (e.g. response surfaces, Kriging models) is considered to rapidly explore and capture the Pareto frontier;

4. Investigate both piece-wise linear pressure and pulsating pressure paths;

5. Investigate applications in straight tube, pre-bent tube and industrial part hydroforming to validate the proposed algorithm.

1.3   Dissertation Organization

Finally, the outline of this dissertation work by chapters is:

Chapter 1: Introduction and problem statement

Chapter 2: Literature review

Chapter 3: A hybrid forming severity indicator for tube hydroforming simulation

Chapter 4: Multi-objective optimization and sensitivity analysis for tube hydroforming using normal boundary intersection

Chapter 5: Loading path design using multi-objective genetic algorithm for a straight tube and an industrial part

Chapter 6: Optimization of loading path in hydroforming with pulsating pressure

Chapter 7: Loading path design in multi-stage tube forming

Chapter 8: Conclusions and future work

Chapter 2: Literature Review

In this chapter, the background of this research will first be presented, then the literature on THF optimization will be reviewed. A review of the current optimization software development and their advantages and shortcomings will also be presented. Finally, a new level of metamodelling closely linked to the multi-objective optimization process is introduced.

2.1 Tube hydroforming

2.1.1 Introduction

Tube hydroforming (THF) uses a pressurized fluid and axial compressive forces to plastically deform a tube into a desired shape. A typical straight tube hydroforming process is shown in Fig. 2.1. For parts with a more complex geometry, the process may also include preparing the tube, preforming, hydroforming, trimming or end cutting.

As far as the author could survey, approximately one half of the technical papers written and published on various aspects of hydroforming address THF processes.
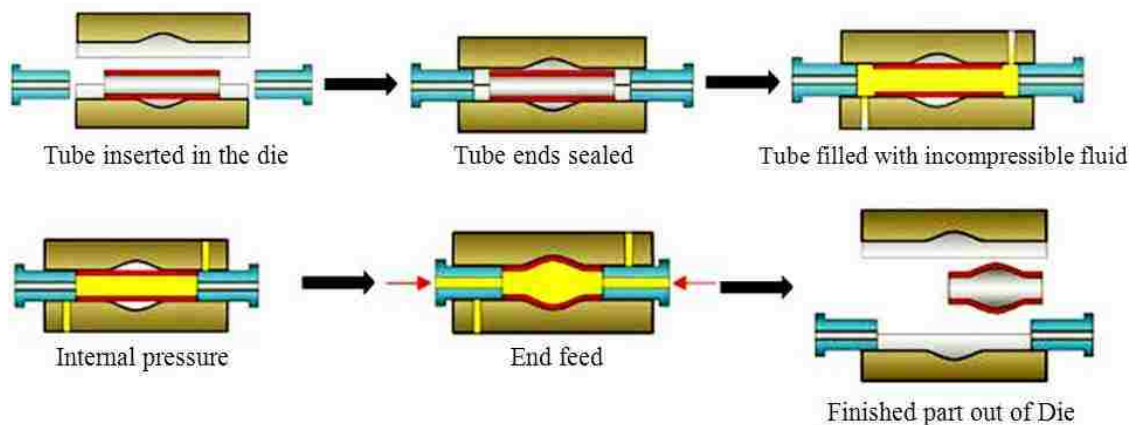
Fig. 2.1 Tube hydroforming process for a straight tube (Adapted from Koç, 2008)

2.1.2 Examples of hydroforming in the automobile industry

Some of the most common applications of tube hydroforming can be found in the automobile industry.   In 2002, the American automobile maker, Chrysler, began incorporating hydroforming to help reduce chassis vibration on its redesigned Dodge Ram (http://www.thomasnet.com). Likewise, General Motors' (GM) suppliers began using hydroforming to create suspension parts. There was an eventual increase of approximately 20 percent in manufacturing productivity for GM, and the switch to hydroforming may have contributed to the gain. GM continues to use hydroforming in its production methods. In 2006, it became one of the first automakers to use this process to create structural products on vehicles (Pontiac, Chevrolet) for several of its brands. Other examples of hydroforming in the automobile industry include the making of engine cradles for various, Ford, and Chrysler models. The process has also been used by several European automobile manufacturers, such as Volkswagen, who switched from deep drawing to hydroforming in order to create unibody frames for some of their vehicles. In addition, parts such as roof pillars, frame rails, engine cradles, rear axles, and exhaust manifolds are widely manufactured using tube hydroforming techniques (Ahmetoglu and Altan, 2000; Dohmann and Hartl, 1997). Fig. 2.2 illustrates some typical hydroformed tubular parts in an automobile.

As noted by many researchers (Ahmetoglu and Altan, 2000; Asnafi, 1999; Asnafi and Skogsgardh, 2000; Rimkus et al., 2000; Jirathearanat et al. 2004; Koç, 2003,2004; Koç and Altan, 2002; Ahmed and Hashmi 1998) the success of the hydroforming process depends on a proper combination of simultaneously applied internal pressure and axial load. Therefore, it is vital to determine a method of obtaining the optimal loading path (internal pressure vs. axial feeding) in order to ensure robust manufacturing.
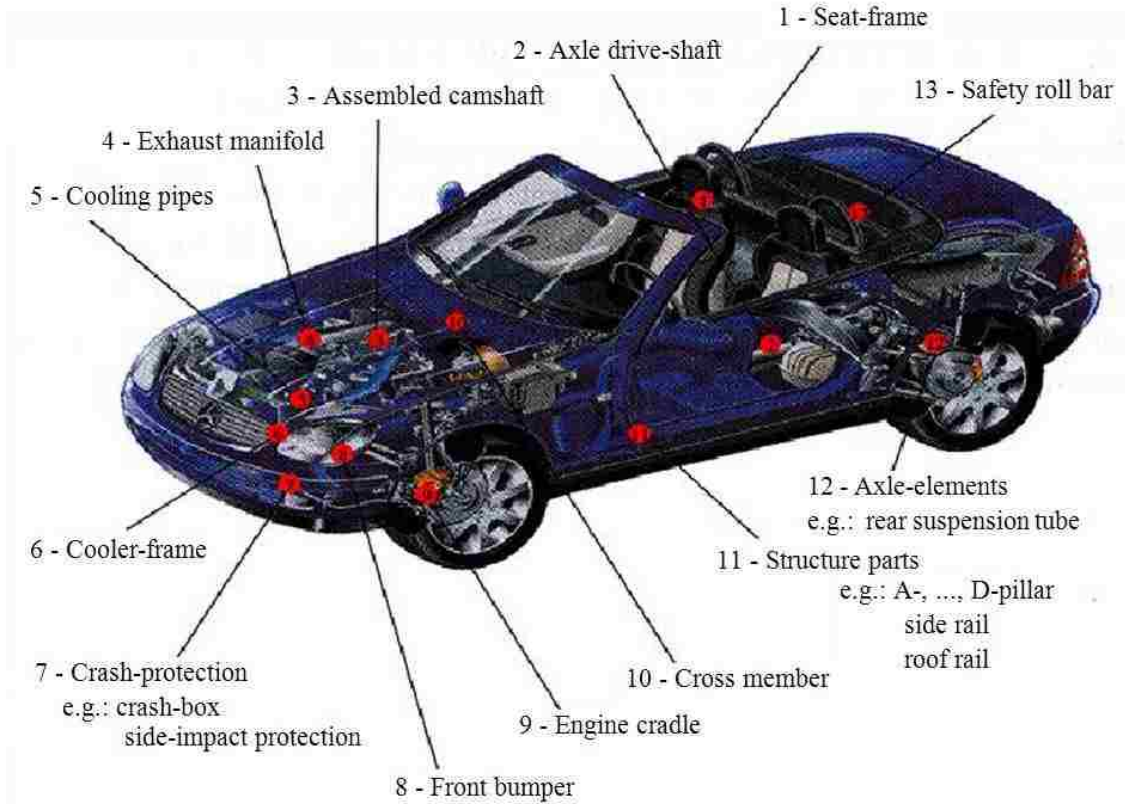
Fig. 2.2 Typical hydroformed parts in an automobile (Adapted from http://nsm.eng.ohio-state.edu/Advances_in_Hydro.swf)

2.2 Conventional design method of loading path

After the 1970's, a number of studies were carried out on different aspects of tube bulging, among these being the work of Hashmi (1981,1983), Hashmi and Crampton (1985), Dohmann and Klass (1987), Murata et al. (1989) and Thiruvarudchelvan and Lua (1991), which led to an understanding of tube bulging under axial compressive load. The compressive load, as found in these works, delays the onset of plastic instability by "feeding" extra material into the forming zone.

In order to successfully obtain the final desired hydroformed parts, it is necessary to study the influence of the forming parameters on the hydroformability. The influence of material properties and process parameters on the THF process has been investigated by means of experiments, analytical models, and finite element simulations. For instance,

Rama et al. (2003) developed a two-dimensional numerical method based on membrane theory to explicitly relate the deformation sequence with the pressure loads for tube expansion. However, the loading parameters (i.e.pressure and end feed) are still largely determined by the experience of hydroforming press operators.

Prior to the introduction of an analytical method, some early experiments were performed to achieve better bulge forming. Limb et al. (1973) carried out bulge forming of tubes of different metals and alloys with different wall thicknesses. It was found that increasing the internal pressure incrementally in steps during the axial load application was the most satisfactory method of bulging thin walled tubes. Manabe et al. (1984) carried out experiments using a computer-controlled testing apparatus to examine the influence of linear and non-linear loading paths on the behavior of thin-walled aluminum tubes during hydroforming. Thiruvarudchelvan and Lua (1991) developed a device for applying an axial compressive force proportional to the internal pressure and obtained an optimum ratio for maximum bulging. Dohmann and Hartl (1994,1996) presented a flexible tool system that divided the die into segments that can be driven separately during the process. Bieling (1992) carried out a number of experiments of bulge forming with tubes and hollow shafts to investigate a range of suitable bulge forming parameters.

2.2.1 Analytical method

Bieling (1992) developed a group of equations to determine the suitable internal pressure and axial force for stepped cross-sectional tubes. Ahmed and Hashmi (1997) provided a theoretical method for bulge forming to estimate the internal pressure, axial load and clamping load which are required to design the dies, punches and accessories for the process.

Asnafi (1999) analytically investigated the limits during the free forming, and the influence of material and process parameters on the loading path and the forming result. Only free-forming was treated in this work. Asnafi and Skogsgardh (2000) completed stroke-controlled hydroforming with free-forming theoretically and experimentally. The

forming limit curve (FLC) was used as an aid to finite-element simulations in component and process design. The study showed that the FLC of the tube material must be determined by bulge test. Kim and Kim (2002) used the analytical models to determine the forming limits for the THF process and demonstrated how the loading path and material parameters of the strain hardening exponent (n-value) and anisotropic parameter (r-value) influenced the forming results.

Rimkus et al. (2000), Jirathearanat et al. (2004) and Koç (2002, 2003) utilized simple analytical methods to obtain initial values of yielding, maximum pressure and axial feeding for the loading path design.

Rimkus et al. (2000) presented formulas and diagrams to aid in the estimation of the load parameters for the hydroforming of steel tubes and especially for the determination of the calibration pressure (the pressure for calibrating small radii or bringing the tube in complete contact with the tool cavities). It was pointed out that the load-curve defined the load history and was influenced by the material, the wall thickness, the tube diameter, the ratios between the wall thickness and the tube diameter and forming radius. To conduct a simulation of the forming process accurately using the finite element method (FEM), it was necessary to calculate the following parameters: (1) the axial force, necessary to control the change of the wall thickness; (2) the forming pressure, required to press the tube into the tool; and (3) the calibration pressure, necessary to achieve the final (smaller) radii. The authors defined a typical load curve in this manner, and calculated the axial force, forming pressure and calibration pressure as shown in Fig. 2.3.
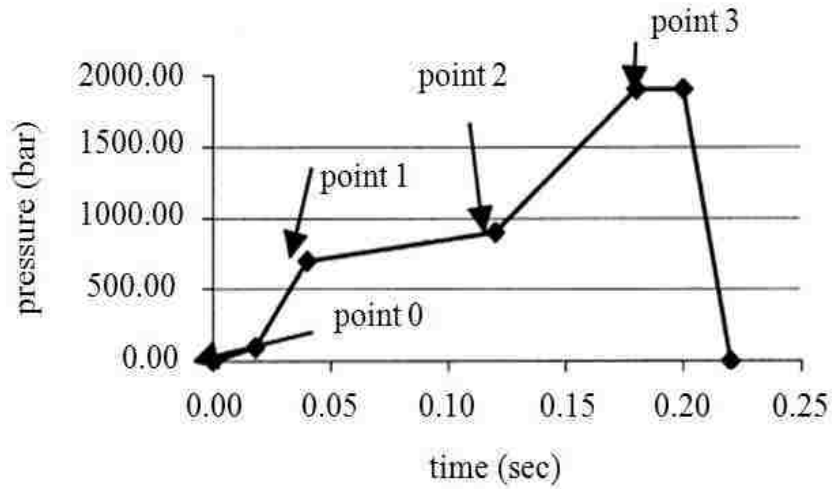
Fig. 2.3   Load-curve for internal pressure vs. time (Adapted from Rimkus et. al, 2000)

In Fig. 2.3, the internal pressures P_{i1} (at point 1) and P_{i2} (at point 2) were determined as follows:

$$P_{i1} = 0.9 P_y$$

(2.1)

$$P_{i2} = (1.2 \sim 1.4) P_y$$

(2.2)

where, P_y is the pressure to yield the tubular part. However, the calibration pressure was determined by the radius-pressure curve, and was affected by the tube wall thickness, the material and the radius which was to be achieved.

Jirathearanat et al. (2004) analytically estimated the initial group of process parameters for Y-shape THF, optimized it using FEA, and confirmed that higher material feeding at the initial stages of hydroforming was beneficial. Koç and Altan (2002) conducted determination of process limits and parameters for hydroforming by applying widely known plasticity, membrane and thin/thick walled tube theories, and analytical predictions were compared with their experimental findings. Koç (1999, 2002) estimated the yield pressure P_y and bursting pressure P_b according to the following relationships (Koç and Altan, 2002).

13

$$P_y = \sigma_y \frac{2\,t_0}{D_0 - t_0}$$

(2.3)

$$P_b = \sigma_{UTS} \frac{2\,t_0}{D_0 - t_0}$$

(2.4)

where σ_y is the yield stress, σ_{UTS} is the ultimate tensile stress of the tube material, t_0 is the initial wall thickness and D_0 is the initial outer diameter. An estimation of the maximum calibration pressure P_c at the moment of die corner filling was obtained based upon an estimation of the pressure required to achieve a certain target corner radius (R_C), according to the following equation (Koç and Altan, 2002):

$$P_c = \frac{2}{\sqrt{3}} \sigma_{UTS} \left[\ln \frac{R_C}{R_C - t} \right]$$

(2.5)

where σ_{UTS} is the ultimate tensile stress of the material and t is the current wall thickness. Eq. (2.5) indicates that the pressure required to achieve a certain corner radius increases as the radius decreases.

Braeutigam and Butsch (1992) proposed an empirical equation that is suitable as a first approximation of the maximum internal pressure required to hydroform a part:

$$P_k \approx 1.2\,\sigma_{UTS} \frac{t}{R_C}$$

(2.6)

Guan et al. (2006, 2008) used Fourier series based finite element analysis to study the axisymmetric bulge of tubes. Four to six Fourier series terms to approximate displacement were used to quickly and efficiently model the cross-section of the tube and accurately predict the final deformed shape and strain distribution.

Smith et al. (2006) proposed an analytical model on corner-forming limit diagrams (CFLD) for THF. The theory accounted for friction effects and accommodated regular shaped polygon die sections. This method was using a closed form approach for capturing friction effects and it was independent of employing the FEM.

14

All these analytical models provide an estimation of the internal pressure at some key stages during the forming process. Moreover, these models have mostly been limited to the axisymmetric bulging of tubes, and as such, are useful during the early stages of the process design. However, due to the highly non-linear nature of the process, theoretical studies to date have produced a relatively limited understanding of the mechanics of the hydroforming process.

2.2.2 Finite Element Method

Undoubtedly, almost all tests of the THF process were conducted experimentally and involved significant costs and time. The computer simulation of THF processes using the finite element method (FEM) has proven to be efficient and useful (Ponthot and Kleinermann, 2006), as it allows for the virtual testing and comparison of several candidate processes, thus avoiding the use of costly "trial and error" prototype tests. Several tools based on FEA simulations and experiments were developed to determine the process window for failure-free hydroforming (Gao et al., 2002; Manabe and Amino, 2002; Strano et al., 2004).

Ahmed and Hashmi (1998, 1999a, 1999b) showed that the FEM was a suitable tool for the simulation of forming processes. They presented theoretical and practical work for the estimation of the load parameters in THF. Gao et al. (2002) suggested a classification of THF processes based on their sensitivity to internal pressure or axial load. Manabe et al. (1984) investigated the optimal ratio between axial stress and internal pressure that produced a more uniform thickness distribution in straight tube hydroforming. Manabe & Amino (2002) also confirmed with both finite element (FE) simulations and experiments that key process and material factors affect the tube wall thickness distribution. They suggested that tube materials with a high strain-hardening coefficient (n-value) and a high anisotropic parameter (r-value) should be selected, and that good lubrication should be maintained to obtain a uniform thickness distribution. However, the optimal loading path was not investigated.

Palumbo et al. (2004) performed experiments and numerical simulations of the forming of a compound part consisting of a cylindrical region (the base) and a square part (the protrusion). Hwang et al. (2002) proposed a mathematical model and a finite element code ''DEFORM'' to examine the relationship between the internal pressure and the bulge height of the tube during the bulge hydroforming process in an open die. The effects of various forming parameters, such as the die entry radius, the initial thickness, the initial length of the tube, etc., upon the forming pressures were discussed. Lei et al. (2001) developed a three-dimensional rigid-plastic finite element model, HydroForm-3D, to analyze several typical hydroforming processes such as tee extrusion, cross-extrusion, the hydroforming process combined with the pre-bent process and subframe. The hydraulic pressure force was applied to the normal direction of the tube workpiece by integrating the pressure with respect to each element's surface area. MacDonald and Hashmi (2000) performed a finite element simulation of the manufacture of cross branches from straight tubes to investigate the effects of varying process parameters. It was concluded that when designing processes to bulge form cross-joints that compressive axial loading should be used in combination with pressure loading where possible; friction should be kept to a minimum where maximum branch height is required and greater tube thickness should be used when seeking to reduce stress and thinning behaviour in the formed component. Yoon et al. (2006) extended the direct design method that was based on ideal forming theory for the design of non-flat preform for THF processes. A preform optimization methodology for non-flat blank solutions was proposed based on the penalty constraint method for the cross sectional shape and length of a tube. The hybrid membrane/shell method was employed to the capture thickness effect while maintaining membrane formulation in the ideal forming theory.

Advantages and disadvantages

The FEM is a powerful method for rapidly designing both prototype and production components. Initial product design by the FEM, however, has often been carried out by trial-and-error in order to investigate the influence of various process parameters. But the trial-and-error approach would require an excessive and unmanageable amount of time to numerically predict the optimal process design. Consequently, an efficient design method

is required that will minimize numerical simulation time, while maintaining a high level of accuracy.

2.3 Optimization method in tube hydroforming

The finite element analysis is able to provide a valuable understanding of the hydroforming process. Nevertheless, the trial-and-error approach to optimizing the process design can be very time consuming. Instead, this iterative FEA method can be performed systematically and automatically in conjunction with various optimization methods, and the determination of the loading path can be treated as a classical optimization problem. Once the optimal loading path is found it can be utilized to maximize the part formability.

There are a variety of optimization strategies which can be classified into two categories: gradient and non-gradient methods (derivative free optimization). Gradient-based methods include the steepest descent method, the Newton, and the Quasi-Newton method used for linear and non-linear static optimization problems. For highly complex problems (optimizing a very large number of design variables), non-gradient-based methods are normally applied, such as response surface methods and genetic algorithms. However, the methods can also be classified in terms of computational intelligence (Engelbrecht, 2007): classical optimization (gradient-based and some of the non-gradient-based methods) and intelligent optimization (e.g. artificial neural networks (ANN), evolutionary computation (EC), swarm intelligence (SI), artificial immune systems (AIS), and fuzzy systems (FS)).

2.3.1 Classical optimization algorithms

2.3.1.1 Conjugate Gradient Method

Many of the problems related to the improvement of product quality and production efficiency can be directly associated with the optimization procedures. Efficient optimization procedures, integrating the classical mathematical methods of optimization

with the finite element method, have been developed and applied to structural engineering and to the area of metal forming.

Yang et al. (2001) sought to determine the optimal hydroforming process design using numerical simulation combined with an optimization tool that is based on the gradient method and sequential quadratic programming. A B-spline curve with six control points was used to describe the load path. The tube thickness variation was minimized. In addition, the thickness sensitivity analysis with respect to initial pressure was carried out. Fann and Hsiao (2003) applied the conjugate gradient method with the FE method to investigate how various loading conditions affect the thickness distribution in the tube wall and the part geometry. They also sought to determine an optimal loading condition using both a batch mode and a sequential mode, where the batch mode defined in their study was used to optimize all the process variables at once in view of their influence on the final result. The sequential mode was used to optimize the loading conditions one stage at a time in view of their effect on the results at each intermediate forming stage. The sequential mode generated a loading path with better tube quality than that generated with batch mode.

Lorenzo et al. (2006) proposed an integrated approach which combines FEM simulations and gradient-based optimization techniques with the aim to determine the optimum blank contour in a typical 3-D deep drawing operation. An optimal blank shape was obtained which guarantees that thinning is minimized.

Advantages and disadvantages

Optimization based on the gradient method is a sequential calculation process, and it normally involves only one objective or weighted sum of multiple objectives. Some software, LS-DYNA for example, can be run as a command in the DOS operation system, so that the LS-DYNA process simulation and the related calculation programs generated with Microsoft Visual C++ 6.0 can be integrated as a batch or a script file for DOS to carry out the optimization process.

Since the operation is gradient-based, there are two situations in engineering where applying the finite-difference derivative approximation is inappropriate: when the function evaluations are costly and when they are noisy. In the first case, it may be prohibitive to perform the necessary number of function evaluations (normally no less than the number of variables plus one) to provide a single gradient estimation. In the second case, the gradient estimation may be completely useless. Moreover, in some complex problems, either the derivatives are unobtainable, or the finite differences approximation is expensive. Furthermore, considering the optimization method (*Conjugate Gradient Method* – constrained or non-constrained conditions), it is simple to carry out, but needs a good initial point and the penalty scalar for the step adjustment. Consequently, it is difficult to fulfill the multi-objective optimization using the conjugate gradient method.

2.3.1.2 Self-feeding and adaptive simulation method

Aue-U-Lan et al. (2004) proposed to use *self-feeding* (SF) and *adaptive simulation* (AS) to find robust and cost effective techniques to determine optimal loading paths. The implementation of these two approaches is now presented.

(1) SF approach

This method was designed to restrict the search for the loading path to a proper family of curves and to select the optimum within this family. This method contains two steps:

1) Determine the relationship between internal pressure (P) and axial feed (d_{ax}), where the process is simulated by imposing only the internal pressure versus time. The friction at the interface is assumed to be zero.

2) Determine the displacement versus time at the node located at the ends of the tube and the maximum thinning on the deforming tube. This information is used to estimate approximately how much the axial feed should be in order to avoid excessive thinning of the hydroformed tube. In this simulation step, a friction coefficient is prescribed and the

axial feed is increased by a certain amount using a scaling factor, α ($\alpha^{\star}$SF), as shown in Fig. 2.4. This scaling factor was varied until a successful part is formed.
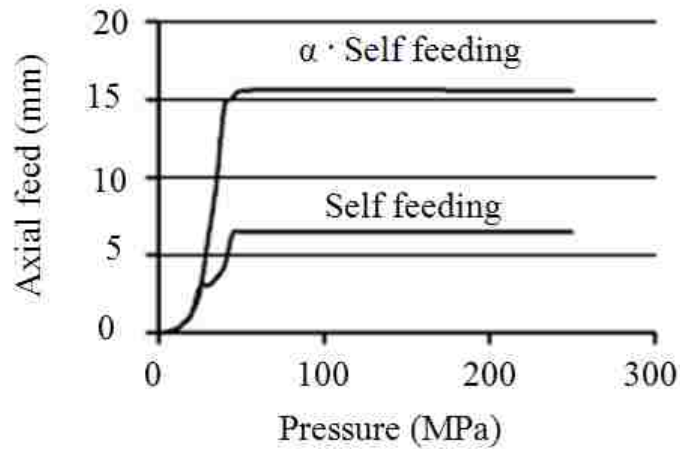
Fig. 2.4 SF loading paths: α is a scale factor to increase the amount of axial feeding (Adapted from Aue-U-Lan et al., 2004)

(2) AS approach
The principal idea of the AS method is to feed the material into the deformation zone as much as possible without any wrinkles or fracture. At the beginning of the simulation, the tube is "deformed" by pressurizing to the yield pressure (Pi_y). Then, axial feeding is applied in the simulation, while maintaining the pressure at Pi_y, until wrinkles are detected. The wrinkles are then eliminated by pressurizing the tube without any axial feeding. Once the wrinkles are eliminated, the tube is subject to axial feeding at a constant pressure (see Fig. 2.5). These steps are repeated until a part without wrinkles or excessive thinning is obtained.
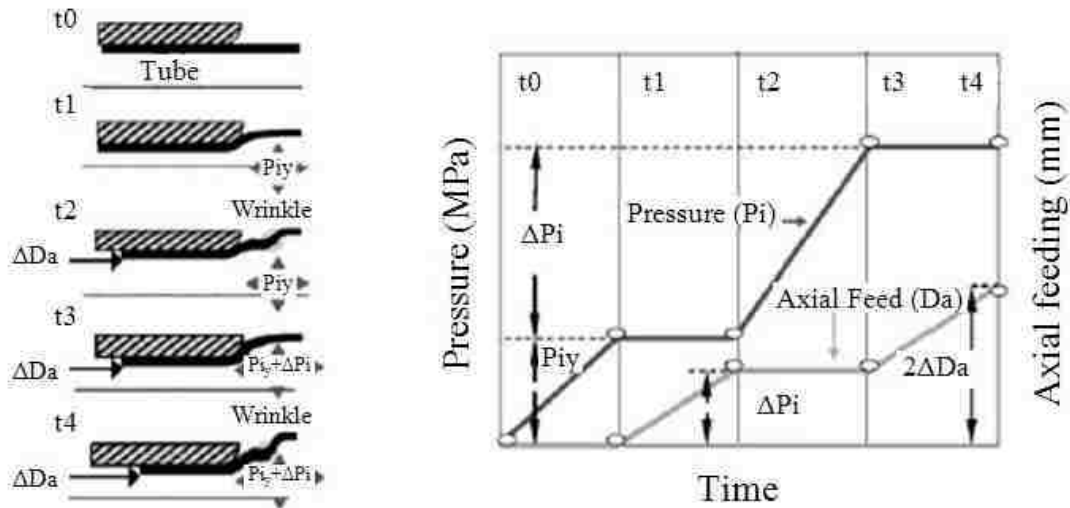
Fig. 2.5 Schematic procedure of the AS (Pi: internal pressure, ΔPi: internal pressure increment, Piy: yield pressure, ΔDa: axial feed increment). (Adapted from Aue-U-Lan et al., 2004)

The SF is a "systematic trial-and-error" approach for establishing a family of loading paths via FEA. The THF experiments done using this approach have shown that SF can significantly reduce the number of trial runs necessary for process development. However, these two methods sometimes failed to find an optimal solution.

2.3.2 Intelligent optimization algorithms
2.3.2.1 Fuzzy adaptive method

Though it is possible to determine suitable process parameters by repeating a series of FE simulations, this trial-and-error process can be extremely time-consuming. In order to reduce the time for optimization, some researchers combined the fuzzy method with FE simulation to identify the optimal loading path. Adaptive simulation uses different judgment rules in order to improve the results of the simulation: when defects or quality conditions are detected the loading path is automatically adjusted.

Fuzzy expert systems are advanced systems that use fuzzy rules and approximate reasoning. A database-assisted fuzzy control system is able to automatically optimize the process without any expert assistance by utilizing a knowledge database. The process control program is an additional user-defined subroutine that plays the role of the

processor, sensor and actuator in a real closed-loop system. Process control can be accomplished by using the current feed-back to modify the control parameters for next step of analysis. The control values are determined automatically based on artificial intelligence (AI) rules in the user-defined subroutine. The simulated results of the next step may include the effect of the process-controlled path.

Wu (2003) investigated the adaptive simulation of T-shape tube hydroforming by combining the FE code LS-DYNA with a fuzzy logic controller subroutine. During the simulation process (Fig. 2.6), subroutines can adjust the loading path according to the values of the minimum tube thickness and its variance. The goal of a better thickness distribution at the side branch of the formed part was achieved. Comparing with other linear loading paths, this adaptive control method led to better results.
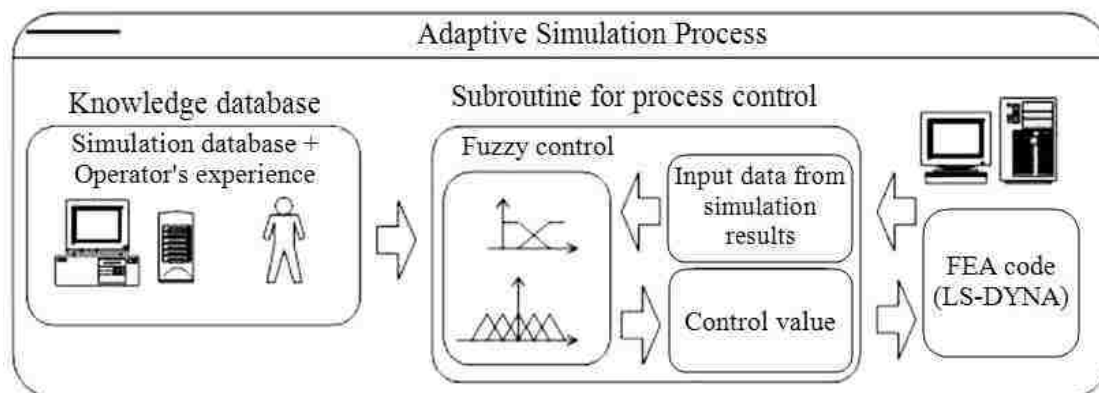
Fig. 2.6 The process of the adaptive simulation (Adapted from Wu, 2003)

Strano et al. (2004) investigated both a self-feeding simulation approach and an adaptive simulation approach to determine successful loading paths in a timely manner. Strano *et al.* (2001) proposed a defect criterion based on the geometry to detect the wrinkling phenomenon, and implemented it into different commercial FEA software. Miyamoto et al. (2001) used a fuzzy controller (the member function was variation of the bulge height and branch contact area) to discuss the effect of branch punch to the forming thickness. Manabe *et al.* (2002) proposed an approach using a virtual-forming system with FE simulation, the new database-assisted fuzzy adaptive process control system for THF. Manabe *et al.* (2006) applied the database-assisted fuzzy process control algorithm to T-

branch forming with a counterpunch with a validation of an aluminum alloy THF. An adequate loading path was searched using the fuzzy control algorithm, and the quality of the hydroformed product was improved compared to parts that were formed with a loading path determined on the basis of experience. Ray et al. (2004) determined the optimal load paths for X- and T-shaped hydroformed parts using FE simulations and an intelligent fuzzy logic-based load control algorithm: this enabled them to maximize part expansion while simultaneously maintaining wall thickness, forming stresses and plastic strains within the allowable limits. Aydemir et al. (2005) presented an adaptive method using a fuzzy knowledge-based controller to obtain a more efficient process control for THF processes, and therefore avoiding the onset of wrinkling and bursting with the help of dedicated stability criteria. The wrinkling criterion uses an energy-based indicator inspired by the plastic bifurcation theory. For necking followed by bursting, a criterion based on the forming limit curve was employed. Park et al. (2005) analyzed the empirical relationships between process parameters and hydroformability by fuzzy rules. Many process parameters were converted to a quantitative relationship by the use of approximate reasoning of a fuzzy expert system. Finally, Lorenzo et al. (2004a, 2004b) proposed a fuzzy system integrated with a FE code to obtain a closed-loop control for process design.

Advantages and disadvantages
The fuzzy adaptive method may well reduce the amount of simulation. Compared to optimization methods the fuzzy method required less simulation time and is easier to implement. However, the accuracy of this method depended on the selection of fuzzy rules and the member function.

2.3.2.2 Genetic algorithms

To reduce defects in THF, the applied internal pressure must be high enough to suppress buckling but low enough so as not to cause tube bursting. In conventional process simulation procedures, a pressure profile and feed rate must be supplied as an input to the finite element program. Based on the results of each finite element simulation, an

improved pressure profile and feed rate can be identified based on intuition and experience. Although adaptive simulation and fuzzy control can be used to find an appropriate loading path, it may not lead to an optimal solution within a reasonable time. There is a need, therefore, to develop an improved methodology to determine the loading paths.

Abedrabbo et al. (2005, 2009) presented a method using a Genetic Algorithm (GA) search method in combination with LS-DYNA to optimize the process parameters to determine the best loading paths of THF in a square-shaped die. Their goal was to maximize formability by identifying the optimal internal hydraulic pressure and feed rate while ensuring that the strains in the part did not exceed the forming limit curve (FLC). The hierarchical evolutionary engineering design system (HEEDS) was used in combination with the nonlinear finite element code LS-DYNA. Compared to the best results of a manual optimization procedure, a 55% increase in expansion was achieved by the automated procedure.

Roy et al. (1997) described an adaptive micro-genetic algorithm (µGA) for design optimization of process variables in multi-stage metal forming processes (e.g. multi-pass cold wire drawing, multi-pass cold drawing of a tubular profile and cold forging of an automotive bar).

Advantages and disadvantages

While many design optimization approaches are limited to a small number of design variables, hybrid genetic algorithms carry out a productive search over hundreds of variables at a time. As mentioned above, genetic algorithms use multiple autonomous agents to hierarchically decompose a problem into subsets with highly decomposed overlapping relationships. Some commercial software (e.g. HEEDS) combines evolutionary search algorithms with local optimization techniques. However, since there

are only rare applications of this approach to THF, further improvements are needed, such as the optimization of multiple objectives.

2.3.3 Summary of the classical and intelligent method

While classical optimization (CO) algorithms have been shown to be very successful (and more efficient than intelligent algorithms like GAs) in linear, quadratic, strongly convex, unimodal and other specialized problems, GAs have been shown to be more efficient for discontinuous, non-differentiable, multimodal and noisy problems. GA and CO differ mainly in the search process and the information about the search space that is used to guide the search process:

• The search process: CO uses deterministic rules to move from one point in the search space to the next point. GA, on the other hand, uses probabilistic transition rules (Engelbrecht, 2007). Also, GA applies a parallel search of the search space, while CO uses a sequential search. A GA search starts from a diverse set of initial points, which allows for a parallel search of a large area of the search space. CO starts from one point, successively adjusting this point to move toward the optimum.

• Search surface information: CO uses derivative information, usually first order or second-order, of the search space to guide the path to the optimum. GA, on the other hand, uses no derivative information. The fitness value (i.e. the objective value) of individual candidate solutions is used to guide the search.

2.3.4 Multi-objective optimization

Recently, multi-objective optimization algorithms have been increasingly applied to metal forming processes in which several objectives must be achieved simultaneously. Hereinafter, some concepts related to this algorithm are briefly discussed.

2.3.4.1 Multi-objective optimization problem (MOP)

Considering a generic minimization problem, a general formulation of the MOP can be presented in mathematical notation as Eq. (2.7)

Minimize: $F(x) = [\ F_1(x), F_2(x), ..., F_m(x)\ ]^T$

subject to:

$h(x) = 0$

$g(x) \leq 0$ (2.7)

$x^L \leq x \leq x^U$

where F is the vector of objective functions, $x \in R^n$ is the vector of decision variables, h and g are the possible sets of equality and inequality constraints, respectively, and x^L and x^U are the lower and upper bounds for the decision variables. Finally, n is the number of variables and m is the number of objectives.

2.3.4.2 Pareto optimality

Pareto optimality is defined using the concept of domination (Zitzler and Thiele, 1999). Given two parameter vectors **a** and **b**, **a** *dominates* **b** if and only if (iff) **a** is at least as good as **b** in all objectives, and better in at least one. Similarly, **a** is *equivalent to* **b** iff **a** and **b** are identical to one another in all objectives. A parameter vector **a** is *Pareto optimal* iff **a** is non-dominated with respect to the set of all allowed parameter vectors. Pareto optimal vectors are characterized by the fact that improvement in any one objective means worsening at least one other objective.

The *Pareto optimal set* is the set of all Pareto optimal parameter vectors, and the corresponding set of objective vectors is the *Pareto optimal front*. Fig. 2.7 shows the Pareto front for two objectives. The Pareto optimal set is a subset of the search space, whereas the Pareto optimal front is a subset of the solution space.

As mentioned earlier, most real world optimization problems are in fact non-linear multi-objective optimization problems; i.e., they are concerned with several (often conflicting) objective functions that must be optimized simultaneously. In general, the solution that is simultaneously optimal for all objectives (the utopia point O in Fig. 2.7) is not feasible and the real purpose of multi-objective optimization is to generate the set of so-called Pareto-optimal solutions, i.e. the set of solutions that represents the best alternatives.

Mathematically, a feasible solution x^* is a Pareto-optimal (or non-dominated, or non-inferior, or efficient) solution if there exists no x such that $F_i(x) \leq F_i(x^*)$ for all $i=1, ..., n$ with $F_j(x) < F_j(x^*)$ for at least one $j=1,...,m$. This definition signifies that all non-dominated solutions are optimal in the sense that it is not possible to improve one objective without degrading one or more of the other ones. After obtaining the set of Pareto-optimal solutions, the designer is able to select a suitable compromise between all objectives. In order to help the decision-making process, it is important to find a set of solutions as diverse as possible and uniformly distributed along the Pareto front.

For Pareto optimality (Fig. 2.7), there are several methods available to determine the Pareto set (weak or strong), such as the weighted sum method, the ε-constraint method, the goal attainment method and the multi-objective GA method. In this work, the Normal
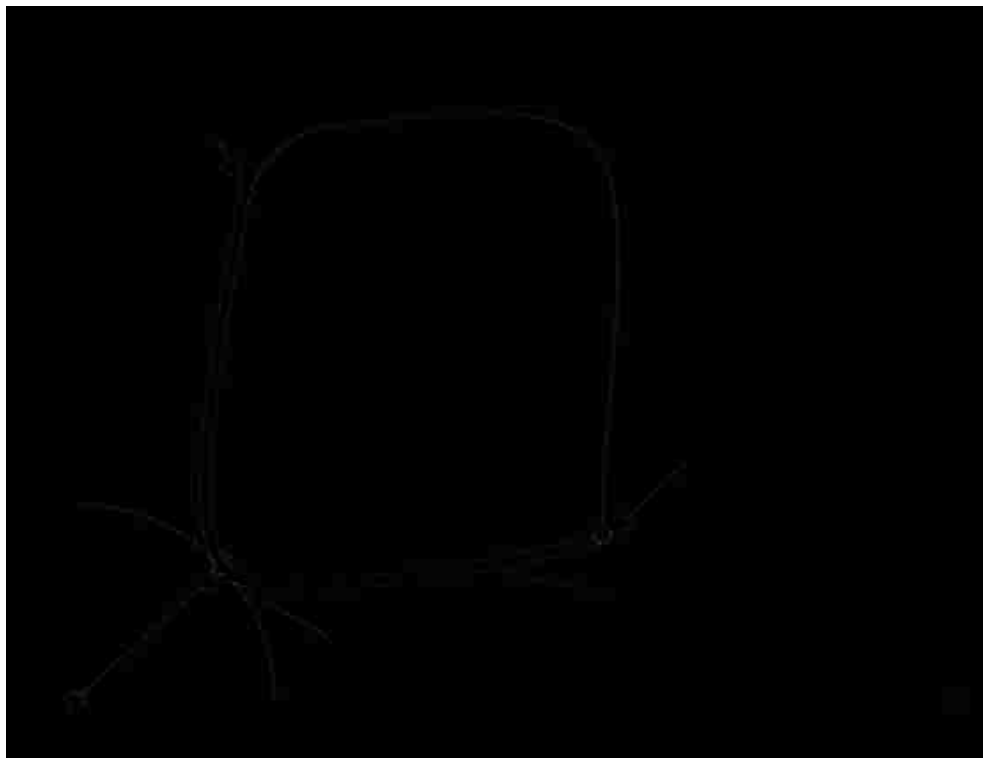
Fig. 2.7 Pareto-optimal solution for two objectives

Boundary Intersection (NBI) method and Multi-objective Optimization Genetic Algorithm (MOGA) were chosen to obtain the Pareto set.

2.3.4.3 Surrogate model

A surrogate model, or meta-model, is constructed to replace the time-consuming FE simulation, and will be used together with the multi-objective optimization algorithms to find the optimal loading path parameters in hydroforming applications. Fig. 2.8 shows the entire philosophy of surrogate modelling in the form of a flow chart.

More details of this method can be found in section 2.3.5.
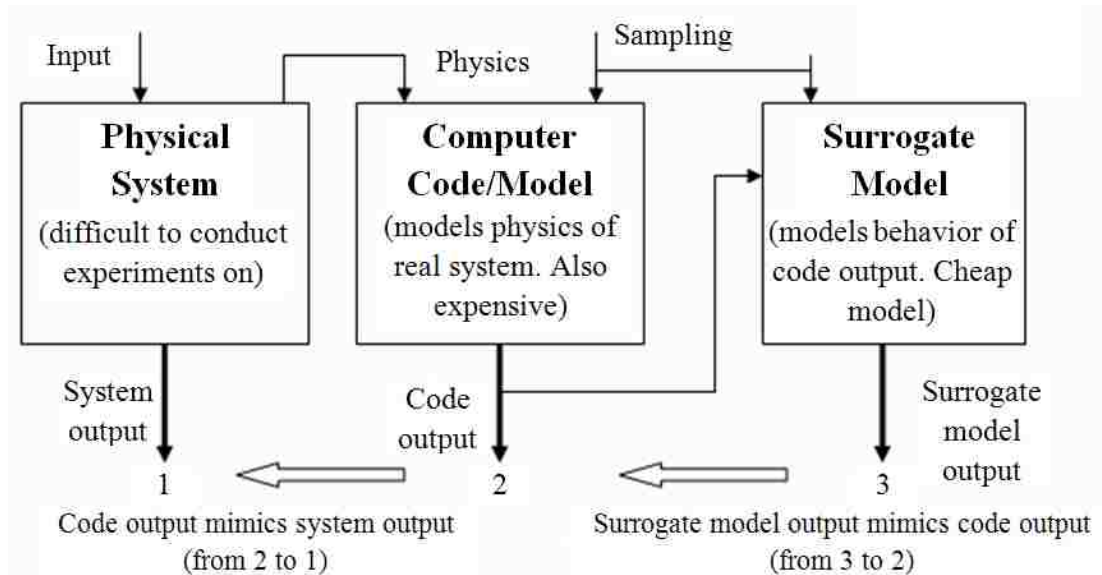
Fig. 2.8 Surrogate modelling philosophy (Adapted from Kulkarni, 2006)

2.3.4.4 Taguchi method

The Taguchi method has been widely used for robust design and quality engineering in industry (Taguchi, 1981; Ross, 1988). The Taguchi method utilizes a mathematical tool of orthogonal array experiments to study a large number of decision variables with a small number of experiments. It also uses a generic signal-to-noise (S/N) ratio to quantify the present variation for robust design against noises. According to Taguchi method, the loss function, which is equivalent to objective function, can be divided into three characteristics, including "lower-the-better", "nominal-the-better", or "higher-the-better " (Taguchi, 1981).

The S/N ratio for the lower-the-better characteristics related to the tube hydroforming is given by

$$S/N = -10\log\left(\frac{1}{n}\sum_{i=1}^{n} y_i^2\right)$$

(2.8)

where y_i indicates the measured objectives, and n is the number of simulation repetitions under the same design parameter conditions. Regardless of the definition of the S/N, a greater S/N ratio always corresponds to a better quality characteristic.

In the Taguchi method, a statistical method of analysis of variance (ANOVA) is further employed to quantitatively investigate the effects of the parameters on objectives. A design parameter is considered to be significant if its influence is large compared to the virtual experimental error.

2.3.4.5 NBI

The NBI method is a preferred approach for multi-objective optimization and was developed by Das and Dennis (1998). The details of this method are provided in Chapter 4.

2.3.4.6 Multiobjective evolutionary algorithm (MOEA)

Since the first studies on evolutionary algorithms (EA), major research and application of EAs in multi-objective optimization, only started in the early of 1990s. However, the effectiveness of evolutionary computation methodologies in the solution of multi-objective optimization problems has generated significant research interest in recent years.

Some basic terminology is given to aid in the understanding of the subsequent work.

1. Parent: a solution used during crossover operation to create a child solution.

2. Children (or Offspring): new solutions (or decision variable vectors) created by a combined effect of crossover and mutation operators.

3. Population: a set of solutions used in one generation of an evolutionary algorithm (EA). The number of solutions in a population is called 'population size'.

4. Fitness: a fitness or a fitness landscape is a function derived from objective function(s), constraint(s) and other problem descriptions which is used in the selection (or reproduction) operator of an EA.

5. Crossover: an operator in which two or more parent solutions (chromosome 1 and 2, Fig. 2.9a) are used to create (through recombination) one or more offspring solutions. The operation is illustrated by swapping two parts at the crossover point in Fig. 2.9a.

6. Mutation: an EA operator which is applied to a single solution to create a new perturbed solution (Fig. 2.9b). A fundamental difference with a crossover operator is that mutation is applied to a single solution, whereas crossover is applied to more than one solution.

Chromosome 1	10011 | 001100110
Chromosome 2	11001 | 110001010
Offspring 1	11001 | 001100110
Offspring 2	10011 | 110001010

Old Offspring 1	100111001100110
Old Offspring 2	110011010001010
New Offspring 1	100101001110110
New Offspring 2	110011110001000

(a) Crossover   (b) Mutation

Fig. 2.9 The crossover and mutation operations in EA

A number of evolutionary multi-objective optimization (EMO) methodologies have been developed, such as Non-dominated Sorting Genetic Algorithm (NSGA) and its second generation (NSGA-II), Strength Pareto Evolutionary Algorithm (SPEA), and Pareto-Archived Evolution Strategy (PAES) (Deb, 2008), and are being continuously improved in order to achieve better performance (Deb, 2008). Multi-objective genetic algorithm (MOGA) stands for the class of those methods that use genetic algorithms. These techniques have illustrated their superiority over traditional multiobjective optimization techniques and are now considered to be a robust optimization tool. Fig. 2.9 shows a schematic of a two-step multi-objective optimization procedure. The reasons for their popularity are many. Evolutionary optimization (EO) has become increasingly popular because *i*) it does not require any derivative information, *ii*) it is relatively simple to implement and *iii*) it has wide-spread applications.

The NSGA-II algorithm developed by Deb et al. (2002) has been a popular optimization tool in recent years. It adopts an elitism strategy and crowding-distance calculation, which offer a much better spread of solutions and better convergence in most problems near the true Pareto-optimal front compared to Pareto-archived evolution strategy and strength-Pareto Evolutionary Algorithm – two other elitist multi-objective evolutionary algorithms (MOEA) that pay special attention to creating a diverse Pareto-optimal front. The algorithm of NSGA-II and its improvements will be detailed in chapter 5.
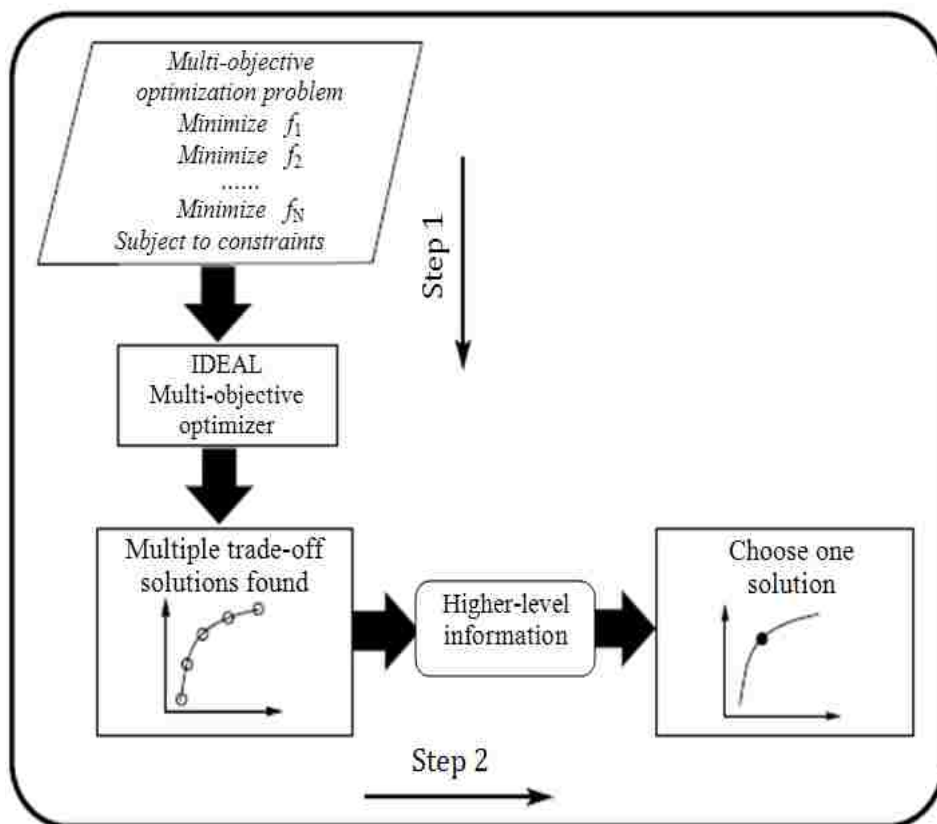
Fig. 2.10 Schematic of a two-step multiobjective optimization procedure (Adapted from Deb, 2008)

2.3.5 Meta-model based multi-objective optimization

By properly constructing meta-models, designers can address the challenge posed by prohibitively high computational times. The resulting approximation is computationally efficient functions and allows for a comprehensive exploration of the design space, and may yield significantly improved designs. The literature review also shows the trend in THF: from single-objective optimization to multi-objective optimization; from direct FE simulation to meta-model based optimization.

In order to accelerate the calculations, a variety of surrogate methods are used to substitute the FEA simulations: Polynomial regression (Myers and Montgomery, 2002), Radial basis functions (Hussain et al., 2002), ANN (Rafiq, 2001) and Kriging models (Strano, 2006). It is obvious that the allocation of the sampling points used to build the approximation have an effect on the final performance of the surrogate model. Many schemes and criteria have been proposed to allocate a-priori the sample points in a convex domain of interest: Factorial design, Box-Behnken, Koshal, Central Composite design, D-Optimal and Space-filling design. All these efforts are made to approach the true response surface of the practical problems. It is practically difficult to conclude which one is most suitable for allocation and reduction of sampling points to reach a desired precision.

There are normally three stages that describe this methodology:
   1) First stage: design of experiments (DOE).
   2) Second stage: selection and construction of a surrogate model.
   3) Third stage: multi-objective optimization.

2.3.5.1 Design of experiments

The design of experiments (DOE) is a powerful tool to analyze the influence of process variables over some specific range, which is an unknown function of these process variables. DOE involves planning a set of experiments. When the results of these experiments are analyzed, they help to identify optimal conditions and the factors that

most influence the results. Statistical approval to experimental design is necessary if we wish to draw meaningful conclusions from the data (Montgomery, 1997).

This section compares several experimental design schemes, such as factorial design, central composite design, D-optimal design, and latin hypercubes.

Factorial design

Factorial designs include full factorial design and fractional factorial design. Both these designs are characterized by the terms factor and level. In the optimization of the tubular hydroforming process, a factor would represent a specific process variable, and the level would represent the magnitude of this variable. Consider a 2^3 full factorial design, for example, where there are two levels and three factors.

(a)   (b)
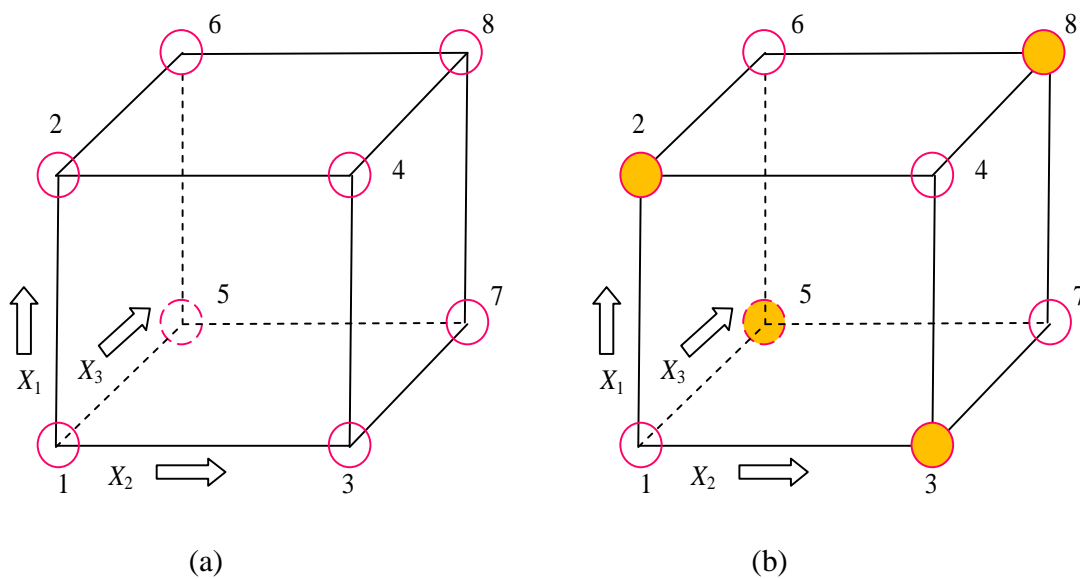
Fig. 2.11 A two level full factorial design (factors X1, X2, X3); (b) fractional design

A fractional design is a fraction of a full factorial design, and is created by blocking some of the design nodes; e.g. the fractional factorial design shown in Fig. 2.11 b) is designed with nodes 1, 4, 6, 7 only, and nodes 2, 3, 5 and 8 have been blocked.

Central composite design

This design uses the 2^n factorial design, the center point, and the 'face center' points and therefore consists of $P = 2^n + 2n + 1$ experimental design points. For $n = 3$, the coordinates of the nodes are:
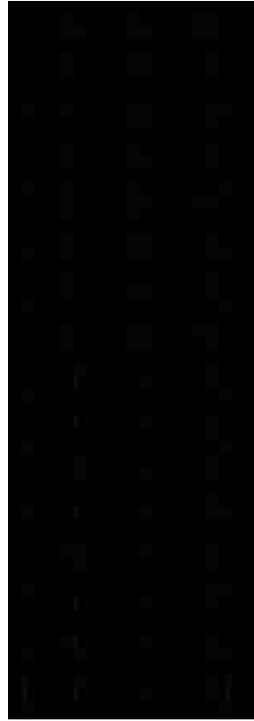
where the value of α is: $\alpha = \sqrt[4]{2^n}$.   (2.9)

The points are used to fit a second-order function.

D-optimal design

The D-optimality criterion is the most widely used criterion for selecting data points for computer generated DOE. The D-optimality criterion maximizes the determinant of the moment matrix, W, which is defined (e.g., Myers and Montgomery, 2002) as

$$W = \frac{X^T X}{k}$$ (2.10)

where k is the number of sampling points. A related measure is the D-efficiency:

$$D_{eff} = \frac{\left(Det\left[X^T X\right]\right)^{1/p}}{k}$$ (2.11)

where p is the total number of parameters included in the response surface model (the order of the matrix W), X is an $k\times(p+1)$ matrix (also defined in eq. 2.14). If all variables are normalized so that they vary from -1 to 1, then the maximum value of D_{eff} is 1. Furthermore, the quality of the set of points can then be measured by D_{eff} (Todoroki and Ishikawa, 2004).

Latin hypercubes

Latin hypercube sampling (LHS) was developed to address the need for uncertainty assessment for a particular class of problems. Latin hypercube sampling, due to McKay et al. (1979), is a strategy for generating random sample points ensuring that all portions of the vector space are represented. Consider the case where we wish to sample m points in the n-dimensional vector space $D \in R^{n}$. The Latin hypercube sampling strategy is as follows (Lophaven et al., 2002):

1. Divide the interval of each dimension into m non-overlapping intervals having equal probability (here we consider a uniform distribution, so the intervals should have equal size).
2. Sample randomly from a uniform distribution a point in each interval in each dimension.
3. Pair randomly (equal likely combinations) the point from each dimension.

This method was found to be more accurate than random sampling and stratified sampling in estimating the means, variances and distribution functions of an output. Moreover, it ensures that each of the input variables has all portions of its range represented. It can cope with many input variables and is computationally inexpensive to generate.

2.3.5.2 Approximation techniques

In order to accelerate the optimization, a variety of surrogate methods have been used to limit the number of FEA simulations: polynomial regression (Myers and Montgomery, 2002), radial basis functions (Hussain et al., 2002), ANN (Rafiq, 2001) and Kriging models (Strano, 2006) are some of the most common techniques. However, the design of

sample points used to build the approximation has an influence on the performance of the surrogate model. Many schemes and criteria have been proposed to assign *a-priori* the sample points in a convex domain of interest, such as the factorial design, Koshal, central composite design, D-optimal and space-filling design (Stander et al., 2007) (Table 2.1). Every effort is made to approach the true response surface of the practical problems. However, it is difficult to conclude which one is most suitable for the assignment of sampling points to reach a desired accuracy.

Table 2.1 Number of experimental points required for experimental designs (Stander et al., 2007)

Number of Variables n	Linear approximation			Quadratic approximation			Central Composite
	Koshal	D-optimal	Factorial	Koshal	D-optimal	Factorial	
1	2	4	2	3	4	3	3
2	3	5	4	6	10	9	9
3	4	7	8	10	16	27	15
4	5	8	16	15	23	81	25
5	6	10	32	21	32	243	43
6	7	11	64	28	43	729	77
7	8	13	128	36	55	2187	143
8	9	14	256	45	68	6561	273
9	10	16	512	55	83	19683	531
10	11	17	1024	66	100	59049	1045

Response surface method

By far the most popular technique for building meta-models in engineering is the traditional response surface method (RSM), which typically employs second-order polynomial models that are fit using least-squares regression techniques.

RSM is a collection of statistical and mathematical methods that are useful for modelling and analyzing engineering problems. In this technique, the main objective is to optimize the response surface that is influenced by various process parameters. RSM also quantifies the relationship between the controllable input parameters and the obtained response surfaces (Myers and Montgomery, 2002).

Response surface methodology is applied to obtain an approximation to a response function in terms of predictor variables. The response model is generally written as:

$$y = f(\boldsymbol{x}) + \varepsilon \qquad (2.12)$$

where y is the response, $x=(x_1, x_2, \ldots, x_n)$ are predictor variables, and ε is random error that is assumed to be normally distributed with mean zero and variance σ^2. The error, ε_i, at each observation is assumed to be independent and identically distributed. The function $f(x)$ is normally selected to be a polynomial. For a quadratic polynomial, $f(x)$ is written as:

$$y = \beta_0 + \sum_{i=1}^{n} \beta_i x_i + \sum_{i=1, j>i}^{n} \beta_{ij} x_i x_j \tag{2.13}$$

where β represents unknown coefficients. The response model can also be rewritten in matrix form as:

$$y = X\beta + \varepsilon \tag{2.14}$$

where ε is the error vector. The unbiased estimator b of the coefficient vector β is obtained using the least square error method as:

$$b = (X^T X)^{-1} X^T Y \tag{2.15}$$

By obtaining b, the vector of coefficients from Eq. (2.14), the response surface is prepared.

Kriging method

A FE simulation is a repeatable deterministic process; however, when an established analytical model based on some limited data is used to predict "new" data, the output becomes uncertain due to the limited information that was used to define the "black box" model. The Kriging (or DACE) technique, which originated from the field of spatial statistics, was developed to represent stochastic variables. The response is modelled as a realization of a regression model and a random process (Lophaven et al., 2002). The universal model can be expressed as:

$$Y(x) = \sum_{i=1}^{p} \beta_i f_i(x) + Z(x) \tag{2.16}$$

where the coefficients β_i (i=1,...p) are the regression parameters, $f_i(x)$ (i=1,...p) are known functions of x; $Z(x)$ is a random process with mean zero, variance σ^2, and non zero covariance

$$Cov(w, x) = \sigma_k^2 \rho(\theta, w, x), k = 1, 2, \ldots, p \tag{2.17}$$

where σ_k^2 is the process variance of the kth component of the response and $\rho(\theta, w_i, x_i)$ is the correlation model. Usually, the stochastic process is stationary, which implies that the correlation $\rho(\theta, w_i, x_i)$ depends only on w_i-x_i, namely

$$\rho(\theta, w_i, x_i) = \rho(\theta, w_i - x_i) \tag{2.18}$$

A Gaussian correlation function (2.19) and a surrogate model with polynomial order 2 are typically used.

$$\rho(\theta, w_i, x_i) = \exp\left[-\sum_{i=1}^{n} \theta_i |w_i - x_i|^2\right] \tag{2.19}$$

Unlike response surfaces, however, the Kriging method has found extremely limited use in hydroforming optimization since its introduction by Sacks et al. (1989).

Comparison of RSM and Kriging method

Fig. 2.12 lists the most common approximation techniques and the way these models are constructed. The differences between the RSM and Kriging methods are shown in Fig. 2.13 and 2.14. More details can be found in Simpson et al. (1998, 2001).
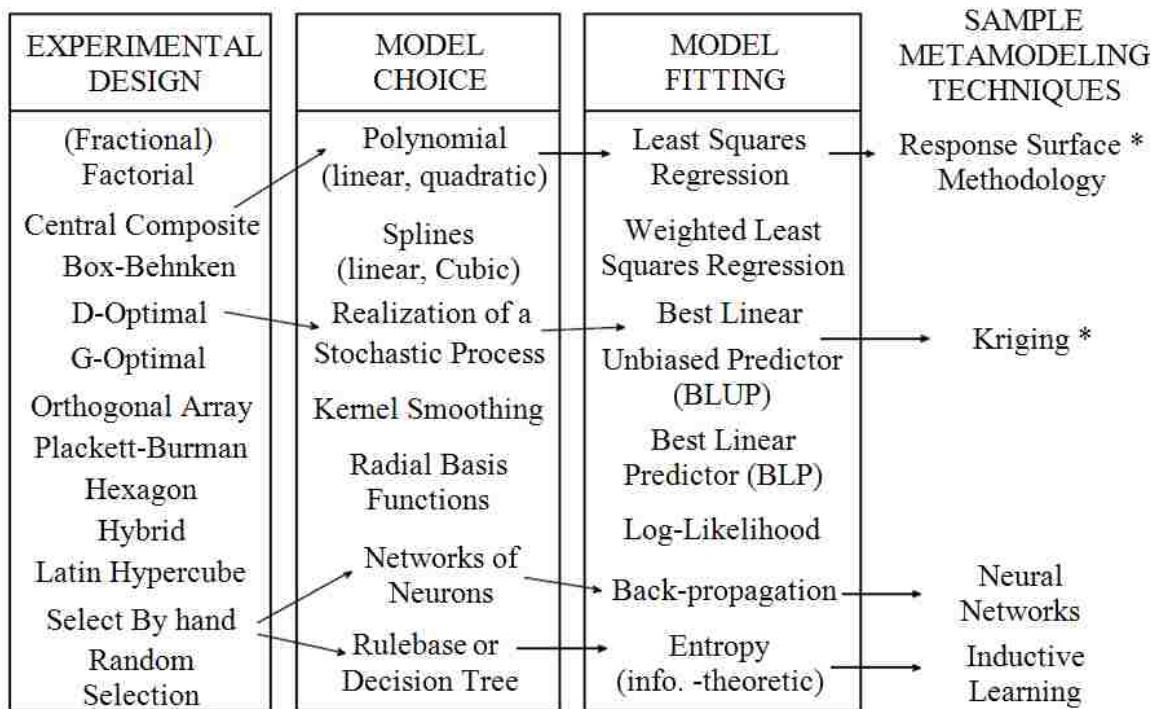
Fig. 2.12 Approximation techniques (Simpson et al., 1998)

- General form of a response surface:

$$y(\mathbf{x}) = f(\mathbf{x}) + \varepsilon$$

where:
  - $y(\mathbf{x})$ is unknown function of interest
  - $f(\mathbf{x})$ is a polynomial function of $\mathbf{x}$
  - $\varepsilon \sim$ i.i.d. $N(\mu=0, \sigma^2 \neq 0, \text{Cov}=0)$

Dome   Ridge

Rising Ridge   Saddle

Example Response Surfaces
(Box and Draper, 1987)

- Remarks:
  - $f(\mathbf{x})$ dictates "global" behavior of model
  - $f(\mathbf{x})$ is often first- or second-order polynomial
  - statistical measures (e.g., t-statistic and F-test) for validation may not be applicable when computer codes are deterministic

Fig. 2.13 Response surface methodology (i.i.d: independent and identically distributed) (Simpson et al.,1998)
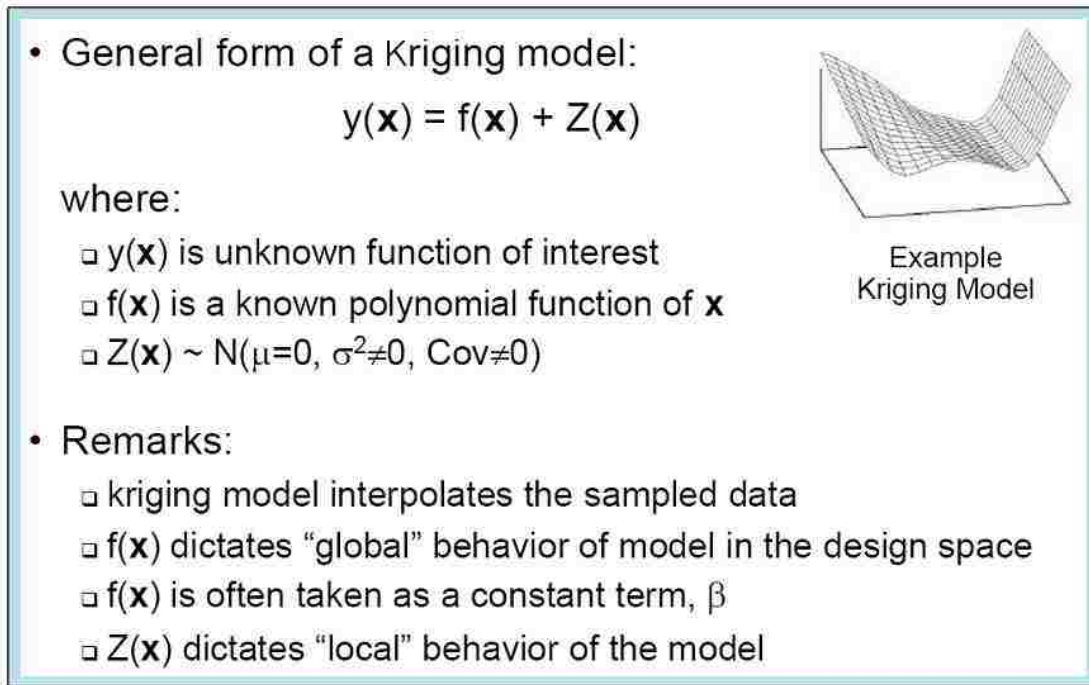
Fig. 2.14 Kriging model (Simpson et al.,1998)

2.3.6 Literature of multi-objective optimization in tube hydroforming

Li B. et al. (2006) developed a method to analyze the effects of the forming parameters on the uniformity of tube wall thickness by using the Taguchi method and FEA, and determined the optimal combination of forming parameters for the process. In his work, a free-form THF process was employed to find the optimal combination of forming parameters that leads to the highest bulge ratio and the lowest thinning ratio. A multi-objective optimization approach was proposed by simultaneously maximizing the bulge ratio and minimizing the thinning ratio and was solved by using a weighted goal-attainment method. Furthermore, Li B. et al. (2007) studied the robustness of the hydroforming process using the Taguchi method to minimize the variation and the average value of the thinning ratio. A two-dimensional cross-extrusion hydroformed tube was employed to illustrate the effectiveness of this approach. However, the influence of loading path was not investigated since the process did not include end feeding.

Ingarao et al. (2009) integrated numerical simulations, response surface methodology and Pareto optimal solution search techniques to design a complex Y-shaped tubular hydroformed part. In particular, the calibration of internal fluid pressure and counterpunch force was investigated with a view to achieving three different quality objectives: minimize thinning, reduce under-filling and improve the accuracy of the final fillet radius at the bulge zone corner. The weighted sum method was applied and integrated with the e-constraint procedure in order to perform a multi-objective optimization and to determine the optimal Pareto solutions.

Consequently, the quality requirements of tubular hydroformed parts have led to a challenging problem of developing multi-objective optimization algorithms to explore a process window or Pareto loading path with regard to the above-mentioned constraints and objectives.

2.4 Review of available software in metal forming optimization

Some applications of metal forming optimization using commercial software can be found in the literature. For instance, Imaninejad et al. (2005) utilized the commercial optimization software LS-OPT® and FE analysis to determine the optimum loading paths for closed-die and T-joint tube hydroforming. However, two major factors have hindered the development of automatic optimization of the THF process, namely a lack of smooth data exchange between commercial FEA programs and user-defined optimization algorithms and failure criteria, especially when dealing with multi-objectives.

Currently, optimization modules are only offered by some of the better-known FEA software packages, such as ABAQUS, PAM-STAMP, ANSYS and LS-DYNA. Although these software packages provide their own interface for users to modify the input parameters (process or material parameters) and extract the output data (stress/strain and structure response), the optimization algorithms and criteria are relatively limited. In the LS-OPT program (Stander et al., 2009) for example, the failure criterion is limited to processes with linear strain paths, and it is difficult for the user to optimize multi-stage

metal forming processes. Moreover, since the optimization algorithms are typically based on response surface methodology (RSM) and Artificial Neural Networks (ANN) (which will be discussed in more detail in section 2.5.2), it is difficult for the user to concurrently check the precision of the surrogate model for unknown data. Although a non-dominated sorting genetic algorithm (NSGA-II) was incorporated into the latest version of LS-OPT V3.4 for multi-objective optimization, the constraint-handling technique has not been explicitly introduced. Similar issues exist in other popular software packages such as ABAQUS and PAM-OPT.

As stated above, modern metal forming system design requires extensive use of simulation-based design and analysis tools (i.e. finite element analysis – FEA), which requires prohibitively long computational times to obtain results from such complex models, especially when seeking to optimize the forming process. In order to comprehensively explore the design space, a meta-model based optimization tool was introduced to THF and will be presented in Chapter 4.

Chapter 3: A Hybrid Forming Severity Indicator for Tube Hydroforming Simulation

To investigate the process parameters, it is necessary to understand what kind of failures might occur during the hydroforming process and how to prevent these failures from occurring. According to the literature review, the primary failures in tube hydroforming can be classified into three modes: necking/fracture, buckling/wrinkling and severe thinning.

3.1   Failure modes of THF

In the tube hydroforming process a tube must be shaped to conform to the inner surface of the hydroform die through simultaneous application of an internal fluid pressure and an axial compressive force (Fig. 3.1). The final shape of the part is determined by the die shape and by the way in which these parameters evolve throughout the hydroforming process.

Instability modes limit the extent to which the tube can be deformed, and occur when the stress and strain states in a part reach critical levels. The predominant failure modes in tube hydroforming are global buckling, localized wrinkling, necking or bursting, and folding of tubes, as illustrated in Fig. 3.2, and reported by Dohmann and Hartl (1996,1997), Koç and Altan (2002), Chu and Xu (2004a), Zhang (1999), and Xia (2001).
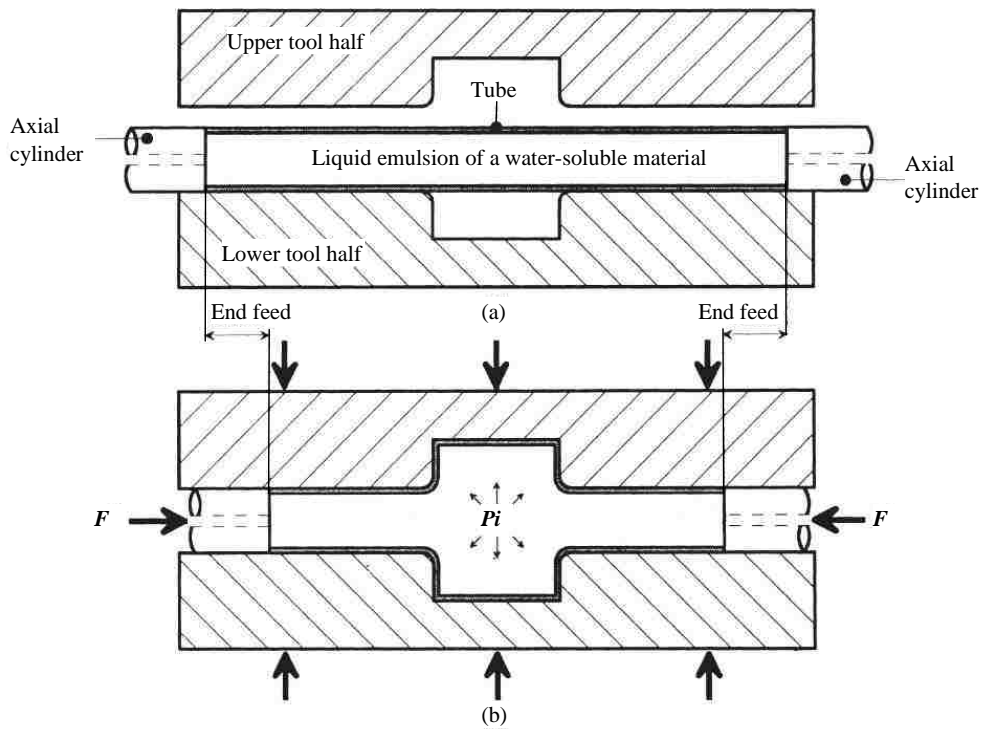
Fig. 3.1 The principle of tube hydroforming: (a) original tube shape and (b) final tube shape (before unloading). Adapted from Asnafi (1999).

Buckling   Wrinkling   Bursting   Folding-inwardly
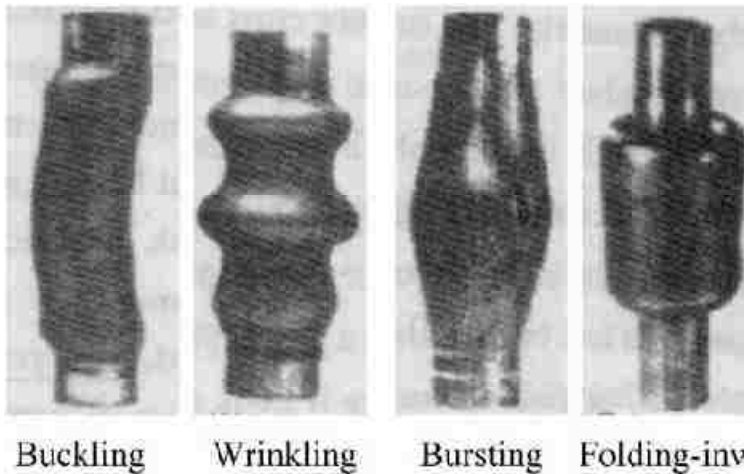
Fig. 3.2 Diagram showing various failure modes in tube hydroforming (Adapted from Dohmann and Hartl, 1996)

Buckling occurs when eccentric compressive forces develop in the tube and exceed the instability limit. Buckling in THF process occurs during the initial stages of deformation when strain levels are small (Koç and Altan, 2002). With regard to the loading path,

buckling takes place at this stage when high axial load might be accompanied by an insufficient increase of section modulus of the tube (Zhang, 1999). The risk of buckling increases for longer tubes with thicker walls. To avoid buckling, simple estimations of permissible load for the corresponding free length of the tube can be made based on analytical assumptions (Koç and Altan, 2002).

Wrinkling is usually observed during both initial and intermediate stages of hydroforming and is not related to the length of the tube, but to the wall thickness (Koç and Altan, 2002). Wrinkles are sometimes unavoidable in the intake regions of the die, but can later be eliminated by increasing the internal pressure. Wrinkling occurs because of excessive axial loading or insufficient internal pressure. Nevertheless, some wrinkles cannot be ironed out or could require substantially higher internal pressure, which might not be attainable due to limited press clamping load capability (Sorine, 2007).

Bursting occurs when a tube reaches a critical amount of expansion under the influence of large tensile forces (Koç and Altan, 2002). Fracture is often preceded by necking. Once necking starts, the deformation and thinning become non-uniform throughout the part. As a consequence, strain localizes causing necking to proceed very rapidly towards fracture. This process is highly sensitive to friction between the tube and the die wall. High friction forces can cause material to stick to the die surface, decreasing its flow into the deformation zone. This in turn triggers strain localization and subsequent splitting of the material (Sorine, 2007).

Inward folding occurs when tubes are expanded in dies where tube wall material is forced into the die by the end-feed punches, or in areas of heavily-expanded thin tubes. Folds can occur under excessively high axial force (Dohmann and Hartl, 1997).

It was noted that even though the cause of wrinkling is also excessive compressive loading, the way buckling and wrinkling take place are quite different depending on the geometrical configuration of the tubular component. Buckling of tubes as a column is observed when a tube is long and has relatively thick walls. Wrinkling tends to occur in tubes with thin walls. However, there is no definite boundary between buckling and

wrinkling conditions since they are both dependent on a combination of many other factors such as material, boundary conditions, geometry, imperfections and loading types (Koç and Altan, 2002). In tube hydroforming, plastic buckling and wrinkling analyses are common interests. On the other hand, in aircraft and oil industry, structural (elastic) instability is the case.

3.2   Strain based forming limit diagram (FLD)

During the last few decades, different methods have been proposed to assess the severity of metal forming processes. The most useful of these has been the forming limit diagram (FLD). This method is widely used in factory and research laboratories because of its simplicity and ease of use.

The concept of FLDs, as it is known today, was developed by Keeler and Backofen (1963) and extended by Goodwin (1968). Keeler and Goodwin generated FLD in principal strain space in which a forming limit curve (FLC) represents the limit of necking for a given sheet metal (Fig. 3.3). Since then, researchers have developed various experimental and analytical techniques to determine the FLC for a given sheet material. A comprehensive overview of these techniques is given by Green and Black (2002). In the metal forming industry, FLD has been widely used to evaluate the forming severity of stamped components, and this has reduced the lead time and improved the process robustness and product quality (Green, 2008). Furthermore, the FLC was also shown to accurately predict the necking of straight tubes tested in free-expansion.
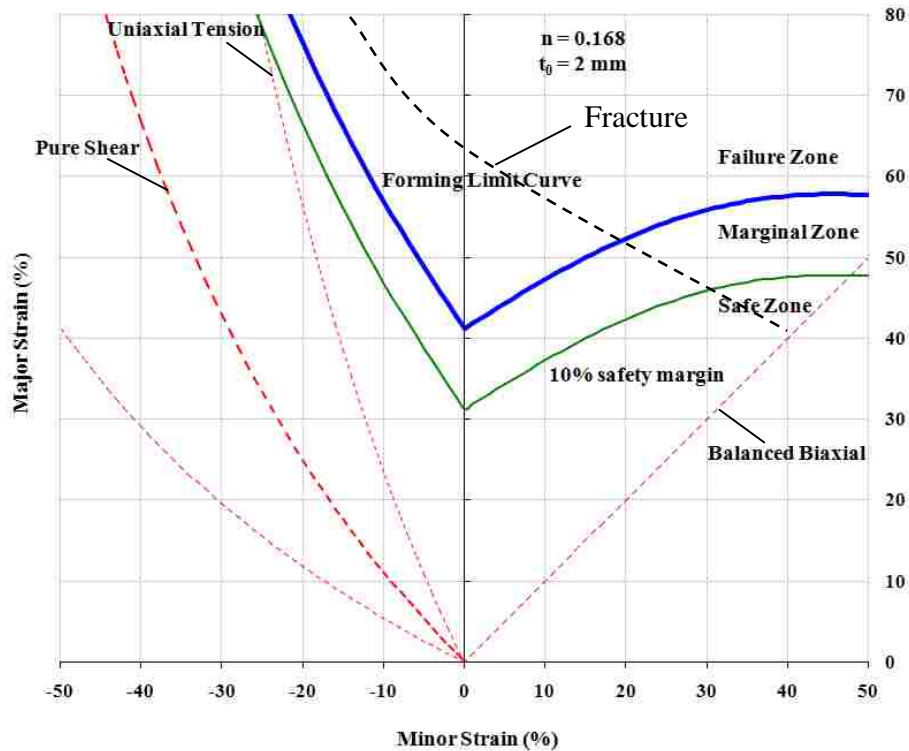
Figure 3.3 The conventional forming limit diagram (FLD) for a low-carbon steel sheet

Building on their observations of plastic instability in low-carbon steel sheets, Keeler and Brazier (1977) developed a very simple empirical relationship that predicts the position of the FLC (i.e. the plane-strain intercept) as a function of the terminal strain hardening coefficient and the initial thickness of the sheet:

$$FLD_0 = (23.3 + 14.13t) \cdot (n/0.21) \tag{3.1}$$

Due to its accuracy, the Keeler-Brazier relationship is still very much in use today, particularly in press-shop applications.

Three approaches have been proposed and utilized to meet the challenge of accurately predicting the FLCs, which are bifurcation analysis, damage model analysis and Marciniak and Kuczynski analysis (Marciniak and Kuczynski, 1967). Bifurcation analysis initiated from the work of Hill (1952), followed by Stören and Rice (1975), Hutchinson and Neale (1978a, 1978b). Damage model analysis assumes microdefects in the material and forming limit is predicted when the evolution of these microdefects

reaches a limit. Tjotta (1992) implemented a damage model for void growth during plastic deformation in finite element model to predict the onset of failure in uniaxial tension and plane strain tension. Huang et al. (2000) adopted a macroscopic yield criterion for anisotropic porous sheet metal to develop a failure prediction methodology that can be used to investigate the failure of sheet metals under forming operations. The M-K analysis was employed to predict failure by assuming a higher void volume fraction inside the randomly oriented imperfection band.

3.2.1 Path dependence of strain-based forming limits

In certain forming processes such as tube bending and hydroforming, the material is subjected to complex, non-linear strain paths. Several researchers (Nakazima,1971;Ghosh and Laukonis,1976;Arrieux et al., 1982;Graf and Hosford, 1993a, 1993b,1994) have demonstrated that complex strain path cause the shape and position of the FLC's to change significantly (Fig. 3.4). This makes it difficult and ambiguous to determine the limit strains for processes that lead to complex strain paths. The development of computational models for complex strain-paths following the Marciniak-Kuczynski (M-K) approach has become an active research field since the early 1980's (see Barata et al., 1985). More recently, Butuc et al. (2002, 2003, 2006), developed a general computer code to predict the FLC in the case of complex load paths using various hardening models (both phenomenological – Swift, Voce, and miocrostructural ones). Cao and Yao (2000, 2002) analyzed the influence of the changing strain paths on the limit strains. A more extensive review of this subject can be found in Green and Stoughton (2004) and Green (2008).
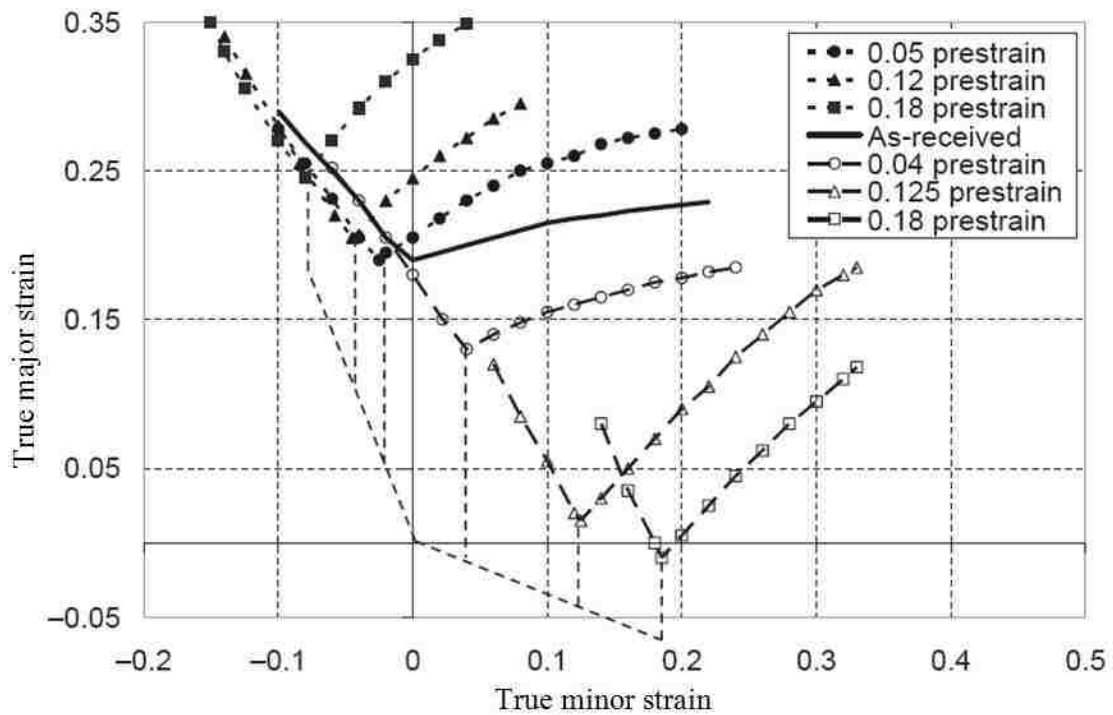
Figure 3.4 Strain path-dependency of FLC (Adapted from Graf and Hosford, 1993a)
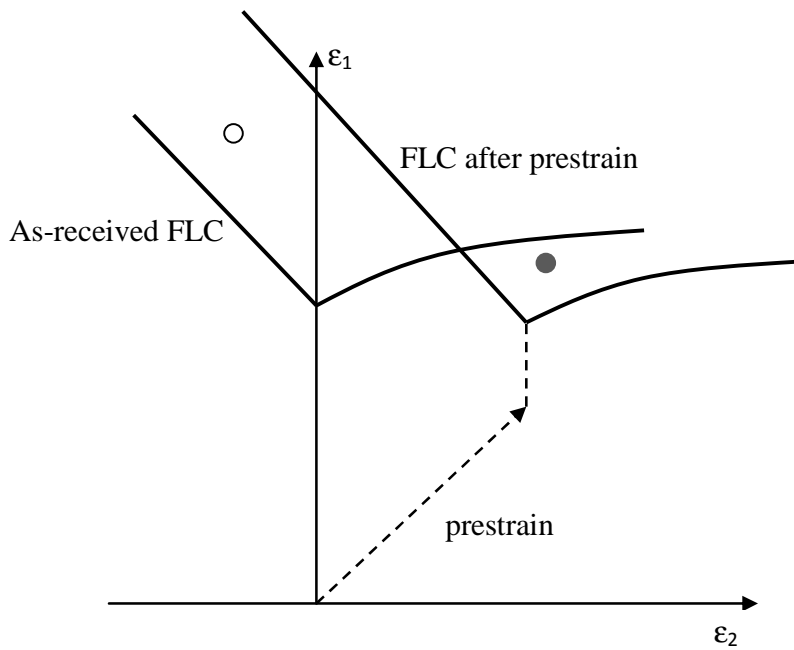
Fig 3.5 Prestraining in biaxial tension shifts the FLC down and to the right (Adapted from Hosford and Caddell, 2007).

Figure 3.5 illustrates the importance of using the correct FLC to evaluate the forming severity of a part that was subject to a non-linear strain history. This figure shows that prestraining in biaxial tension shifts the FLC down and to the right. After the prestraining strains corresponding to the open circle would be possible, but those corresponding to the black dot would cause failure. Therefore, it is generally accepted that the FLD should only be used in applications where the strain path is quasi linear (Graf and Hosford, 1993a, 1993b,1994) .

3.3   Stress-based FLD

Similar to the forming limit diagram, a forming limit stress diagram (FLSD) was proposed by Arrieux et al. (1982) and Zhao et al. (1996). Their work showed that regardless of the shape of the as-received FLD and the type of pre-strain (linear, bilinear and trilinear straining) imposed, the FLSDs were almost all identical. In contrast, when plotted in strain space the FLD was very sensitive to the type of strain path.

Stoughton (2000, 2001) generalized the stress-based forming limit criterion and established a procedure for determing the FLSD from the as-received FLD. The uniqueness of the proposed stress based criterion was verified using data from several

(a) FLD   (b) FLSD
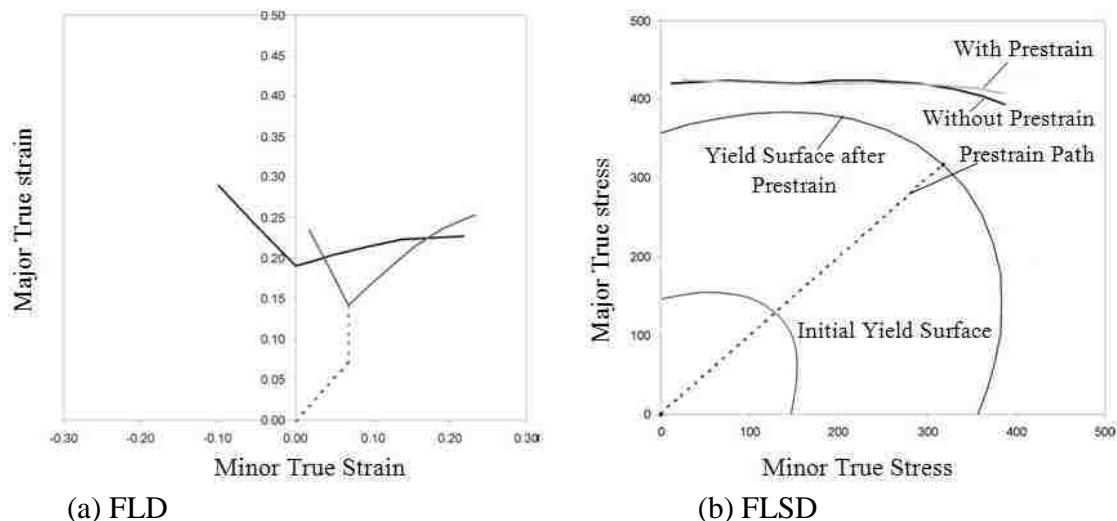
Fig. 3.6 (a) Comparison of the as-received FLC with that after a prestrain to 0.07 strain in equibiaxial tension, and (b) the corresponding FLSC in stress space (Adapted from Stoughton and Zhu, 2004)

non-proportional loading paths for both aluminum and steel alloys. Fig. 3.6 shows that the stressed-based FLC is strain-path independent, indicating that the FLSC can be used to assess forming severity in cases of non-proportional loading. In particular, the FLSC is very well suited for formability analysis after a virtual forming simulation since the numerical simulation code computes the stresses in the part: the stresses in the as-formed component can be directly compared with the FLSC.

One drawback of using the FLSD is that the forming stresses can rarely be measured experimentally. In complex forming operations, strains must be measured on the part and then converted to stresses using elastic–plastic constitutive equations after which the stresses can be compared to stress-based forming limits. Another concern arises when applying stress-based forming limits to dynamic events, such as crashworthiness studies, because of the strong oscillations in stress due to stress wave propagation. To avoid this issue, Gholipour et al. (2004) considered the application of a damage-based constitutive model, namely the Gurson–Tvergaard–Needleman model, to predict damage evolution over the forming and impact history. It was shown that this approach is useful in predicting formability of the alloys considered in their research, under combined tube bending and hydroforming operations.

3.4   General objectives for defect-free tube hydroforming

In tubular hydroforming, a first priority is to produce a defect-free product while satisfying the specified geometric constraints. So, it is necessary to define objective functions in terms of accepted quality standards. Consequently, general failure objectives that consider necking/fracture, wrinkling and severe thinning were proposed to evaluate the quality of a hydroformed part.

Since the forming limit stress curve (FLSC) has been shown to be almost insensitive to strain path effects, an optimization technique should make use of the FLSC to assess the severity of the forming process in order to be more widely applicable.

In this work, the FLSC for a given tube material was determined from the experimental strain-based FLC by following the mapping procedure outlined by Stoughton (2000). Furthermore, Stoughton & Yoon (2005) pointed out that the most critical stress states attained during the forming simulation ought to be evaluated against the forming limit stress curve (FLSC), and not merely the stress states recorded for post-processing purposes. Therefore, in order to account for the widest possible range of failures, a multi-objective failure criterion was adopted to evaluate the effects of load path, and the types of failures considered were, necking or splitting in the tube wall, wrinkling and severe thinning.

The objective functions were taken to be the difference in terms of major stress (i.e. d_f) (Fig. 3.7b) between the maximum stress in the formed part and the FLSC at the corresponding minor stress, the sum of the total distance d_w, and the sum of the square of distance d_{th} as defined by equations (3.2) to (3.5), where the notation i (i=1, 2, ...N) is the element number, and N is the total number of elements in the tube.

Objective function for necking or fracture:

$$\sigma_1^{max} = Max(\sigma_1^1, \sigma_1^2, ..., \sigma_1^N)$$

$$Obj\_f = d_f = \left| \sigma_1^{max} - \sigma_f \right| \tag{3.2}$$

where σ_1^{max} is the numerically calculated maximum principal stress in element i (i=1 to N) and σ_f is the corresponding forming stress limit (Fig. 3.7b). The optimization will seek to maximize this objective function because a greater distance signifies a reduced tendency for plastic instability or fracture to take place. However, the maximum principal stress may be greater than the stress limit. In this case, a scale coefficient k is introduced to
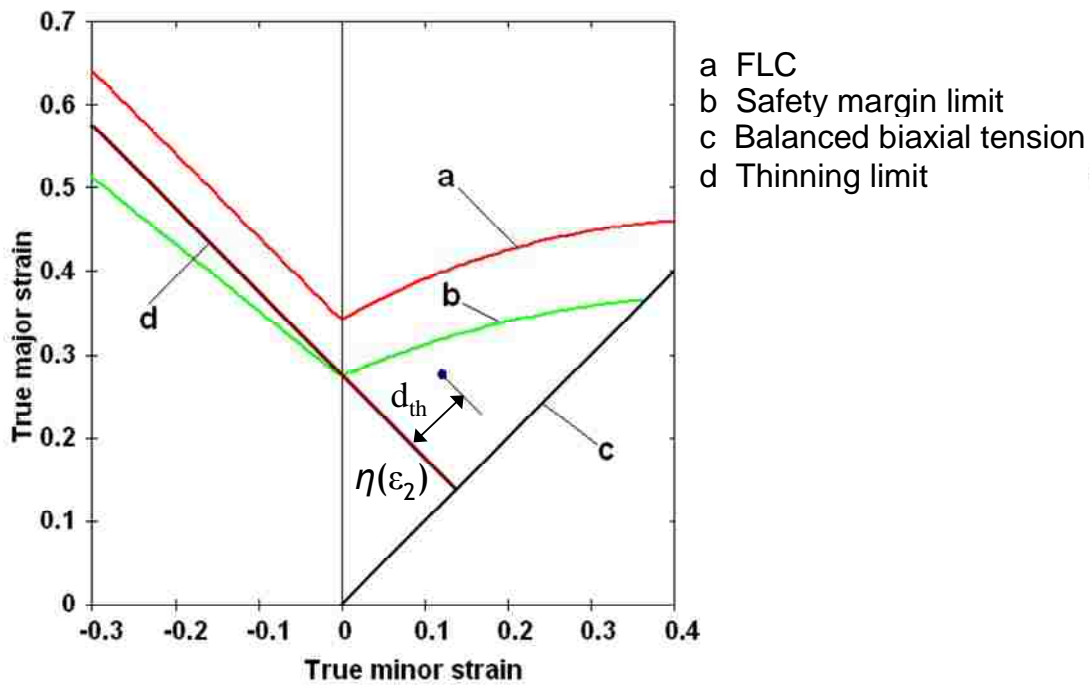
a)
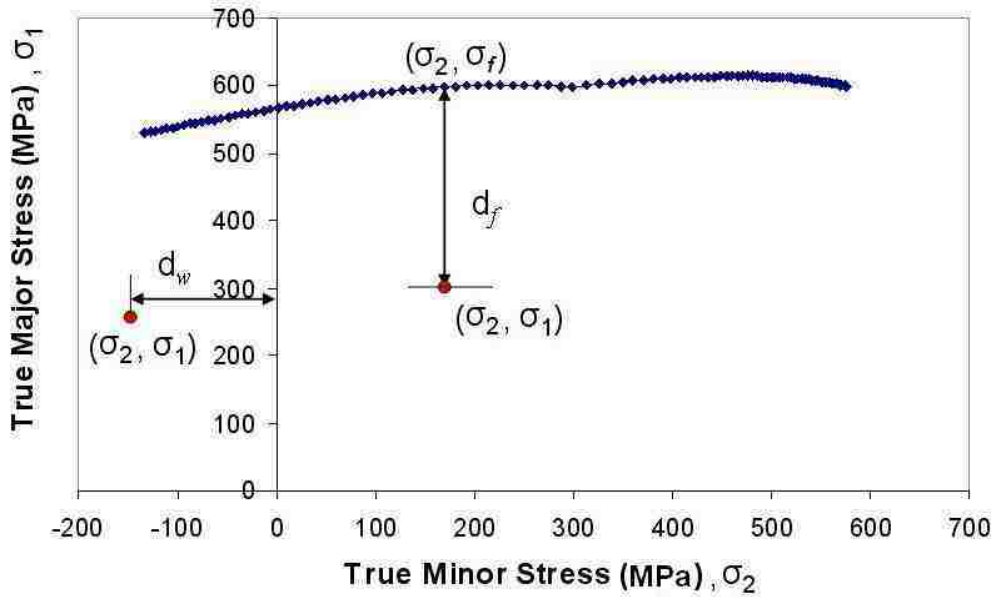
b)

Fig. 3.7 Graphical interpretation of the objective functions on a) the FLD and b) the FLSD

scale up the stress limit σ_f. Therefore, for the sake of convenience, Equation (3.2) is rewritten as a minimization in Equation (3.3):

$$f_1 = Obj\_f = \frac{1}{d_f} = \frac{1}{\left|\sigma_1^{max} - k\sigma_f\right|} \tag{3.3}$$

where k is a scaling factor intended to prevent the maximum stress from exceeding the stress forming limit; the value of k is determined by the user's experience and may vary between 1.1 and 2.5.

Objective function for wrinkling:

$$f_2 = \begin{cases} Obj\_w = \sum\limits_{i=1}^{n}\left|d_w^i\right| = \sum\limits_{i=1}^{n}\left|\sigma_2^i\right| & \sigma_2^i < 0 \\ Obj\_w = 0 & \sigma_2^i \geq 0 \end{cases} \tag{3.4}$$

where d_w is the distance from a point (σ_1, σ_2) in stress space to the major stress axis as shown in Fig. 3.7b.

Objective function for severe thinning:

$$f_3 = \begin{cases} Obj\_th = \sum\limits_{i=1}^{n}(d_{th}^i)^2 & \varepsilon_1^i > \eta(\varepsilon_2^i) \\ Obj\_th = 0 & \varepsilon_1^i \leq \eta(\varepsilon_2^i) \end{cases} \tag{3.5}$$

where ε_1 is the major strain in element i, and $\eta(\varepsilon_2)$ is the thinning limit d (Fig. 3.7a). d_{th} is the minimum distance from a point $(\varepsilon_1, \varepsilon_2)$ in strain space to the limit d. In order to optimize the hydroforming process, the minimum value of each of these objective functions is sought.

When it comes to a specific hydroforming application, this model is sufficiently flexible to add specific objectives and constraints to the above general objectives. When hydroforming T-shaped and Y-shaped tubular parts, for example, the requirements related to a specified bulge height, the conformity of the final part and the die, and the wall thickness distribution in the final part would also be an indispensable geometrical objective.

Chapter 4: Multi-objective Optimization and Sensitivity Analysis for Tube Hydroforming Using Normal Boundary Intersection

4.1   Introduction

In order to avoid the defects caused by excessive internal pressure or inadequate end-feed forces, it is necessary to ensure that these process parameters are kept within a small process window (Fig. 4.1) throughout the hydroforming operation. When the forming process is not sufficiently robust the part may fail as a result of necking or fracture, wrinkling or severe thinning, as mentioned in the previous chapter. Therefore, the determination of the loading path (i.e. pressure vs. end-feed displacement) plays a vital role in the production of quality hydroformed components. Consequently, the objective of this chapter is to establish a methodology to determine the optimal loading path for tubular hydroformed parts.
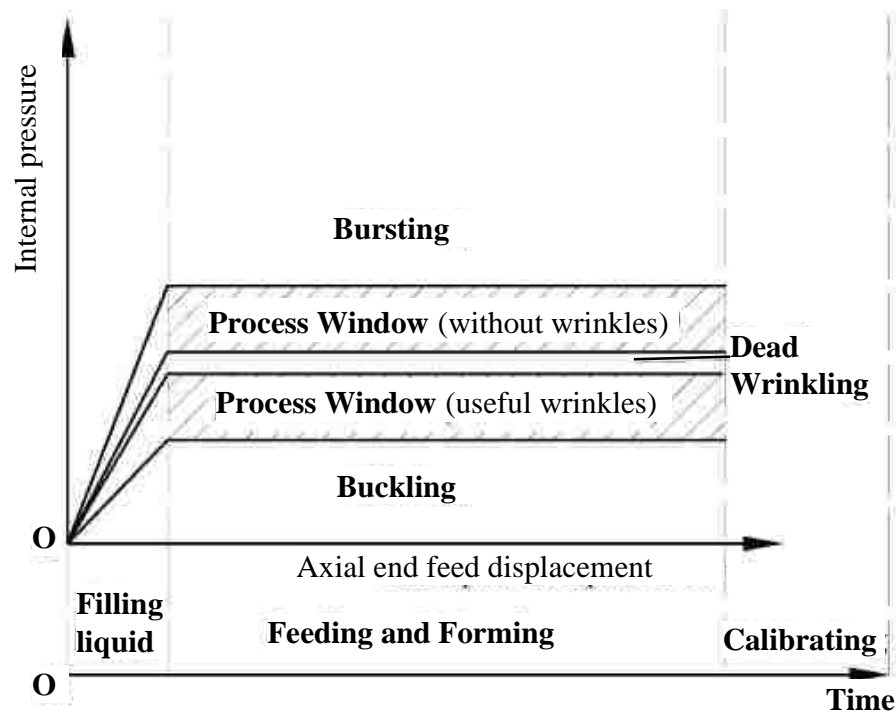
Fig. 4.1 Process windows for tube hydroforming. (Adapted from Yuan et al., 2007)

To correctly carry out tube hydroforming, it is advantageous to investigate the sensitivity of the tube responses to variations in geometrical dimensions, material properties and process parameters (e.g. loading path). Since there is no explicit relationship between forming severity and loading path, it is very difficult to perform a sensitivity analysis by analytical methods. Experimental methods would be very expensive and at times, impossible. Numerical simulation is an effective and less expensive way to carry out the sensitivity analysis.

The Taguchi method has been shown to be an effective design of experiments for a variety of industrial applications. It employs an orthogonal array to study a large parameter space using only a small number of experiments. Another benefit of the Taguchi approach is that it determines the relative contribution of each factor to process reliability by the analysis of variance (ANOVA) statistical method. This allows design efforts to be concentrated on the most sensitive factors. Therefore the optimal loading path can be determined by carrying out finite element simulations of the hydroforming process, in combination with the Taguchi method.

It can be seen from the literature review (Chapter 2), that most optimization efforts have been limited to a single objective and fail to consider all the quality criteria for hydroformed parts. Indeed, after a comprehensive review of optimization of metal forming problems, Bonte et al. (2008) state that "modelling is mostly done in an arbitrary way, addressing the specific problem of the considered metal forming process only. Furthermore, the selection of the optimization algorithm is also mainly related to that specific problem". Moreover, multiple design objectives may be difficult to describe with an explicit function. The optimization of loading path is a multi-objective decision-making problem, and as such, it may have a set of alternative solutions rather than a single optimal solution.

When dealing with multi-objective optimization problems (MOPs), classical optimization methods such as multi-criterion decision-making methods suggest converting MOPs to a single-objective optimization problem by emphasizing one particular Pareto-optimal

solution. Common multi-objective solution methods are the weighted sum method, the å-constraint method and the goal attainment method. In addition, there are a variety of multi-objective genetic algorithms in the literature, such as NSGA-II, SPEA, and PAES. But apart from NSGA-II, which is implemented in LS-OPT® (Stander et al., 2009) for the optimization of metal forming processes, no other algorithm appears to have been used to optimize tube hydroforming. A further investigation of NSGA-II algorithm will be presented in the next chapter.

This chapter begins with the algorithm of normal boundary intersection . The next section describes the proposed methodology for determining the optimum loading path in regard to achieving defect-free parts. In the following section, multi-objective functions are defined on the basis of failure criteria that are used to evaluate the quality of thin-walled structures. In the next section, the proposed optimization methodology is applied to the corner-fill benchmark test in which a straight tube is expanded in a die with a square cross-section. Finally, some conclusions are drawn in the last section.

4.2   Response surface methodology

The basic idea of response surface methodology (RSM) was introduced in chapter 2. It was used to construct surrogate approximations to each objective and constraint. In this chapter, a second order polynomial with the following expression was used:

$$y = \beta_0 + \sum_{i=1}^{n} x_i \beta_i + \sum_{i=1}^{n} \beta_{ii} x_i^2 + \sum_{p=1}^{n-1} \sum_{i=p+1}^{n} \beta_{pi} x_p x_i + \varepsilon \tag{4.1}$$

The regression coefficients $\overline{\beta}$ of the quadratic response surface are defined as follows:

$$\overline{\beta}_0 = \frac{1}{k} \sum_j y_j = \overline{y} \qquad ; \qquad \overline{\beta}_i = \sum_j x_{ij} y_j \bigg/ \sum_j x_{ij}^2$$

$$\overline{\beta}_{ii} = \sum_j x_{ij}^2 y_j \bigg/ \sum_j \left(x_{ij}^2 \right)^2 \qquad \overline{\beta}_{pi} = \sum_j x_{pj} x_{ij} y_j \bigg/ \sum_j \left(x_{pj} x_{ij} \right)^2 \tag{4.2}$$

4.3   Normal Boundary Intersection

The NBI method is a preferred approach for multi-objective optimization and was developed by Das and Dennis (1998). NBI and its derivatives offer the advantage that they are applicable for all dimensions, produce points evenly distributed on the Pareto surface and can be combined with a Pareto filter to identify non-Pareto points on the boundary of the feasible region (Cramer et al., 2006). However, NBI is seldom used for tube hydroforming applications, no doubt because of its complex theoretical background and the fact that explicit MOP software is not readily available.

Some terminologies were defined herein to understand how NBI works. The *Convex Hull of Individual Minima* (CHIM) is defined as the set of points that are linear combinations of $F(x_i^*) - F^*$ for $i=1, \ldots, m$, where x_i^* is the global optimal solution of $F_i(x)$ and F^* is the *shadow minimum* (or *utopia point*), i.e. the vector containing the individual global minima of the objectives (Seferlis and Georgiadis, 2004). The pay-off matrix is defined as an $m \times m$ matrix whose i^{th} column is $F(x_i^*) - F^*$. Given a vector β, $\Phi\cdot\beta$ defines a point on the CHIM. Mathematically, the so-called NBI subproblem is formulated as:

Maximize t_N (4.3)

Subject to:

$$\Phi \cdot \beta + t_N \cdot \hat{n} = F(x) - F*$$ (4.4)

and the same set of constraints given by Eq. (2.7). $\hat{n}$ is the unit normal to the CHIM pointing to the origin (objectives are redefined with the shadow minimum shifted to the origin), and t_N is a scalar such $\Phi \cdot \beta + t_N \cdot \hat{n}$ represents a point on that normal. This subproblem has to be solved for various β. The global solution to this problem gives the intersection point between the normal and the boundary of the objectives space closest to the origin. In practice, the algorithm uses a quasi-normal direction given by an equally weighted linear combination of the columns of Φ_i multiplied by –1.

There are two steps for implementing the NBI algorithm:

(1) Find the global of each objective individually—shadow minima problem;

(2) Find the "best" set of tradeoff solutions between the objectives.

This method first considers each objective function separately, as an individual single-objective sub-problem. Each sub-problem is solved using a single-objective solver. Afterwards all the NBI sub-problems are solved successively and the "best" set of tradeoff solutions is found. A more detailed description of this method can be found in Rigoni (2004).

Take two objectives of engine output for example. The objectives are: Maximizing the torque (TQ) and minimizing the NOx emissions. The objectives space is shown in Figures 4.2 and 4.3. The figures also show graphically the working of the NBI method, and the aspect of one single NBI-subproblem.

In the first step, the best values of the two objectives were found: point T maximizes the first objective function f_1, and point N minimizes the second objective f_2: point F^* is then the utopia point.

In the second step, the NBI subproblem of Eq. (4.4) was solved and the tradeoff solutions were found. In this example the convex hull of individual minima (CHIM) corresponds to the line segment $\overline{NT}$. Any NBI subproblem is specified giving its barycentric coordinates (weights). For example the NBI subproblem outlined in Fig. 4.3 corresponds to $\beta = (0.5, 0.5)$. These values locate the position of point H along the CHIM: in fact the components of the vector β are, respectively, the normalized lengths of the segments $\overline{NH}$ and $\overline{TH}$ (the normalization is made over the length of the segment $\overline{NT}$). The line n is the quasi-normal direction passing through H, and it represents the constraints introduced by the NBI subproblem. Point P is then the solution of the single-objective constrained NBI-subproblem. The length of the segment HP represents the new variable t_N introduced by the NBI subproblem. Consequently, the Pareto front was found by solving all the subproblems (Fig. 4.3 b).
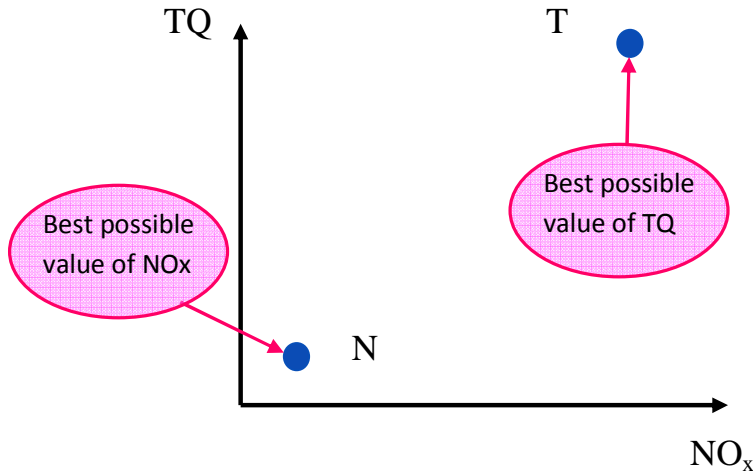
Fig. 4.2 Finding the shadow minima in step 1 (represented by two dots N and T)
(Adapted from http://biounder.kaist.ac.kr/board/bx/docs/matlabman/cage.pdf)
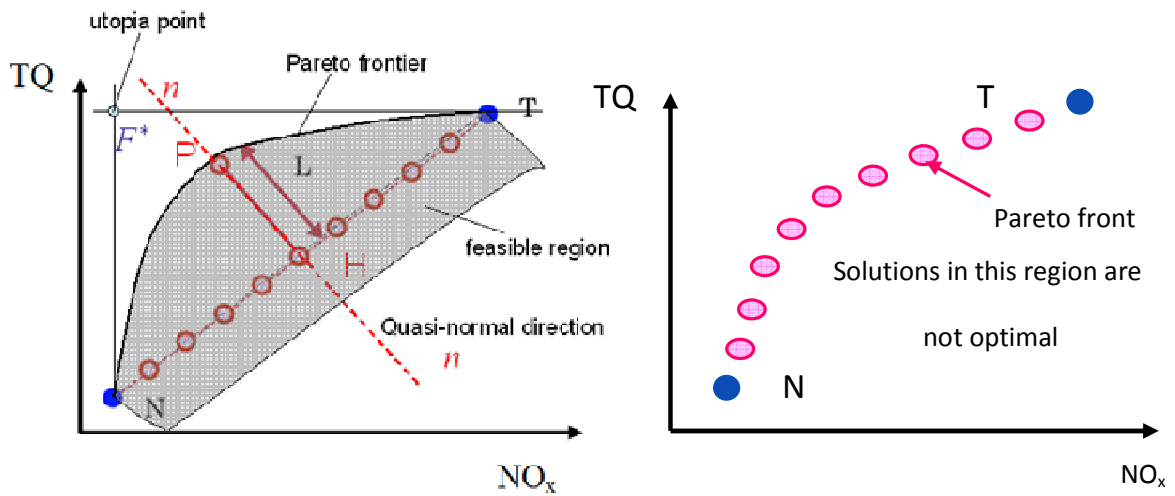
(a) NBI subproblem   (b) Pareto front

Fig. 4.3 Finding the best set of trade-off solutions in step 2

(Adapted from http://biounder.kaist.ac.kr/board/bx/docs/matlabman/cage.pdf)

L_2 norm

A widely used method known as the L_p norm proposed by Eschenauer *et al.* (1990), was
used to find one solution among the various Pareto solutions that has a minimum value.

60

As shown in Fig. 2.7, the L_2 norm represents the minimum distance from the Pareto frontier to the utopia point and the optimal compromise solution is thus obtained as the minimum L_2 norm (Pareto) solution. Consequently, this method is generalized for the determination of Pareto optimum in n-dimensional space with n objectives ($n \geq 2$). This solution was determined according to the following expression:

$$\text{Minimize } L_p = \left[\sum_{i=1}^{m} (f_i(x) - f_i^*)^p \right]^{1/p} \tag{4.5}$$

where $f_i(x)$ and f_i^* are the values of the ith objective function at a feasible point and at the Utopia point ($f_i^* = 0$ in this case), respectively. The most common applications of the L_p norm are the L_1, L_2 and L_∞ norms (where $p=1$, 2 and ∞). In this study, the L_2 norm ($p=2$) was used: this method is also referred to as the minimized distance method.

4.4   A RSM based optimization algorithm for tube hydroforming

The procedure for carrying out the optimization is described as follows:

1. Identify the design space and implement a first run with L9 orthogonal array (OA)

2. Carry out virtual experiments using a DOE and FEA to produce samples

      (i) Sensitivity analysis with ANOVA to select key factors

      (ii) Additional run with L18 OA to create a refined parameter space

3. Construct a surrogate multi-objective model with RSM

4. Optimize and obtain the Pareto solution set

5. Verify the optimum result (with minimum L_2 norm value) with a FEA.

6. Repeat Step 2 to Step 5. Stop when the accuracy criterion is met and go to Step 7

7. Last run with minimum value of L_2 norm, output results.

A flowchart of the procedure is shown in Fig. 4.4. Fig. 4.5 illustrates the interface with FEA to calculate the objectives of necking/fracture, wrinkling and severe thinning.
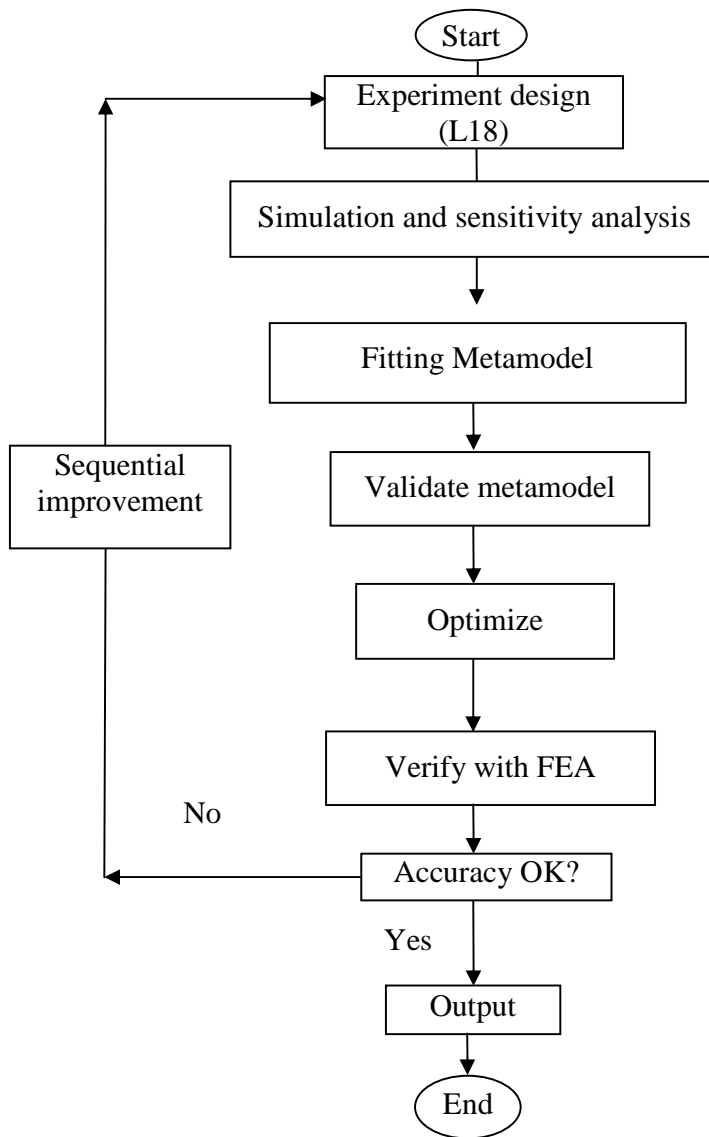
Fig. 4.4 Metamodel based optimization
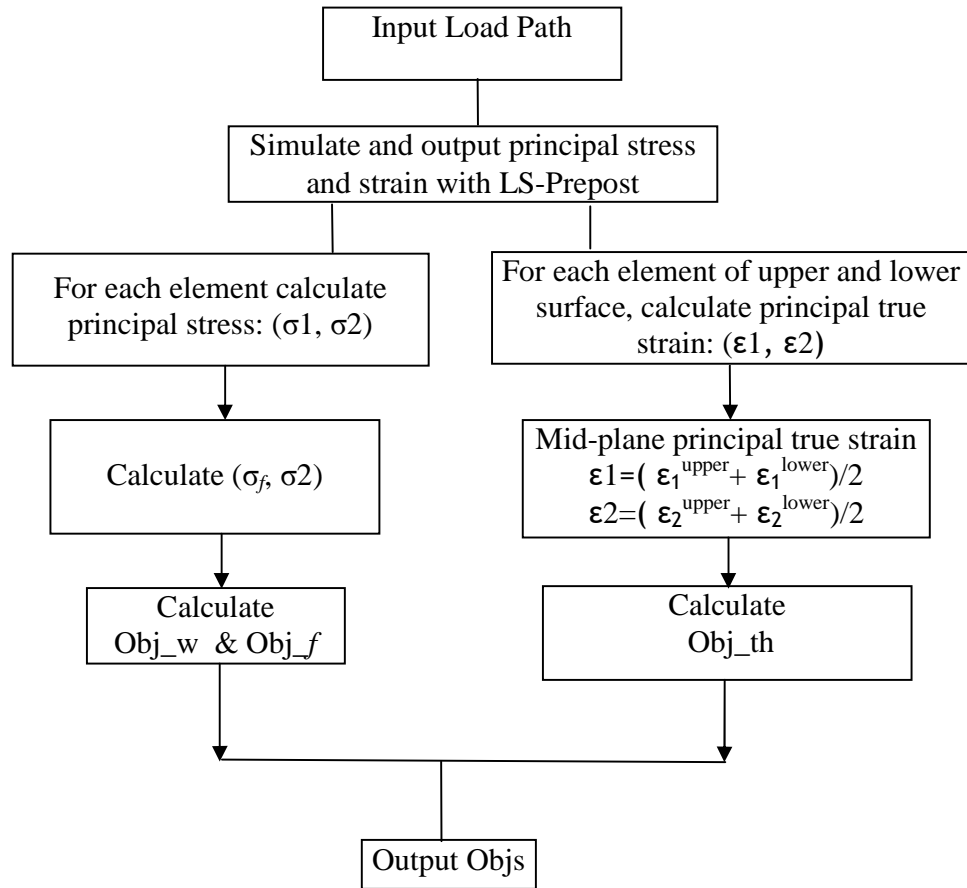
Fig. 4.5 Interface with FEA to calculate the objectives of necking/fracture, wrinkling and severe thinning

4.5 Implementation

The proposed algorithm described in Section 4.4 was implemented in MATLAB R2008a. After obtaining the RSM models, the NBI optimization algorithm in the Model-Based Calibration Toolbox was selected to search for the Pareto optimal solutions.

4.6 Application to straight tube hydroforming

In this section, the optimization model is applied to the hydroforming of a straight tube in a die with a square cross-section.

4.6.1 Objectives and optimization model for tube hydroforming with square die

As the pressure inside a tube is increased, the tube wall gradually expands into the corner of the square hydroforming die and the radius of the tube wall decreases. The corner radius is an important geometric factor that correlates with the formability of the tube: the more formable the tube material is, the smaller the corner radius that can be achieved. In addition to the three objectives of necking/fracture, wrinkling and severe thinning listed in Eq. (3.3)-(3.5), for the corner filling simulation, another objective function for the corner radius was defined as:

$$f_4 = Obj\_r = Radius\,(N1, N2, N3) \tag{4.5}$$

where $N1$, $N2$ and $N3$ (Fig. 4.6) are three nodes located in the corner of the part at the mid-section of the expanded region. It was assumed that the circle that passes through these three points is tangent to the adjacent die surfaces.
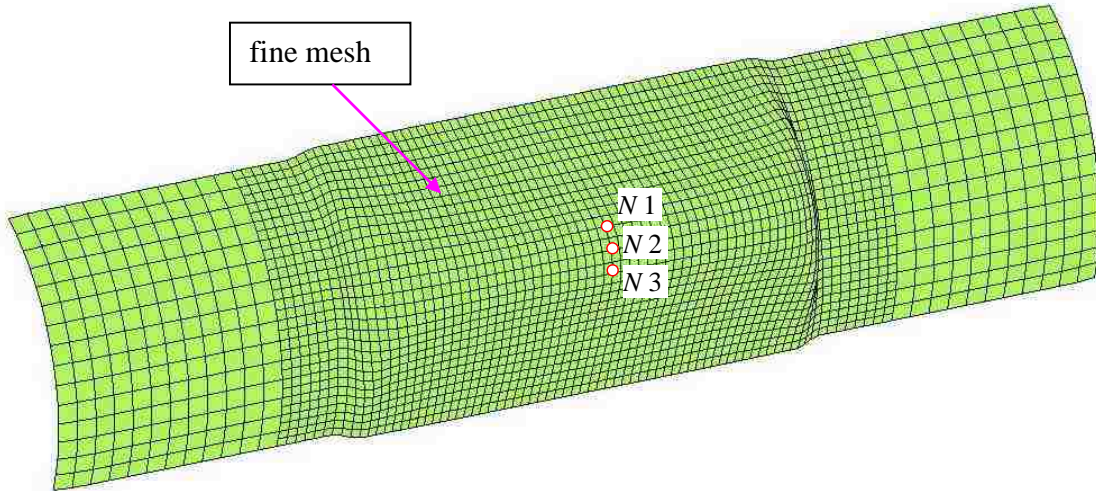
Fig. 4.6 Location of three nodes used to measure the corner radius

Consequently, this hydroforming problem yielded the following mathematical optimization model:

Find $\mathbf{X} = [x_1, x_2, ..., x_n]^T$

to minimize MOP: $F(\mathbf{X}) = (f_1(\mathbf{X}), f_2(\mathbf{X}), f_3(\mathbf{X}), f_4(\mathbf{X}))$ \hfill (4.6)

subject to $\quad g_1(X) = f_1(X) - 0.6 \le 0$, $\qquad g_2(X) = 0.2 - f_1(X) \le 0$

$$g_3(X) = f_2(X) - 0.6 \le 0 \quad , \qquad g_4(X) = 0.2 - f_2(X) \le 0$$

$$g_5(X) = f_3(X) - 0.6 \le 0 \quad , \qquad g_6(X) = 0.2 - f_3(X) \le 0 \qquad (4.7)$$

$$g_7(X) = f_4(X) - 0.6 \le 0 \quad , \qquad g_8(X) = 0.2 - f_4(X) \le 0$$

$$X^L \le X \le X^U$$

where $f_i(X)$ (i=1 to 4) are normalized values between 0.2 and 0.6 determined by RSM corresponding to equations (3.3) to (3.5) and (4.5), respectively. The normalized range [0.2, 0.6] was determined to avoid numerical problem related to dividing by zero, which occurs often in the normalized region of [-1,1]. Parameter variables X is also a normalized vector of pressure (with (n-1) nodes, i.e. x_1 to x_{n-1}) and end feed (x_n). The vector length n is determined after the pressure nodes were decided by sensitivity analysis.

4.6.2 Finite Element Simulation with LS-DYNA®

In this study, straight tube hydroforming in a square die under various load paths was simulated using the finite element method. This simple forming process is commonly referred to as the corner-fill test. Fig. 4.7 shows a FE model of the corner-fill test set up with LS-DYNA® (Hallquist, 2007). Corner filling is generally carried out to investigate the formability of the tube material in the hoop direction of the tube (i.e. cross section A-A). In cross-section B-B (Fig. 4.7), the tube wall is subject to bending as well as
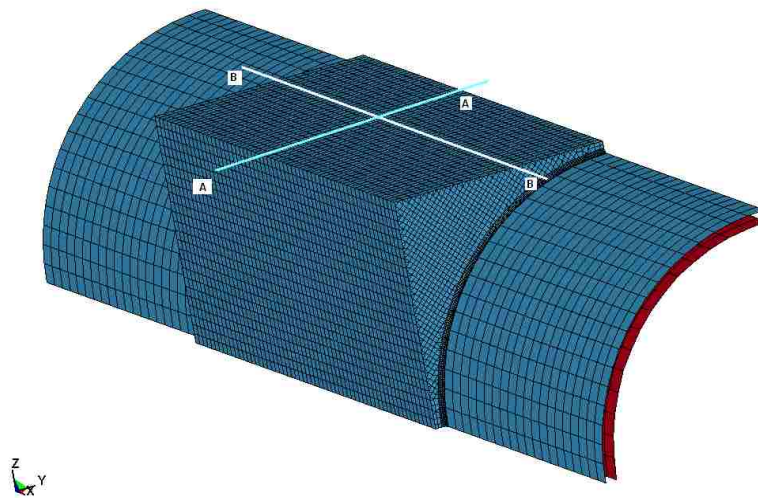
Fig. 4.7 One quarter of the FE model of straight tube hydroforming

expansion. Therefore, the strain path becomes non-linear during this hydroforming process. The geometry of cross-section A-A for the tube and the die is shown in Fig. 4.8. The distance between the outer surface of the tube and the inner surface of the die was set to 3.0 mm. The outside tube diameter was 90 mm and the tube wall thickness was 2 mm.
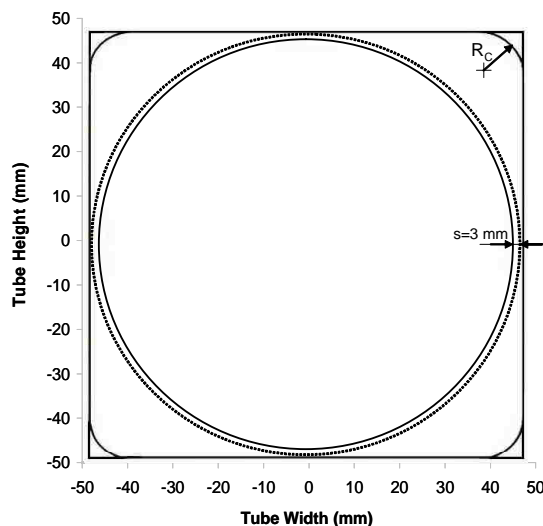
Fig.4.8 Geometry of the cross-section of die and tube (R_C is the final corner radius of the deformed tube)

The die surface was considered to be rigid. The as-received tube was considered to be mild steel and the mechanical properties of this material are listed in Table 4.1. The tube was modelled using Belytschko-Tsay shell elements, with 7 integration points through the thickness. The material hardening law was defined by a piece-wise linear representation of the uniaxial stress-strain curve ("*MAT_PIECEWISE_LINEAR_ PLASTICITY" material model in LS-DYNA[®]). Due to symmetry, only one quarter of the die and tube were modelled and appropriate boundary conditions were applied along the planes of symmetry. The model was discretized into 10,902 nodes and 10,025 shell elements (2,565 elements for the tube and 7,460 elements for the die). After comparing different mesh sizes, it was determined that a fine mesh was needed to capture more accurate stress and strain results in the middle section of the tube. A fine mesh (Fig. 4.6) was applied to this section using "*CONSTRAINED_ ADAPTIVITY" in order to

achieve more accurate stress and strain predictions. The time scaling method was used with different termination times, and it was found that a termination time of 0.005 s was able to achieve a good energy balance with a reasonably low kinetic energy.

An internal pressure was applied to the tube according to the load curve shown in Fig. 4.9. An end-feed displacement was applied to both ends of the tube node sets. Finally, the coefficient of friction for the contact interface between the tube and the die was set to a value of $\mu = 0.1$ based on twist-compression test data (Reid, 2002).

Table 4.1: Tube properties

Mechanical properties	
Density	7800 kg/m^3
Young's modulus	210 GPa
Strength coefficient	601.8 MPa
Hardening exponent n	0.168
Poisson's ratio	0.3
Yield stress	265 MPa
Ultimate tensile stress	380 MPa
Geometric parameters	
Length of tube L_0	280 mm
Outer radius of tube r_0	45 mm
Thickness of tube t_0	2.0 mm
Bulge width	120 mm

4.6.3 Virtual Experiment Design of Loading Path

In their investigations, Imaninejad et al. (2005) and Al-Qureshi & Moriera Filho (2001) concluded that increasing the number of loading path segments approximating the optimum load curve not only increases the computational efficiency but also produces final components with a more uniform thickness distribution and/or larger bulge heights. Therefore, the loading path for straight-tube hydroforming was constructed with four parameters: P1, P2, and P3 which are three levels of internal pressure (and correspond with the pre-expansion, expansion and calibration stages) and D, the displacement applied at the tube ends. Accordingly, a five-stage path was chosen for the internal pressure in the current sensitivity study (Fig. 4.9). The total simulation time was 0.005 s. In order to generate a small corner radius, the calibration pressure was set to a much higher value.
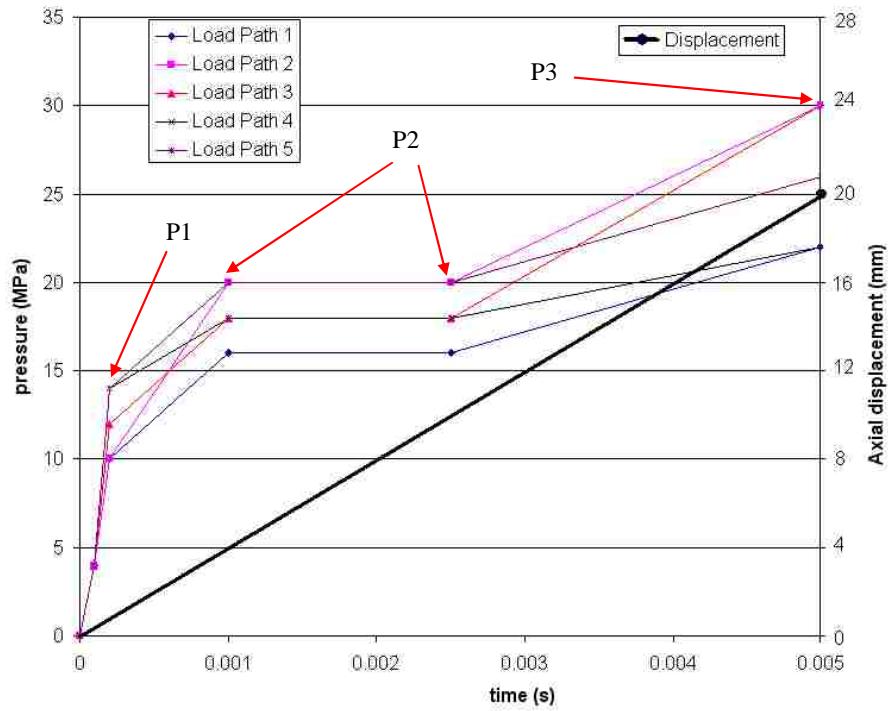
Fig. 4.9 Piecewise linear load curve for internal pressure and axial end feed displacement

The yield pressure P1 was initially estimated according to the relationship (Koç and Altan, 2002) of equation (2.3):

$$P_y = \sigma_y \, \frac{2\,t_0}{D_0 - t_0} = 12.33 \text{ MPa}$$

where σ_y is the yield stress of the tube material, t_0 is the initial wall thickness and D_0 is the initial outer diameter. An estimation of the maximum calibration pressure P3 was also obtained based upon an estimation of the pressure required to achieve a certain target corner radius (R_C), according to the equation (2.5). The calibration pressure P3 was estimated to be in the range of $30 \leq P3 \leq 90$ MPa.

The Taguchi orthogonal array is a design of experiments that has the advantage of introducing a sensitivity analysis by ANOVA, and was utilized for the DOE in this case. On the basis of estimated yield and calibration pressures, an orthogonal array (L$_9$(3^4)) of

four factors with three levels for each was developed for the virtual experiments. Table 4.2 shows the values of each loading path parameters in this Taguchi orthogonal array.

Table 4.2: $L_9(3^4)$ orthogonal array

Run No.	Layout	P1 (MPa)	P2 (MPa)	P3 (MPa)	D (mm)
1	1111	10	20	30	8
2	1222	10	25	45	10
3	1333	10	30	60	12
4	2123	14	20	45	12
5	2231	14	25	60	8
6	2312	14	30	30	10
7	3132	18	20	60	10
8	3213	18	25	30	12
9	3321	18	30	45	8

The hydroforming simulations showed that the strain path in the most critical element was typically non-linear regardless of the loading conditions (see Fig. 4.10). The true major strain and true minor strain were the circumferential strain and axial strain, respectively. During the final stage of hydroforming, the tube wall actually undergoes bending as it fills the corner of the die, thus causing the strain path to become non-linear. Therefore it can be seen that even a very simple hydroforming process such as this requires a failure criterion that is strain-path independent.
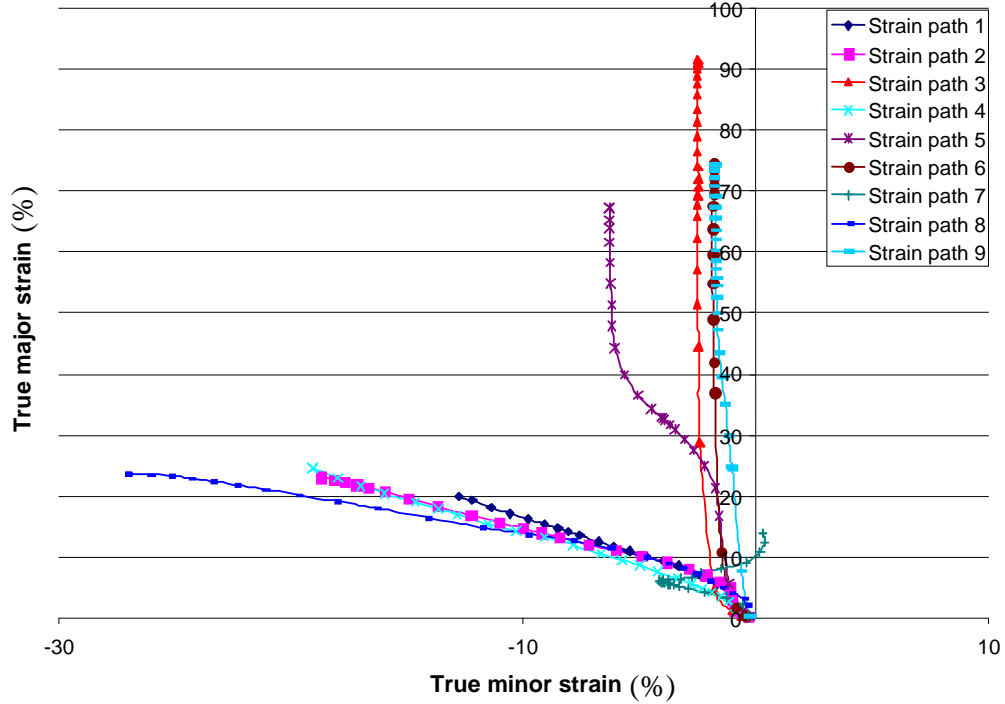
Fig. 4.10 Predicted strain paths in the most critical element (maximum major stress) for each loading condition in the DOE

4.6.4 Results and Analysis

For multi-objective problems, each objective function has a different magnitude and different units, and it is not possible to evaluate the quality of the simulated tubes directly from the values of the objective function. Therefore, after obtaining the results for each virtual experiment, the objective values were normalized to a dimensionless value between 0.2 and 0.8 (Table 4.3). The following formulae were used for this normalization procedure:

$$N_f = 0.2 + 0.6 \left(\frac{Obj\_f}{Obj\_f_{\max}} \right)$$

$$N_w = 0.2 + 0.6 \left(\frac{Obj\_w}{Obj\_w_{\max}} \right) \qquad (4.8)$$

$$N_{th} = 0.2 + 0.6\left(\frac{Obj\_th}{Obj\_th_{max}}\right)$$

$$N_r = 0.2 + 0.6\left(\frac{Obj\_r}{Obj\_r_{max}}\right)$$

where N_f, N_w, N_{th} and N_r are the normalized values for the objective of necking/fracture, wrinkling, severe thinning and corner radius, respectively. *Obj_f*, *Obj_w*, *Obj_th* and *Obj_r* are the values of the four objective functions. *Obj_f_max*, *Obj_w_max*, *Obj_th_max* and *Obj_r_max* are the maximum values of each objective function obtained in the numerical simulations. Although there are various ways to normalize these objective functions, the normalization method does not actually affect the Pareto ranking.

After the objective functions were determined, the Signal-to-Noise ratio (eq. 2.8) was calculated for each run, as follows:

$$S/N = -10\log\left(\frac{y_i^2}{n}\right) \tag{4.9}$$

where y_i are the normalized values of the four objectives, calculated from Eq. (4.8) and provided in Table 4.3, and n is the number of repeat tests ($n = 1$ in this study). Regardless of the definition of the S/N, a greater S/N ratio always corresponds to a better quality characteristic.

Table 4.3: Factor responses with L_2 norm value and S/N ratio for each objective

Run No.	f_1 (MPa)	f_2 (10^4) (MPa)	f_3	f_4 (mm)	Normalization					S/N ratio			
					f_1	f_2	f_3	f_4	L_2 norm value	f_1	f_2	f_3	f_4
1	146.3	0.65	0	18.83	0.4308	0.2653	0.2000	0.8000	0.9675	7.31	11.52	13.98	1.94
2	126.9	4.37	0.001	13.65	0.4662	0.6382	0.2001	0.6350	1.0333	6.63	3.90	13.97	3.94
3	56.3	5.98	4.786	10.59	0.8000	0.8000	0.8000	0.5375	1.4862	1.94	1.94	1.94	5.39
4	124.2	3.74	0	14.48	0.4719	0.5747	0.2000	0.6613	1.0150	6.52	4.81	13.98	3.59
5	81.8	1.81	0.512	12.03	0.6128	0.3819	0.2642	0.5834	0.9651	4.25	8.36	11.56	4.68
6	72.7	2.35	2.19	14.79	0.6643	0.4353	0.4747	0.6712	1.1431	3.55	7.22	6.47	3.46
7	108.2	2.09	0	12.62	0.5122	0.4100	0.2000	0.6020	**0.9126**	5.81	7.74	13.98	4.41
8	123.1	2.28	0	17.56	0.4744	0.4286	0.2000	0.7595	1.0127	6.48	7.36	13.98	2.39
9	72.2	4.14	1.307	12.84	0.6679	0.6146	0.3639	0.6091	1.1521	3.51	4.23	8.78	4.31

By using L_2 norm, the Pareto set can be calculated as shown in Table 4.3, where the minimum value of the L_2 norm is in bold font.

Since FE simulations require substantial preparation and execution time, a surrogate model or "response surface model" can be constructed to obtain the prediction of objectives using a reduced number of FE simulations. Koç et al. (2000) presented low-cost RSM models to predict the protrusion height of "T-shaped" hydroformed parts, and the method was shown to provide an economical prediction and optimization of this height as a function of geometrical parameters subject to thinning of the wall in the protrusion region.

For this straight tube hydroforming case, a further DOE with a L18 orthogonal array (Table 4.4) was carried out and used to fit the RSM model.

Table 4.4: L18(3^6) orthogonal array

Run No.	P1 (MPa)	P2 (MPa)	P3 (MPa)	P4 (MPa)	P5 (MPa)	end feed (mm)
1	10	20	26	30	40	10
2	10	24	28	32	60	12
3	10	28	30	34	80	14
4	14	20	26	32	60	14
5	14	24	28	34	80	10
6	14	28	30	30	40	12
7	18	20	28	30	80	12
8	18	24	30	32	40	14
9	18	28	26	34	60	10
10	10	20	30	34	60	12
11	10	24	26	30	80	14
12	10	28	28	32	40	10
13	14	20	28	32	40	14
14	14	24	30	34	60	10
15	14	28	26	30	80	12
16	18	20	30	34	80	10
17	18	24	26	30	40	12
18	18	28	28	32	60	14

From the analysis of variance (ANOVA) for the L9 orthogonal array, it was evident that P2 and P3 are more significant parameters for the four objectives. Therefore, two intermediate pressure factors were inserted between P2 (at time 2.5ms, Fig.4.9) and P3, and the parameters that define the loading path were then renamed as P1, P2 (at time 1.0 ms), P3 (at time 2.5 ms), P4 (at time 3.5 ms), P5 (at time 5.0 ms) and D.

The simulation results for the 18 load paths are presented in Table 4.5 as well as the Pareto solutions obtained using L_2 norm.

Table 4.5: Factor responses with L_2 norm value and S/N ratio for
each objective of the L18 orthogonal array

Run No.	f_1 (MPa)	f_2 (10^4) (MPa)	f_3	f_4 (mm)	Normalization				S/N ratio				
					f_1	f_2	f_3	f_4	L_2 norm value	f_1	f_2	f_3	f_4
1	129.7	2.69	0.00006	14.34	0.4133	0.4922	0.2000	0.7663	1.019	7.7	6.2	14.0	2.3
2	57.2	4.31	2.89	10.85	0.6840	0.6692	0.3377	0.6282	1.193	3.3	3.5	9.4	4.0
3	46.1	3.95	12.58	8.26	0.8000	0.6301	0.8000	0.5261	1.398	1.9	4.0	1.9	5.6
4	103.2	5.52	0.0	11.70	0.4680	0.8000	0.2000	0.6618	1.156	6.6	1.9	14.0	3.6
5	55.6	3.53	2.97	9.11	0.6975	0.5840	0.3416	0.5597	1.121	3.1	4.7	9.3	5.0
6	64.2	1.89	4.23	12.85	0.6311	0.4061	0.4020	0.7075	1.107	4.0	7.8	7.9	3.0
7	96.1	3.29	0.0	10.10	0.4878	0.5582	0.2000	0.5986	0.974	6.2	5.1	14.0	4.5
8	94.6	2.69	0.10	15.20	0.4924	0.4924	0.2050	0.8000	1.080	6.2	6.2	13.8	1.9
9	52.7	4.24	5.79	9.32	0.7247	0.6615	0.4762	0.5681	1.230	2.8	3.6	6.4	4.9
10	110.1	4.60	0.01	11.75	0.4512	0.7009	0.2007	0.6641	1.085	6.9	3.1	14.0	3.6
11	48.2	4.65	7.42	7.75	0.7745	0.7059	0.5538	0.5061	1.289	2.2	3.0	5.1	5.9
12	57.2	2.32	6.52	11.40	0.6833	0.4522	0.5109	0.6501	1.164	3.3	6.9	5.8	3.7
13	121.7	3.26	0.00004	15.08	0.4274	0.5545	0.2000	0.7953	1.078	7.4	5.1	14.0	2.0
14	51.3	4.24	3.42	10.26	0.7394	0.6614	0.3629	0.6051	1.217	2.6	3.6	8.8	4.4
15	50.4	3.49	7.76	8.55	0.7493	0.5799	0.5702	0.5374	1.230	2.5	4.7	4.9	5.4
16	99.1	2.39	0.20	9.95	0.4792	0.4602	0.2098	0.5929	**0.915**	6.4	6.7	13.6	4.5
17	82.0	3.08	0.30	15.10	0.5373	0.5348	0.2145	0.7962	1.120	5.4	5.4	13.4	2.0
18	58.0	2.86	3.58	11.45	0.6770	0.5107	0.3707	0.6519	1.132	3.4	5.8	8.6	3.7

It was also noted that Runs No. 7 and 16 were the two optimal runs with the lowest values of L_2 norm (see Table 4.5). The corner radius for Runs No. 7 and 16 is 10.10 mm and 9.95 mm, respectively.

For each objective, the ANOVA showed the sensitivity of each factor (Fig.4.11). They are provided below from the most sensitive to the least sensitive:
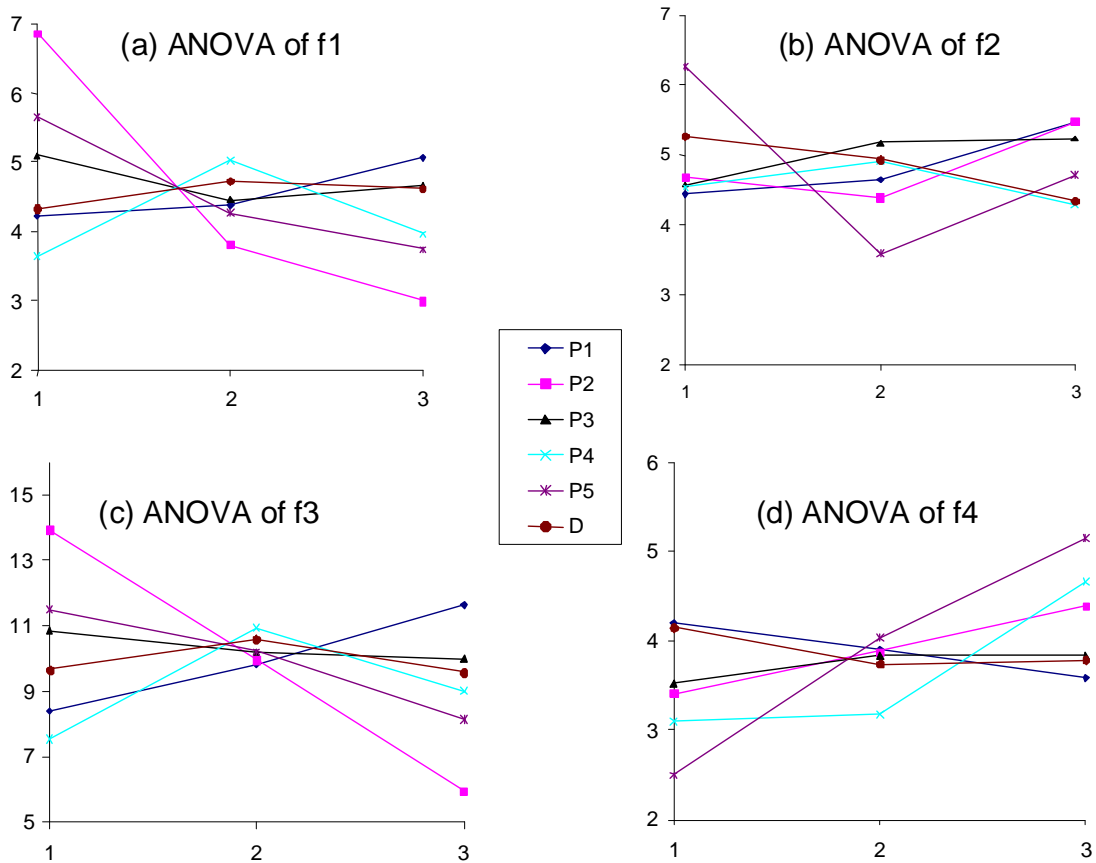
Fig. 4.11 ANOVA of four objectives with each loading path parameter

(1) For the fracture objective (f1): P2 P5 P4 P1 P3 D;

(2) For the wrinkling objective (f2): P5 P2 P1 D P3 P4;

(3) For the objective of severe thinning (f3): P2 P4 P5 P1 D P3, and

(4) For the corner radius objective (f4): P5 P4 P2 P1 D P3, which showed that P3 is the least sensitive factor in the loading path variable settings.

Therefore, P3 was set to a constant value of 28 MPa and was omitted when setting up the RSM model.

In order to obtain the global optimum loading path with the smallest corner radius (i.e. maximum expansion into the corner of the die) without failure, a quadratic RSM model based on methods described in Section 4.2.3 was generated using the L18 simulation results with the parameter set {P1, P2, P4, P5, D}.

According to central composite design for the response surface method, the parameter vector {P1, P2, P4, P5, D} can be transformed to the range [0.2, 0.8] using the following transformation:

$$x_1 = 0.2 + 0.6 \cdot \frac{P1 - 10}{8}, \ x_2 = 0.2 + 0.6 \cdot \frac{P2 - 20}{8}, \ x_3 = 0.2 + 0.6 \cdot \frac{P4 - 30}{4},$$

$$x_4 = 0.2 + 0.6 \cdot \frac{P5 - 40}{40}, \ x_5 = 0.2 + 0.6 \cdot \frac{D - 10}{4} \tag{4.12}$$

As a result, the quadratic RSM functions were obtained for each objective and then were input to the NBI optimization toolbox to find the Pareto optimal solutions.

The parameter options for the NBI algorithm were selected as follows: the number of tradeoff points per objective pair was 10; for shadow minima options, the maximum
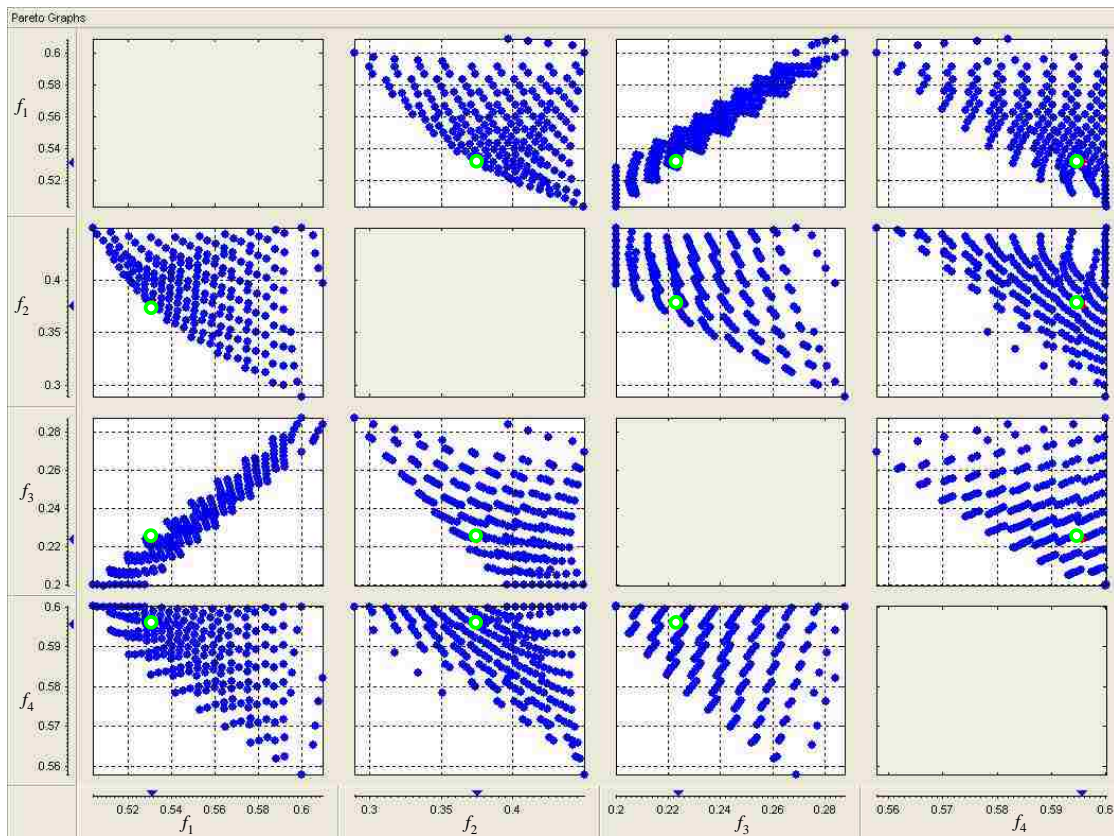
Fig. 4.12 Pareto sets with regard to objectives of fracture (f_1), wrinkling (f_2), severe thinning (f_3) and corner radius (f_4), where one solution is highlighted as a larger dot.

function evaluations were 100; the maximum iterations were 20; the tolerances for each function, variable and constraint were all set to a default value (0.0001). The options for the NBI sub-problem were chosen the same as shadow minima. There were 220 sub-problems and the Pareto set was found (Fig. 4.12) after 20 minutes of computation on a HP xw9300 workstation with AMD Opteron™ Processor 248, 2.19 GHz, with 4 GB of RAM.

In Fig. 4.12, the non-dominated optimal solutions of the numerical example provide the complete picture of the trade-off between the objectives. Minimizing fracture is equal to minimizing severe thinning (f1 vs. f3), and maximizing wrinkling (f1 vs. f2), which indicated that except for the f1 and f3 objectives, the objectives are always in conflict. Since the NBI method produced a Pareto set of 220 solutions, a FE calculation was performed with the optimum loading path generated by the L_2 norm calculation in order to verify the optimum solution.

In total, there were two batches of 18 FE simulations that were each carried out to make sequential improvements to the RSM model. For each batch, an additional FE run was carried out to validate the optimum solution determined by the NBI method. The two FEA results and the prediction of RSM are shown in Table 6. The good correlation between these two results demonstrates the effectiveness of the RSM. Table 4.7 represents the global optimum loading path parameters, obtained with a minimum L_2 norm value, within the Pareto solution set.

Table 4.6: Two optimum solutions obtained with the NBI method using L_2 norm and FEA for verification

	f_1 (MPa)	f_2 (10^4) (MPa)	f_3	f_4 (mm)	Normalization				Pareto L_2 Norm value	
					f_1	f_2	f_3	f_4	Prediction	Calculation
RSM #1	555.4	2.184	1.84	11.08	0.2498	0.4376	0.2879	0.6374	0.862	
FEA #1	91.7	2.186	1.77	9.20	0.5016	0.4379	0.2844	0.5634		0.917
RSM #2	89.4	0.039	0.99	8.78	0.5096	0.2043	0.2473	0.5468	0.813	
FEA #2	94.6	2.034	0.86	9.08	0.4924	0.3641	0.2411	0.5586		0.863

Table 4.7: Loading path parameters for the global optimum solution

P1(MPa)	P2(MPa)	P3(MPa)	P4(MPa)	P5(MPa)	D(mm)
19	19.03	28	34	83.761	10.06

The optimal value of L_2 norm is: F = 0.813, whereas the FEA result is 0.863 (Table 4.6). The prediction error is 5.78%, which is within an acceptable range. The parameter vector for this objective value is X = [0.8 0.2183 0.2 0.6513 0.2093]^T, and represents a loading path defined by the values in Table 4.7 and shown in Fig. 4.12.

Table 4.8 Comparison of objectives of final optimum (L_2 norm value) and intermediate results

Run	Max. stress (MPa)	f_1 (MPa)	f_2 (10^4) (MPa)	f_3	f_4 (mm)
L9 optimum	551	108	2.0941	0	12.62
L18 optimum	560	99	2.3916	0.2047	9.95
Final optimum	564	95	2.0339	0.8615	9.08
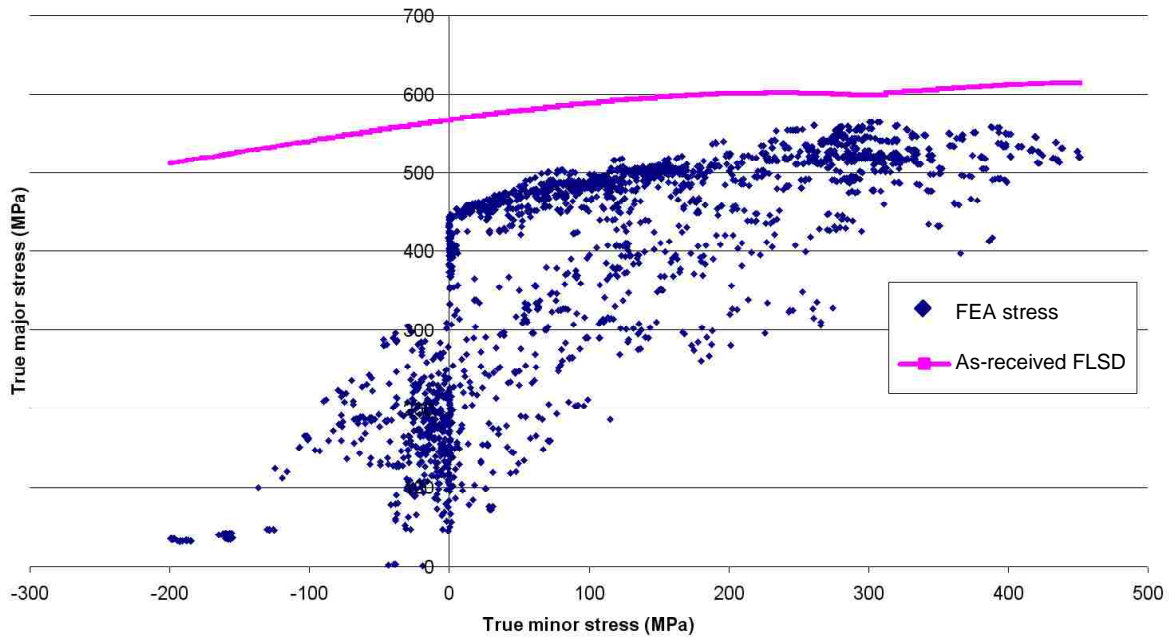
Fig. 4.13 Stresses in the part after it was hydroformed with the loading path defined by the Pareto optimum layout, compared with the FLSC.

It can be seen that the optimum loading path is similar to Run No.16 (Table 4.5) obtained by L_2 norm. However, the optimum loading path leads to a smaller corner radius, compared to the best run (No. 7) in the L9 orthogonal array (Table 4.3) and the best run (No. 16) in the L18 orthogonal array (Table 4.5), by 28% and 8.7%, respectively, and the corner radius decreased from 12.62 mm and 9.95 mm to 9.08 mm. At the same time, there was a slight increase in the maximum stress in the most critical element (by 2.4% and 0.7%), however, the stress remains far below the FLSC (Fig. 4.13). This indicates that the optimum layout leads to a significant improvement in the hydroforming process.

Fig. 4.14 illustrates the evolution of loading path in the optimization process. In total, 36 load paths were plotted, 18 for each of the L18 orthogonal arrays (iterations 1 and 2). Compared to iteration 1 where several load paths lead to failure, the load paths in iteration 2 all resulted in parts without failure. It was shown from the comparison that more end feed was required during the beginning of the process to push material into the die cavity to reduce the risk of failure. It can also be noted in Fig. 4.14 that a Pareto solution set of 220 load paths was generated by the NBI method, and these form a process window that may enhance the process robustness compared to a single optimal solution obtained by the L_2 norm method. These results will be further discussed in the next section.
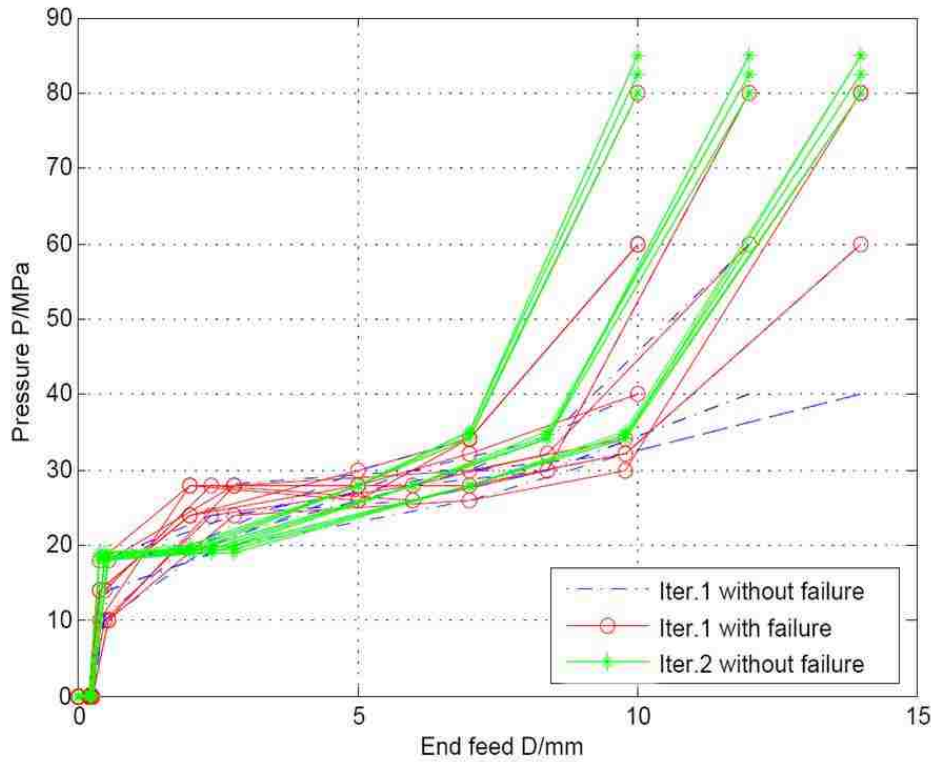
Fig.4.14 Sequential L18 load paths (Iteration 1 and Iteration 2)

4.6.5 Validation with LS-OPT® 4.0

In order to validate the proposed optimization method, the same hydroforming example was optimized with the commercial optimization software LS-OPT® 4.0, often used for metal forming applications (Stander et al., 2009). The program requires the input of design variables, optimization algorithms and parameters, which can be provided using a graphic user interface (GUI). Once again, the objective was to minimize the corner radius during die filling. The constraints available in LS-OPT® 4.0 are the thinning ratio in the tube wall and the FLD. The FLD was embedded in the software as a constraint to make sure no failure occurs. The constraints can be written as:

$$\Delta t(x) \leq 0.35$$
$$g^{FLD}(x) < 0$$

$$(4.13)$$

where, $\ddot{A}t$ is the thickness reduction which is positive when the thickness is reduced. The FLD constraint is satisfied (i.e. the strains lie under the FLC) when $g^{FLD}(x) < 0$. The parameters in the LS-OPT® GUI are listed in Table 4.9 and the codes are listed in

Appendix C and D. It can be noted that 180 load paths (6 iterations of 30 runs each) were simulated with each method in LS-OPT®, whereas only 36 load paths were simulated with the NBI method. The hybrid algorithms were used, which start with the genetic algorithm (GA) or adaptive simulated annealing (ASA) to find an approximate global optimum after which a leapfrog optimizer for constrained minimization is used to sharpen the solution. The solution to a hybrid algorithm will be at least as good as the one provided by the global optimizer (ASA or GA).

Table 4.9 Algorithms and parameters in LS-OPT® GUI

strategy	variables (load parameters)	sampling	Algorithms
sequential with domain reduction (SRSM)	P1: 10-19 P2: 19-28 P3: 26-28 P4: 30-35 P5: 40-85 D: 10-14	1) metamodel: polynomial; order: linear; 2) point-selection: D-optimal; 3) Total Number of simulation points: 30	1) hybrid ASA with default settings 2) hybrid GA with population size: 200 and number of generations: 250

Table 4.10 Optimum results obtained using LS-OPT® (unit: mm for radius)

	Hybrid ASA			Hybrid GA		
	computed	predicted	absolute prediction error (%)	computed	predicted	absolute prediction error (%)
Thickness reduction (%)	31.37	35	11.6	23.20	28.21	21.59
FLC	-0.02	-7.3e-8	N/A	-0.002	-0.028	N/A
Radius	9.81	9.51	3.1	9.50	9.51	0.11

Table 4.10 indicates that the loading path obtained using the hybrid GA produced a smaller corner radius (9.50 mm) than the one using the hybrid ASA algorithm (9.81 mm). However, the minimized corner radius obtained using the hybrid GA in LS-OPT® 4.0 was larger than the minimum radius predicted with the NBI method (9.08 mm), and this with fewer simulations. Figure 4.15 also shows that the loading path obtained with the hybrid GA is close to the upper bound of the 220 Pareto set using the NBI method.

Therefore, compared with the above mentioned optimization methods that have been applied in tube hydroforming, the recent NBI method has the ability to generate a process window (Fig. 4.15) rather than a single load path, because it was designed to generate Pareto fronts with an even spread of points. Consequently, from this standpoint the multi-objective optimization strategy that was combined with the NBI algorithm can guarantee a more robust process than the solution provided by LS-OPT® with a single objective optimization strategy.
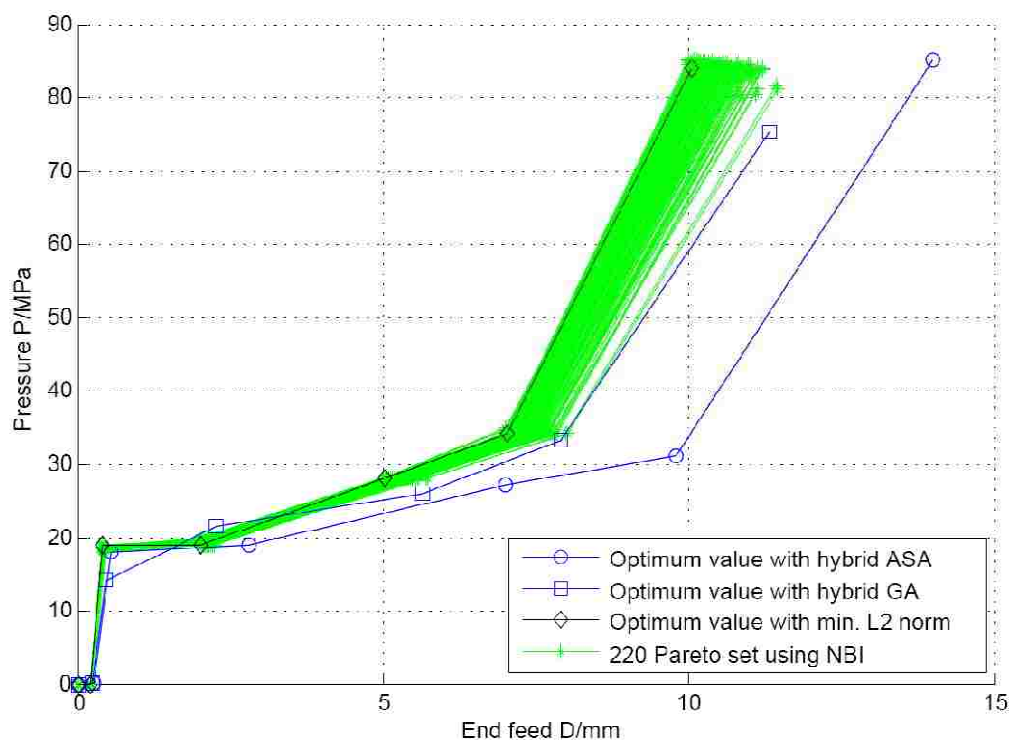
Fig. 4.15 Comparison of load paths obtained with the proposed multi-objective algorithm and with the single-objective strategy of LS-OPT®

4.6.6 Conclusions

In this chapter, a multi-objective optimization algorithm combined with the Taguchi statistical method and FEA was developed to determine the optimal loading path for a simple tube hydroforming process. In addition, an ANOVA was used to determine the sensitivity of the hydroforming process to the various parameters that define the load path.

The optimal load paths were obtained using both the proposed NBI approach and the single-objective approach with the commercial optimization software LS-OPT$^®$ 4.0. The following conclusions can be drawn from this study:

1) The sensitivity analysis helped to identify the most significant factors for loading path optimization and reduced the computational cost.

2) Sequential response surface models were constructed and applied to the global optimization of the load path. This provided explicit surrogate models for tube hydroforming with acceptable accuracy and limited the number of simulations that were required.

3) The FLC and the FLSC were found to be very effective to evaluate the influence of the loading path on the forming severity of hydroformed parts. The FLSC was required to evaluate the risk of necking or fracture and wrinkling since these are dependent on the stress state, and the FLC was more advantageous to evaluate the risk of excessive thinning.

4) With regards to multi-objective optimization, the NBI method was very effective in finding the Pareto-optimum load path. It also indicated a complete picture of the trade-off between the objectives from the optimal set. Minimizing the risk of fracture is equivalent to minimizing severe thinning, and maximizing wrinkling. Apart from the objectives of fracture and severe thinning, the objectives were always in conflict.

5) The investigation showed the robustness of the tube hydroforming process with an appropriate loading path set. Compared with the hybrid methods (ASA and GA) in LS-OPT® 4.0, the optimization method with NBI was shown to provide a greater process window guaranteeing a more robust hydroforming process.

Chapter 5: Loading path design using multi-objective genetic algorithm for a straight tube and an industrial part

In this chapter, a state-of-the-art evolutionary multi-objective optimization (EMO) methodology—nondominated sorting genetic algorithm (NSGA-II) is introduced for loading path design. First, the Kriging metamodel is introduced into the EMO method, and the accuracy assessment of the model is presented. In the next section, a coupled method that combines NSGA-II and the Kriging method is proposed. In the following section, an enhancement of the coupled method is presented by the addition of a hybrid global and local search. These methods are then validated with case studies: tube hydroforming of a square-shaped part and an industrial part. Some conclusions are then drawn in the final section.

5.1 Kriging metamodel

The Kriging model has been shown to be a global model in contrast to response surfaces which are local models, employing normally distributed basis functions, so both an expected sampling value and variance are obtained for each test point (Goovaaerts, 1997). For more details of the universal model refer to Chapter 2 (Section 2.5.2.2).

The accuracy of the Kriging response surface model can also be measured by checking the predictability of its response using the prediction error sum of squares (PRESS) and R^2 for the prediction (R^2_{pred}) (Myers and Montgomery, 1995). After obtaining the surrogate model, a 10-fold cross-validation technique was used to check the fitting performance for the "new" data. The PRESS statistic and R^2_{pred} of the predictor model were calculated as:

$$PRESS = \sum_{i=1}^{p}(y_i - \hat{y}_i^*)^2 \Big/ p \tag{5.1}$$

$$R^2_{pred} = 1 - \frac{PRESS}{S_{yy}} \tag{5.2}$$

$$S_{yy} = y^T y - \frac{\left(\sum\limits_{i=1}^{p} y_i\right)^2}{p} = \sum\limits_{i=1}^{p} y_i^2 - \frac{\left(\sum\limits_{i=1}^{p} y_i\right)^2}{p} \tag{5.3}$$

where y_i is the actual value, $\hat{y}_i^*$ is the value predicted by the Kriging predictor for the ith testing point, and p is the number of prediction points. S_{yy} is the total sum of squares of the errors. The final PRESS is the average of ten cross-validation tests.

5.2 MOGA and constraint handling technique

5.2.1 MOGA

The aforementioned NBI method was implemented by solving the subproblem, which involved assigning weights to locate point H along the CHIM (See Fig. 4.4). In order to circumvent the difficulty of selecting a relative weight for each objective, a Pareto optimization algorithm (called NSGA-II) which uses a ranking, elitist selection and non-dominated sorting strategy was adopted for this study.

The NSGA-II algorithm developed by Deb et al. (2002) has been a popular optimization tool in recent years. It adopts an elitism strategy and crowding-distance calculation, which offer a much better spread of solutions and better convergence in most problems near the true Pareto-optimal front compared to Pareto-archived Evolution strategy and Strength-Pareto Evolutionary Algorithm – two other elitist multi-objective evolutionary algorithms (MOEA) that pay special attention to creating a diverse Pareto-optimal front.

The principle of this algorithm is illustrated in Fig. 5.1 as follows: the Pareto fronts were sorted to different ranks according to a fitness value (Fig. 5.1a); after this non-dominated sorting, a crowding distance was calculated for each individual (Fig. 5.1b). The purpose of assigning a crowding distance value is to generate a series of uniformly distributed Pareto fronts, which helps to maintain a better diversity of the population.
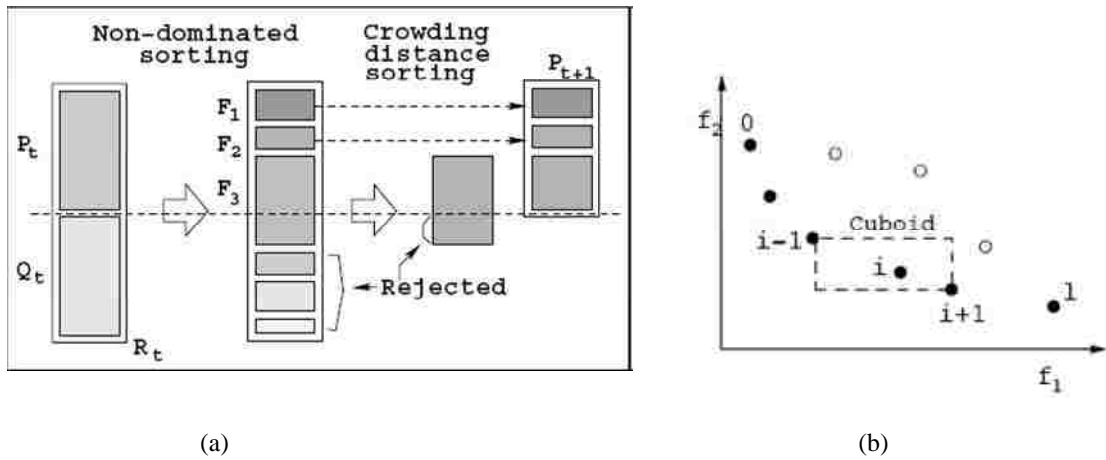
Fig. 5.1 (a) Schematic of the NSGA-II procedure, and (b) the crowding distance calculation (Adapted from Deb et al. 2002)

Goel et al. (2007) noted that in MOEA, the genetic operators may destroy some of the solutions to explore the design space. Introducing elitism in MOEAs alleviates this problem to some extent, but when the number of non-dominated solutions in the combined population exceeds the population size, as happens commonly in elitist MOEAs, some of the non-dominated solutions have to be dropped. This problem is referred to Pareto drift as the Pareto optimal solution is lost, which may lead to a suboptimal global solution.

Therefore, an archiving strategy is suggested to augment NSGA-II, and is referred as archiving NSGA-II (NSGA-IIa) (Goel et al., 2007). The strategy of NSGA-IIa is to keep all the potential non-dominated solutions in one group during the whole evolution process. In this work, the archive was initialized with all non-dominated solutions inherited from the points from the design of experiment (DOE), and then complemented with the potential non-dominated solutions from new generations for which fitness functions were calculated by FEA.

5.2.2 Constraint handling technique

In problems with constraints, it is more difficult to handle violation of the constraints. Most real-world optimization problems have constraints that must be satisfied. Currently, a single-objective genetic algorithm (GA) can employ five different constraint handling strategies: (i) discarding infeasible solutions, (ii) reducing the fitness of infeasible solutions by using a penalty function, (iii) if possible, customizing genetic operators to always produce feasible solutions, (iv) repairing infeasible solutions, and (v) hybrid methods. Handling of constraints has not been adequately researched for multi-objective GAs (Konak et al. 2006). For example, all major multi-objective GA assume problems have no constraints.

In general, constraint handling strategies (i), (iii) and (iv) are suitable for both the single-objective GA and MOGA. However, for the most widely used penalty function strategies, it is not straightforward in MOGA, since it operates on the fitness assignment of an objective value, while for MOGA the fitness assignment is usually based on the non-dominance rank of each solution.

In the constrained NSGA-II, a method using the category (iv) is described to handle three different non-dominated rankings. Wang and Yin (2008) proposed a method of M+1 non-dominated sorting to solve the constraints in engineering design problems (M and 1 referred to the number of objectives and the overall constraint violation). Favuzza et al. (2006) proposed two crowded comparison operators for constraints handling in electric distribution network design. Deb et al. (2002) proposed the constraint-domination concept and a binary tournament selection method based on it, which was called the constrained tournament method. The main advantages of the constrained tournament method are that it requires fewer parameters and it can be easily integrated into multi-objective GA. The NSGA-II algorithm was accessible at the Matlab center (Seshadri, 2006). However, the constraint-handling program is not available. Since there are no constraint-handling programs available, NSGA-II users must develop their own constraint-handling technique.

Hence, in this work a hybrid constraint handling method was proposed (Fig. 5.2), which aims to utilize the simple operation of the penalty function method and also the tournament selection method. This method can be described as follows.

Step 1: Weeding out the infeasible solutions in the process of generating new children. Evaluate each child using the Kriging model and eliminating those with a constraint violation.

Following the initiation of the population, new children were generated through genetic operations (mutation and crossover). The objective values of the children were evaluated with the Kriging predictor. If any of the objective values violated the boundary, then it was marked with over =1. Then the program continually generated new children until it met the constraints (with over =0). Though this satisfaction of the constraints may be pseudo feasible since the true objective values probably still violated the boundaries, the violation would be small by using a well-established Kriging model. Moreover, the operation in Step 2 will help to keep the feasible solutions and eventually eliminate the infeasible solutions.

Step 2: Ranking by constraint violation (Stage I, Fig. 5.2)

The comparison mechanism considered here, operated on those solutions having a constraint violation and arranged a rank for each solution (See Appendix A). The measure for the constraint-violation (CV) values was calculated as:

$$CV = \sum_{i=1}^{l} |g_i(x)| \tag{5.4}$$

if there is constraint violation, i.e. $g_i(x) > 0$; l is the number of constraints. CV equals 0 if there is no constraint violation and $g_i(x) \le 0$.

Step 3: Ranking of general NSGA-II with non-dominated sorting, crowding distance sorting and elitism selection (Stage II, Fig. 5.2)

The algorithm operated in such a way that the CV operator was carried out for the merged population made up of the parent and the offspring. It dominated during both the early and late stages of the execution of the MOGA, however, the conventional NSGA-II dominated the selection of population for the next generation when the number of feasible individuals in the merged population had reached the designed population number.
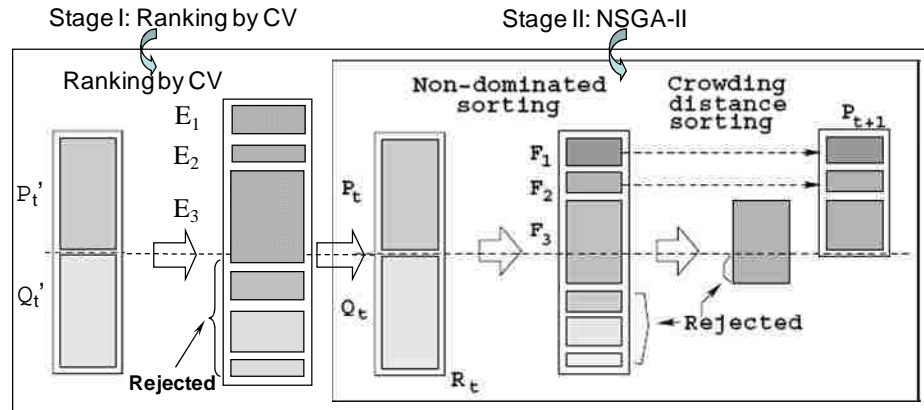
Fig. 5.2 Constrained NSGA-II algorithm (Adapted from Deb et al., 2002)

5.3 MOGA I (Global Search) and MOGA II (Hybrid Global and Local Search or H-MOGA)

5.3.1 MOGA I

In this algorithm, a selection method based on the ranking of constraint violation (CV) (when there is constraint violation) and a second ranking of non-domination of objectives and local crowding distance (when no constraint violation occurs) is described. What makes this algorithm different from other NSGA-II applications is the innovative sequential constraint algorithm. The flowchart of MOGA-I is presented in Fig. 5.3.

The selection procedure of the MOGA is described as follows.

(1) Generate the parent population P_t' (see Fig. 5.2)

(2) Create the offspring Q_t' through the crossover and mutation operators. The objective function values are calculated using the Kriging predictor. If the generation

reaches a predefined interval (say, five generations), the FE program is called to obtain the objective function values for each offspring.
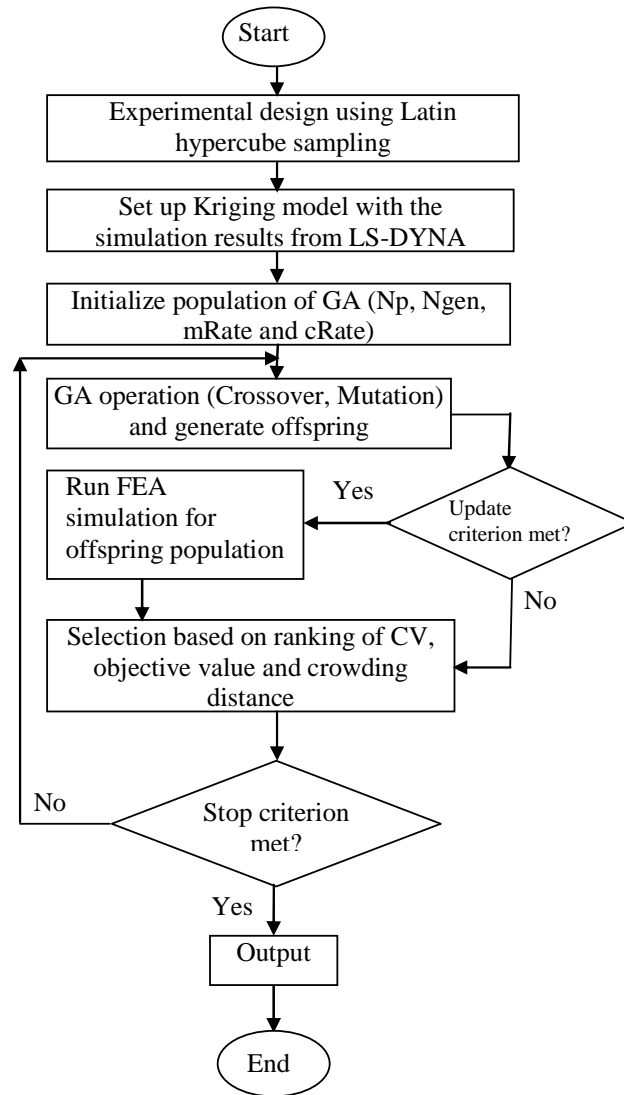
Fig. 5.3 Flowchart of optimization strategy using Kriging predictor for generating both new points and offsprings

(3) Recombine the parent and child populations into a new population $U_t = P_t' \cup Q_t'$. Carry out non-dominated sorting for CV first. Assign a rank for each individual as

E=E1, E2,... (Fig. 5.2 and 5.4). If the number of U_t exceeds the current population size N, go to step (4); If else go to (5).

(4) Recombine the parent and child populations into a new population $R_t = P_t \cup Q_t$. Do non-dominated sorting for objective rank and crowding distance, and assign a rank for each individual (F=F1, F2,...) (Fig. 5.2 and 5.4).

(5) Select the next generation P_{t+1}. An elitist individual is transferred to the next population with a size N.

(6) Steps (1) to (5) are repeated to generate subsequent generations. The process is terminated when the predetermined number of generations is reached.
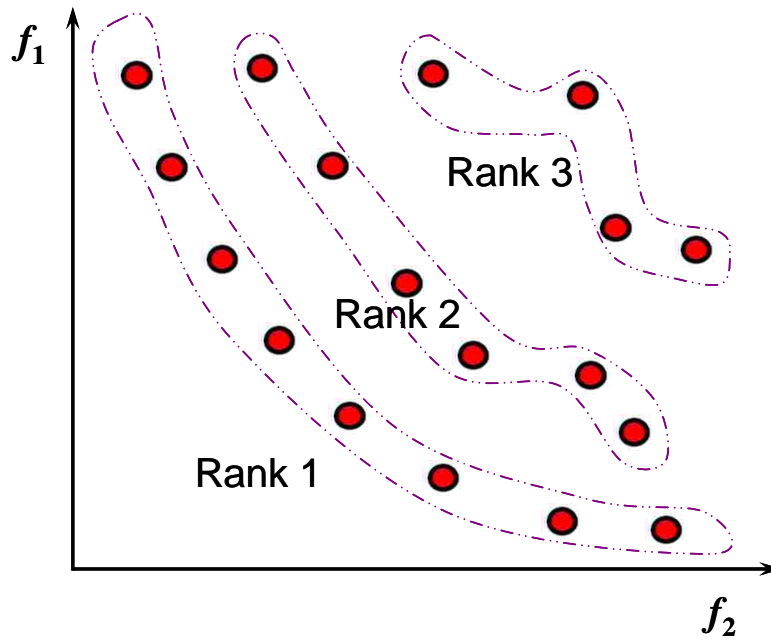
Fig. 5.4 MOGA ranking strategy

The algorithm was used to optimize the loading path of the same square-shaped tube hydroforming problem as the one described in Chapter 4. The results will be presented in section 5.5 and compared to those solutions obtained in Chapter 4 with the NBI method.

5.3.2 MOGA II (H-MOGA)

In multi-objective optimization problems with four or more objectives, the predefined Kriging model may not reach a desirable prediction accuracy for all objectives of the new points. As pointed out by Hughes (2005), one concern with the methods described so far is that fitness assignments based on dominance rank (like NSGA-II) can perform poorly when the number of objectives is greater than three or four. Although the accuracy could be improved by adding more sampling points, the prediction error may still affect the constraint handling and the poor results may be amplified through the effect of Pareto drift (Goel et al., 2008).

The selection procedure of the MOGA II (Fig.5.5) is described as follows.

(1) Initialize the parent population P_t'.

(2) Create the offspring Q_t' through the crossover and mutation operators. The objective function values are calculated using the Kriging predictor.

(3) Check the constraint violation (CV) of each child. If CV>0, randomly generate a new point and evaluate the function by Kriging predictor until the child population is fully filled.

(4) Recombine the parent and child population into a new population $U_t = P_t' \cup Q_t'$. Carry out non-dominated sorting for CV first. Assign a rank for each individual as E=E1, E2,... (Fig. 5.2). If the number of U_t exceeds the current population size N, go to step (5); If else go to (6).

(5) Recombine the parent and child populations into a new population $R_t = P_t \cup Q_t$. Do non-dominated sorting for objective rank and crowding distance, and assign a rank for each individual (F=F1, F2,...) (Fig. 5.2).

(6) Select the next generation P_{t+1}. An elitist individual is transferred to the next population with a size *Np*.

(7) The true objective values are calculated with FEA and then the ranking in step (4)-(5) is run once again for the actual values.

(8) Steps (1) to (7) are repeated to generate subsequent generations. The MOGA process is terminated when the stop criterion, such as a predetermined number of generations, is satisfied.

(9) The local search is done after the Pareto solution set is obtained. The sequential quadratic programming algorithm in MATLAB® was used as the local optimizer.

It was noted that, in order to utilize the information from constraint violations, the amount of infeasibility (or the extent of constraint violation) was used for ranking the solutions. During the first several stages (e.g. n=1 to 10), the constraint information was used to explore additional design points near the boundary by keeping those individuals that were found to violate the constraints after obtaining the actual objective values by FEA. However, as stated above, with the genetic operation continuing, these points end up being automatically eliminated.

The method shown in Fig. 5.5 differed from the previously proposed method (Fig. 5.3) in the function evaluation: the former proposed a local search and direct FEA analysis for function evaluation while the latter completed the function evaluation wholly by using an updated Kriging model modified to obtain a higher accuracy. However, as was already noted, the latter method may not reach a global Pareto solution efficiently when there are four and more objectives.
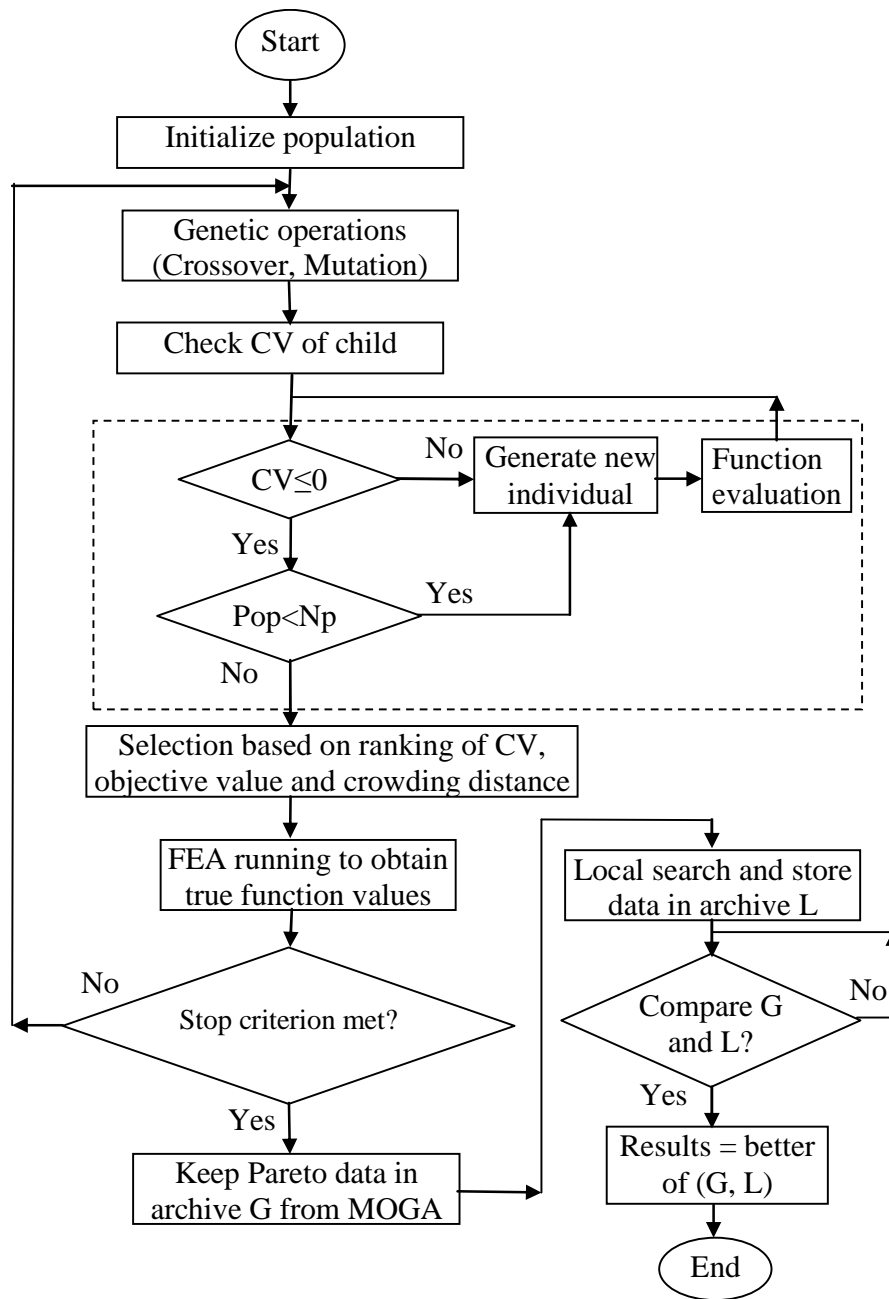
Fig. 5.5 Flowchart of optimization strategy with the Kriging predictor used only for generating new points and FEA used for generating offsprings

5.4   Case study 1: Straight tube hydroforming using Algorithm I

5.4.1 The FE model

For convenience, the hydroforming of a straight tube in a die with square-shaped cross-section (Section 4.6) is shown again in Fig. 5.6. The FE mesh and the cross-section are shown in Fig. 5.6a and 5.6b, respectively. The forming process consisted of pressurizing and expanding the tube a radial distance *s* until it contacted the die. The tube ends were simultaneously subjected to end-feed to supply more material into the die cavity and thus to avoid severe thinning. More FE details and the tube properties can be found in section 4.6.2.

(a)   *(b)*
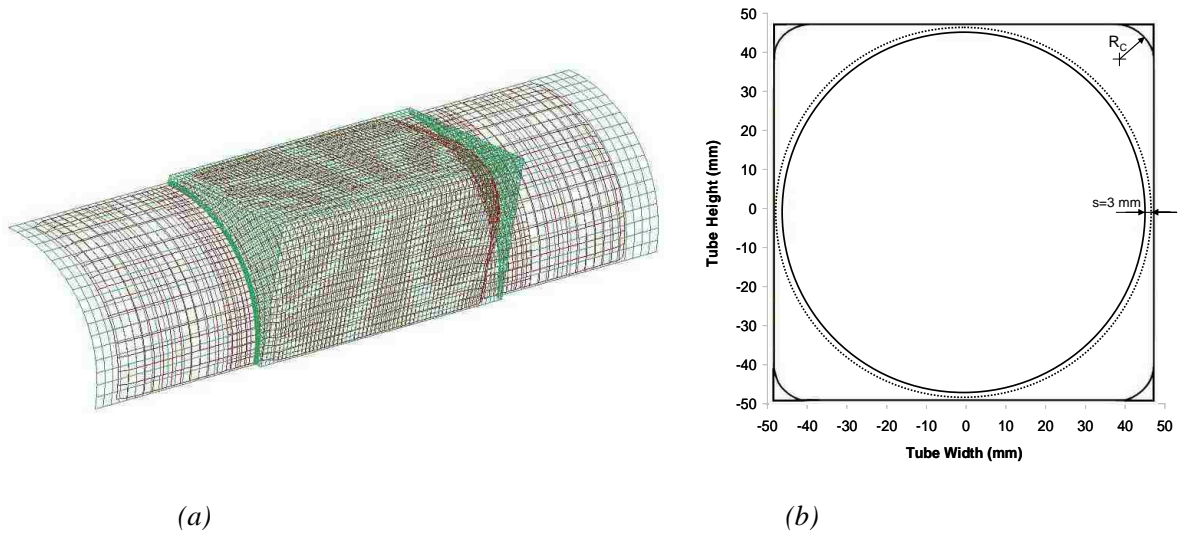
Fig 5.6 (a) One quarter of the FE model (b) Geometry of the cross-section of die and tube (R_C is the final corner radius of deformed tube)

5.4.2 Optimization procedure

The primary objective of this tube hydroforming problem is to maximize the amount of expansion of the tube wall into the corners of the die, or in other words, to minimize the corner radius, and therefore the following objective function is given as:

$$f_4 = R_C \tag{5.5}$$

In addition, the formability objectives Eq. (3.3) to (3.5) must also be minimized. Therefore, the problem can be summarized by the following formulation which places constraints on each objective:

Minimize $\quad F(x) = [f_1(x), f_2(x), f_3(x), f_4(x)]$ $\hspace{3cm}$ (5.6)

s.t. $\quad 0.2 \le f_1 \le 0.75; \quad 0.2 \le f_2 \le 0.75$ $\hspace{2.5cm}$ (5.7)

$\qquad 0.2 \le f_3 \le 0.30; \quad 0.2 \le f_4 \le 0.60$

where x is the normalized vector of design variables: $x = [P1, P2, P3, P4, P5, D]^T$. The ranges of each design variable are the same after normalization: $0.2 \le x_i \le 0.8$, $i = 1, 2, ... 5$.

Simulations were carried out with the commercial FE software LS-DYNA (Hallquist, 2007). First, the loading path was defined such that the pressure vs. time curve is a piecewise linear curve and the end feed vs. time curve is linear. A sensitivity analysis was then performed to identify the least sensitive factors. Then a design of experiments was carried out and the simulation results were used to establish a surrogate Kriging model. The model was validated with the k-fold cross-validation method to confirm the model had been accurately set up. The MOGA was used to carry out the optimization using the Kriging model to predict the objective functions for each loading path within the population. During the optimization process, the Kriging model was updated every five generations by calling LS-DYNA to carry out another series of simulations. This process

(a) $\hspace{8cm}$ *(b)*
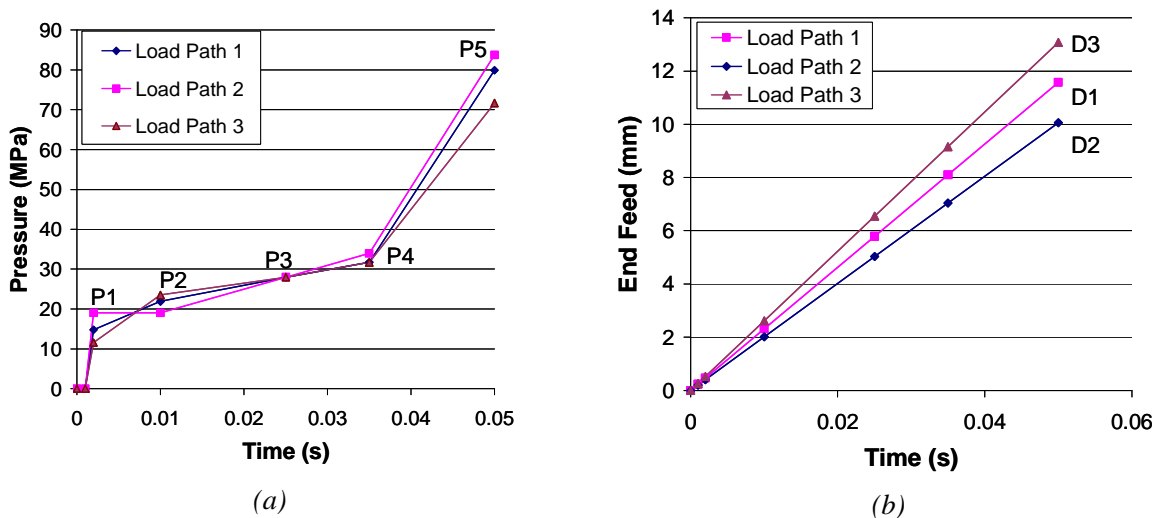
Fig 5.7 Load curve for *(a)* internal pressure; and *(b)* axial end feed displacement

was repeated for a predetermined number of generations. This procedure is described in the flowchart in Fig. 5.3.

5.4.3 Design of experiments

The loading path was designed with five parameters for pressure and one for end feed, namely P1, P2, P3, P4, P5 and D (Fig. 5.7a). P1 to P5 are different pressure levels, in MPa, (P1 is the yield pressure, P2, P3 and P4 are intermediate pressure levels and P5 is the calibration pressure) and D is the maximum end feed, in mm, at the end of the process. The ranges selected for each design variable are as follows:

$$10 \leq P1 \leq 18; \quad 20 \leq P2 \leq 28; \quad 26 \leq P3 \leq 30$$
$$30 \leq P4 \leq 34; \quad 40 \leq P5 \leq 80; \quad 10 \leq D \leq 14$$

(5.8)

According to the sensitivity analysis, parameter P3 was shown to be the least sensitive, and it was set to a constant P3 = 28 MPa and omitted from the surrogate model, leaving only 5 design parameters.

The design of experiments consisted of the Latin hypercube sampling (LHS) method. In order to build a quadratic model, Mehnen et al. (2007) proposed that the minimum number of experiments should be $k = [d(d-1)/2+3d+1]$, where d is the number of design parameters to be optimized. In this work, $d = 5$ therefore $k = 26$. But in order to increase the accuracy of the model, the number of experiments was taken to be 40.

The Kriging method was used to establish a surrogate model. After obtaining the model, a 10-fold cross-validation was completed to check the fitting performance of the "new" data.

5.4.4 Strategy for automatic data processing

Once the 40 FE simulations specified by the design of experiments were carried out, the objective functions were calculated from the stresses and strains in each element of the FE model, and for each experiment. In order to automate the entire analysis, the stresses and strains were extracted from the DYNAIN file that is automatically generated by LS-

DYNA. However, additional calculations were required to obtain the principal stresses and principal strains since the "DYNAIN" file only provides the six stress components (at seven integration points) and the six strain components (at the upper and lower surfaces). Therefore a user-defined program was developed in VC++ to carry out the transformations and calculate the principal stresses and strains.

Principal stresses and strains were determined by calculating the eigenvalues of the stress and strain tensors, respectively. Since shell elements were used in the FE model, it was also necessary to determine which two principal strains lie in the plane of the shell element and which one represents the through-thickness strain as this is required in the calculation of the objective function that evaluates thinning severity. This identification was done by correlating the plane normal vector with the strain direction cosines (Fig. 5.8). This computation was done sequentially for both the upper and lower surfaces of each element in the model.

Data exchange was carried out with the user-defined VC++ program which called for the automatic generation of LS-DYNA output files.
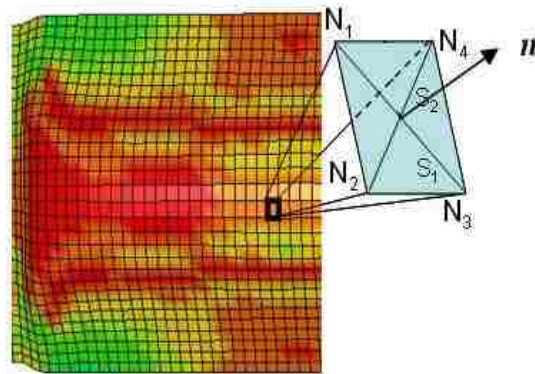
Fig 5.8 Principal strain determination for shell elements (where $\vec{n} = \overrightarrow{S_1} \times \overrightarrow{S_2}$, $\overrightarrow{S_1} = \overrightarrow{N_1 N_3}$, $\overrightarrow{S_2} = \overrightarrow{N_2 N_4}$)

5.4.5 Results

The surrogate model was established with 40 simulations using the Kriging method. The errors of the predictor model for the four objective functions were 0.0089, 0.0046, 0.0075 and 0.0013, respectively. Optimized results were obtained after 40-generation evolutions using constrained NSGA-II. The Pareto solution set was plotted to show every pair of objectives (Fig. 5.9). In this figure, it can be shown that the smallest corner radius obtained is located at point Q, where f4 = 0.5341, which corresponds to a corner radius of 8.57 mm. The other objective values are 84.18 MPa, 32216 MPa and 0.2 for f1, f2 and f3, respectively.
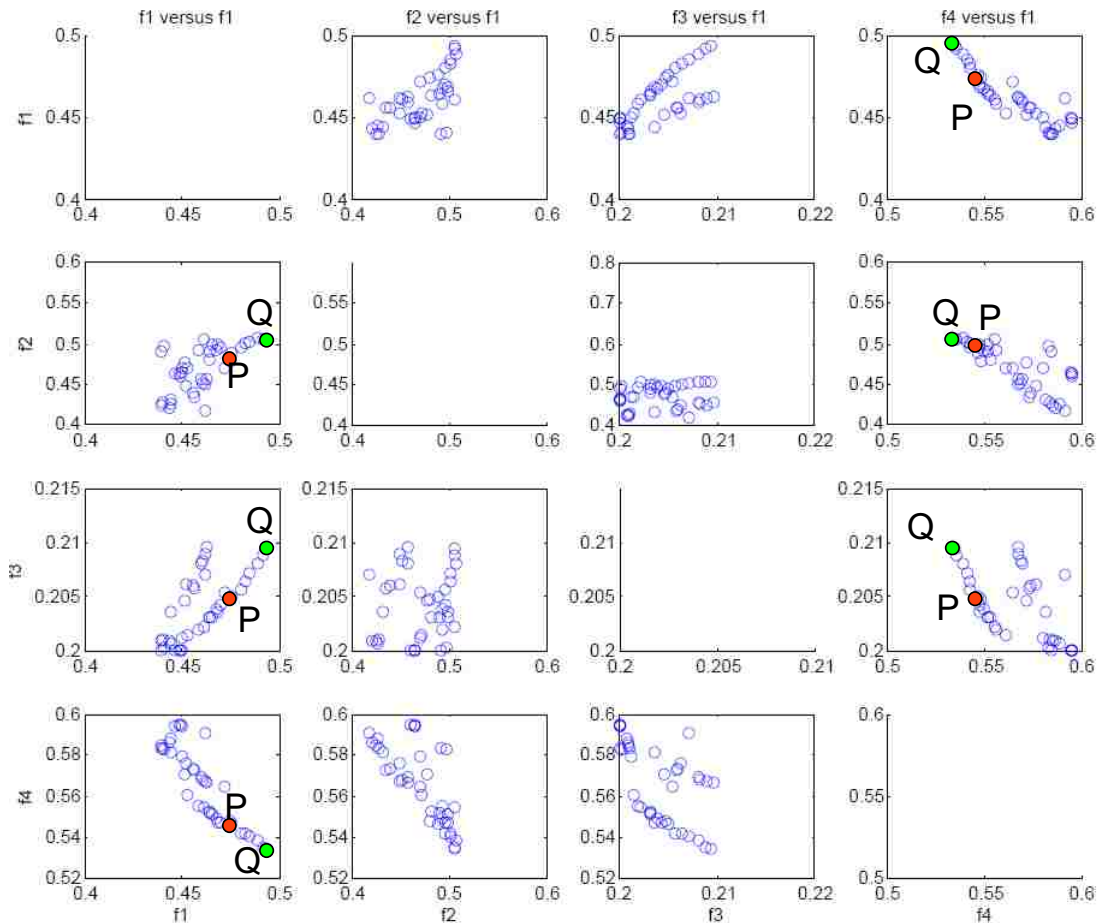
Fig 5.9 Pareto graph with comparison of each objective pair (Q is the solution with minimum corner radii; P is the point where f1 monotonically increases with a decrease of f4)

However, it was also noted that after the corner radius reaches point P, the value of objective functions f4 and f2 increased rapidly with the decrease of corner radius. The corner radius at P is 8.88 mm, corresponding to fracture/necking objectives f1=89.59 MPa, severe thinning f2=0.104 and wrinkling f3=30342 MPa. It may then be concluded that point P is an unstable point, where a small decrease in corner radius will result in a dramatic decrease in the tube thickness and lead to a rapidly increasing deformation of the tube.

Fig 5.10a shows the stress distribution in the part after it was hydroformed with the loading path defined by the Pareto optimum layout, and compared with the FLSD. It was shown that the maximum stress in the part is approximately 25MPa below the stress forming limit, which ensures the part would be safely hydroformed. Fig 5.10b, in contrast, shows the stress distribution for a loading path which leads to failure.
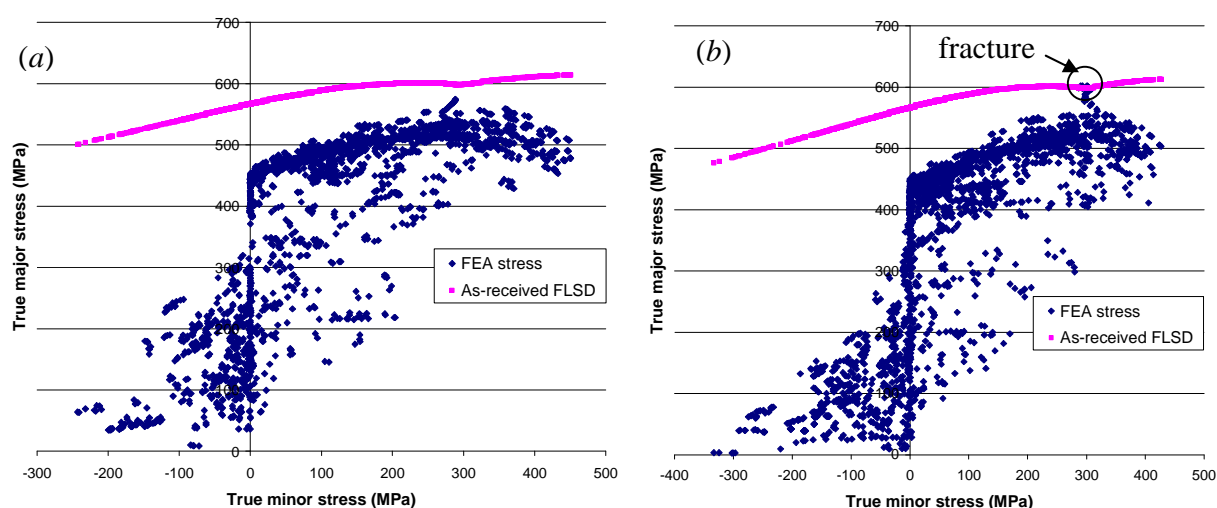
Fig 5.10 Stresses in the part after it was hydroformed with the loading path defined by (*a*) the Pareto optimum layout and (*b*) One leading to failure, compared with the FLSD.

5.4.6 Discussion

A ratio of corner radius to thickness $r/t = 4.28$ was obtained with MOGA. This is much smaller than the ratio $r/t = 4.54$ obtained with the Normal Boundary Intersection (NBI) method (see Chapter 4). The load paths are also compared with the optimization result obtained by NBI method and one with failure (Fig. 5.11, Tables 5.1 and 5.2) where

loading path 1 is the optimum loading path obtained with the MOGA, loading path 2 is the optimum loading path that was obtained with the NBI method and loading path 3 leads to failure. However, this does not mean that the NBI method is inferior, because the NBI method requires less calculation time and less sampling points and can generate an evenly distributed solution set.

A comparison between load paths 1 and 2 (See Fig. 5.11, Tables 5.1 and 5.2), indicates that loading path 1 has a larger rate of pressure increase (or larger $\Delta P/\Delta D$) at stage 1
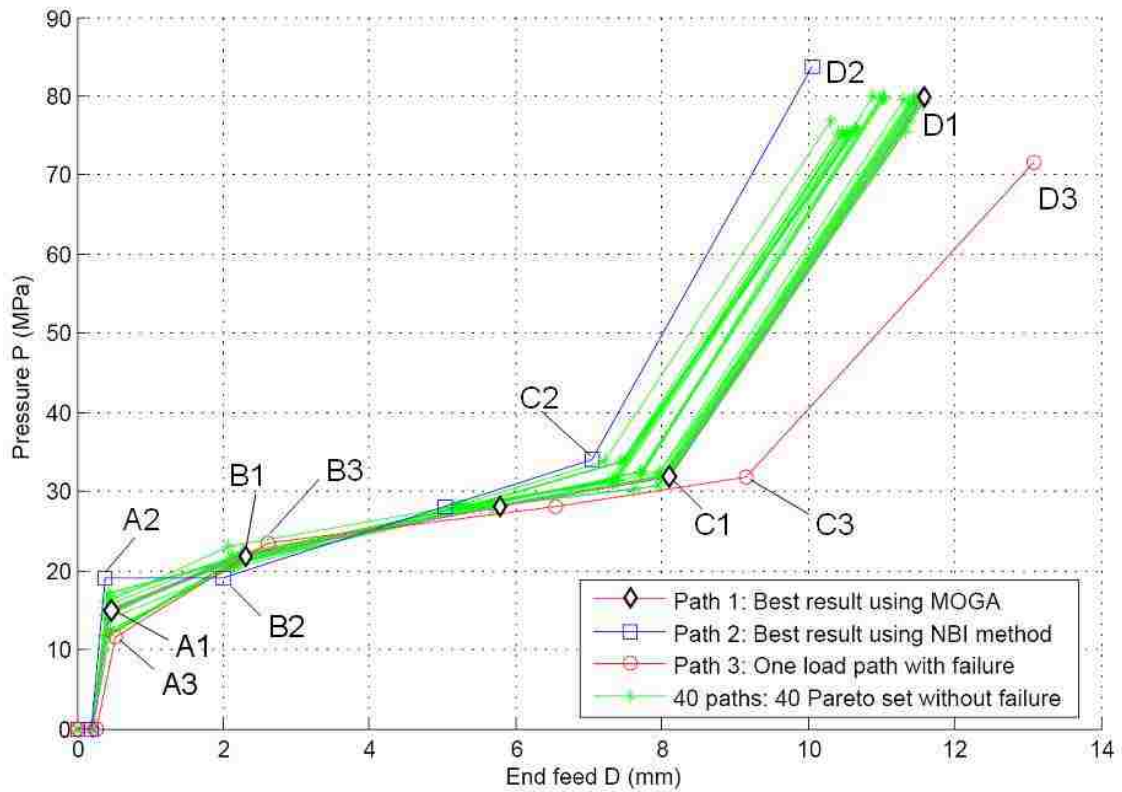
Fig 5.11 Comparison of optimal loading path using MOGA, NBI method and one with failure

Table 5.1. Three different load paths

	P1 (MPa)	P2 (MPa)	P3 (MPa)	P4 (MPa)	P5 (MPa)	D (mm)
Path 1	14.8	21.91	28	31.76	79.93	11.57
Path 2	19	19.03	28	34	83.76	10.06
Path 3	11.56	23.52	28	31.71	71.66	13.08

Table 5.2. Comparison of the forming results with different loading paths

	Stage 1		Slope	Stage 2		Slope	final objective results			
	ΔP (MPa)	ΔD (mm)	$\Delta P/\Delta D$	ΔP (MPa)	ΔD (mm)	$\Delta P/\Delta D$	f1 (MPa)	f2 (MPa)	f3	f4 (mm)
Path 1	7.11	1.9	3.07	9.85	5.8	1.22	84	32216	0.200	8.57
Path 2	0.03	1.6	0.015	15	5	2.13	95	20339	0.862	9.082
Path 3	11.96	2.1	4.57	8.19	6.5	0.89	56.32	53474	2.899	8.01

compared to loading path 2, but has greater rate of end feed (smaller $\Delta P/\Delta D$) at stage 2 compared to load path 2.

Loading path 3 displays the greatest rate of pressure increase ($\Delta P/\Delta D$) at stage 1 and the smallest one at stage 2 (Table 5.2). From the comparison, it can be seen that the loading path with the greatest $\Delta P/\Delta D$ slope at deformation stage 1, and a smallest $\Delta P/\Delta D$ slope at stage 2 (i.e. loading path 3) is able to achieve the smallest corner radius. On the contrary, a loading path having the smallest $\Delta P/\Delta D$ slope in stage 1 and the greatest $\Delta P/\Delta D$ slope in stage 2 (i.e. loading path 2), is able to produce a part with the least forming severity (greater safety factor), but fails to minimize the corner radius. Therefore, the optimum loading path is a compromise between load paths 2 and 3. Loading path 1 (obtained with MOGA) is a compromise between loading path 2 and 3 and leads to a safe part in which wall-thinning is minimized and a smaller corner radius is achieved. This is the most desirable load path.

It also appears that loading path 1 applied less pressure at the end of the calibration stage than loading path 2, but results in a smaller corner radius. Therefore, a smaller corner radius is not achieved by merely increasing the calibration pressure, but by applying an appropriate match of the pressure and end-feed. Meanwhile, it is important to notice that in the calibration stage (beyond C1 or C2), the final set of 40 Pareto load paths (Fig. 5.11) exhibited almost the same $\Delta P/\Delta D$ slope: the curves are practically parallel with each other. This observation underscores the fact that the loading path during the early stages of deformation is more critical to the success of the hydroforming operation than the final calibration stage. Therefore, close attention should be paid to the design of the first part of the load path.

In regards to computation costs, the run time for FE simulations for one generation with a population of 40 experiments using a HP xw9300 workstation with 2.19 GHz AMD Opteron™ Processor 248 with 4 GB of RAM was about 4hrs without considering optimization time. If the layouts in this case study were completely carried out by FE simulation, the total simulation time would be 40×4=160 hrs. However, the proposed method using a combination of FEA and a hybrid Kriging model only requires 8 FE updates, and a CPU time of 8×4=32 hrs, which is one fifth of the former calculation.

The cross-validation accuracy after eight series of FE simulation updates (every five generations) is also examined: the errors of the predictor model for the four objectives f1, f2, f3 and f4 were 0.0043, 0.0012, 0.0037 and 0.0013, respectively. It is noted that the errors of the predictor model obtained in Section 4 for the four objectives (prior to the MOGA optimization) were 0.0089, 0.0046, 0.0075 and 0.0013. The prediction error for f4 remained the same; this indicates that the initial Kriging model was accurately set up with 40 samples. However, the errors for the other objectives (f1, f2 and f3) decreased by a half compared to the initial Kriging model. As such, the overall prediction accuracy has greatly improved.

5.4.7 Conclusions for case study 1

A method of searching for the global optimization using MOGA combined with a recurrently updated Kriging model was proposed. The overall prediction accuracy of the surrogate model was shown to double for three of the four objectives. The multi-objective functions used to evaluate forming severity were established based on both the FLD and the FLSD. A Kriging model was established for each objective to improve the optimization efficiency, and was updated every five generations through FE simulation. The Pareto optimal sets were obtained for all four objectives. The optimal loading path was able to achieve a minimum ratio of corner radius to wall thickness r/t=4.28 and it was shown to lead to a safer and more robust hydroforming process.

5.5 Case study 2: Straight tube hydroforming considering local thinning using H-MOGA

The straight tube corner fill problem described in section 5.6.1 was also optimized using the MOGA II (H-MOGA) which imposes greater restrictions in tube thinning: i.e. no more than 30% thickness strain.

5.5.1 Design variables

The design variables for the loading path included five parameters for pressure and one for end feed, namely P1, P2, P3, P4, P5 and D (Fig. 5.8). P1 to P5 were different pressure levels, in MPa, (P1 was the yield pressure, P2, P3 and P4 were the intermediate pressure levels and P5 was the calibration pressure) and D was the maximum end feed, in mm, at the end of the process. The ranges selected for each design variable were as follows:

$$10 \leq P1 \leq 19; \quad 20 \leq P2 \leq 28; \quad 26 \leq P3 \leq 28$$
$$30 \leq P4 \leq 35; \quad 40 \leq P5 \leq 85; \quad 10 \leq D \leq 14$$

(5.9)

All the design variables and the objective values were linearly normalized between 0.2 and 0.8.

5.5.2 Design objective function and constraints

The loading path design of corner-filling tube hydroforming has two primary objectives: (1) improvement of die-filling at the corner and, (2) minimizing thinning of the tube wall, while satisfying the forming limits defined by the stress/strain forming limit diagram.

The primary objective of the current tube hydroforming problem is to maximize the amount of expansion of the tube wall into the corners of the die, or in other words, to minimize the corner radius. Once again the corner radius objective function is defined as:

$$f_4 = R_C$$

(5.10)

The function (3.5) of severe thinning was evaluated on every element in the tube. In reality, the local thickness reduction may reach a limit. Hence, the maximum local thinning ratio was employed to minimize the function:

$$f_5 = (t_0 - t_{\min}) \times 100\% / t_0 \tag{5.11}$$

where t_0 is the original tube thickness, and t_{min} is the final minimum thickness on the deformed tube. The constraint for f_5 is: $f_5 < 30\%$.

Again, the objectives of formability (Eq. (3.2) to (3.5)) must also be minimized, and the problem can be summarized by the following formulation which places constraints on each objective:

Minimize $\quad F(x) = [f_1(x), f_2(x), f_3(x), f_4(x), f_5(x)]$

s.t. $\quad 0.2 \leq f_1 \leq 0.75; \quad 0.2 \leq f_2 \leq 0.75$

$\qquad 0.2 \leq f_3 \leq 0.30; \quad 0.2 \leq f_4 \leq 0.60; \quad 0.2 \leq f_5 \leq 0.38$ $\tag{5.12}$

where x is the normalized vector of design variables: $x = [P1, P2, P3, P4, P5, D]^T$. The ranges of each design variable are the same after normalization: $0.2 \leq x_i \leq 0.8$, $i = 1,2,...6$.

It can be noted that the five objectives are different and some of them may be conflicting on the design domain. Therefore, the objectives may not reach one single optimal solution to satisfy each objective at the same time.

5.5.3 Kriging surrogate model

The design of experiments was carried out using the Latin hypercube sampling (LHS) method. A group of 50 runs was adopted to obtain a more precise model (Appendix B). Then, the 10-fold cross-validation was implemented and the PRESS value was obtained for the model with regard to each objective. The data was divided into 10 subsets. Nine of the subsets were input as the training data and the last one was used as the testing data. The total average error of the cross-validation was obtained as the estimation of the precision.

The quality of the Kriging model is demonstrated by the error and correlation values in Table 5.3. The PRESS error for each objective was low, and f4 had the lowest value. Except for objective f2, the Kriging response surface for all of the other objectives had a high adjusted coefficient of determination which indicated an explanation above 92.69% of the variability in predicting new observations. The result for f2 was a little low, but the value was still acceptable.

Table 5.3 Accuracy of response surface of objectives

	f1	f2	f3	f4	f5
# of observations	50	50	50	50	50
PRESS	0.0040	0.0050	0.0065	0.0008	0.0012
R^2_{pred}	0.9339	0.7408	0.9269	0.9557	0.9611
SST	0.0606	0.0193	0.0885	0.0186	0.0302

5.5.4 Results

The optimization was implemented with MOGA in 15 generations. The elitist chromosomes were saved in an independent archive for each generation. Fig. 5.12 shows three stages in the evolution of the optimization with regard to the 4th and 5th objectives: the 1st generation, the 15th generation and the final archived solution set. From Fig. 5.12, it can be seen that both objectives (i.e. the minimum corner radius f4 and the minimum thinning ratio f5 evolved efficiently toward the Utopia point, which is defined as the point (0,0). The archiving successfully retained the elitist solutions in each generation. Three solutions, including two extreme points and one with the second minimum L_2 norm, were selected for investigation.

Table 5.4 lists the normalized values and actual objective values (in bold). It was noted from Table 5.4 that solution A has the smallest corner radius (f4) of 9.165 mm among the three solutions, but the greatest local thinning ratio (f5). Solution C has the smallest thinning ratio, but the greatest corner radius of 10.13 mm. This indicates that these two objectives are in opposition to each other. Moreover, Solution B has a larger stress

objective value (lower stress safety margin), L_2 norm and corner radius than solution A, but its thinning (local and global) and wrinkling values are smaller. Generally, it was difficult to determine which solution is better based on one objective. Therefore, the final decision for the best solution should be made with the designer's specific criterion or preference. In this work, the decision was made according to the preferences to corner
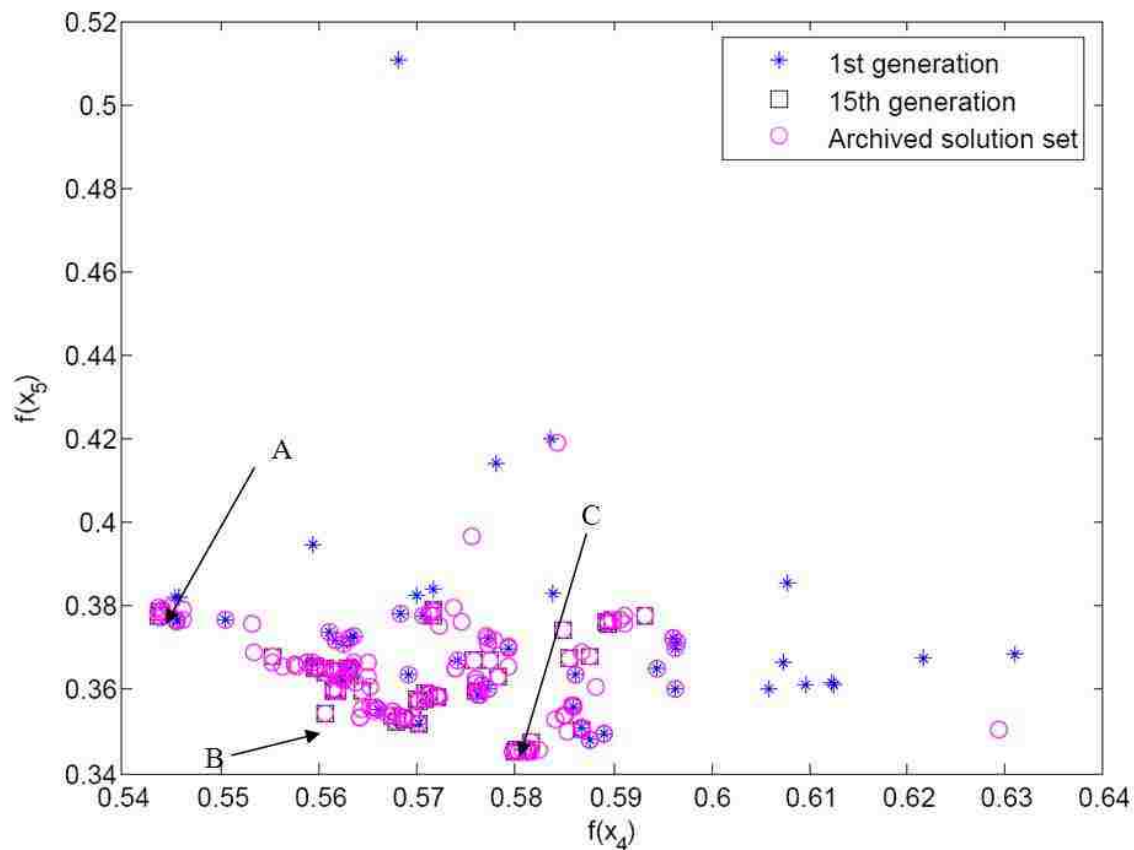
Fig. 5.12 The evolution of the 4th and 5th objectives (generations 1, 15 and archived set)

Table 5.4. The objectives of the three selected points (without units)

	f1	f2	f3	f4	f5	L_2 norm
A (Norm*)	0.4511	0.5914	0.2078	0.5437	0.3775	0.6619
B (Norm)	0.4519	0.46836	0.20012	0.5607	0.3542	0.6632
C (Norm)	0.4513	0.606	0.200003	0.5799	0.3450	0.6748
A (True**)	**-98.42**	**260946**	**0.1629**	**9.1650**	**0.2958**	—
B (True)	**-98.06**	**178909**	**0.002436**	**9.6198**	**0.2569**	—
C (True)	**-98.32**	**270663**	**0.000067**	**10.130**	**0.2417**	—

* norm: normalization;

** True: FEA results.
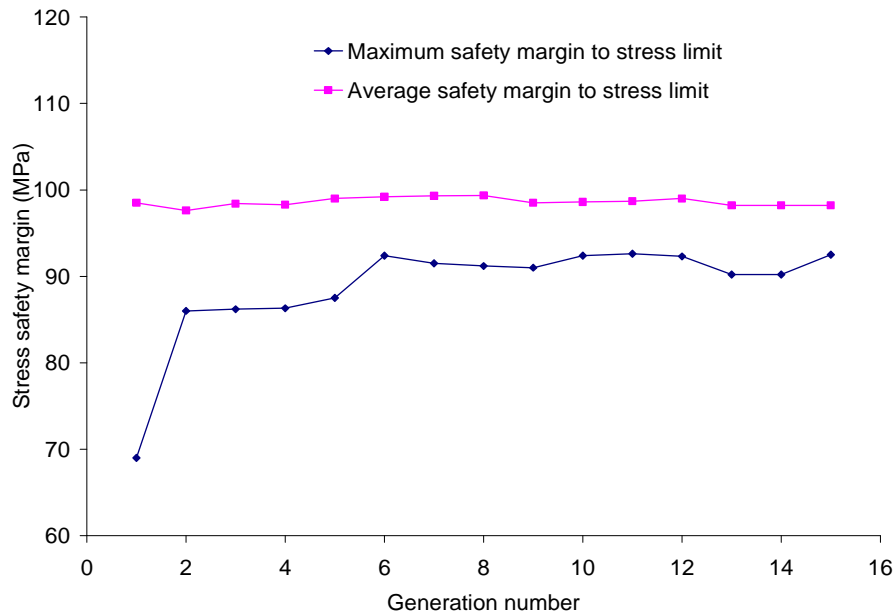
Fig. 5.13 The evolution of the stress safety margin (the y axis: absolute value of f1)

radius and thinning ratio by local search.

If the stress safety margin for this hydroforming process is defined as the difference in major stress between the most critical stress state in the part and the SFLC, Fig. 5.13 shows that the maximum safety margin improved after 15 generations. It indicated that though the average f1 value did not vary much, the maximum safety margin to stress limit had decreased and approached a value of 91 MPa in the last generation. This can be seen as a upper limit value for safe margin of stress to obtain a defect free part in this hydroforming. It was believed that this improved safety margin to stress limit will benefit the forming process for generating a quality part.

Therefore, it can be seen that the maximum stress margin value has been improved for the last population after optimization. In the next step of the local search, it can be assumed that all of the design points in the nearest domain of the Pareto front had met the formability safety requirements which were represented by the objectives.

5.5.5 Local search using sequential quadratic programming (SQP)

In the above constraint handling study, the boundary of the local thinning ratio was relaxed from a normalized value of 0.38 to 0.44 (corresponding to an increase in maximum thinning ratio from 30% to 40%) to investigate the effect of boundary size on the efficiency of the search. A second archived data set was therefore determined and is plotted in Fig. 5.14. From the comparison of the two sets shown in Fig. 5.14, it was verified that the first archived set consists of a more uniform distribution and better Pareto solutions (approaching closer to the origin). Nevertheless, it should also be noted that by relaxing the boundary of the thinning ratio objective f5 improved somewhat (see circled region A in Fig. 5.14). This means that it is possible to improve the results in this small region A which is close to those solutions having minimum corner radius.
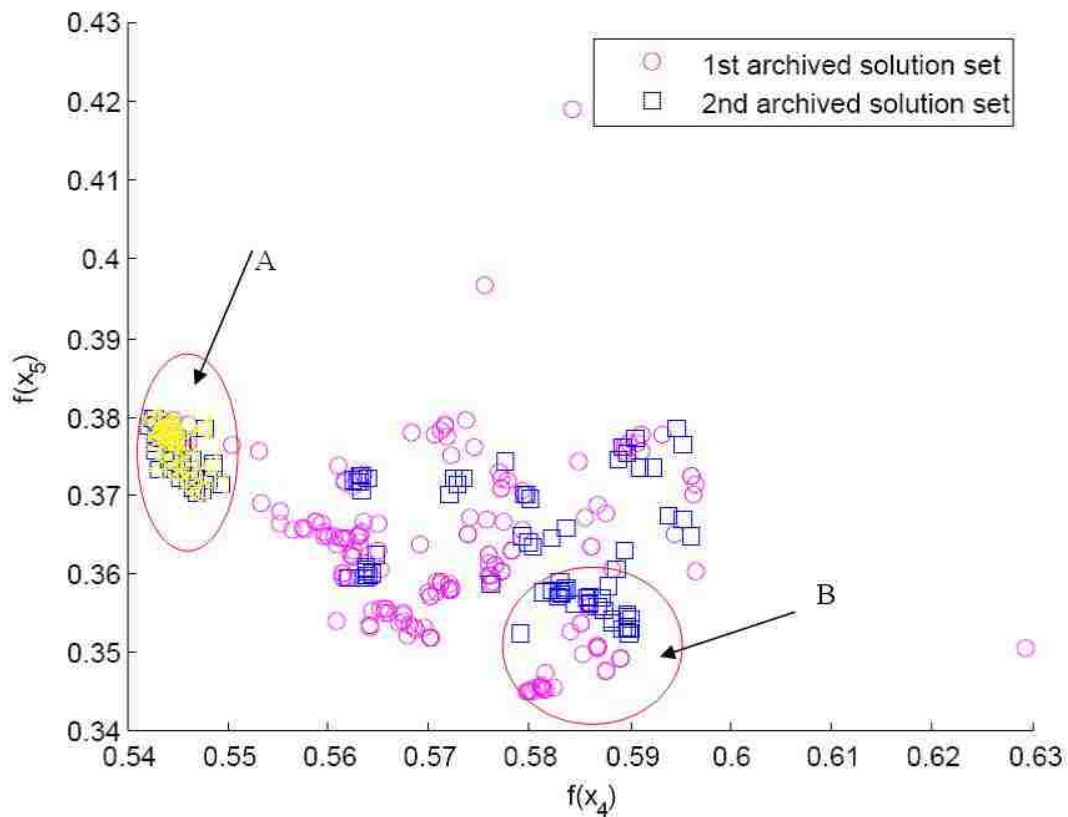
Fig. 5.14 Comparison of two archived data sets

The data from regions A and B (Fig. 5.14) were used to establish a Kriging response surface model for local search in these two regions, respectively. Only the two objectives of corner radius and local minimum thinning ratio were kept in the new dataset for setting up the Kriging model. The datasets had a matrix of 50×8 and 55×8 in size, which were extracted from 361×11 dataset. The SQP algorithm with function FMINCON in Matlab 2008a was used to search for the local minimum:

```
[optfactors, fval]=
fmincon(@objfunsq,x0,[],[],[],[],lb,ub,@confun);
```

The results were plotted in the circle in Fig. 5.16.
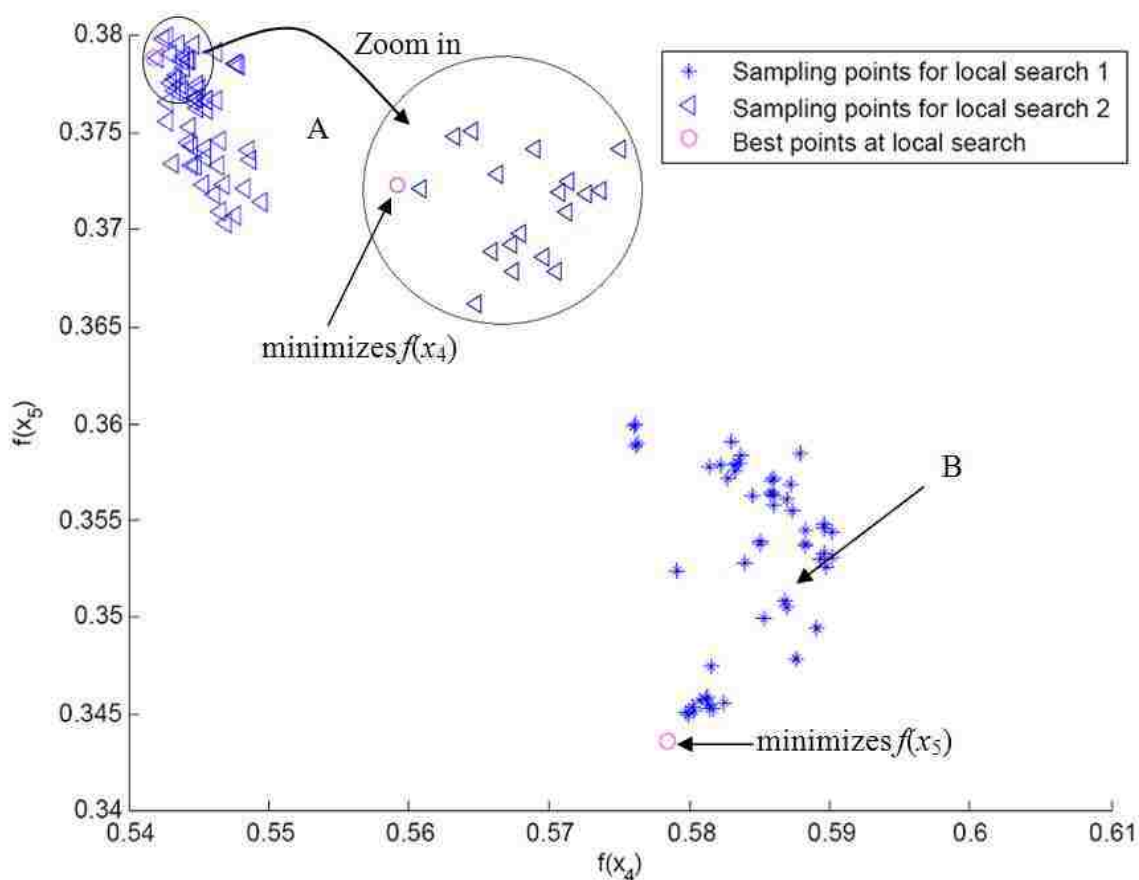
Fig. 5.15 Best results of local search and sampling points in zoomed region A and region B

For the local search in both regions, the local minima were obtained after approximately 40 seconds of run time. Fig. 5.15 shows an enlargement of region where it can be seen

that the minimum was slightly better than the value obtained by MOGA I. For the local search in region B, there was a significant improvement. The optimized results (with *) were presented and compared to the two archived data sets (shown in Table 5.5 and 5.6).

Table 5.5 Local search result in region A

	f4	f5	L2 norm	f1	f2	f3
Local min A$^+$	0.5418	0.3789	0.6619	0.4705	0.4131	0.2057
Global best 1	0.5437	0.3775	0.6619	0.4511	0.5914	0.2078
Global best 2	0.5421	0.3788	0.6613	0.4665	0.6208	0.2069
Local min A$^\Delta$	9.115	0.298	—	-91.35	142089	0.1187
Global best 1	9.165	0.296	—	-98.42	260946	0.1629
Global best 2	9.123	0.298	—	-92.72	280533	0.1467

Table 5.6 Local search result in region B

	f4	f5	L2 norm	f1	f2	f3
Local min B$^+$	0.5785	0.3436	0.6728	0.4508	0.6011	0.2000
Global best 3	0.5799	0.3450	0.6748	0.4513	0.6060	0.2000
Local min B$^\Delta$	10.09	0.239	—	-98.53	267381	1.26E-5
Global best 3	10.13	0.242	—	-98.32	270663	6.72E-5

$^+$ Prediction of local search;

$^\Delta$ FEA results of local search;

The load paths for these two final minimum objectives through local search were plotted and compared with the Pareto loading path solutions using MOGA I (Fig. 5.16).

5.5.6 Results validation and discussion

The predicted results (with +) in the local searches were examined by two additional FEA runs and were also presented in Tables 5.5 and 5.6 (with Δ).
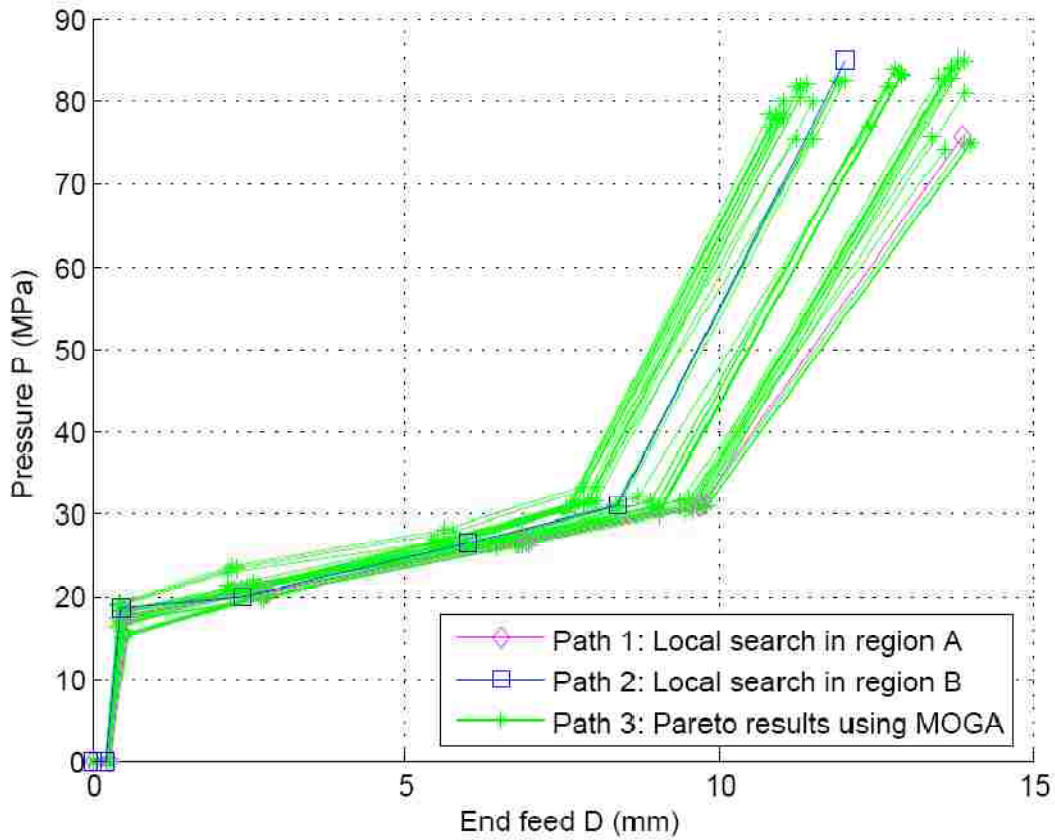
Fig. 5.16 Comparison of the loading path from MOGA and local searches

Note: Global best 1 and 3 were from the first archived solution set using global search; Global best 2 was from the second archived solution set using global search; Local min represented for local search.

Since the solution from the local search was better than that from the MOGA search, the final minimum corner radius was chosen to be 9.115mm in region A with the preference of a smaller corner radius; meanwhile, the other objective (f5) under the same loading path had reached a thinning ratio of 29.8% which is less than 30%. The stress safety margin is 91.35 MPa, which indicates a very safe process. Meanwhile, if less thinning was preferred, the final decision could also be chosen from Region B, which represents a maximum thinning of 23.9% and a corner radius of 10.09 mm. The results also show that the other objectives improved in terms of the stress safety margin of 98.53 MPa, wrinkling of 267381 MPa and thinning value of 1.26e-5.

5.5.7 Conclusions for case study 2

In this study a hybrid global and local search optimization strategy was proposed and applied to designing the loading path of a hydroformed tubular part with a square cross-section. The constraint handling technique was developed and coupled with the conventional NSGA-II. The following conclusions can be drawn:

1. A constraint handling algorithm was applied and implemented to the multi-objective optimization with more than three objectives, which incorporated the ranking of constraint violations and a second ranking of non-domination of objectives and local crowding distance.

2. A hybrid algorithm H-MOGA combining the global search (using MOGA) and local search (using SQP) for multi-objective optimization was proposed and applied to the optimization of a hydroformed tube. The case study showed better results, with smaller corner radius and thickness thinning ratio being obtained compared to the single MOGA search.

3. The optimization problem with five objectives was investigated. It was noted that the proposed method, which uses the Kriging predictor to generate new points, with constraint handling and FE calculation for evaluating new offsprings can achieve a good performance in terms of both accuracy and efficiency in dealing with more than three objectives.

4. Visualization was used to assist in decision-making and to search for the Pareto solutions. It is suggested that the plotting of results be focused on the preferred objectives.

5. This case study showed that the stress safety margin improved when the corner filling and thinning objectives were achieved. The improved stress safety margin leads to a more robust forming process and a better quality part.

5.6   Case study 3: Inverse Analysis Using MOGA for Hydroforming of A Refrigerator Door Handle

5.6.1 Introduction

Inverse analysis has been widely used to determine material characteristics and process parameters during metal forming operations. Computer simulation using the finite element method (FEM) has been effectively used to identify constitutive models and their input parameters. FE simulations require several kinds of input parameters (Aue-U-Lan et al., 2004;Imaninejad et al., 2005), such as tool geometry, mesh, loading conditions, non-linear constitutive laws, friction laws, etc. Similarly, the simulation output may be evaluated in terms of part quality, forming severity, shape conformity, structural stability or production cost. Consequently, the problem becomes a multiple input and multiple output (MIMO) inverse problem.

Ponthot and Kleinermann[41] (2006) proposed a cascade optimization methodology for two categories of MIMO inverse problems in metal forming simulation: (1) parameter identification; and (2) shape/process optimization. The first category involves evaluating the material parameters for material constitutive models that would lead to the most accurate results with respect to physical experiments, i.e. minimizing the difference between experimental results and FEM simulations. On the other hand, the second category involves determining the initial geometry of the specimen and/or the shape of the forming tools, as well as some parameters of the process itself, in order to provide the desired final geometry after the forming process. Eight types of non-linear gradient based algorithms were compared in each case study and it was shown that the algorithm named "Levenberg-Marquart + Conjugate gradient + globally convergent 3MA (Modified Method of Moving Asymptotes)" is the most effective in terms of robustness and accuracy. However, it can be noted that only a single objective function was used in all these cases.

Peñuelas et al. (2009) proposed a method to determine the elasto-plastic and damage parameters on small punch tests, which was based on the inverse method, the design of experiments, the polynomial curve adjustment and the evolutionary multi-objective optimization. It was applied to identify ten different parameters which were characterized with either macro-mechanical or micromechanical models in each of five stages of the load-displacement curve, i.e. elastic deformation, elasto-plastic transition zone, generalized plastic deformation, plastic instability and fracture initiation, fracture softening and final fracture stages.

In this study, an inverse method of loading path design in tube hydroforming of a refrigerator door handle is presented. The motivation is to inversely analyze the loading path in terms of internal pressure vs. time and end-feed displacement vs. time, and to verify the applicability of developed algorithms. The proposed multi-objective optimization algorithm MOGA-I was used to determine the hydroforming loading path parameters.

5.6.2 Geometry of the Tube and the Die

The part under consideration is a refrigerator door handle (Fig. 5.17), which is produced by Schuler Inc. A straight tube is first bent with a bend angle of approximately 24 degrees and a radius of curvature of R=447.5 mm. The influence of bending is not significant since the maximum bending strain is only about 2.8%. The bent tube is hydroformed and the straight portion of the tube is then trimmed off to produce the final part. The objective of this study is to determine the process parameters (pressure and end feed) which will lead to a hydroformed part that fully conforms to the die shape without any failure occurring.

5.6.3 FEA Model

The tube material is an annealed 304 stainless steel whose mechanical properties are given in Table 5.7. The upper and lower dies were modelled as rigid bodies with a total of

14,598 elements. The mid-surface of the tube was modelled with 19,848 Belytschko-Tsay shell elements (Fig 5.18), having five integration points through the thickness. An isotropic material model based on the von Mises yield criterion and named "MAT_PIECEWISE_LINEAR_ PLASTICITY" (No. 24 in LS-DYNA) was chosen to represent the hardening behaviour and the true stress-strain curve is given in Fig 5.19. Coulomb's coefficient of friction was set to 0.05 for the contact interface. In addition, a COF of 0.1 was also applied to study the sensitivity of the loading path with regard to friction.

Table 5.7 Mechanical Properties and Geometry of the Tube (provided by Schüler Inc.)

Strength Coefficient (MPa)	Yield stress (MPa)	Ultimate tensile stress (MPa)	Density (kg/m^3)	Young's modulus (GPa)	Poisson's ratio	Hardening exponent n	Outer Diameter (mm)	Length (mm)	Thickness (mm)
75	276	665	8000	193	0.3	0.43	25.4	1250	1.6
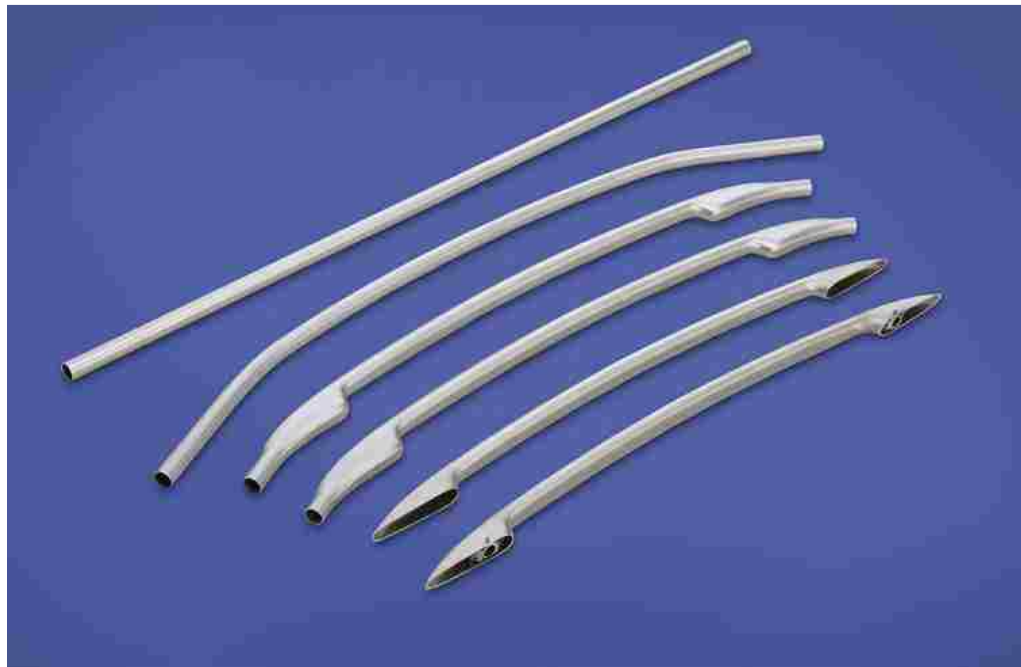
Fig. 5.17 Forming process of a refrigerator door handle (courtesy of Schüler Inc.)
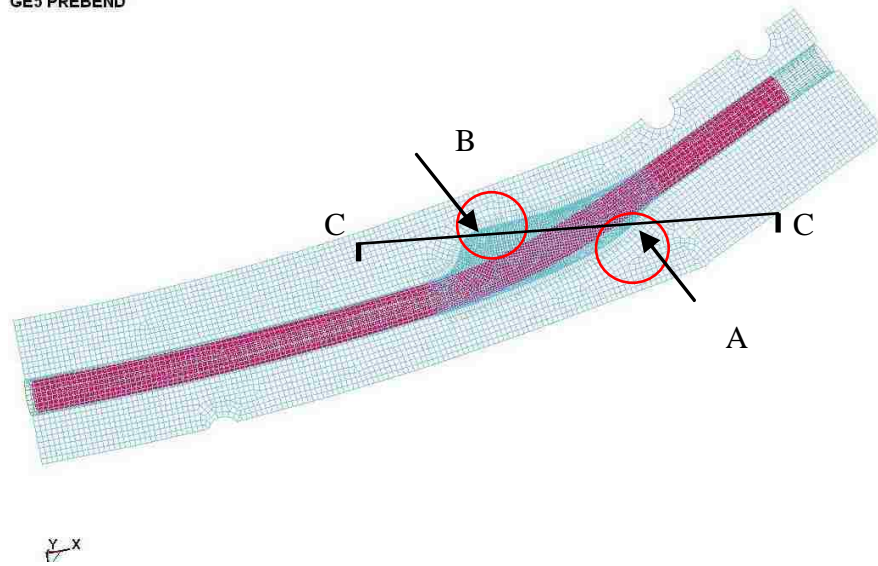
Fig. 5.18 Finite element mesh
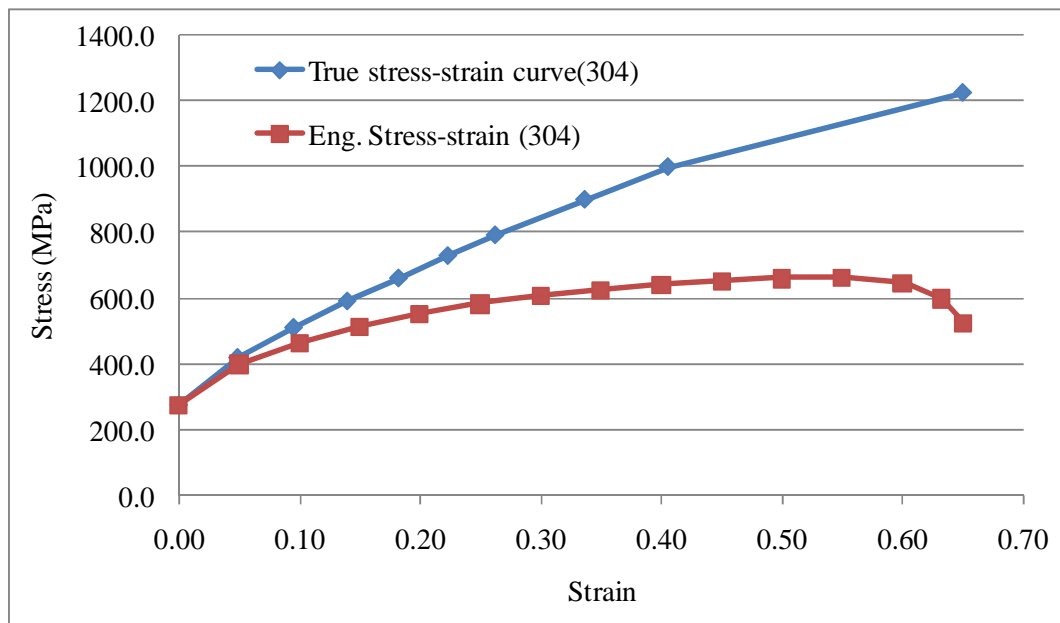
Fig. 5.19 Stress-strain curve (true and engineering)

5.6.4 Loading path Design and Sensitivity Analysis

The loading path was defined such that the pressure vs. time curve was a piecewise linear profile and the end feed vs. time curve was linear. A sensitivity analysis was then performed to identify the most sensitive factors in the hydroforming process. Two sequential L18 orthogonal arrays were carried out to identify the ranges of pressure and

116

end feed parameters. A loading path was finally selected with 12 parameters, which consisted of 7 pressure variables (P1~P7) and 5 end-feed displacement variables (D1~D5), as shown in Fig 5.20.
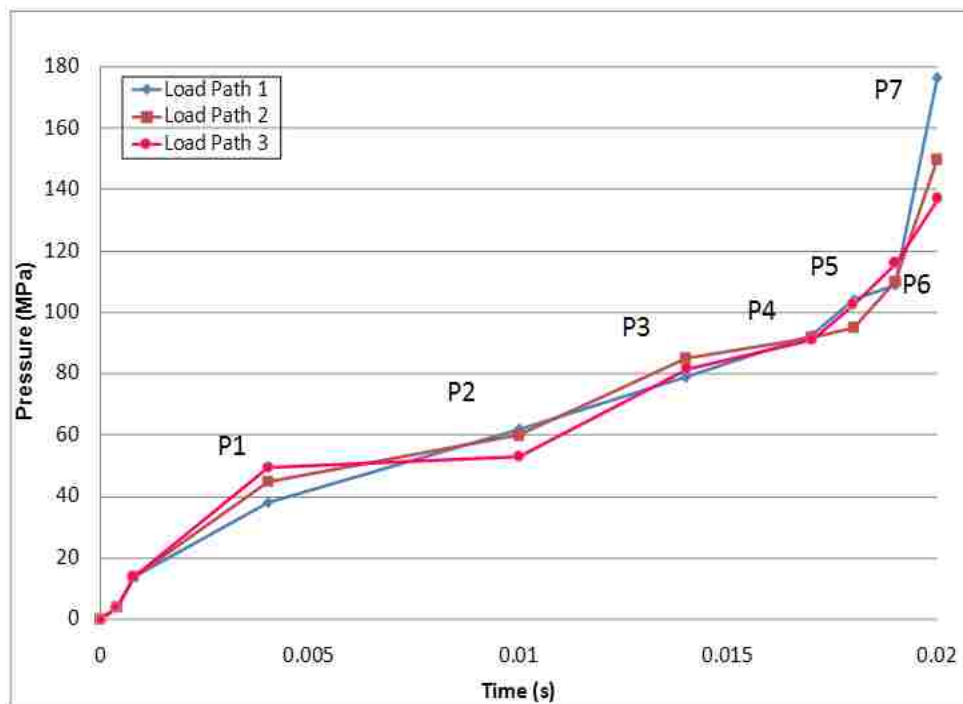
(a) Internal pressure

Fig. 5.20 Loading path design
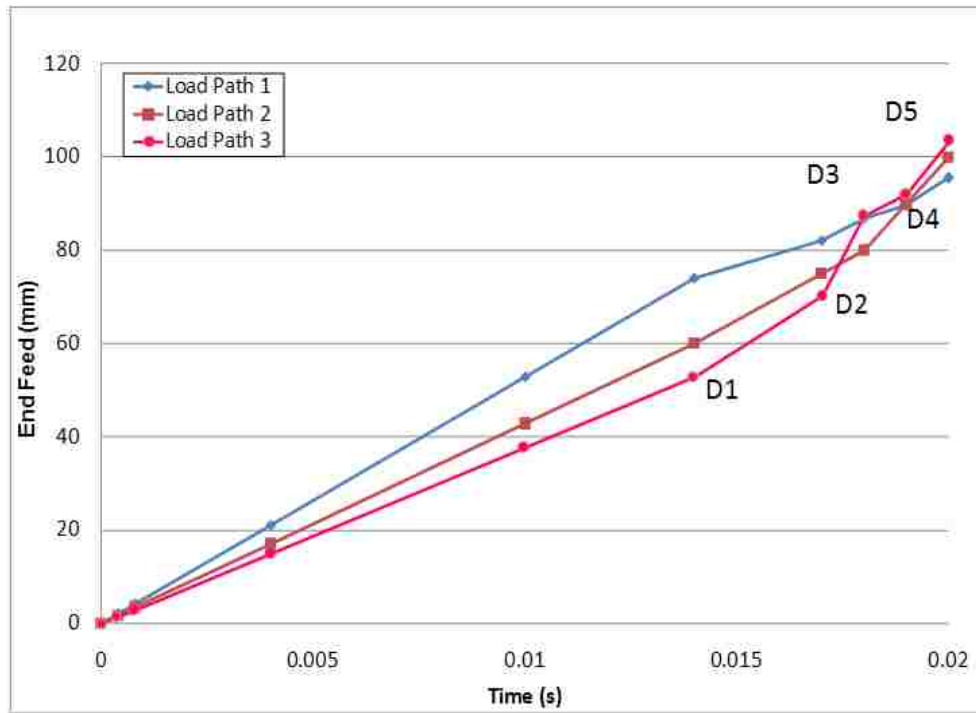
(b) Axial end feed displacement

Fig. 5.20 Loading path design (Continued)

5.6.5 Process optimization

As mentioned earlier, process optimization problems are one category of inverse problems. When a specific part geometry is required, it is necessary to quantify any deviation from the desired shape. This can be done by projecting the nodes on the external surface of the deformed mesh onto the desired shape and by computing the gap between each node and the prescribed shape (Fig 5.21). In this work, one objective was, therefore, defined as the root of the average sum of square of the gaps:

$$f(\vec{x}) = \sqrt{\frac{1}{n} \sum_{i=1}^{n} (gap_i(\vec{x}))^2}. \tag{5.13}$$

where $\vec{x}$ is the vector of control variables to be optimized, n is the number of projected nodes, i.e. the dimension of vector $\vec{x}$, and gap_i is the gap between the ith projected node and the prescribed shape.
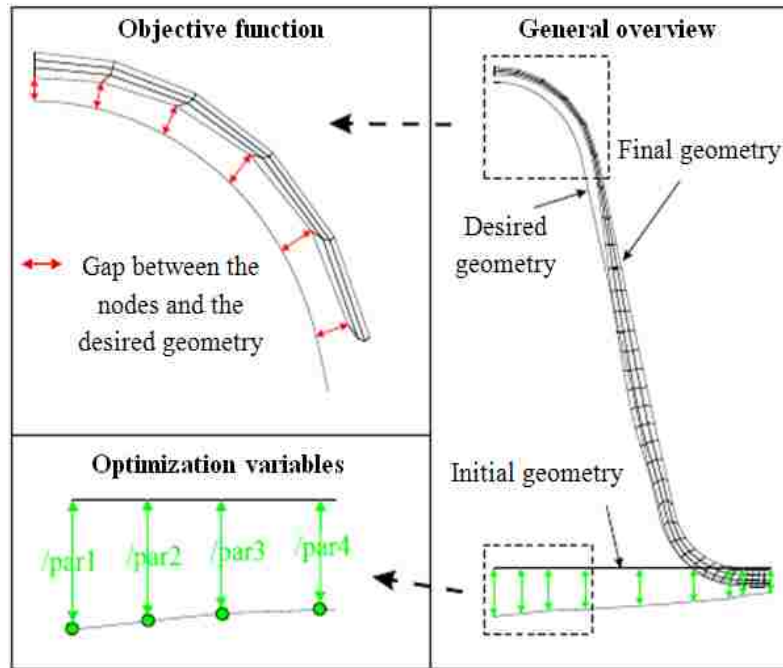
Fig. 5.21 An example of objective function and optimization variables, where par1 to par4 are optimization variables (Adapted from Ponthot and J.P. Kleinermann, 2006)

The vector of control variables $\bar{x}$ is chosen as a function of the loading path parameters:

$$\vec{x} \ = \ x\,(\,\vec{P}\,,\,\vec{D}\,) \tag{5.14}$$

where $\vec{P}$ and $\vec{D}$ are the vector of the pressure points and the end feed points obtained from the screening analysis.

In this study, two representative points (node number 14272 and 15291 in Fig 5.22(a) and 5.22(b), respectively) at the lower and upper sides of the deformed tube were used to measure the gap between the die shape and the deformed tube shape.
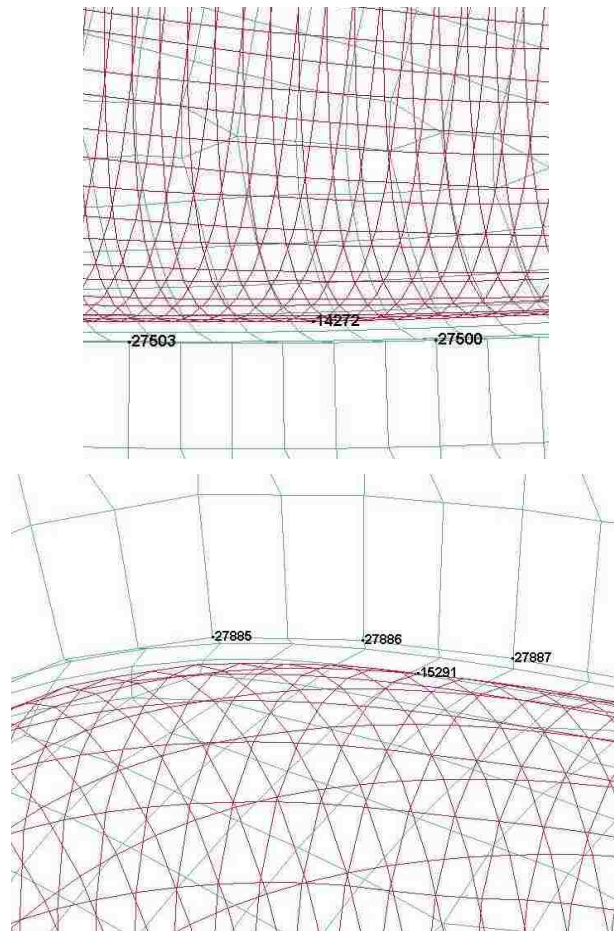
(a) zoom-in of zone A in Fig. 5.18 (b) Zoom-in of zone B in Fig. 5.18

Fig. 5.22 (a) Measure of distance d1 in the lower die and (b) Measure of distance d2 in the upper die

5.6.6 Inverse strategy

The proposed methodology in this research is based on a combination of the inverse method, a design of experiments, numerical simulations, the Kriging predictor and multi-objective genetic algorithms.

It can be noted from equation (5.13), that the shape conformity objective is a single objective. Therefore, a single objective optimization algorithm will be used to solve this type of problem such as BFGS algorithms, or conjugated gradient, etc. However, the derivative of the equilibrium equation (either the continuum-based or the discretized

equation) is difficult to obtain. At the same time, the constraints of the problem may form a non-convex domain of solutions. Evolutionary algorithms (GA and GP) are more suitable for solving the current problem since they do not require the difficult calculation of sensitivities, and they have the tendency to find the global optimum and can take advantage of parallel computing. However, evolutionary algorithms require a rather large number of function evaluations and this has been regarded by some as a serious drawback. Nevertheless, this can be solved by implementing RSM or the Kriging surrogate method to reduce the cost of time-consuming function evaluations.

5.6.7 Objective Functions

The direct calculation was first established and adjusted before the reverse analysis. The material parameters were determined and the validation of the simulation was performed as shown in Fig. 5.23. It was noted that the two curves are almost identical up to a strain $\varepsilon = 0.5$, and the maximum relative difference in stress is 2.3% when $\varepsilon > 0.5$.

In the following step, the inverse parameters were identified. The complete hydroforming process requires the determination of a considerable number of variables such as pressure, end feed, coefficient of friction (COF) (μ), simulation time (T). However, some parameters can be obtained from the literature or from previous experience. Time T was set to be 0.002s. To study the sensitivity of the COF in the hydroforming process, two levels of the coefficient of friction were considered, i.e. 0.05 and 0.1. So the total number of parameters was reduced to the pressure and the end feed displacement, and these were represented by twelve variables: P1 to P7 for the pressure and D1 to D5 for the end feed (Fig. 5.20).
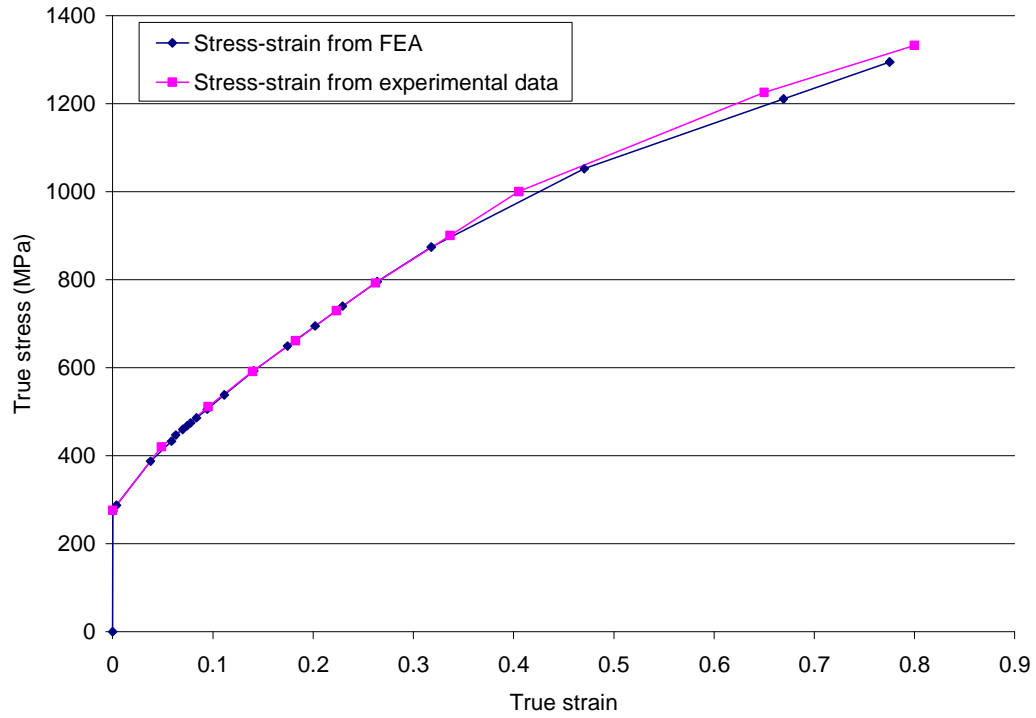
Fig. 5.23 Validation of simulation by comparing the stress-strain response from FEA and extrapolated experimental data

The objectives included two measures of die filling, which are d1 and d2 (See Fig 5.22). Furthermore, the hydroforming process should be able to overcome the difficulty of either excessive internal pressure or excessive end feed, where the former will lead to a burst or fracture and the latter will result in wrinkling or buckling. Generally, these constraints generate a small process window for tube hydroforming. In this paper, constraints were transformed into objectives and then objective functions were minimized. The objectives of necking/fracture, wrinkling, severe thinning were adopted for global evaluation (An et al., 2009), and maximum thinning was used for local assessment. The objective functions are presented in Equations (5.15) to (5.20) as follows:

$$f_1 = Obj\_f = \frac{1}{d_f} = \frac{1}{Max\left|\sigma_1^i - \sigma_f^i\right|} \tag{5.15}$$

$$f_2 = \begin{cases} Obj\_w = \sum_{i=1}^{n} |d_w^i| = \sum_{i=1}^{n} |\sigma_2^i| & \sigma_2^i < 0 \\ Obj\_w = 0 & \sigma_2^i \geq 0 \end{cases}$$ (5.16)

$$f_3 = \begin{cases} Obj\_th = \sum_{i=1}^{n} (d_{th}^i)^2 & \varepsilon_1^i > \eta(\varepsilon_2^i) \\ Obj\_th = 0 & \varepsilon_1^i \leq \eta(\varepsilon_2^i) \end{cases}$$ (5.17)

$$f_4 = d1 = Distance\ (N14272, Line\ (N27500, N27503))$$ (5.18)

$$f_5 = d2 = Distance(N15291, Line\ (N27886, N27887))$$ (5.19)

$$f_6 = (t_0 - t_{min}) \times 100\% / t_0$$ (5.20)

where t_0 and t_{min} are the original tube thickness and the minimum thickness of the deformed tube, respectively.

5.6.8 Optimization Results for Loading Path

This multi-objective optimization problem was solved using the evolutionary genetic algorithm NSGA-IIa. The genetic operators were crossover and mutation with a crossover rate Cr=0.9 and a mutation rate mr=0.2. The generation number was 20 with a population size of 50. In addition, the Kriging method was used to replace time-consuming FE simulations in the evaluation of functions during genetic operations.

Fig. 5.24 shows the Pareto sets obtained in the last generation for three pairs of objectives (i.e. f1 vs. f2, f1 vs. f6 and f1 vs. f3) as well as all the solutions obtained in all generations that lead to a safe hydroforming process (but where the thinning ratio may be larger than the 30% constraint). Table 5.8 shows a comparison of the objectives for two optimum load paths obtained with coefficients of friction of 0.05 and 0.1, respectively.
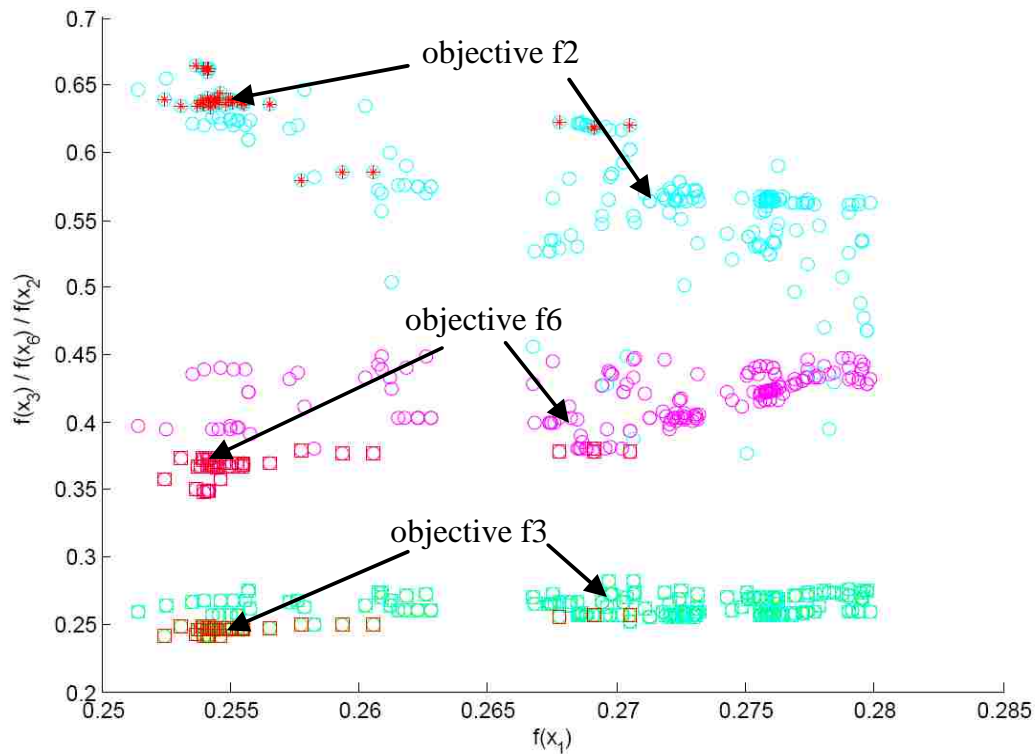
Fig. 5.24 Pareto optimal set for four objectives (f2, f6 and f3 vs. f1). (The squares show the final solution set with a constraint of maximum thickness reduction of 30%)

Table 5.8 Comparison of the objectives for two optimum load paths with different COF values

COF	f1 fracture/ necking (MPa)	f2 wrinkling (10^7 MPa)	f3 thinning	f4 dist1 (mm)	f5 dist2 (mm)	f6 maximum thinning ratio (%)	FLSD limit (MPa)	Max. stress (MPa)
0.05	-2224	1.04	0	0.83	0.97	24.69	1647	1069
0.1	-2073	0.89	0	0.66	0.94	29.68	1628	1183

The corresponding input parameters were identified and are listed in Table 5.9 and shown in Fig. 5.25. Results indicate that the optimal loading path with the lower COF (0.05) requires a slightly lower calibration pressure and greater end feed to deform the tube to the die shape. This indicates that good lubrication contributes to move the tube material into the die cavity. Improved friction conditions also help to reduce wall thinning (the maximum thinning was 24.69%), and to increase the safety margin under the stress limit (the maximum principal stress is 1069 MPa).

Table 5.9. Pressure and end feed parameters for two coefficients of friction

COF	Pressure (MPa)							End Feed (mm)				
	P1	P2	P3	P4	P5	P6	P7	D1	D2	D3	D4	D5
0.05	49.98	56.49	72.15	90.15	102.0	108.4	133.4	50.08	72.11	83.15	94.89	106.60
0.1	47.25	51.06	73.72	87.47	101.2	108.3	136.9	50.45	73.55	83.17	94.77	103.82
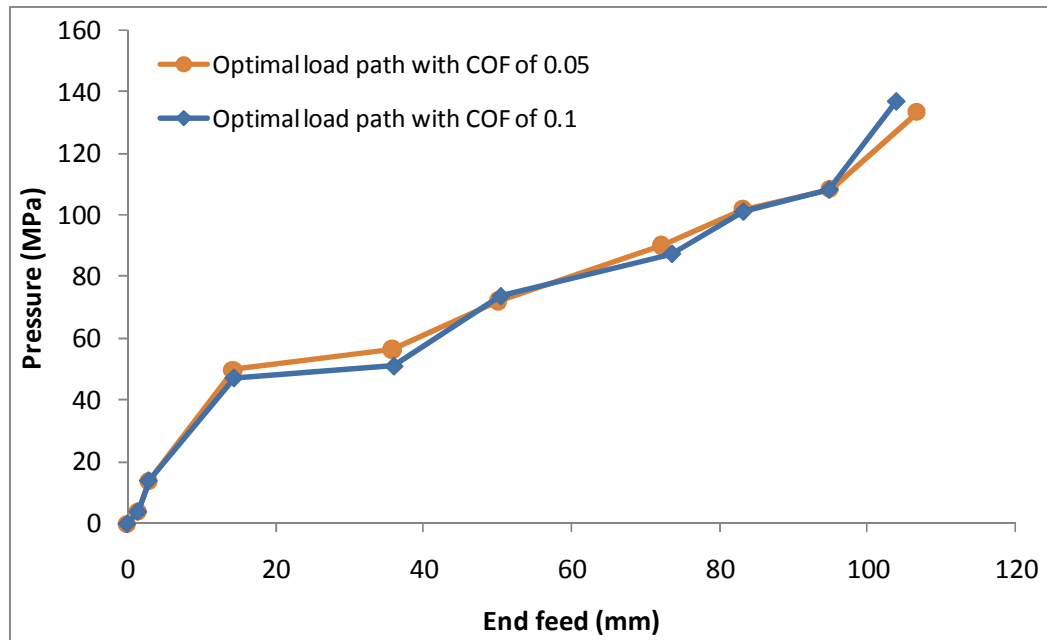
Fig. 5.25 The comparison of loading paths for two COF (0.05 and 0.1, respectively)

In the actual manufacturing process, good lubrication is maintained by applying a dry film onto the tube and a coating on the die. Therefore, in order to be consistent with actual forming conditions, the simulation that was carried out with a COF of 0.05 was chosen for further discussion.

(a)
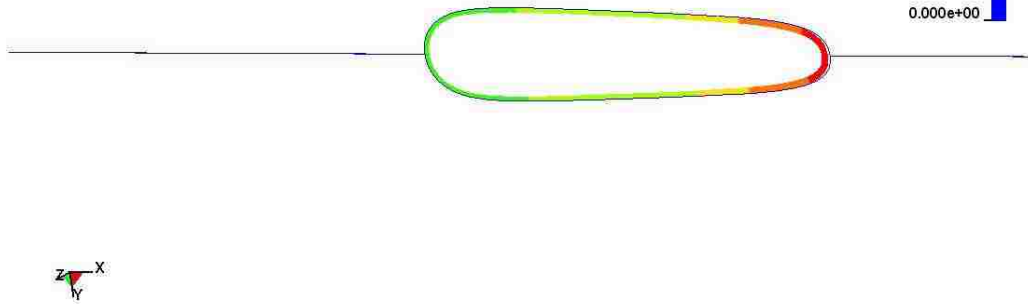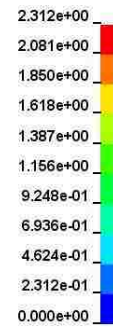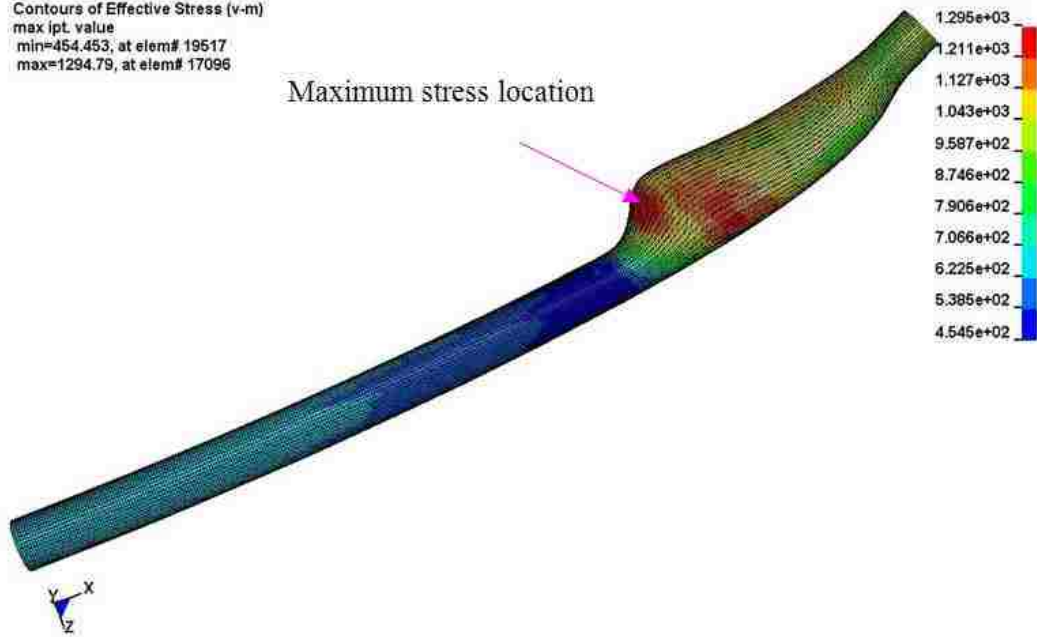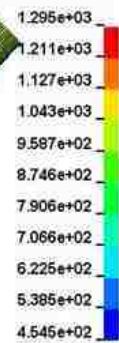
(b)

Fig. 5.26 (a) The tube filling and the thickness distribution in a cross-section

(b) The effective stress distribution and the maximum stress

Fig. 5.26(a) shows a cross-section of the expanded tube in the die cavity and the wall thickness distribution when the COF is 0.05. This figure indicates that the tube has fully filled the die cavity. The minimum thickness is 1.205 mm and is located on the left side of the elliptical cross-section in Fig 5.26(a), which was cut along a plane through section C-C in Fig 5.18.

The stress analysis showed that the maximum effective stress is 1295 MPa at the location identified in Fig 5.26(b). The maximum major principal stress is 1069 MPa (Table 5.8). However, this stress is significantly lower than the stress forming limit at this location, which is 1647 MPa. Therefore, the deformed part is very safe in this simulation.

The optimized loading path was compared with four actual load paths that have produced acceptable parts. The calculated calibration/maximum pressure is 133.4 MPa, and the maximum end feed is 106.6 mm. In this study, a time scale of 400 was used to correlate the simulation with the industrial hydroforming process (Fig 5.27), but this does not affect the pressure vs. end feed load path. This shows, however, that the calculated and actual load paths correlate very well in several aspects: the yield pressure, the calibration pressure and total end feed (See bold values in Table 5.10). Among the four actual load paths, Path 4 is the closest to the optimal result (Fig 5.27a and 5.27b).

The experimental validation was not carried out because of an interruption in the demand for this part.

Table 5.10 Comparison of the Predicted and Actual Load Paths

	Yield Pressure (MPa)	Calibration Pressure (MPa)	Total End Feed (mm)
simulation	57.3	133.4	106.6
Actual values	Path1: 60.0	133.8	111.0
	Path2: 45.3	127.0	122.3
	Path3: 63.0	132.0	102.3
	Path4: 57.3	133.3	102.7

5.6.9 Conclusions

An inverse problem of loading path design in tube hydroforming of a refrigerator door handle was presented and solved using a multi-objective optimization method. The inverse method was coupled with a design of experiment, the Kriging predictor, the evolutionary NSGS-II algorithm and finite element simulations of the hydroforming process. The loading path parameters that were obtained included seven pressure variables and five end-feed variables. The results were compared with actual load paths of the hydroforming process, and the calculated key values agreed very well with those recorded during production.

(a)
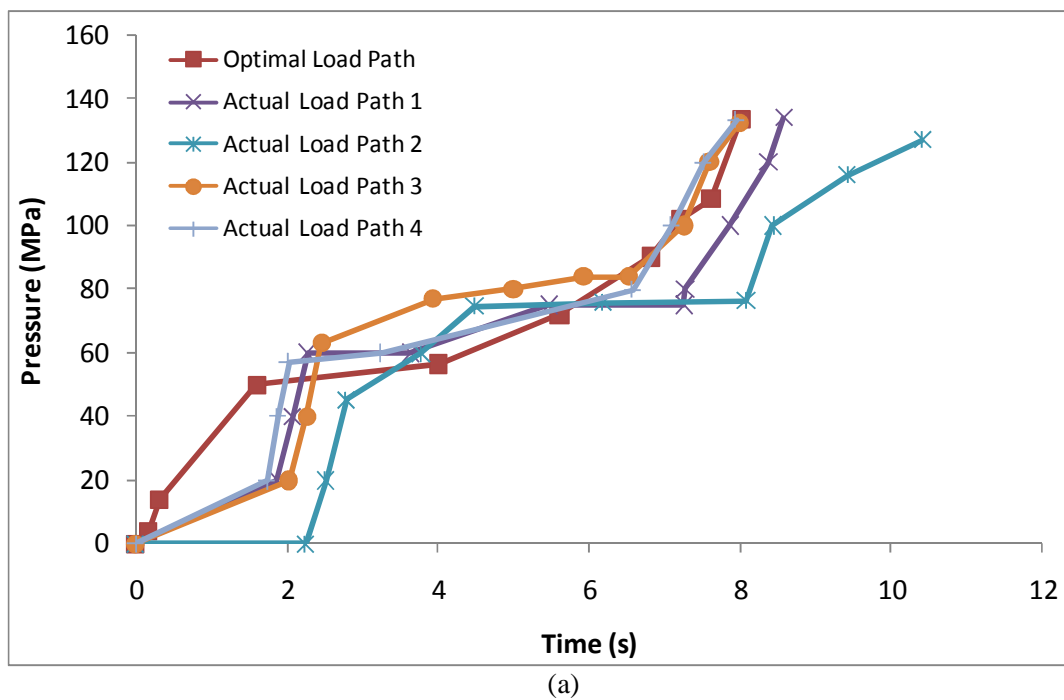
Fig. 5.27 Comparison to the actual load path: (a) Pressure vs. time and (b) End feed vs. time
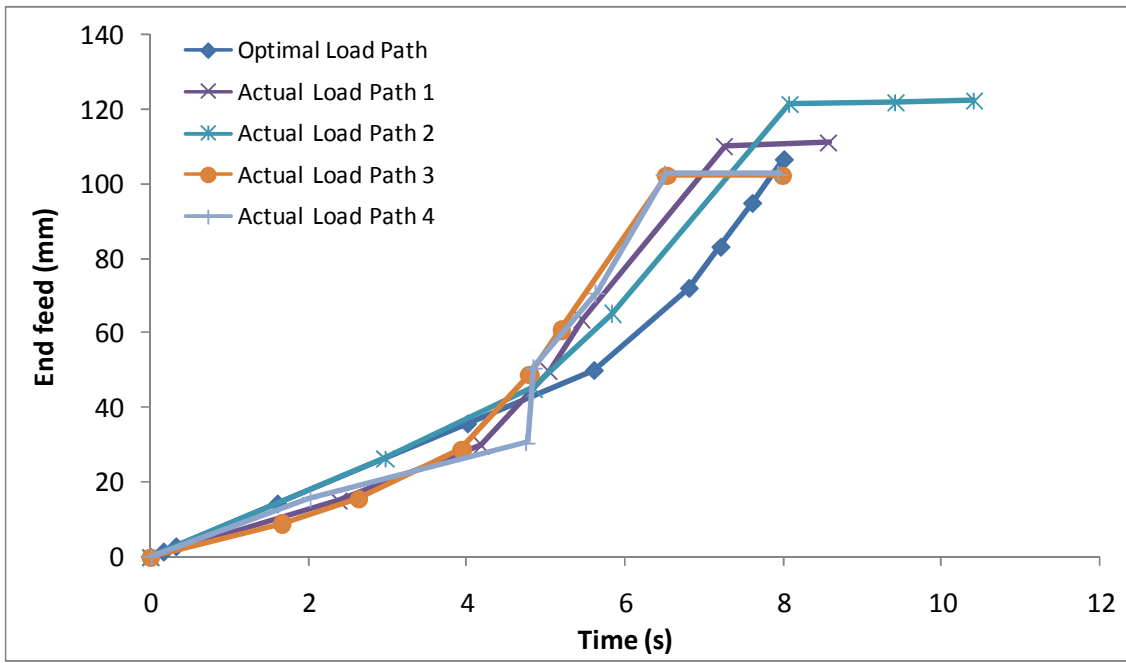
Fig. 5.27 (b) End feed vs. time (Continued)

Chapter 6: Optimization of Loading Path in Hydroforming with Pulsating Pressure

6.1   Introduction

In order to determine the optimum loading path in hydroforming applications, numerous systematic studies have been carried out with the aid of finite element analysis (FEA) (Manabe et al., 2006;Ray and Mac Donald, 2004;Aue-U-Lan, 2004). The most common load paths tend to be linear or piece-wise linear (in terms of pressure vs. time and end feed vs. time). Recently, a forming technology using internal pulsating pressure was employed to deform a tube (Loh-Mousavi et al., 2008; Mori et al., 2007). In this process, the internal pressure oscillated during the hydroforming of a tube in a square or T-shaped die.

The mechanism by which a pulsating pressure can improve the uniformity of expansion in the bulge region was clearly addressed by Mori et al. (2007), and will be presented in section 6.2. In pulsating hydroforming, the effect of amplitude and frequency on the uniformity of the deformation and on the ability of the tube to fill the die cavity is significant. Different levels of amplitude and frequency have been applied to a T-shaped hydroformed part to examine the effects on tube thickness distribution and die filling (Loh-Mousavi et al., 2008). Both the simulation and the experiments revealed that the formability improved with a decrease in frequency, and with an increase in amplitude. However, the optimal parameters for a pulsating hydroforming process were never reported in the literature.

In the present study, three types of load paths were applied to hydroform the same T-shaped component as reported by Loh-Mousavi et al. (2008) and these are described in section 6.3. The finite element model of the forming process is described in section 6.4. In the fifth section, an optimization strategy is introduced and applied to optimize the parameters that control a pulsating load path. Considering the existence of non-linear strain paths in typical hydroforming applications, a stress-based forming limit diagram (FLD) was used to evaluate the severity of the process in terms of the risk of necking/

fracture, wrinkling and severe thinning. The optimization procedure was carried out with a multi-objective genetic algorithm (MOGA) in combination with a series of numerical simulations of the hydroforming process. Finally, results of the optimized process are discussed, and conclusions are drawn in the last section.

6.2   Mechanism of pulsating hydroforming

As stated by Mori et al. (2007), the stress components vary with the osillation of internal pressure (Fig. 6.1). The hydroformed tube showed a uniform expansion in both simulation and experiment. The change in axial and hoop stress components was explained to have caused such a phenomenon (Fig. 6.2). Similarly, Yuan et al. (2007) stated that the intermediate wrinkles can be considered as an alternative approach for obtaining preforms by accumulating material into the expanding area. Therefore, the
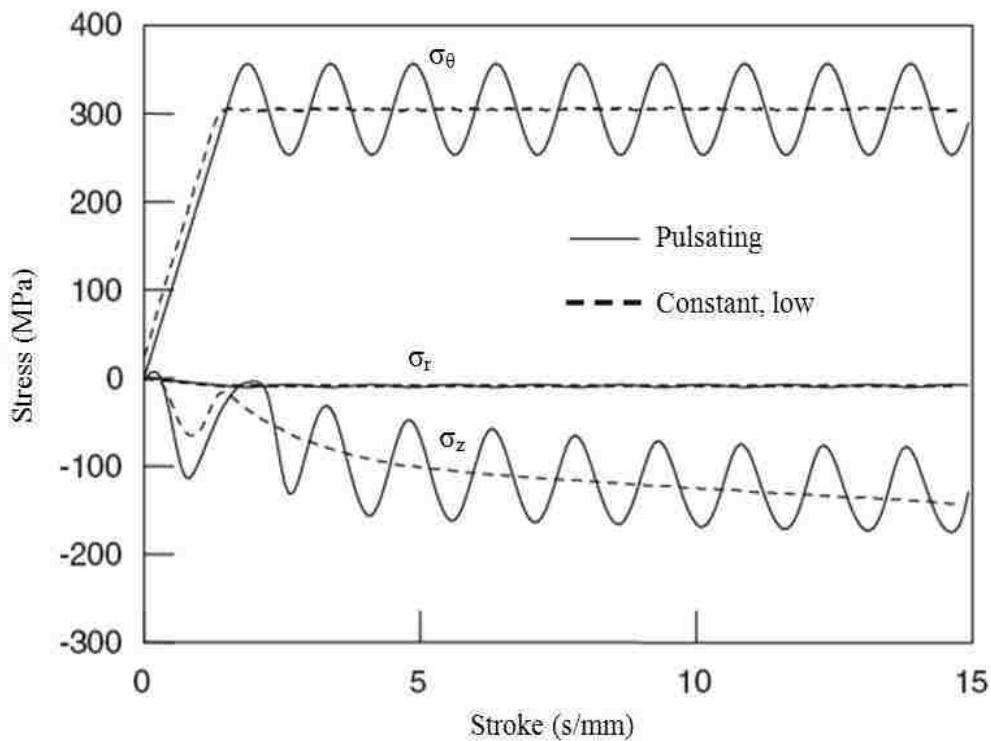
Fig. 6.1 Calculated oscillation of stress components during pulsating hydroforming (Adapted from Mori et al., 2007)
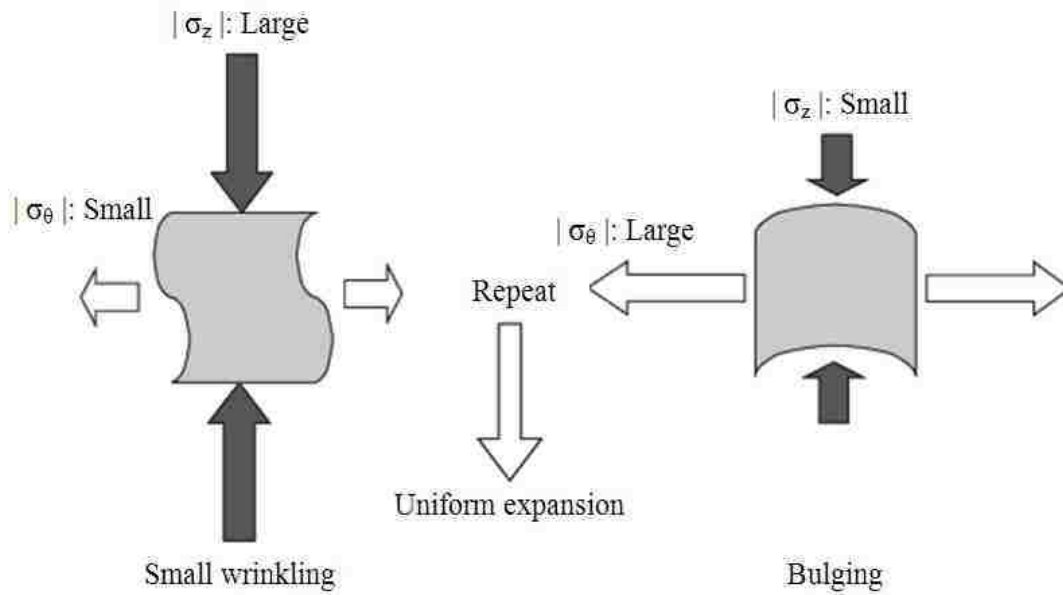
Fig. 6.2 Cause of uniform expansion in pulsating hydroforming by change in stress components (Adapted from Mori et al., 2007)

recurring wrinkles and bulge generated by the alternate higher axial force and internal pressure helped the tube to deform in a stable and uniform manner.

6.3   Loading path design for hydroforming

Three types of pressure paths, i.e. a higher, piecewise linear pressure (HP), a lower, piecewise linear pressure (LP) and a pulsating pressure (PP) (see Fig. 6.3) were applied to examine the effect of internal pressure on the forming severity and thickness distribution of a T-shaped tubular part. For the PP load path, the amplitude of the oscillating pressure was 7 MPa and the frequency was 1.33 cycles/mm of end feed, when the end feed was in the range of 1 to 15 mm. The equation for a pulsating pressure can be expressed as:

$$p = A_p \sin 2\pi\omega(s-1) + p_0 \tag{6.1}$$

where A_p is the amplitude of the pressure curve, ω is the number of cycles per unit end feed, p_0 is the mean value of the pulsating pressure, and s is the end feed. The HP loading path corresponds with the upper bound of the pulsating pressure peaks. The parameters

for each pressure curve are listed in Table 6.1. For each of the three load paths, the end feed was linearly increased from 0 mm to 15 mm.

Table 6.1. Three types of pressure paths

load path	P1 (s=1mm)	P2 (s= 12mm)	P3 (s= 15mm)
HP	25	32	62
LP	17	25	62
PP	25	25	62
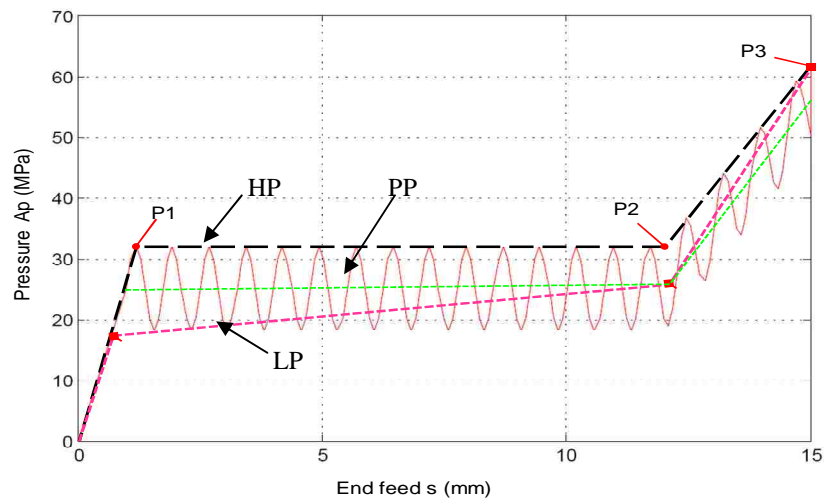
Fig. 6.3 Three types of loading paths applied to a T-shaped hydroformed part

6.4   Finite element model

The T-shaped part was made of mild steel and the tube mechanical properties were provided by Loh-Mousavi et al. (2008) and are listed in Table 6.2. The outer die and two end-feed punches were modelled as a rigid body in LS-DYNA v.971 (Hallquist, 2007). The tube was modelled with 3480 Belytschko-Tsay shell elements, each having five integration points through the thickness. A material model designated as "MAT_PIECEWISE_LINEAR_PLASTICITY" (No. 24) was selected to represent the hardening behavior. Tube-die friction was modelled with the penalty-based contact algorithms in the commercial program LS-DYNA. Coulomb's coefficient of friction was set to 0.1 for the contact interface. Fig. 6.4 shows the geometry of the tools and the tube and Fig. 6.5 shows the mesh. The forming process consisted of pressurizing a tube to

133

cause it to bulge out and protrude a vertical distance s until it contacts a fixed upper die. As the internal pressure increases the tube wall gradually fills the die cavity and the maximum filling ratio is determined by the formability of the tube and the efficiency of the hydroforming process.

Table 6.2. Mechanical properties of the tube

Strength coefficient (MPa)	Yield stress (MPa)	Density (kg/m^3)	Young's modulus (GPa)	Poisson's ratio	Hardening exponent n	Outer diameter (mm)	Initial wall thickness (mm)
510	290	7800	210	0.3	0.12	38.4	1.1
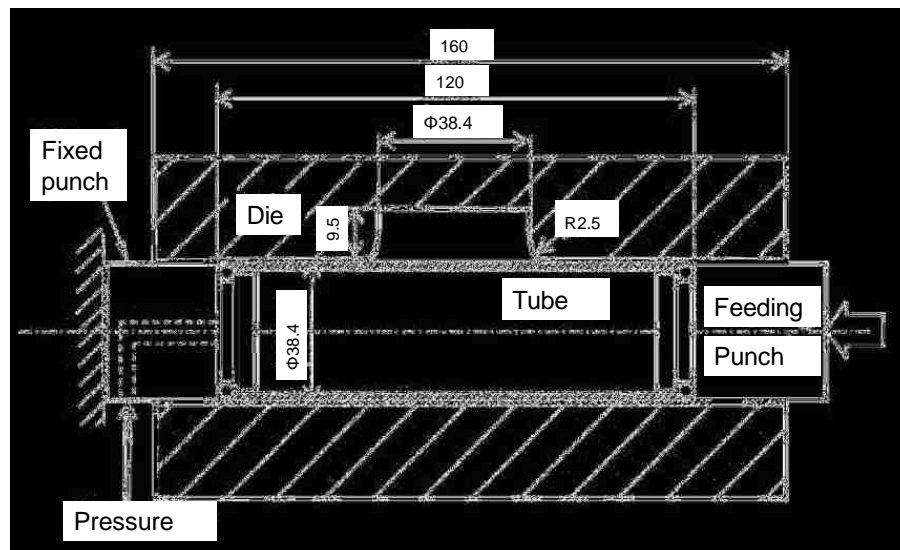
Fig. 6.4 Geometry of the tube and the T-shaped hydroform die (Adapted from Loh-Mousavi et al., 2008)

TUBE HYDROFORMING (T=1.1)

1. Tube blank
2. Tee-shape die
3. Fixed counter punch
4. Fixed punch
5. Feeding punch
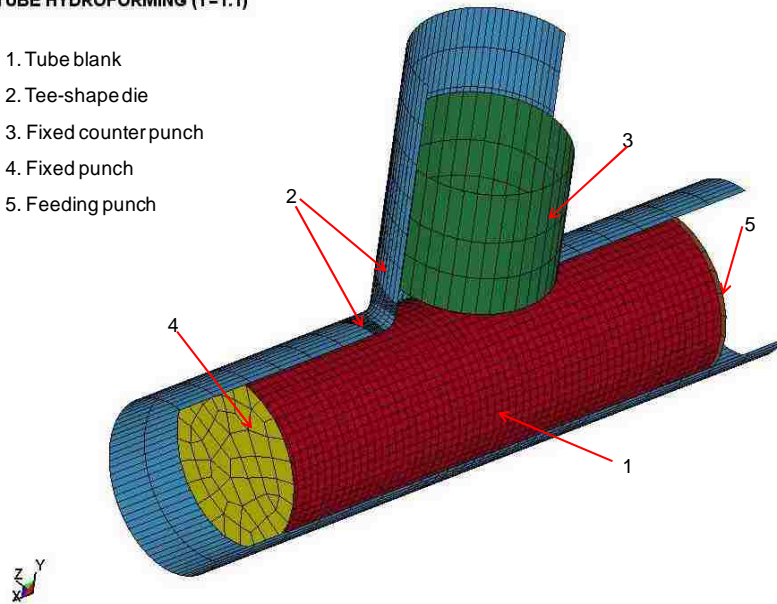
Fig. 6.5 The finite element meshes

The simulation results are presented in Table 6.3 and Fig. 6.6. The comparison of the maximum effective stresses, strains and deformed tube characteristics, such as die filling and minimum thickness, are given for the three types of load paths (Table 6.3). Fig. 6.6 shows the thickness distribution of the protrusion, as well as the degree to which the die cavity was filled. It can be seen that the loading path with the higher pressure (HP) led to a severe reduction of the tube thickness, which exceeds the conventional thinning limit of 20%. In comparison, the other two load paths (LP and PP) generate a higher die filling ratio (above 85%) and less thinning (the minimum thickness is around 0.69 mm). Compared to the LP load path, the PP path achieved a slightly better thickness distribution and die filling ratio. In addition, it was noted that the PP caused a reduction of the maximum effective stress from 508 MPa for HP and 505 MPa for LP load paths to 486 MPa for the PP load path, which increases the safety margin of the hydroforming process. Hence, the pulsating pressure can generate a tube with less wall thinning and a more uniform thickness in the forming zone.

Table 6.3 FEA results with three load paths

	Maximum effective stress (MPa)	Effective strain at three levels			Die Filling ratio (%)	Minimum thickness (mm)
		Lower	Medium	Upper		
HP	508	0.884	0.896	0.890**	91.9	0.464
LP	505	0.534	0.658	0.590*	85.9	0.688
PP	486	0.560	0.552	0.555**	86.4	0.691

* the three strain values are for different elements

** the three strain values are for the same element
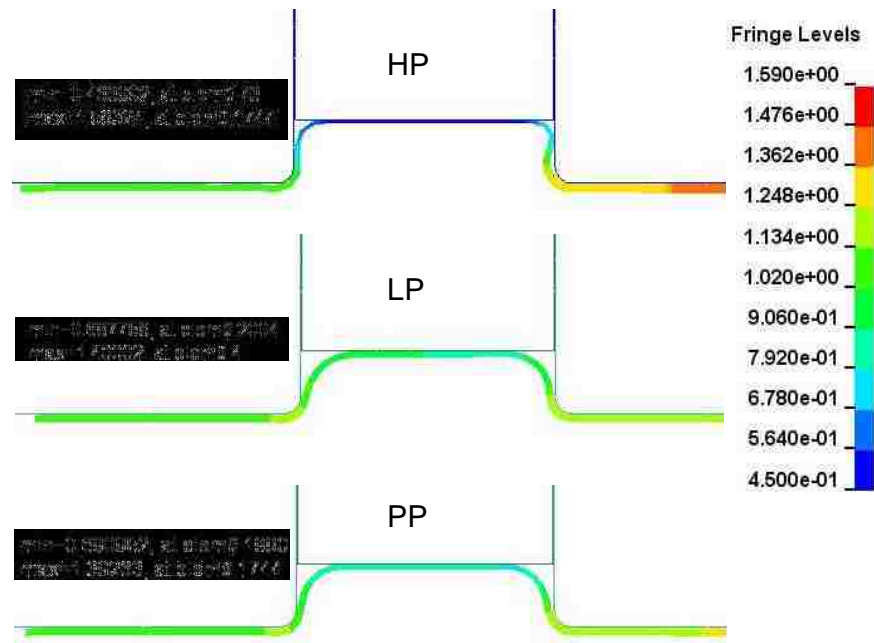
Fig. 6.6 Thickness distributions of the formed protrusions with three different load paths

6.5 Optimization procedure

In this section, the two parameters that define the pulsating internal pressure, i.e. the amplitude and frequency, were further investigated in order to determine an optimal load path.

6.5.1 The MOGA algorithm

For the T-shaped hydroformed component under consideration, there are also competing objectives: there is a need to reduce the risk of necking/fracture and wrinkling, minimize thinning, but also to achieve a specified geometry while maintaining a reasonably uniform thickness distribution throughout the part: this constitutes a problem of multiple objectives. In order to circumvent the difficulty of selecting a relative weight for each objective, the Pareto optimization algorithm proposed in Section 5.5.1 (called MOGA-I) which uses a ranking and non-dominated sorting strategy was adopted for this study.

6.5.2 Mathematical model of the T-shape pulsating hydroforming

The objectives in this application include the forming severity functions and the quality requirements such as thickness distribution and die filling.

6.5.2.1 Forming severity functions

The three objective functions required to achieve defect-free tube hydroforming are those that minimize necking/fracture, wrinkling and severe thinning. These objective functions are described in detail in Chapter 3, but are listed below for convenience.

$$f_1 = Obj\_f = \frac{1}{d_f} = \frac{1}{\left|\sigma_1^{max} - k\sigma_f\right|} \tag{6.2}$$

$$f_2 = \begin{cases} Obj\_w = \sum_{i=1}^{n}\left|d_w^i\right| = \sum_{i=1}^{n}\left|\sigma_2^i\right| & \sigma_2^i < 0 \\ Obj\_w = 0 & \sigma_2^i \geq 0 \end{cases} \tag{6.3}$$

$$f_3 = \begin{cases} Obj\_th = \sum_{i=1}^{n}(d_{th}^i)^2 & \varepsilon_1^i > \eta(\varepsilon_2^i) \\ Obj\_th = 0 & \varepsilon_1^i \leq \eta(\varepsilon_2^i) \end{cases} \tag{6.4}$$

6.5.2.2 Objective functions of maximum thinning and die filling

The above function of severe thinning was evaluated for every element in the tube. In reality, the local thickness reduction may reach a limit. Hence, the maximum local thinning was employed to minimize the function:

$$f_4 = t - t_{min} \tag{6.5}$$

where t is the original tube thickness, and t_{min} is the final minimum thickness in the deformed tube.

The die filling was calculated in the central cross-section of the deformed tube. This function is also designed to be minimized:

$$f_5 = 1 - \frac{A}{A_0} = \frac{A_0 - A}{A_0} \tag{6.6}$$
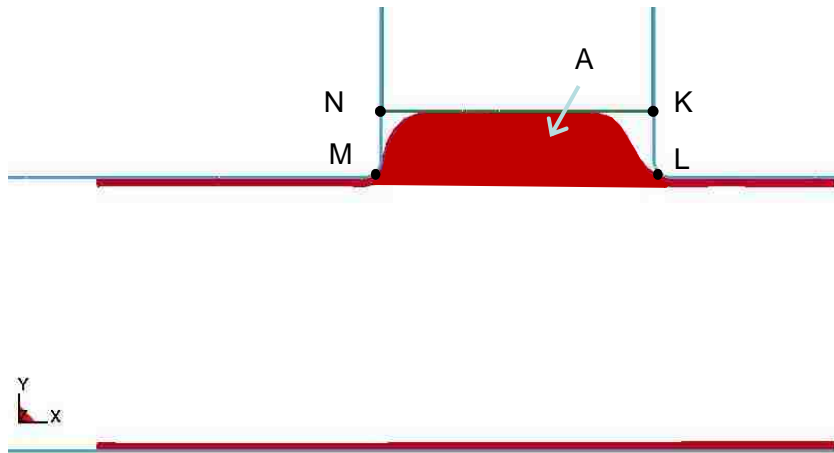
Fig. 6.7 Calculation of the die filling of the tube protrusion

where A_0 is the total area of the die cavity (area of MNKL) and A is the area filled by the protruding tube wall (shaded area in Fig. 6.7).

Therefore, the following mathematical function can be written as:

Minimize $\qquad F(x) = [f_1(x), f_2(x), f_3(x), f_4(x), f_5(x)]$ (6.7)

138

s.t. $0.2 \le f_1 \le 0.75;$ $0.2 \le f_2 \le 0.75$ (6.8)

$0.2 \le f_3 \le 0.30;$ $0.2 \le f_4 \le 0.60;$ $0.2 \le f_5 \le 0.6$

where x is the normalized vector of design variables: $x = [A_p, \omega]^{\mathrm{T}}$, $2 \le A_p \le 10$, $0.1 \le \omega \le 2$. The ranges of each design variable are the same after normalization: $0.2 \le x_i \le 0.8$, $i = 1, 2$.

6.6. Results and discussion

The MOGA was initialized with a population size of 40 and a generation of 50. The crossover and mutation probability are 0.9 and 0.2, respectively. The Pareto set for optimized results were obtained after 50-generation evolutions using constrained NSGA-II. The L_2 norm was used to choose the layout with the minimum L_2 norm value and the results are listed in Table 6.4. The optimum loading path has a pressure amplitude of 9.91 MPa and a frequency of 2 cycles/mm (Table 6.4). The objective values were 0.4170, 0.5659, 0.2099, 0.2881 and 0.3431 for objectives f_1, f_2, f_3, f_4 and f_5, respectively.

Table 6.4 Optimal results using MOGA with a minimum L_2 norm

	Pulsating parameters		final objective results					L_2 norm
	Amplitude A_p (MPa)	frequency ω (cycles/mm)	f_1 (MPa)	f_2 (MPa)	f_3	f_4	f_5 (mm)	
Normalized value	0.675	0.80	0.4170	0.5659	0.2099	0.2881	0.3431	0.8596
Optimum load path	9.91	2	147.458	182960	0.3296	0.8531	0.862	____
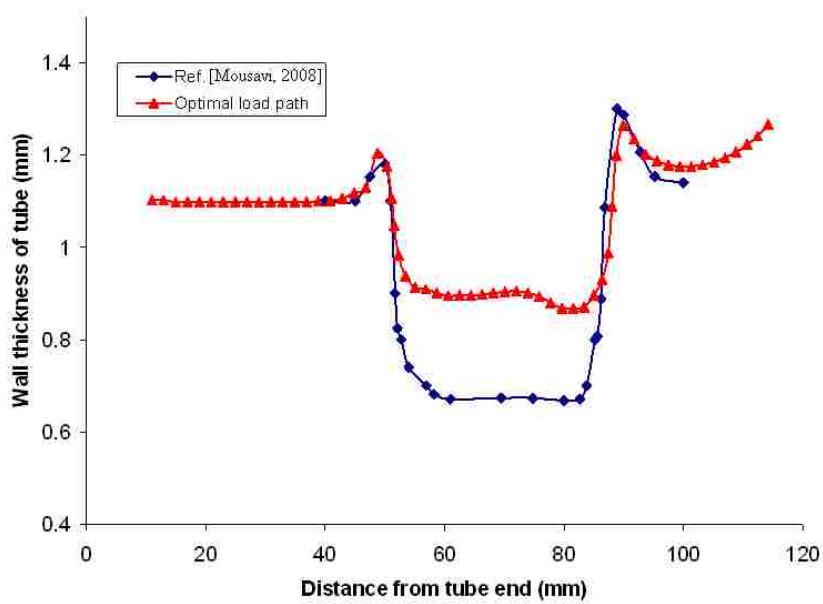
(a)
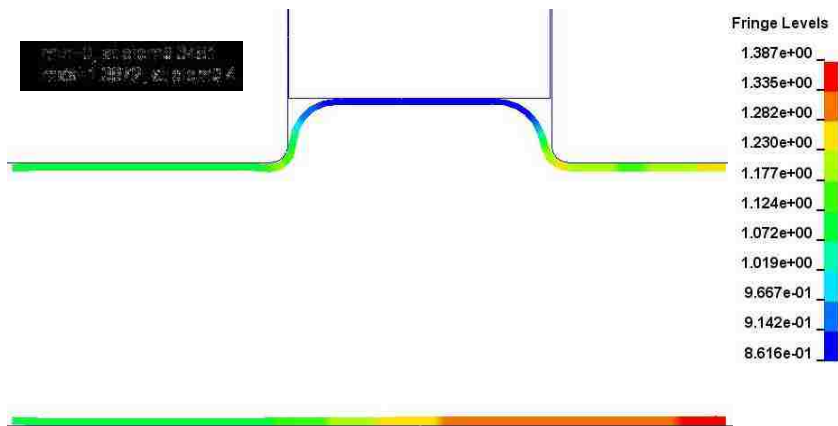
(b)

Fig. 6.8 (a) The thickness distribution and (b) die filling in the part with the optimum loading path

The minimum thickness and die filling ratio achieved when using the parameters provided by Loh-Mousavi et al. (2008) were calculated to be 0.69mm and 85%, respectively. In contrast, the minimum thickness for the optimized process is 0.862 mm – significantly better than with the non-optimized process – and the die filling ratio is 85.31%. It can be seen that there is only a minor change in the die filling ratio when using optimization, however, the improvement in minimum thickness is significant, as it

increased by 25%. Compared to the PP result obtained in Section 6.4, the die filling ratio is only 1.1% lower for the optimum load path, whilst the tube thickness is much thicker with a 25% increase of 0.171 mm. Since the objectives of maximizing die filling and minimizing wall thinning are in conflict with each other when the total end feed is fixed, the optimum loading path leads to a trade-off between these two objectives. This explains why the minimum tube thickness has significantly improved and the die filling ratio has slightly decreased. However, the optimized result shows a uniform thickness distribution in the central cross-section of the protrusion (Fig. 6.8b).

6.7   Conclusions

A loading path optimization for a hydroformed T-shaped part was investigated with MOGA. The objectives were to minimize the forming severity in terms of the risk of necking/fracture, wrinkling and severe thinning with both the FLD and the FLSD, to minimize wall thinning and maximize the die filling ratio. The following conclusions can be drawn:

1. The comparison between the three types of load paths – the higher pressure (HP), the lower pressure (LP) and the pulsating pressure (PP) indicated that the pulsating pressure can generate a more uniform wall thickness than the other two load paths. In addition, the process safety margin increased as a result of the maximum effective stress being significantly reduced.

2. The amplitude and frequency of the pulsating pressure were optimized with MOGA. Compared to experimental results from the literature, the optimal loading path reduced the amount of thinning by 25% compared with experimental results (Loh-Mousavi et al. (2008)), and a die filling ratio of 85.31% was achieved, which is just slightly higher than the experimental result.

3. The multi-objective genetic algorithm with constraint handling method was shown to be effective in obtaining a Pareto set of the objectives. A compromise solution can be reached among a conflicting series of objectives, which enables one or more objectives to be improved without adversely affecting the others.

Chapter 7: Loading path design in multi-stage tube forming

7.1   Introduction

When manufacturing automobile tubular components, such as engine cradles (Fig.7.1), frame rails, subframes and cross-members, pre-bending and pre-forming operations are often required prior to hydroforming (Lee et al., 2005). Also the success of the tube hydroforming process is largely determined by the preceding forming operations.

Pre-bending is generally needed so that a tube will fit into the hydroforming die. The effect of pre-bending, which changes the strain and thickness in the tube, should be well understood in order to improve the amount of residual ductility for the subsequent tube hydroforming operation (Oliveira et al., 2005). For hydroforming applications, the two main methods of bending tubes are hydrobending and rotary-draw bending.
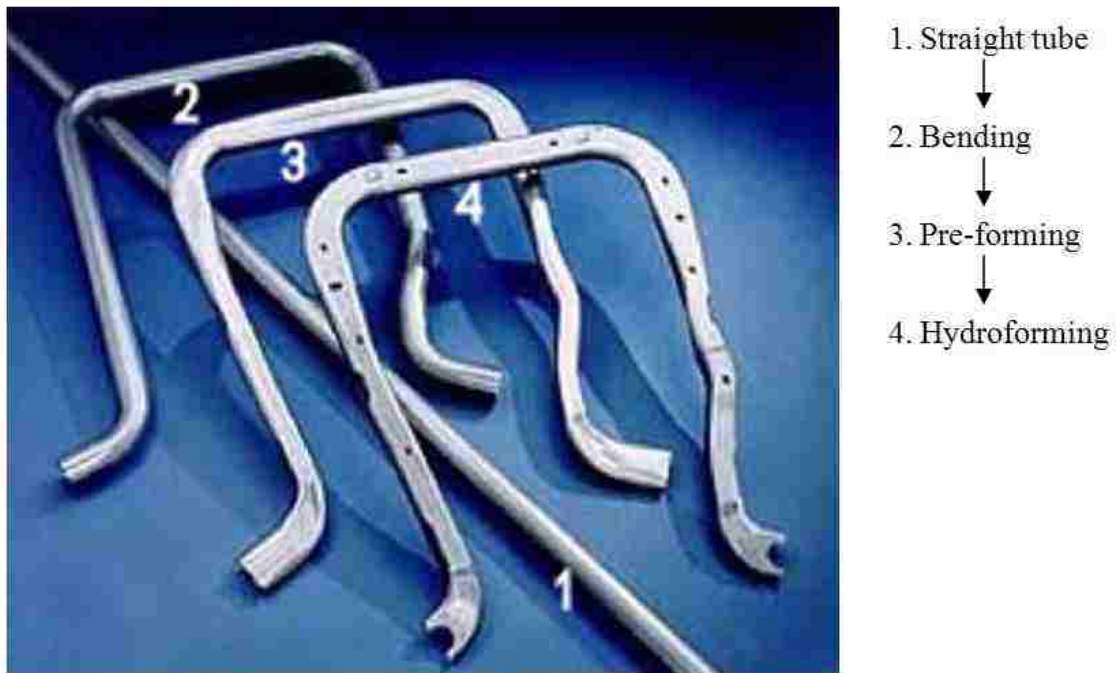
Fig. 7.1 Typical production steps for an automobile engine cradle (Adapted from Schuler Hydroforming Inc.)

7.2 Rotary-draw bending

Rotary-draw bending is one of the most versatile, accurate and cost-effective methods of bending thin-walled tubes. Rotary-draw tube bending provides consistent bends with repeatable thickness and strain distributions, which is particularly important for the success of subsequent hydroforming operations (Ahmetoglu and Altan, 2000; Dyment et al., 2003; Bardelcik and Worswick, 2005a).
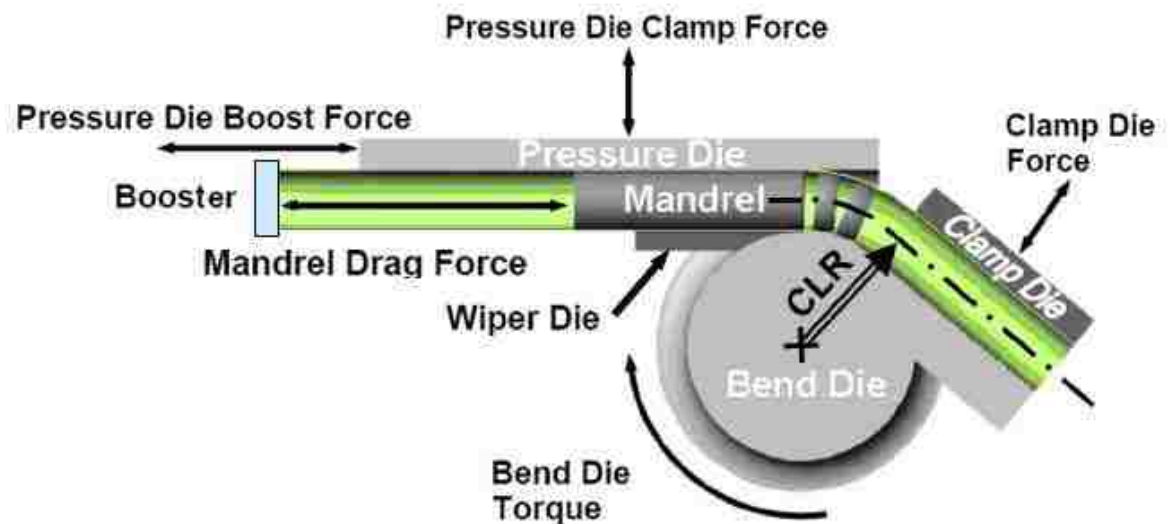
Fig. 7.2 Rotary-draw tube bender tools (Adapted from Bardelcik and Worswick, 2005b)

The main tools of the rotary-draw tube bender include the clamp die, the bend die, the wiper die, the pressure die and the mandrel assembly (Figure 7.2). The clamp die grips the tube end and draws the tube around the bend die, with some pushing assistance from the pressure die. For bends with tight radii and small tube wall thickness an optional mandrel can be utilized to prevent cross-sectional collapse and wrinkling on the inside of the bend. The following sections describe key factors controlling the rotary-draw tube bending process.

7.2.1 Factors affecting bending

Successful tube bending depends on a variety of factors: the ratio of the centerline radius (CLR) of the bend to the tube outer diameter (D or OD), or R/D ratio, lubrication, bending boost, and process variables such as tube/tools clearance, mandrel extension length, and bending velocity.

Yang J. et al. (2001) found that smaller bend radii produced larger thinning of the tube on the outside of the bend and higher levels of cross-sectional distortion. Therefore one of the ways to increase residual formability after the bending operation is to reduce bending strains by increasing the R/D ratio.

The bend difficulty factor (DF) or bend factor (Singh, 2003) is defined in such a way as to describe the feasibility of bending:

$$DF = \frac{Wall\ Factor}{DOB}$$

(7.1)

Where, the wall factor is the ratio of tube OD to wall thickness (T); and DOB is the bend ratio (R/D). And they are formulated as:

$$Wall\ Factor = OD/T$$

(7.2)

$$DOB = R/D$$

(7.3)

It was noted that a decrease of the DOB (or R/D ratio) together with an increase in the wall factor is indicative of an increased bend severity (Bardelcik and Worswick, 2005a).

7.2.2 Boost method

Mentella et al. (2008) presented a comparison among five types of boost approaches, including pressure die only, pressure die with connected boost block, and pressure die and independent booster. It was indicated that the independent pressure die and booster technology (the "c" configuration in Fig. 7.3) provided the greatest process flexibility and performance.

a) Pressure die only (a₁ stationary, a₂ follower, a₃ boosted)

b) Pressure die (boosted) with connected boost block

c) Pressure die (c₁ follower, c₂ boosted) and independent axial booster
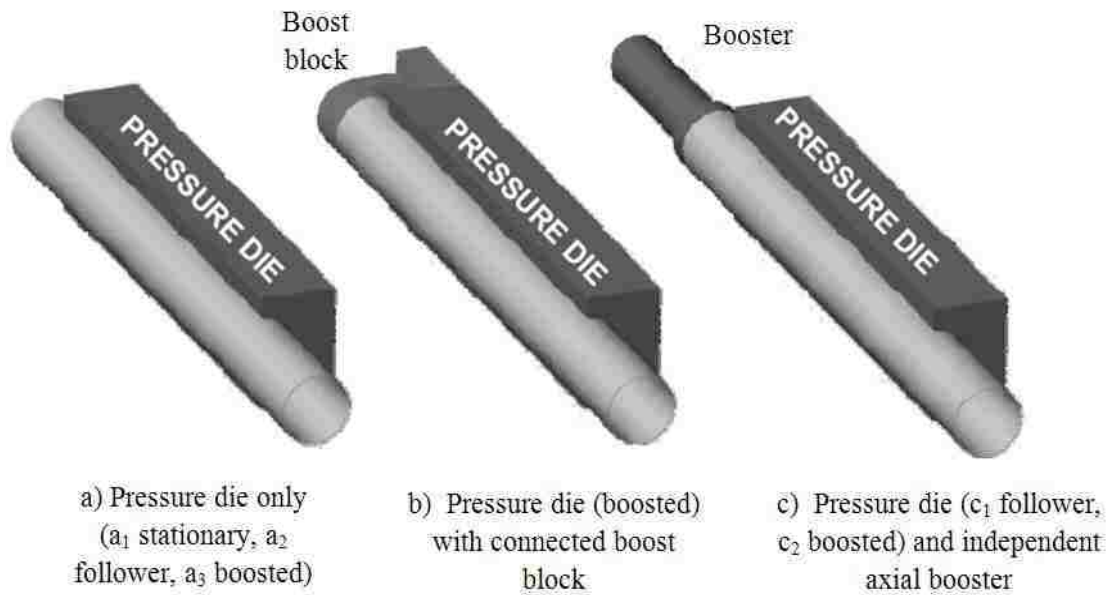
Fig. 7.3 Boost methods (Adapted from Mentella et al., 2008)

Dyment (2003), Dyment et al. (2004) and Bardelcik et al. (2005a) investigated the effect of bending boost on thickness and strain distributions of pre-bent IF, AKDQ and DP600 steel tubes. Comparison of tubes bent with low (95%), medium (100%) and high (105%) boost levels confirmed that the increased boost had an overall positive effect, increasing thickness around the circumference of the tube and decreasing strains on the outside of the bend. The major engineering strain along the outside of the R/D=2.0 bend reduced about 8% with an increase from low to high boost level.

7.3   Bent tube hydroforming

Hydroforming of pre-bent tubes can be carried out at different pressure levels depending on the forming strain and final geometry required for the product (see Fig. 7.4). Yang et al. (2001), Sorine (2007), Koç and Altan (2001), Trana (2002), Dyment et al. (2003), Bardelcik and Worswick (2005a, 2005b) and Oliveira et al. (2005) showed that the ability of a tube to be hydroformed was severely reduced by the pre-bending operation. The bending operation may affect the hydroforming by consuming a large portion of available formability, and a small change in bending strains can significantly affect the hydroformability of the part (Dyment et al. 2003). Bardelcik (2006) pointed out that the

reduction of formability can be compensated by end feeding the tube into the die cavity during hydroforming. Thus, it is possible to improve the hydroforming process by optimizing the load path.
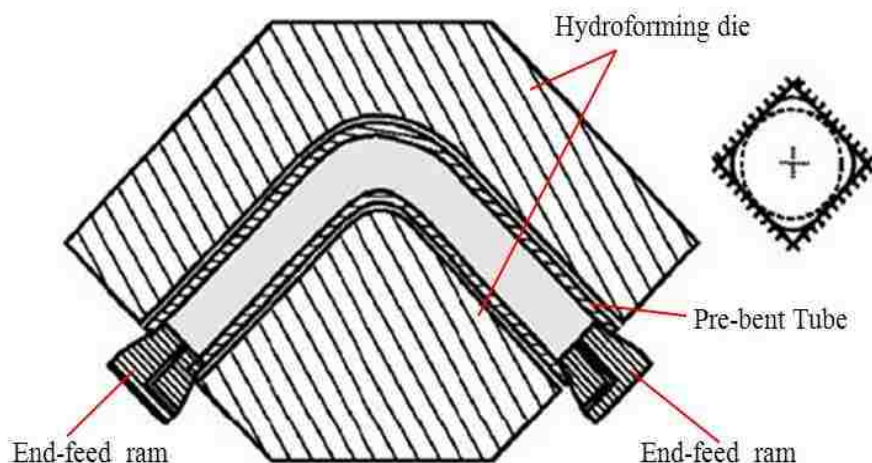
Fig. 7.4 Pre-bend tube hydroforming (Adapted from Simha et al., 2007)

7.4   Simulation of tube bending and hydroforming

The numerical simulation of a tube bending and hydroforming process was carried out with a view to understanding how to optimize the hydroforming loading path in a multi-stage forming process. The finite element simulation was performed with the commercial code LS-DYNA, and results were compared to experimental data published by Bardelcik (2006) in which a straight tube was bent 90º in a rotary draw bender, then hydroformed into a die with a square cross-section. The following sections describe the numerical simulations of this process in more detail.

7.4.1 Material properties

The straight tube was made of DP600 steel and the tube mechanical properties were provided by Bardelcik (2006) and are listed in Table 7.1. The true stress-strain curve of the as-recieved tube is given in Fig. 7.5. A material model "MAT_PIECEWISE_ LINEAR_PLASTICITY" (No. 24) was selected to represent the hardening behaviour.

Table 7.1. Mechanical properties of the tube

Grade	Strength coefficient (MPa)	Yield stress (MPa)	Density (kg/m^3)	Young's modulus (GPa)	Poisson's ratio	Hardening exponent n	Outer diameter (mm)	Initial wall thickness (mm)
DP600	795.8	390	7800	265	0.30	0.115	76.2	1.85

Table 7.2 COF used in tube bending simulations

Die Tool	Higher COF (DP600)	Lower COF (DP600)
Bend/Clamp/Pressure	0.14	0.08
Wiper	0.10	0.04
Mandrel	0.10	0.06
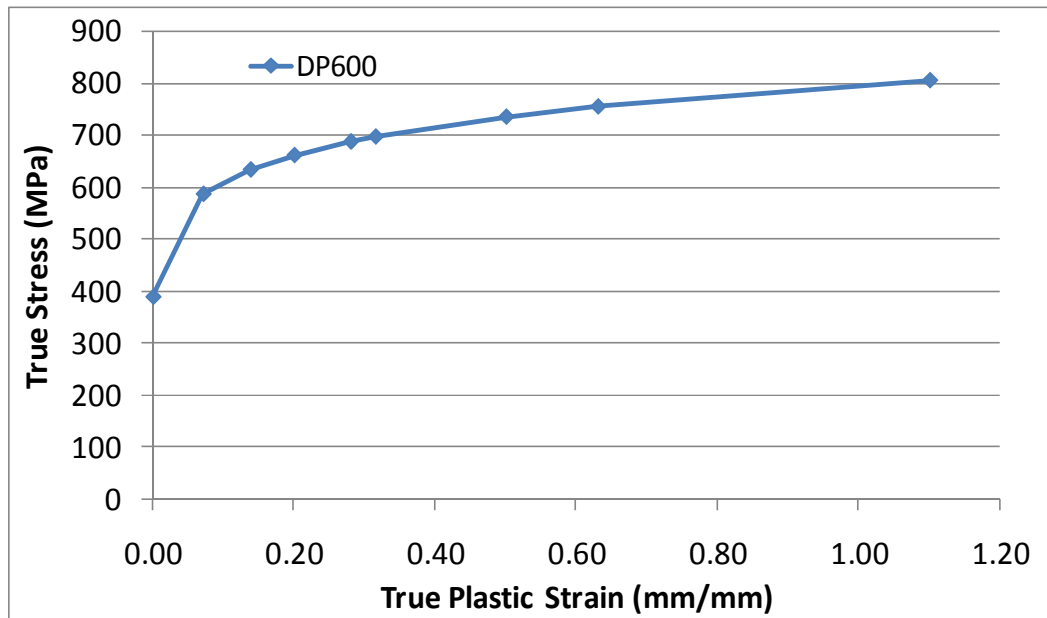
Fig. 7.5 DP600 true stress versus true plastic strain input curve
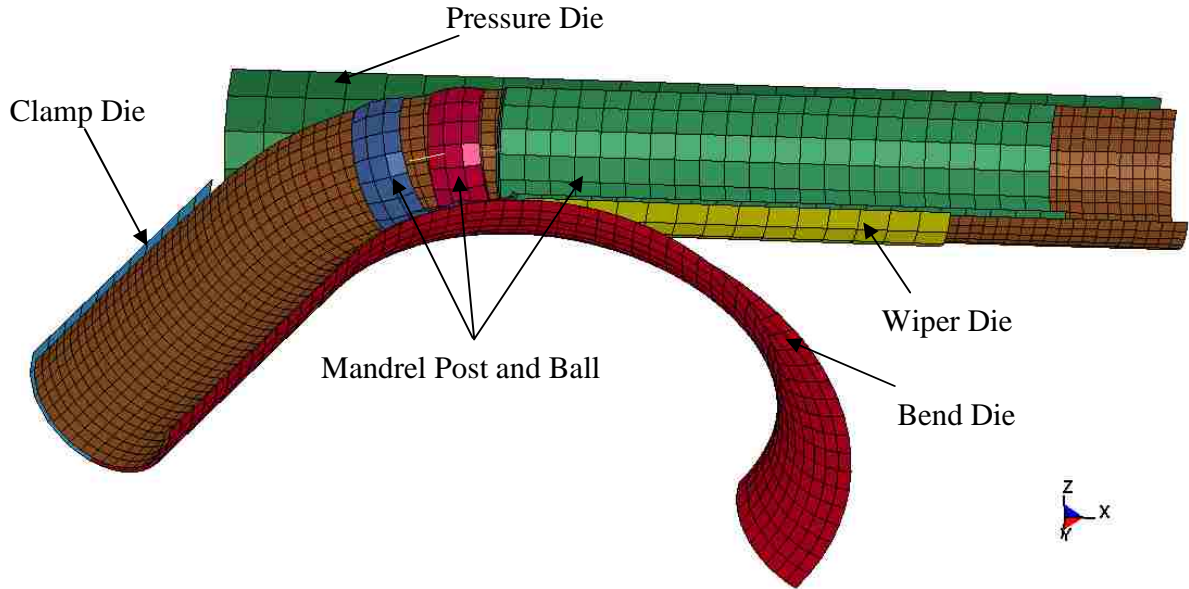
Fig.7.6 FEA mesh of bending setup (half-cut to show the inside tools)

7.4.2 Procedure for the bending simulation

The bending simulation was carried out by modelling the bending tools as rigid bodies. Tube-die friction was modelled with the penalty-based contact algorithms in program LS-DYNA. Coulomb's coefficient of friction were set for each pair of contact interface (Table 7.2). Fig. 7.6 shows geometry and mesh of the tools and the tube.

The tube bending model includes several steps (Fig.7.7): (1) Explicit tube bending; (2) Implicit springback; (3) Trimming. After the bending simulation, a file including the geometry, the plastic strains and stress state at every integration point was obtained and transferred to the hydroforming simulation.
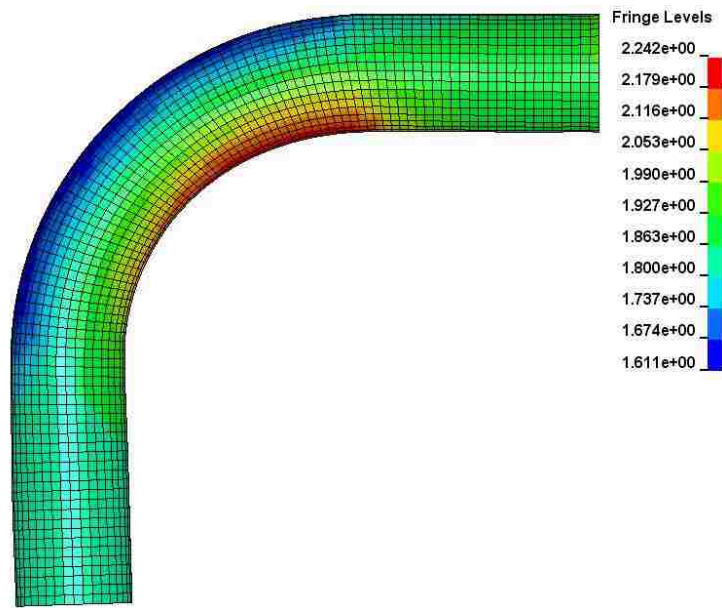
Fig. 7.7 Explicit tube bending simulation (with thickness distribution)

Angle:1.75° degrees
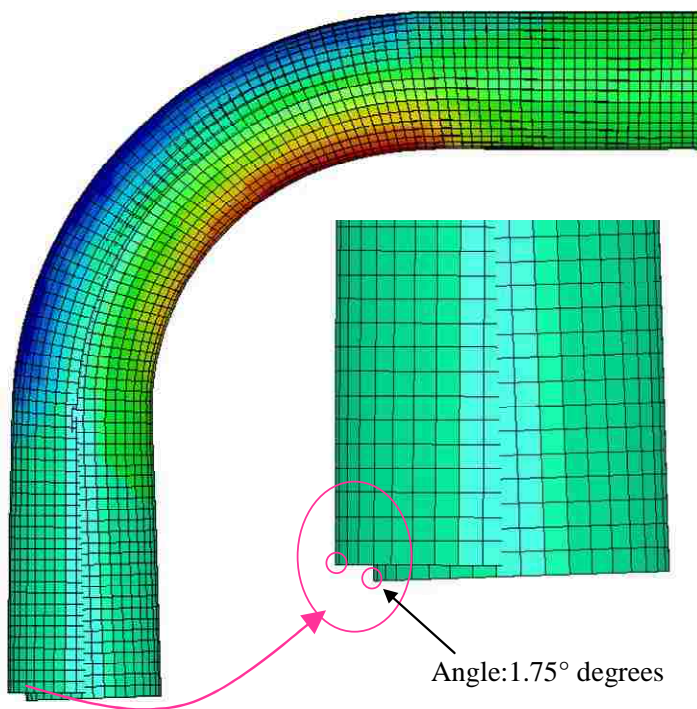
Fig. 7.8 Springback simulation

149
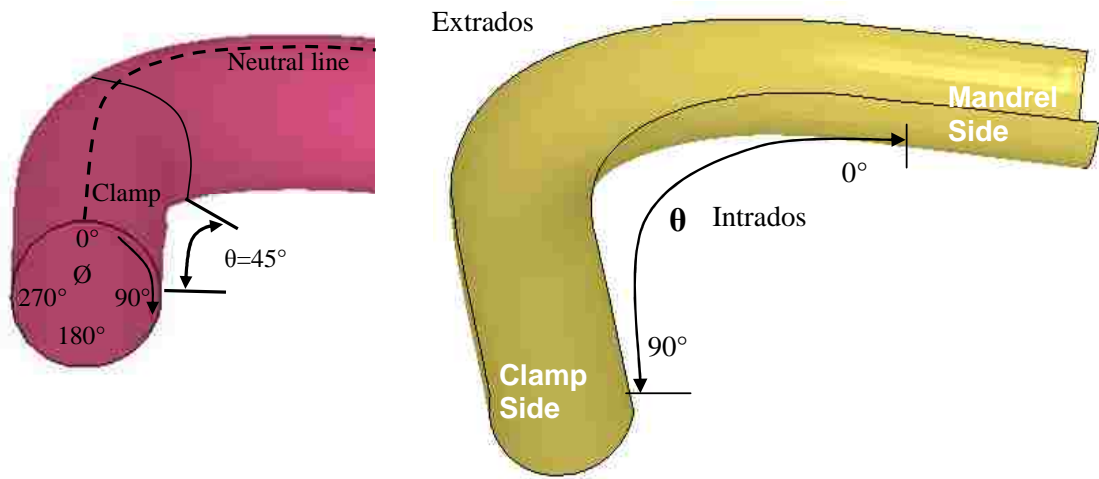
Fig. 7.9 Bent tube measurement (a) Hoop direction (Ø=0° −360°)
 (b) Bend arc direction (θ=0° − 90°)

7.4.3 Hydroforming simulation

In the hydroforming simulation of the pre-bent tube, a file generated from the tube bending history was utilized as an input, and the top view of the half-cut mesh is shown in Fig. 7.10.
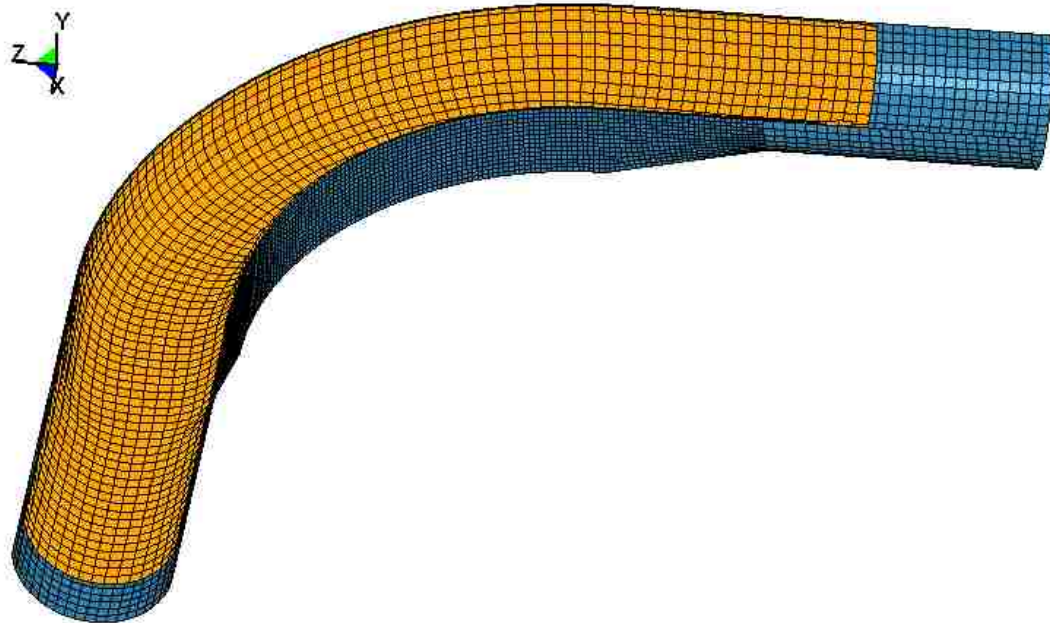
Fig. 7.10 Hydroforming setup and mesh (half-cut)

Fig. 7.11 (a) shows the experimental cross-section of a bent and hydroformed tube in the final stage of deformation (Bardelcik, 2006). Fig. 7.11 (b) shows the predicted cross-section of the same part at an intermediate stage in the simulation, which shows the same deformation trend as the experiment. This simulation demonstrated the fact that in prebent tube hydroforming, the extrados deforms first, and the tube fills the extrados corners better than the intrados corners of the bent tube.
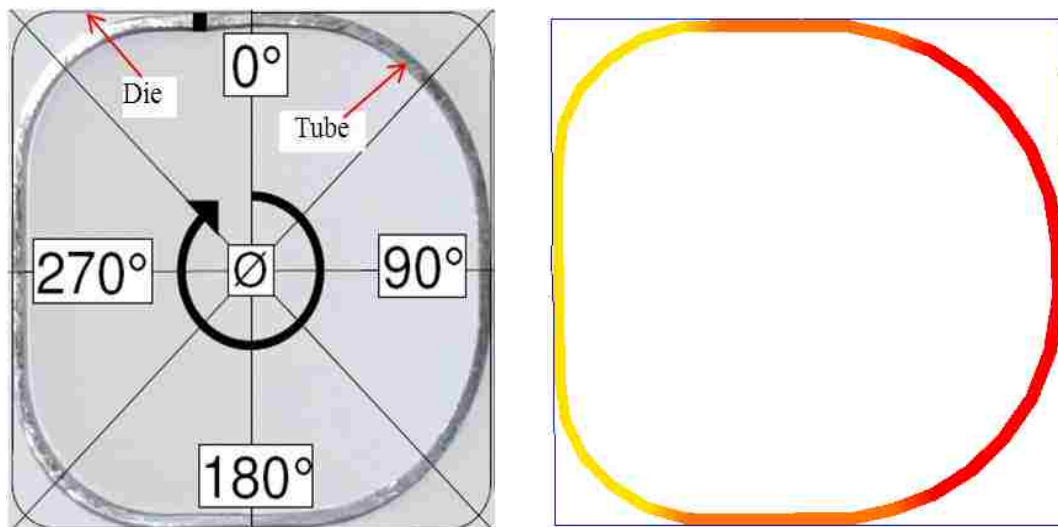
Fig. 7.11 (a) Experimental result of the prebent tube (Adapted from Bardelcik, 2006)
(b) One simulation result ($\theta = 45°$)

7.4.4 Results of tube bending simulations (Strain and thickness)

In this study, the main objective was to investigate the effect of loading path on pre-bent tube hydroformability. Therefore, the factors that affect the bending results, such as different levels of boost force, pressure force, mandrel location etc, were not thoroughly studied, but a suitable setting was selected for each of these bending parameters and was maintained throughout the simulations.

The bending process was simulated using the parameters provided by Bardelcik et al., 2005c with a R/D=2.5. The medium boost (MB) was applied through the pressure die and an independent booster (style "c" in Fig. 7.3). The tube ends were allowed to move in the

x- and z-directions for applying the end feed. The die was fixed. In this simulation, the COF between the tube and the die was selected as 0.035.

The strain and thickness distributions were presented and compared to the experimental results of Bardelcik et al.(2005c). For better comparison, the bending result with R/D=2.0 (Bardelcik, 2006) is also listed in Table 7.3. The results showed a good agreement in strain and thickness distribution for R/D=2.5. However, the bending results for R/D=2.0 showed much larger strains and thickness reduction compared with experimental data.

Table 7.3 The Comparison of predicted and experimental strains and thickness

| R/D | True strain (%) | | | | | | Maximum/Minimum thickness (mm) | | | |
| | Circumference | | Arc Intrados | | Arc Extrados | | | | | |
	Major	Minor	Major	Minor	Major	Minor	Thickness /(Angle) (mm/°)	Reduction (%)	Thickness /(Angle) (mm/°)	Reduction (%)
2.5	15.2	-23.3	7.12	-24.3	18.8	-4.90	2.242 (30°)	-21.2	1.6109 (60°)	12.90
R/D2.5 Ref.[1]*	20.48	-22.31	5.78	-24.26	21.16	-7.15	2.207 (30°)	-19.3	1.631(60°)	11.8
R/D2.0 Ref.[2]**	24.3	-30.1	3.92	-29.2	25.3	-5.48	2.290 (45°)	-23.8	1.5175 (75°)	17.97

* Ref.[1]: Bardelcik et al.(2005c)
** Ref.[2]: Bardelcik, 2006
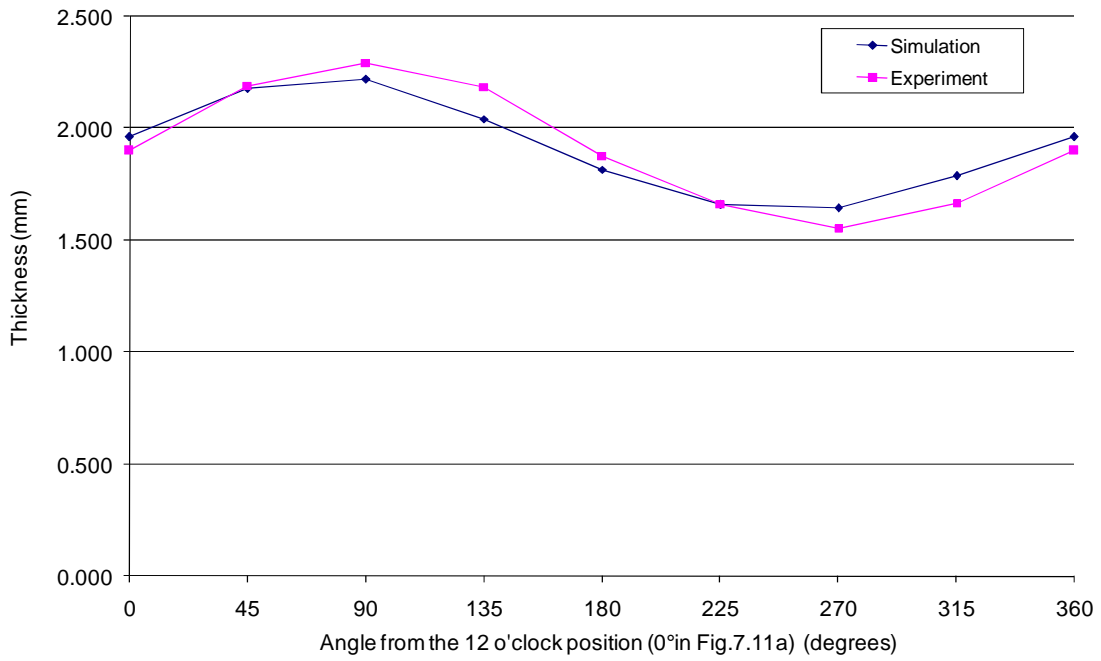
Fig. 7.12 Predicted and experimental thickness distribution in the hoop direction at the middle of the bend (θ = 45°)(Bardelcik, 2005c)
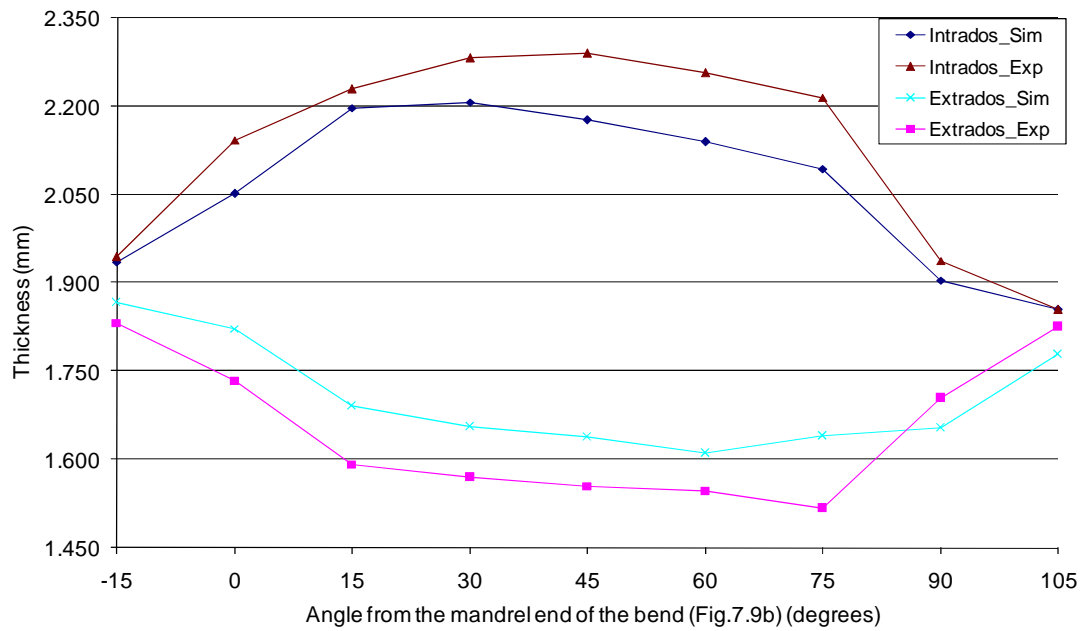
Fig. 7.13 Predicted and experimental thickness distribution along the length of the bent tube

153
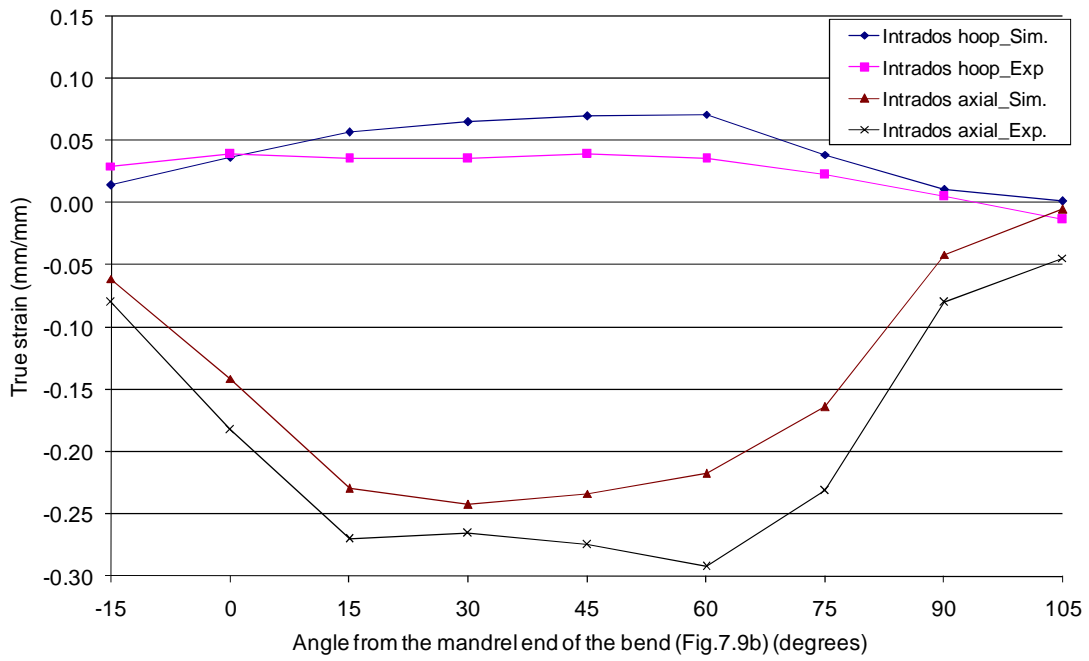
Fig. 7.14 Predicted and experimental strain distribution along the length of the bent tube (Intrados)
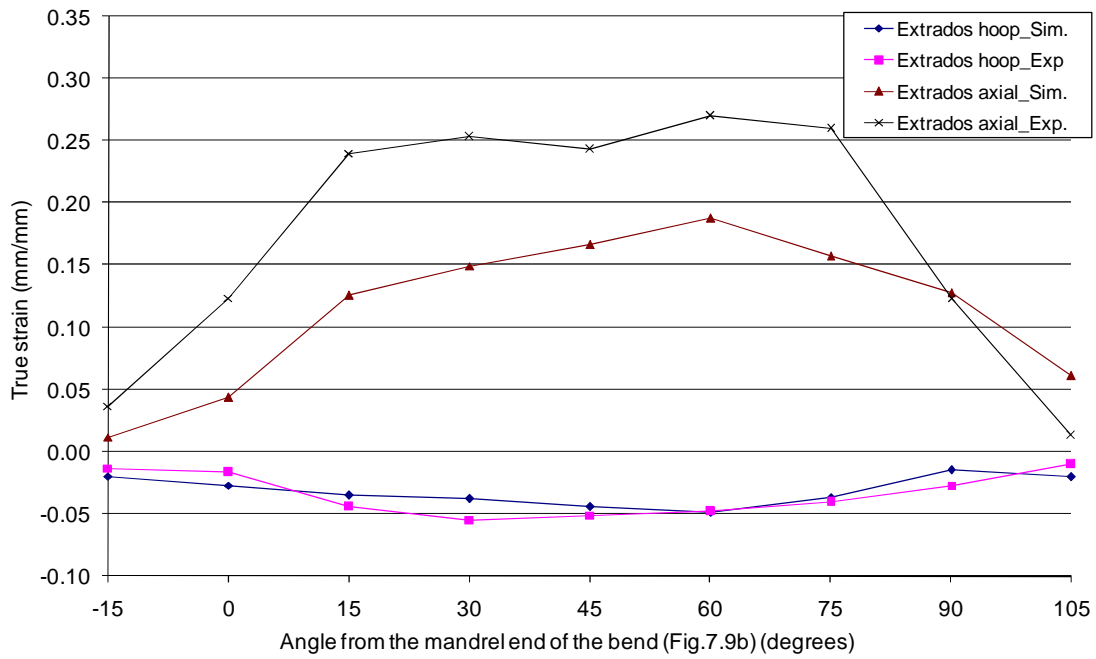
Fig. 7.15 Predicted and experimental strain distribution along the length of the bent tube (Extrados)
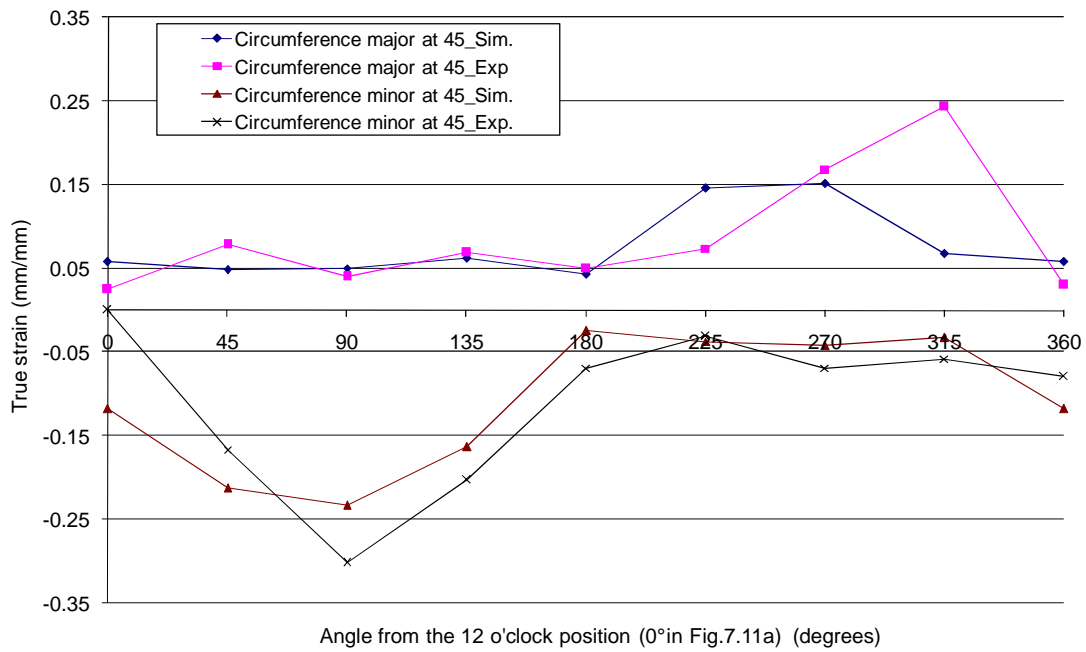
Fig. 7.16 Predicted and experimental strain distribution in the hoop direction of the bent tube

7.5 Optimization of Pre-bent tube hydroforming

7.5.1 Objective Functions

Two of the objectives for the optimization of the hydroforming process included the corner radii (R1 and R2) in the intrados and extrados of the bend at $\theta = 45°$; both these corner radii show the extent to which the die is filled (Fig 7.17). The corner radius can be easily converted into a corner fill expansion which can then be correlated to the actual expansion of the tube wall as it would be measured by an LVDT located in the corner of the die and oriented toward the centre of the tube (this calculation is provided in Appendix E).
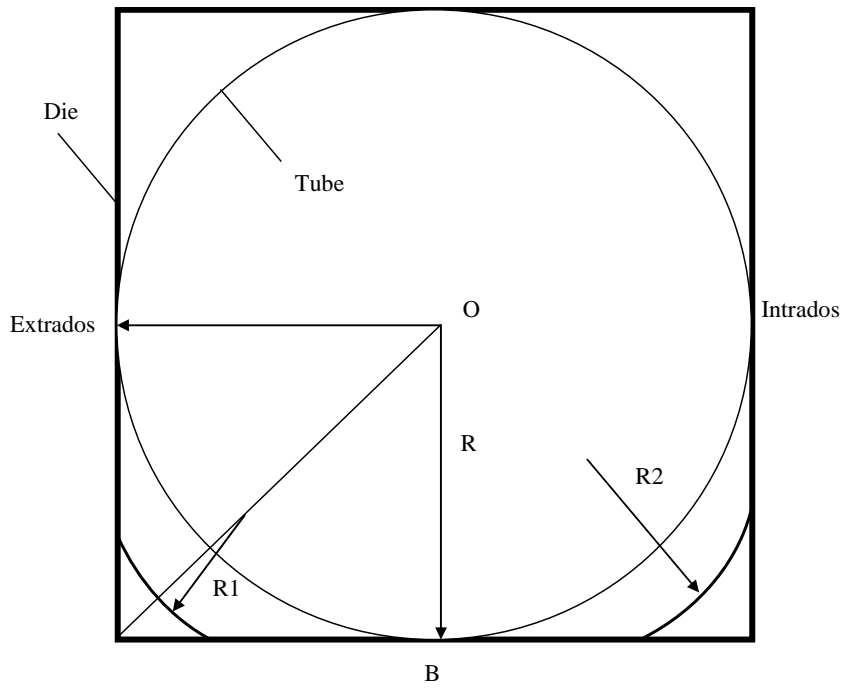
Fig. 7.17 Corner radius in intrados (R2) and extrados (R1) of the bent tube

The objectives of necking/fracture, wrinkling, and severe thinning were adopted for global evaluation, and maximum thinning was used for local assessment. The objective functions are presented in Equations (7.1) to (7.6) as follows:

$$f_1 = Obj\_f = \frac{1}{d_f} = \frac{1}{Max\left|\sigma_1^i - \sigma_f^i\right|} \tag{7.1}$$

$$f_2 = \begin{cases} Obj\_w = \sum_{i=1}^{n}\left|d_w^i\right| = \sum_{i=1}^{n}\left|\sigma_2^i\right| & \sigma_2^i < 0 \\ Obj\_w = 0 & \sigma_2^i \geq 0 \end{cases} \tag{7.2}$$

$$f_3 = \begin{cases} Obj\_th = \sum_{i=1}^{n}(d_{th}^i)^2 & \varepsilon_1^i > \eta(\varepsilon_2^i) \\ Obj\_th = 0 & \varepsilon_1^i \leq \eta(\varepsilon_2^i) \end{cases} \tag{7.3}$$

156

$$f_4 = (t - t_{\min}) \times 100\% / t \tag{7.4}$$

$$f_5 = R1 \quad \text{(extrados)} \tag{7.5}$$

$$f_6 = R2 \quad \text{(intrados)} \tag{7.6}$$

Therefore, the problem can be summarized by the following formulation which places constraints on each objective:

$$\text{Minimize} \quad F(x) = [f_1(x), f_2(x), f_3(x), f_4(x), f_5(x), f_6(x)] \tag{7.7}$$

$$\text{s.t.} \quad \begin{array}{lll} 0.2 \leq f_1 \leq 0.70; & 0.2 \leq f_2 \leq 0.70; & 0.2 \leq f_3 \leq 0.30; \\ 0.2 \leq f_4 \leq 0.35; & 0.2 \leq f_5 \leq 0.70; & 0.2 \leq f_6 \leq 0.70; \end{array} \tag{7.8}$$

where x is the normalized vector of design variables: $x = [P1, P2, P3, P4, P5, D]^T$. The ranges of each design variable are the same after normalization: $0.2 \leq x_i \leq 0.8$, $i = 1, 2, \ldots 5$.

7.5.2 Design of experiments

The loading path was designed with five parameters for pressure and one for end feed, namely P1, P2, P3, P4, P5 and D (See Fig. 5.9a). P1 to P5 are different pressure levels, in MPa, and D is the maximum end feed, in mm, at the end of the process. The ranges selected for each design variable are as follows:

$$\begin{array}{lll} 10 \leq P1 \leq 18; & 20 \leq P2 \leq 50; & 50 \leq P3 \leq 70 \\ 80 \leq P4 \leq 100; & 100 \leq P5 \leq 150; & 10 \leq D \leq 50 \end{array} \tag{7.9}$$

The design of experiments was carried out by Latin hypercube sampling (LHS) with 50 sampling points. Then, a 10-fold cross-validation was implemented and the PRESS value was obtained for the model with regard to each objective. The quality of the Kriging model is given in Table 7.4. The PRESS error for each objective was low, and f_2 had the lowest value. The Kriging response surface for all of the other objectives had a high adjusted coefficient of determination which indicated an explanation above 89.94% of the variability in predicting new observations.

Table 7.4 Accuracy of response surface of the objectives

	f_1	f_2	f_3	f_4	f_5	f_6
Number of observations	50	50	50	50	50	50
PRESS	0.0159	0.0079	0.0733	0.0426	0.0239	0.0096
R^2_{pred}	0.8994	0.9962	0.9557	0.9721	0.9125	0.9099
SST	0.0025	0.0166	0.1213	0.0650	0.0065	0.0010

7.5.3 Results obtained using MOGA-I

The optimization was implemented with MOGA-I in 15 generations. An archived dataset was recorded to keep the elitist individuals. The L_2 norm was used to choose the layout with the minimum L_2 norm value in the archived set. Fig. 7.18 indicates the evolution of the loading path from the first population to the 15th generation.

The current optimum loading path obtained using MOGA-I has a minimum L_2 norm value of 0.8143 (Table 7.5). The objective values were 0.6587, 0.5936, 0.2000, 0.2889, 0.5419 and 0.5358 for objectives f_1, f_2, f_3, f_4, f_5 and f_6, respectively. The corner fill expansions are 11.50 mm (CFE=70.8%) and 12.59 mm (CFE=77.7%) for inside and outside corner, respectively (Table 7.6).

Table 7.5 The optimal loading path obtained using MOGA

	P1 (MPa)	P2 (MPa)	P3 (MPa)	P4 (MPa)	P5 (MPa)	D (mm)	L2 norm
Normalized value	0.7538	0.5672	0.2741	0.5229	0.7893	0.6991	0.8143
Loading path 1	17.38	38.36	52.47	90.76	149.11	43.28	–

Table 7.6 The objectives obtained by current optimal load path

	Final objective results						Corner expansion (mm)	
	f_1 (MPa)	f_2 (10^6) (MPa)	f_3	f_4	f_5 (mm)	f_6 (mm)	Outside corner (mm)	Inside corner (mm)
Normalized value	0.6587	0.5936	0.2000	0.2889	0.5419	0.5358	–	–
Optimal Path 1	-981	1.640	0	0.148	8.55	11.19	12.59 (77.7%)	11.50 (70.8%)
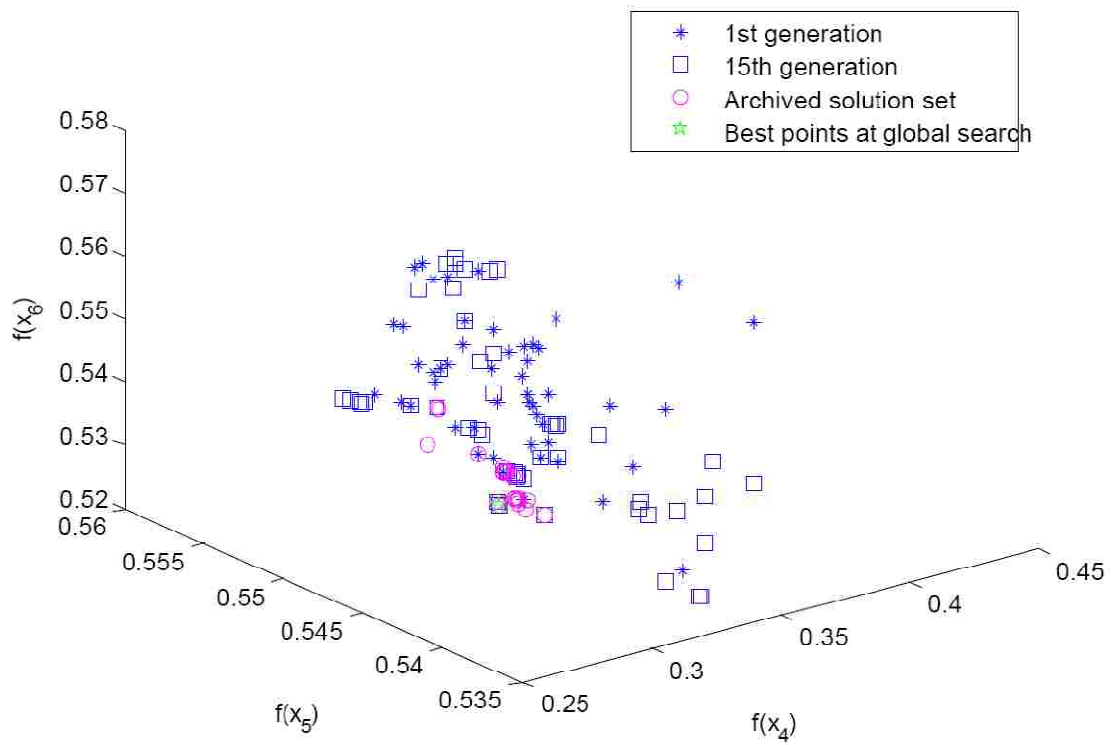
Fig. 7.18 Evolution of the three objectives f4, f5 and f6 in 3D plot
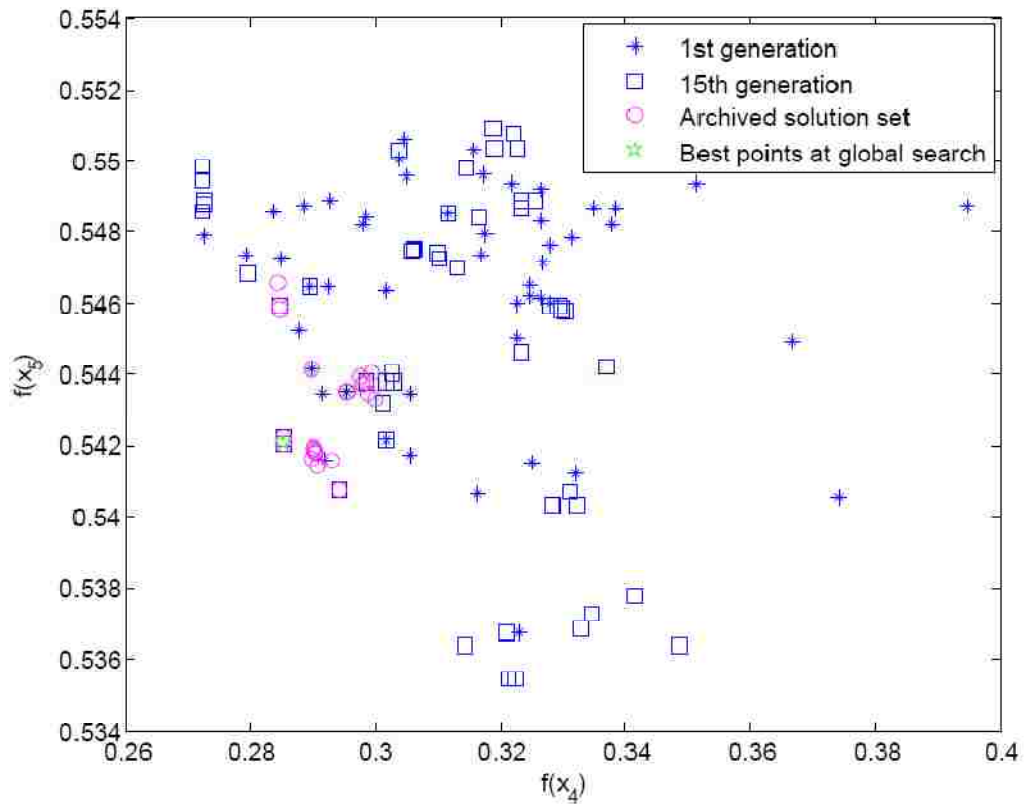
Fig.7.19 Evolution of the two objectives f4 and f5 in 2D plot
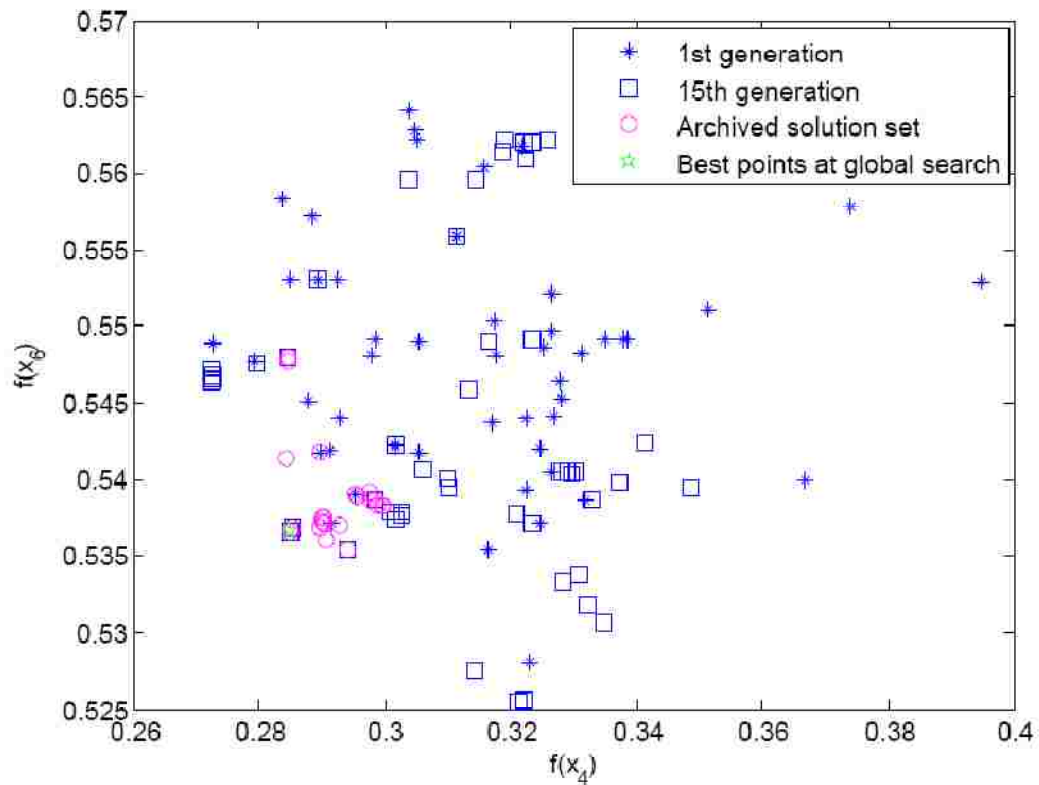
Fig. 7.20 Evolution of the two objectives f4 and f6 in 2D plot
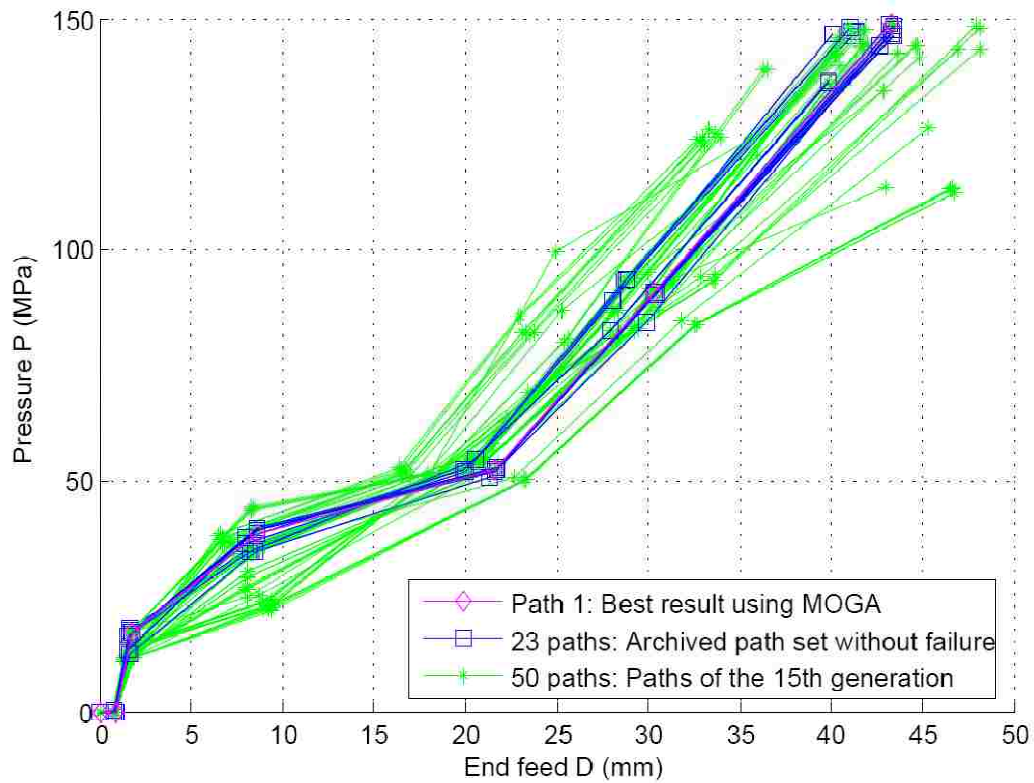
Fig. 7.21 Comparison of the optimum loading path set

7.5.4 Discussion of the stress history

Once optimum results were obtained using the global search, the stress history was further investigated. It was noticed that the minimum value of the maximum principal stress at all seven integration points in the element with the minimum final thickness (No. 1798) had exceeded the FLSC (Fig. 7.22). The maximum principal stress in this element is plotted in Fig. 7.23 for additional detail. It was noticed that the principal stress value in the final stage (point E in Fig. 7.23) is below the FLSD limit, however, during the stress history, there were three points (A, B and C) that surpassed the FLSC (Fig. 7.22) at the simulation time period of t = 1 ms to 2 ms. The stress at Point D is high but it is below the limit of Fig. 7.22. From the loading path curve (Fig. 7.21), it indicated that the excessive stress occurred during the deformation stage when the end feed was between D=10 mm and 20 mm. Consequently, a subsequent local search of the optimal loading path for this stage (D=10 to 20 mm) was implemented.
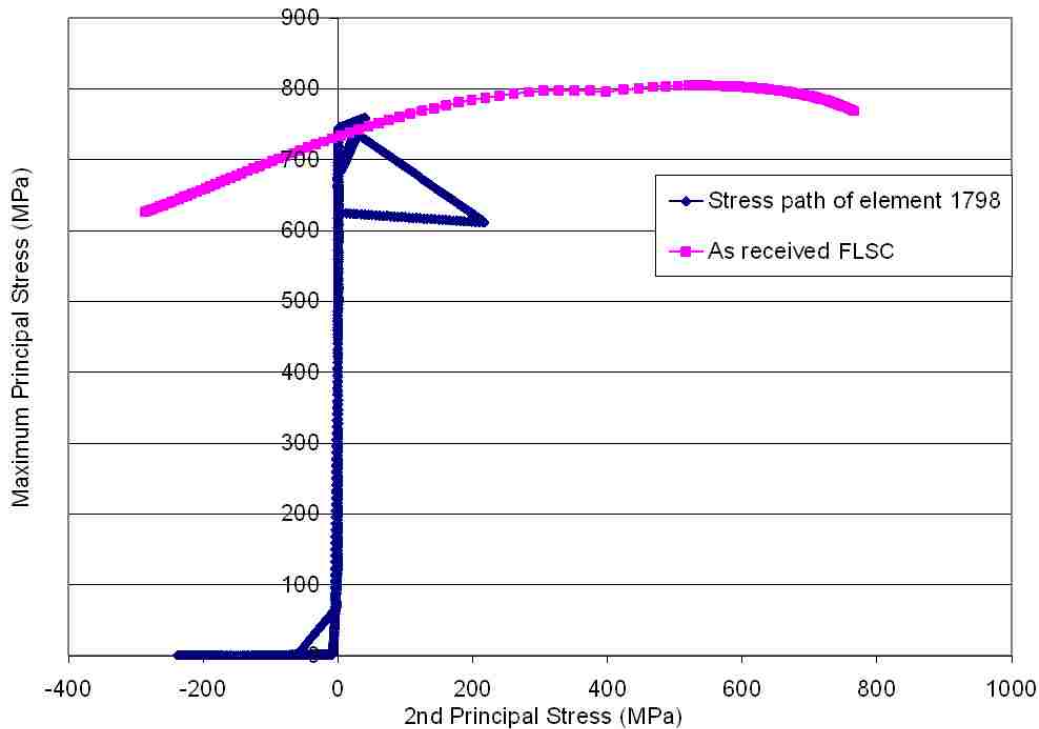
Fig. 7.22 Stress path for element 1798 with the minimum thickness
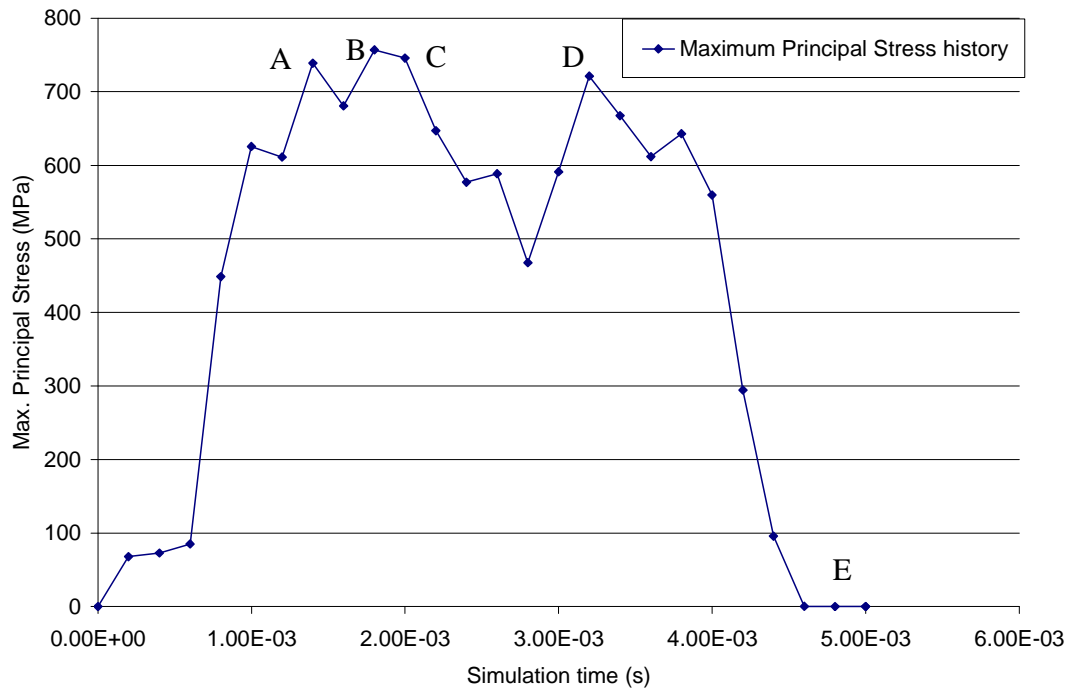
Fig. 7.23 History of maximum principal stress for element 1798 (Minimum value among all 7 integration points)

A Latin hypercube sampling method with 50 seeds was carried out to find solutions with a positive safety margin in the stress forming limit diagram. The parameters were defined as shown in Table 7.7. Within this group of solutions, 41 of them presented major principal stresses that were under the forming limit stress curve (FLSC) (Fig. 7.26). However, the remaining 9 simulations showed stresses above the FLSC. It was noted that the generated FLSC was in good coincidence with the reference (Bardelcik and Worswick, 2005). The best result was selected to be with a minimum L_2 norm value for objectives f_4, f_5 and f_6. The optimal loading path is listed in Table 7.8. The generated objectives were listed and compared to the experimental results in Table 7.9.

It was noted in the experiment that the minimum corner radius was 12.22 mm, and the maximum corner expansion was 10.73 mm for the hydroformed part with a medium mandrel boost (MB) in pre-bending. However, the optimized loading path was able to reduce the corner fill radius to 8.73 mm and 11.24 mm for the extrados and intrados of

the bend, respectively. The corner fill expansion was improved by 16.7% (or 1.79 mm) compared to the maximum expansion of 10.73 mm obtained experimentally.

The geometry of the part after the hydroforming simulation is shown in Fig. 7.25. The predicted tube thickness is 1.613 mm at the extrados and 1.722 mm at the intrados. Compared to the calculated tube thickness after bending which was 1.62 mm at the extrados and 2.124 mm at the intrados, the thickness reduction due to hydroforming remained almost the same at the extrados (-12.8%), but decreased somewhat at the intrados (i.e. −6.9% thickness reduction compared to the original thickness).

Table 7.7 The parameters for local search

time $(10^{-3}s)$	P1 (MPa)	P2 (MPa)	P3 (MPa)	D1 (mm)	D2 (mm)	D3 (mm)
t = 1.0	28-38			8-9		
t = 2.5		42-50			21-28	
t = 5.0			140-149.5			40-43.5

Table 7.8 The optimal load path

	P1 (MPa)	P2 (MPa)	P3 (MPa)	P4 (MPa)	P5 (MPa)	D (mm)	L_2 norm
Normalized value	0.2801	0.3843	0.7669	0.3877	0.2166	0.7082	0.8167
Optimal load path	29.34	44.46	148.98	8.31	21.19	42.96	–

Table 7.9 Comparison of the optimal and experimental results (Bardelcik et al. 2005)

	Final objective results						Corner expansion (mm)	
	f_1 (MPa)	f_2 (10^6) (MPa)	f_3	f_4	f_5 (mm)	f_6 (mm)	Outside corner	Inside corner
Normalized value	0.6631	0.5740	0.2	0.2770	0.5493	0.5372	–	–
Optimal Path 2	-972	1.560	0	0.128	8.73	11.24	12.52 (77.2%)	11.48 (70.7%)
Ref.[158]					Minimum radius 12.22 (MB)		Maximum expansion 10.73 mm (MB)	

Note: MB represents for medium mandrel boost
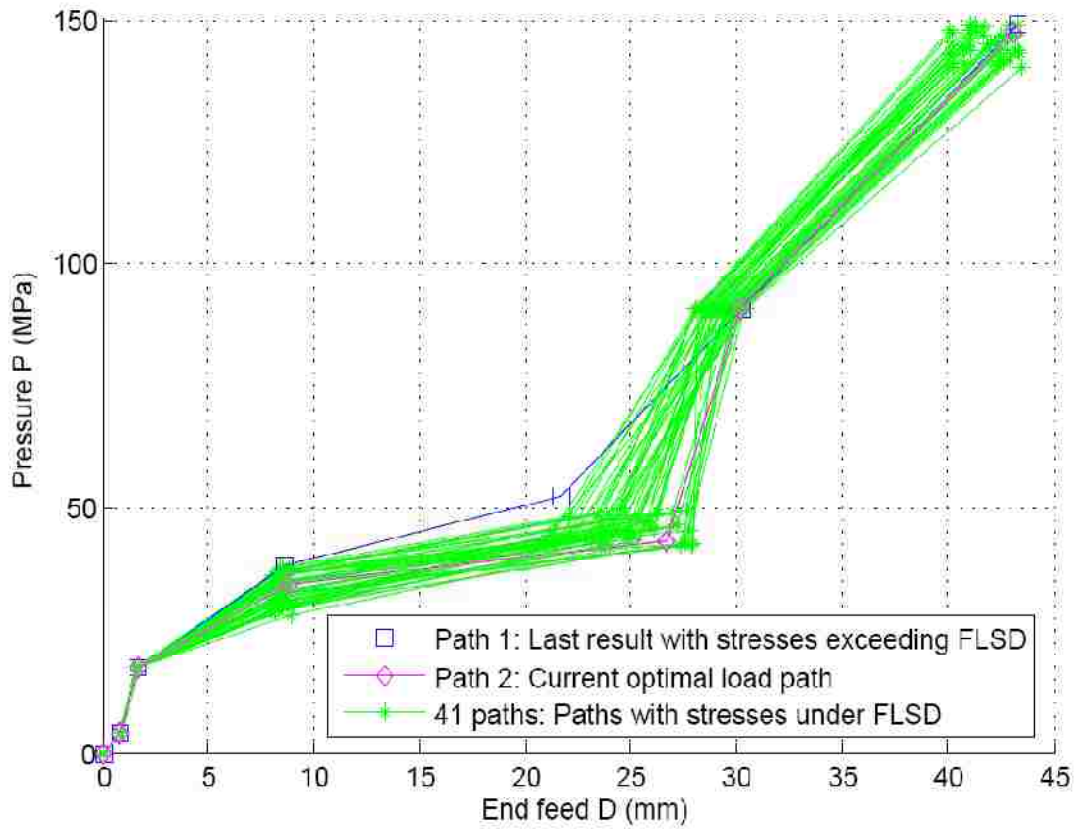
Fig. 7.24 Final optimal loading path with maximum principal stresses under the FLSD limit
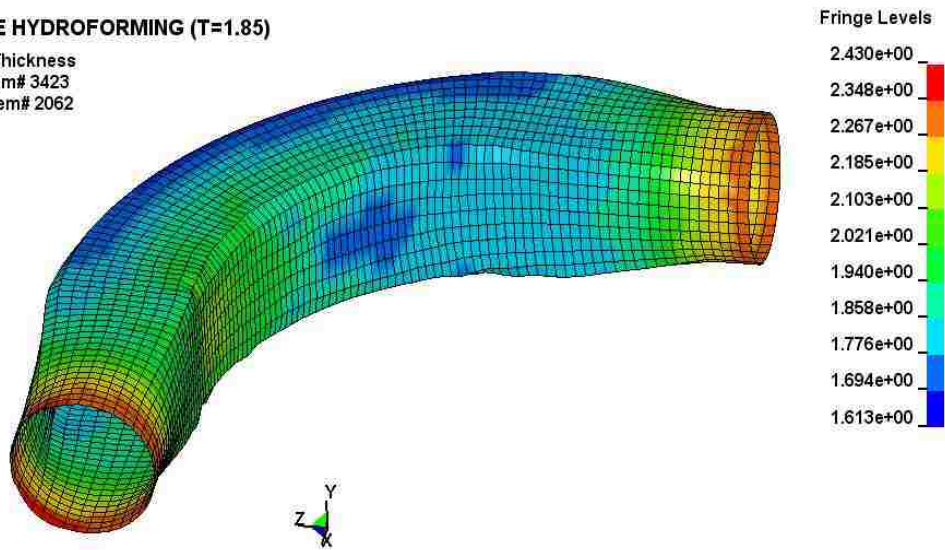
Fig. 7.25 Thickness distribution of the tube hydroformed with the optimal loading path

164
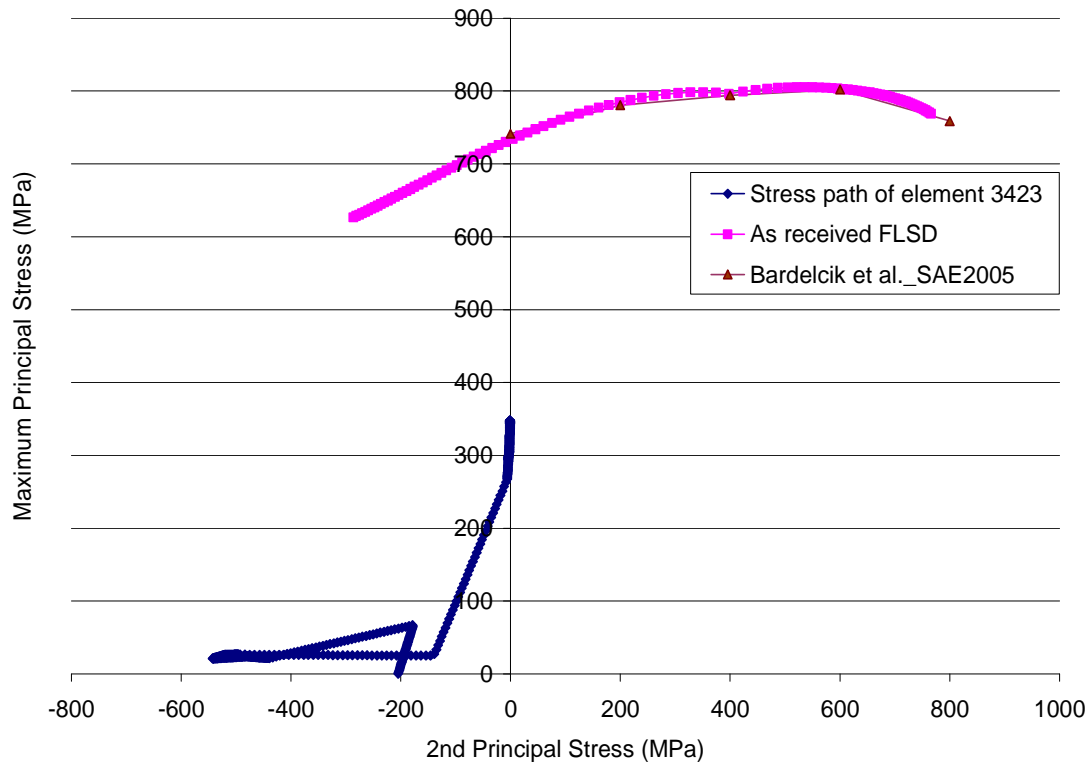
Fig. 7.26 Stress path and FLSD for element 3423

In this study a displacement based end feed was numerically applied to the tube ends. In order to determine the end feed forces that were applied for this simulation, the nodal forces were calculated. The maximum total load force in the X and Z directions were almost identical at the tube ends, with a value of 412 kN (Fig. 7.27 and 7.28). Compared to the experimental load path, this predicted loading path was almost four times greater than the maximum end feed force applied for pre-bent tube hydroforming and two times greater than for the straight tube hydroforming, which were 133 kN and 200 kN, respectively. Consequently, it is suggested that the end feed force be significantly increased to generate a better corner fill for pre-bent tube hydroforming in future experiments.
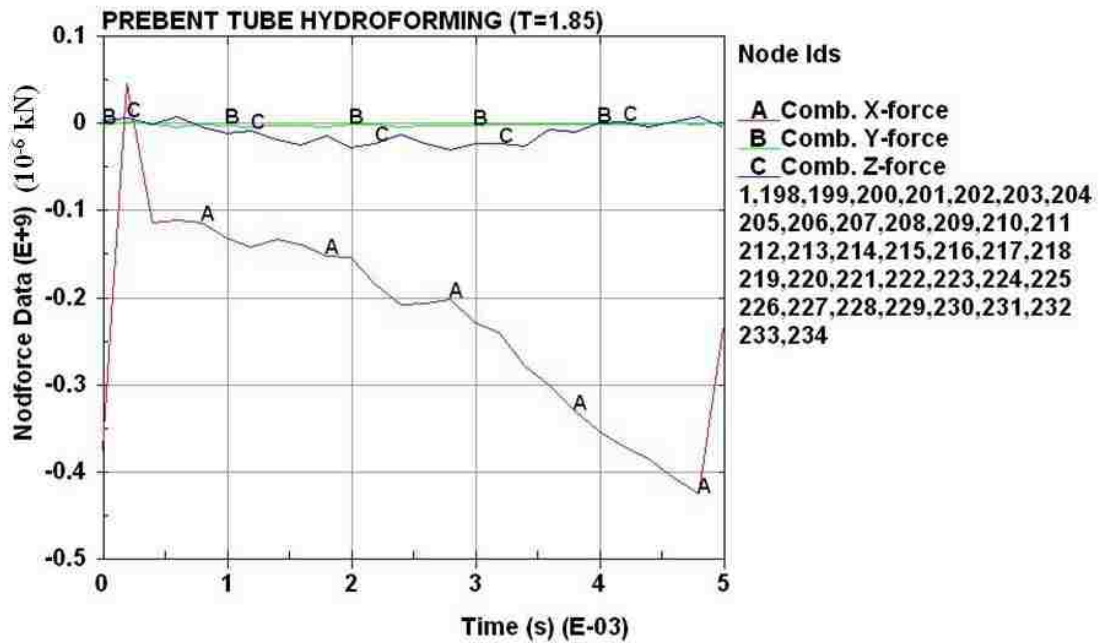
Fig. 7.27 Total load force of the nodes feeding in the X direction
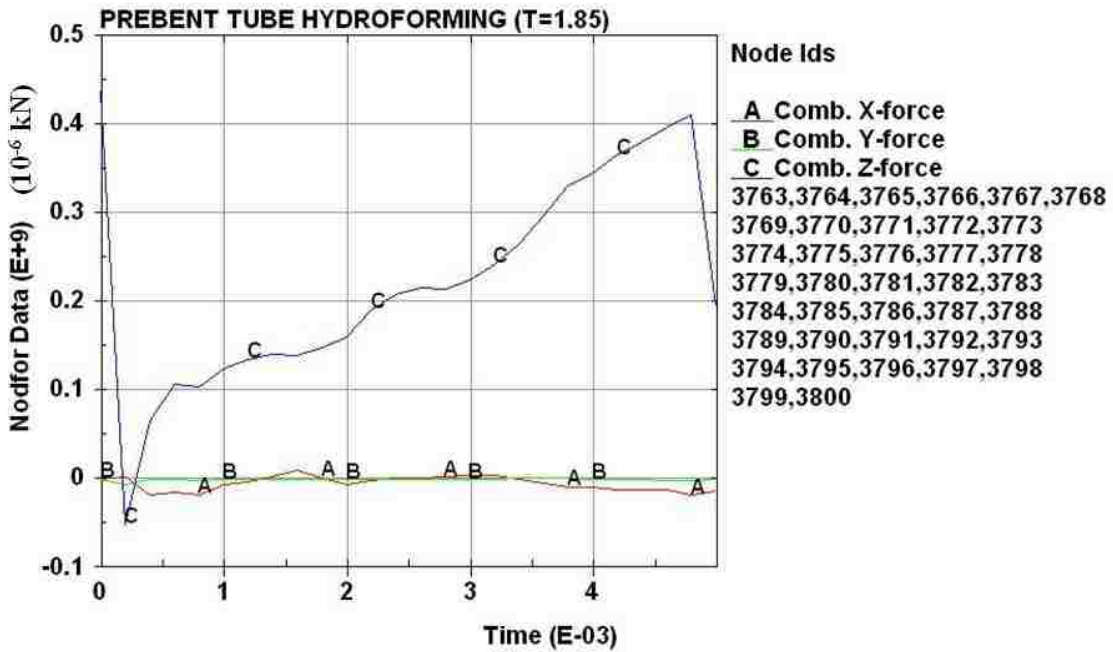
Fig. 7.28 Total load force of the nodes feeding in the Z direction

166

Chapter 8: Conclusions and Future Work

8.1   Conclusions

Engineering design by its very nature is non-linear and multi-objective, often requiring a compromise between disparate and conflicting objectives. The goals of this study were to consider multiple objectives in the development of *a*) a general method for evaluating the forming severity of tubular hydroformed parts, and *b*) strategies for the design and optimization of hydroforming process parameters (i.e. loading path) using finite element simulation. As a result of this work, the following conclusions can be drawn:

1. A hybrid forming severity indicator that combines both the conventional forming limit diagram (FLD) and the forming limit stress diagram (FLSD) was firstly developed to assess the risk of thinning, necking/splitting and wrinkling. This indicator is far more suitable than single indicators such as the FLD or the FLSD for complex and highly nonlinear forming processes. Furthermore, for each specific optimization application, this hybrid indicator can be combined with other objectives of geometry/quality requirements such as die filling and thickness distribution.

2. Two optimization strategies were proposed to solve this type of multi-objective optimization problem: normal boundary intersection (NBI) and multi-objective genetic algorithm (MOGA). The advantages of the NBI algorithm compared to the weighted sum method are that it generates the Pareto solution set with uniformly distributed points and it can be easily applied with Matlab. However, it needs sequential improvements of the RSM model to obtain the global optimum.

3. Compared to the NBI algorithm, a more robust MOGA was implemented and combined with finite element analysis and a Kriging model for optimization. In this MOGA method, several improvements were made in terms of the constraint-handling technique, the automatic updating of the Kriging model, and the combination of global and local searches. This hybrid MOGA was shown to generate better results than the

conventional NSGA-II because of the global and local search strategy adopted for problems with three or more objectives.

4. The proposed methods were applied to the loading path design of several case studies: straight THF in a square-cavity die, T-shaped THF and the hydroforming of an industrial refrigerator door handle. Moreover, the proposed methods were compared with the commercial software LS-OPT4.0, and the results showed that both methods performed better than LS-OPT4.0 to generate a smaller corner radius without failure.

5. An investigation of THF with pulsating pressure in a T-shaped die was completed to optimize the amplitude and frequency of the pulsating curve. The numerical simulations demonstrated that pulsating pressure does indeed improve the formability of the tube hydroforming process. An optimization procedure was implemented to identify the optimal amplitude and frequency of the pulsating pressure. Compared to the published experimental data, this optimization algorithm was able to further improve the formability and generate a quality part with 25% less thinning and a lesser tendency of wrinkling or bursting.

6. The MOGA method was further utilized to optimize a multi-stage forming process in which a tube was pre-bent prior to THF. With the optimal loading path, the corner fill expansion significantly increased at both the intrados (CFE of 11.48 mm) and extrados (CFE of 12.52 mm) of the bent and hydroformed part, which represented a 16.7% increase compared to the maximum expansion of 10.73 mm obtained experimentally. It was also noted that the wall thickness of the part hydroformed according to the optimized loading path remained almost the same as that of bent tube at the extrados, and was only slightly less than the original wall thickness at the intrados. This demonstrates that the reduced formability due to pre-bending can be largely compensated by end feeding the tube during hydroforming. Moreover, results showed that a gradually applied axial load may be beneficial to generate a smaller corner fill radius without failure.

8.2 Recommendations for future work

The following recommendations are proposed for further research and development.

1. Consider the effect of through-thickness stress on the forming behaviour of the tube and apply a three-dimensional stress-based failure criterion in the optimization model. The extended stress-based forming limit criterion that was proposed by Simha et al. (2007) is suggested for assessing the through-thickness stress effect.

2. Develop parallel computing using a Message Passing Interface (MPI) platform to enhance the computation capacity and reduce simulation time, especially when considering a large scale finite element model with solid elements.

3. Further investigate the loading path design of complex-shaped hydroformed parts with pulsating pressure to generate a more uniform wall thickness and achieve smaller as-formed radii.

4. Establish a knowledge database and explore adaptive loading path design method for THF control. The expert system and fuzzy logic theory can be used to generate such a database and provide the logic for real-time control of the THF process.

Bibliography

Abedrabbo N., et al. (2005), Optimization of a Tube Hydroforming Process, Red Cedar Technology, MI, 48823, USA, www.redcedartech.com.

Abedrabbo N., et al. (2009), Optimization methods for the tube hydroforming process applied to advanced high-strength steels with experimental verification, J. Mater. Process. Technol., 209:110–123

Ahmetoglu M., Altan T. (2000), Tube hydroforming: state-of-the-art and future trends, J. Mater. Process. Technol., 98:25-33,

Ahmed M., Hashmi M.S.J (1997), Estimation of machine parameters for hydraulic bulge forming of tubular components, , J. Mater. Process. Technol., 64:9-23

Ahmed M., Hashmi M.S.J (1998), Finite-element analysis of bulge forming applying pressure and in-plane compressive load 3, J. Mater. Proces. Technol. 77 (1-3) 95-102.

Ahmed M., Hashmi M.S.J (1999), Three-dimensional finite element simulation of bulge forming, in: Proceedings of the Intl. Conf. on Adv. in Mater. and Process. Technol., AMPT'99 & IMC 16, Vol. 1, Dublin, pp.153-161.

Ahmed M., Hashmi M.S.J (1999), Finite element simulation of manufacturing metal bellows from tubes, in: Proceedings of the Advances in Materials & Processing Technologies 1998, Vol. 11, Kuala Lumpur, pp. 982-989.

Al-Qureshi HA, Moriera Filho LA (2001), Junction Forming in Aluminum Tubes Using an Elastomer Technique. Mater. Manuf. Processes 16:717–724.

An H., Green D. E., Johrendt J. (2009), A global optimization of load path design for tube hydroforming applications using MOGA, IDDRG conference, June, Golden, CO, USA, pp307-318.

Andries P. Engelbrecht (2007), Computational intelligence: An introduction, Second Edition, John Wiley & Sons Ltd., England, ISBN 978-0-470-03561-0.

Arrieux R., Bedrin C. and Boivin M. (1982), Determination of an intrinsic forming limit stress diagram for isotropic metal sheets, Proceedings of the 12th Biennial Congress of the IDDRG, Ste Margherita Ligure, pp. 61–71.

Asnafi N. (1999), Analytical modelling of tube hydroforming, Thin-Walled Structures 34: 295–330

Asnafi N. and Skogsgardh A. (2000), Theoretical and experimental analysis of stroke controlled tube hydroforming, Materials Science and Engineering, 279:95–110

Aue-U-Lan Y., Ngaile G., Altan T. (2004), Optimizing tube hydroforming using process simulation and experimental verification, J. Mater. Process. Technol., 146:137–143.

Aydemir A., et al. (2005), An adaptive simulation approach designed for tube hydroforming processes, J. Mater. Process. Technol., 159:303–310

Barata D.R.A., Barlat F., Jalinier J.M. (1985), Prediction of the forming limit diagrams of anisotropic sheets in linear and non-linear loading. Mat. Sci. Eng. 68:151-164

Bardelcik A., Worswick M.J. (2005a), Numerical investigation into the effects of bending boost and hydroforming end-feed on the hydroformability of DP600 tube, 2005-01-0094, Proceedings of SAE Conference

Bardelcik A., Worswick M.J. (2005b), The effect of element formulation on the prediction of boost in numerical tube bending, Proceedings of Numisheet 2005, pp. 775-780.

Bardelcik A., et al. (2005 c), Tube Bending and Hydroforming of DP600, IF and AKDQ Steel Tube. AUTO21 Group Meeting, March 21.

Bardelcik A. (2006), Effect of pre-bending and hydroforming parameters on the formability of advanced high strength steel tubes, Master Thesis, University of Waterloo.

Bieling P., Untersuchungen zum aufweitstauchen von rohren zu hohlwellen, Dissertation, Universität-Gesamthochschule Paderborn, 1992.

Bonte MHA , van den Boogaard AH, Huétink J (2008), An optimisation strategy for industrial metal forming processes, Modelling, screening and solving of optimisation problems in metal forming. Struct Multidisc Optim 35:571–586

Butuc, C. et al. (2002), A more general model for FLD prediction. J. Materials Proc. Techn. 125-126:213-218

Butuc, C., Gracio, J.J., Barata da Rocha A. (2003), A theoretical study on forming limit diagrams prediction. J. Material Proc. Techn., 142:714–724

Butuc MC, Gracio JJ, Barata D.R.A (2006), An experimental and theoretical analysis on the application of stress-based forming limit criterion. Int. J. Mech. Sci. 48:414-429

Braeutigam and Butsch (1992) Hydroformen - als Ausweg aus der Investitionsklemme, in VDI Berichte Nr 94, Duesseldorf, VDI

Cao, J. et al. (2000), Prediction of localized thinning in sheet metal using a general anisotropic yield criterion. Int. J. Plasticity, 16:1105-1129

Cramer E J, et al. (2006), Multi-objective optimization for complex engineering simulation and its application to nozzle design. 11th AIAA/ISSMO Multidisciplinary Analysis and Optimization Conference 3:1937-1943

Chu, E., Xu, Y. (2004a), Hydroforming of aluminum extrusion tubes for automotive applications. Part I. Buckling, wrinkling and bursting analyses of aluminum tubes. Int. J. Mech. Sci. 46, 263–283.

Chu E., Xu Y. (2004b), Hydroforming of aluminum extrusion tubes for automotive applications. Part II: process window diagram, Int. J. Mech. Sci., 46: 285–297

Das I, Dennis JE (1998), Normal-Boundary Intersection: A New Method for Generating the Pareto Surface in Nonlinear Multicriteria Optimization Problems. SIAM J. on Optimization 8(3):631-657

Deb K, Pratap A, Agarwal S, et al. (2002), A fast and elitist multiobjective genetic algorithm: NSGA-II, IEEE Trans. on Evolutionary Comput., 6(2):182-197.

Deb K. (2008), Introduction to evolutionary multiobjective optimization, Chapter 3 in Multiobjective optimization interactive and evolutionary approaches, Branke J., et al. (Eds.), ISBN-103-540-88907-8, Springer NewYork

Dyment J., Worswick M.J., Normani F., Oliveira D., Khodayari G. (2003), Effect of endfeed on strains and thickness during bending and on the subsequent hydroformability of steel tubes, SAE Paper No. 2003-01-2837

Dyment J. (2004), The Effect of Bending Process on the Hydroformability of Steel Tubes, MASc. Thesis, University of Waterloo.

Dwyer N., et al. (2003), Pre-bending and subsequent hydroforming of tube: simulation and experiment, Proceedings of IBEC2003, Japan, October

Dohmann F., Klass F. (1987), Liquid bulge forming of tubular workpieces, Strips, Sheets and Tubes 4(1):7-10.

Dohmann F. and Hartl C. (1994), Liquid bulge forming as a flexible production method, J. Mater. Proces. Technol. 45:377-382.

Dohmann F., Hartl Ch. (1997), Tube hydroforming – research and practical applications, J. Mater. Process. Technol., 71:174-186

Dohmann F. and Hartl C. (1996), Hydroforming -a method to manufacture light weight parts, J. Mater. Proces. Technol. 60: 669-676.

Eschenauer H, Koski J, Osyczka AE (1990), Multicriteria design optimization: procedures and applications. Berlin, Heidelberg, NY: Springer Corporation

Favuzza S, Ippolito M G, Sanseverino E R (2006), Crowded comparison operators for constraints handling in NSGA-II for optimal design of the compensation system in electrical distribution networks, Adv. Engrg. Info., 20: 201-211

Engelbrecht A.P. (2007), Computational intelligence: An introduction, Second Edition, John Wiley & Sons Ltd., England, ISBN 978-0-470-03561-0.

Fann KJ, Hsiao PY (2003), Optimization of loading conditions for tube hydroforming. J. Mater. Process. Technol., 140:520–524

Gao L., Motsch S., Strano M. (2002), Classification and analysis of tube hydroforming processes with respect to adaptive FEM simulations, J. Mater. Process. Technol., 129:261- 267

Goovaaerts P (1997), Geostatistics for Natural Resources Evolution. New York, NY: Oxford University Press.

Goel T., et al. (2007),Response surface approximation of Pareto optimal front in multi-objective optimization, Compt. Methods Appl. Mech. Engrg. 196:879-893

Guan Y.B., Pourboghrat F. (2008), Fourier series based finite element analysis of tube hydroforming-Generalized plane strain model, J. Mater. Process. Technol., 197:379-392

Guan Y.B., Pourboghrat F, Yu W.R. (2006), Fourier series based finite element analysis of tube hydroforming: An axisymmetric model, Engineering Computations, v 23, n 7: 697-728

Goodwin G.M. (1968), Application of strain analysis to sheet metal forming in the press shop. SAE paper No. 680093.

Gholipour J. et al. (2004), Severity of the bend and its effect on the subsequent hydroforming process for aluminum alloy tube,AIP conference proceedings, n 712, pt.1, p 1089-94, NUMIFORM 2004.

Graf A. F. and Hosford W. F. (1993a), Calculations of forming limit diagrams for changing strain path, *Metallurgical Transactions A*, 24, 2497–2501.

Graf A. F. and Hosford W. F. (1993b), Effect of changing strain paths on forming limit diagram of Al 2008-T4, *Metallurgical Transactions A*, 24, 2503–2512.

Graf A. F. and Hosford W. F. (1994), The influence of strain-path changes on forming limit diagram of Al 6111-T4, *International Journal of Mechanical Sciences*, 10, 897–910.

Green DE and Stoughton TB (2004), Evaluating hydroforming severity using stress–based forming limit diagrams, Proceedings of the 2nd Annual North American Hydroforming Conference, sponsored by SME/TPA, Waterloo, ON,Canada.

Green D.E., Black K.C. (2002), A Visual Technique to Determine the Forming Limit of Sheet Materials, SAE paper 2002-01-1062.

Green DE (2008), Formability Analysis for Tubular Hydroformed Parts, in: Hydroforming for advanced manufacturing (Chapter 5), Woodhead Publishing Ltd., Cambridge, England, ed. M. Koç, ISBN 978-1-84569-328-2

Ghosh A.K., Laukonis J.V. (1976), The influence of strain-path changes on the formability of sheet steel, 9th Biennial Congress of the IDDRG, Sheet Metal Forming and Energy Conservation, ASM Publication

Hallquist J.O. (2007), LS-DYNA. Keyword User's Manual", Ver. 971. LSTC

Hashmi M.S.J. (1981), Radial thickness distribution around a hydraulically bulge formed annealed copper T-joint: Experimental and Theoretical Predictions, 22nd Int. MTDR Conf. Proc..

Hashmi M.S.J. (1983), Forming of tubular components from straight tubing using combined axial load and internal pressure: Theory and Experiment, Proc. Int. Conf. on Dev. on Drawing of Metals, Metals Society.

Hashmi M.S.J., Crampton R. (1985), Hydraulic bulge forming of axisymmetric and asymmetric components: Comparison of Experimental Results and Theoretical Predictions, Int. MTDR Conf. Proc..

Hill, R. (1952), On discontinuous plastic states, with special reference to localized necking in thin sheets. J. Mech. Phys. Solids 1, 19.

Huang H.M., Pan J. and Tang S.C. (2000), Failure prediction in anisotropic sheet metals under forming operations with considderation of rotating principal stretch directions. Int. J. Plasticity 16:611

Hughes E J (2005), Evolutionary Many-Objective Optimisation: Many Once or One Many? In: 2005 IEEE Congress on Evolutionary Computation (CEC'2005), vol. 1, pp. 222–227. IEEE Computer Society Press, Los Alamitos

Hussain M.F., Burton R.R., Joshi S.B.(2002), Metamodeling: radial basis functions, versus polynomials, Europe J Oper Res 138:142–154

Hutchinson, J.W., Neale, K.W. (1978a), Sheet necking—II: time-independent behavior. In: Koistinen, D.P., Wang, N.M. (Eds.), Mechanism of Sheet Metal Forming. Plenum Press, New York, p. 127.

Hutchinson, J.W., Neale, K.W. (1978b), Sheet necking—III: strain-rate effects. In: Koistinen, D.P., Wang, N.M. (Eds.), Mechanism of Sheet Metal Forming. Plenum Press, New York, p. 269.

Hwang Y.M., Lin Y.-K. (2002), Analysis and finite element simulation of the tube bulge hydroforming process,J. Mater. Process. Technol., 125–126: 821–825

Hosford W.F., Caddell R. (2007), Metal forming: Mechanics and metallurgy, third edition, Cambridge University press

Imaninejad M, Subhash G, Loukus A (2005), Load Path Optimization of Tube Hydroforming Process. Int. J. Mach. Tools Manuf. 45:1504–1514.

Ingarao G. et al. (2009), Internal pressure and counterpunch action design in Y-shaped tube hydroforming processes: A multi-objective optimisation approach, Computers and Structures 87:591–602.

Jirathearanat S., Hartl Ch., Altan T. (2004), Hydroforming of Y shapes – product and process design using FEA simulation and experiments, J. Mater. Process. Technol., 146:124-129

Keeler S.P., Backhofen W.A. (1963), Plastic instability and fracture in sheet stretched over rigid punches. ASM Trans. Quart. 56, 25–48.

Keeler S. P. and Brazier w. G. (1977), Relationship between laboratory material characterization and press shop formability, Proceedings of Microalloy 75, Union Carbide, New York, pp. 447–452.

Kim, S. T. and Kim Y.S. (2002), Analytical study for tube hydroforming, J. Mater. Process. Technol., 128:232-239

Konak A, Coit D W, Smith A E (2006), Multi-objective optimization using genetic algorithms: A tutorial, Reliability Engineering and system safety, 91: 992-1007

Koç M, Allen T, Jiratheranat S, Altan T (2000), The use of FEA and design of experiments to establish design guidelines for simple hydroformed parts. Intl. J. Machine Tools & Manufacture, 40:2249–2266

Koç M, Altan T (2002), Prediction of forming limits and parameters in the tube hydroforming process. Intl. J. Machine Tools & Manufacture, 42:123–138

Koç M. (2004), Advances in tube hydroforming – an enabling technology for low-mass vehicle manufacturing – material, lubrication, loading, simulation issues and alternatives, Tsinghua Science and technology, 9(5):527-545

Koç M. (2003), Investigation of the effect of loading path and variation in material properties on robustness of the tube hydroforming process, J. Mater. Process. Technol., 133:276-281

Koç M. (1999), Development of guidelines for tube hydroforming, doctoral dissertation, Columbus OH

Kulkarni A. (2006), Adaptive Sampling based Sampling Strategies for the DACE Surrogate Model for Expensive Black-box functions, AE 497 B.Tech. Project, Dept. of Aerospace Engrg., Indian Institute of Technology, Bombay, April

Lee H., Van Tyne C.J., Field D. (2005), Finite element bending analysis of oval tubes using rotary draw bender for hydroforming applications. J. Mater. Process. Technol., 168:327–335

Lee K-H and Kang D-H (2007), Structural optimization of an automotive door using the kriging interpolation method.Proc. IMechE Vol. 221 Part D: J. Automobile Engineering, DOI: 10.1243/09544070JAUTO, 403:1525-1534.

Lei L.P., et al (2001), Analysis and design of hydroforming processes by the rigid-plastic finite element method, J. Mater. Process. Technol., 114:201–206

Limb M.E., Chakrabarty J. and Garber, S. (1973), the Forming of Axisymmetric and Asymmetric Components from Tube, Proc. Int. M.T.D.R. Conf., pp799-805.

Li B., Nye T.J., Metzger D. R. (2006), Multi-objective optimization of forming parameters for tube hydroforming process based on the Taguchi method. Int J Adv Manuf Technol, 28: 23–30

Li B, Nye TJ, Metzger DR (2007), Improving the reliability of the tube-hydroforming process by the Taguchi method. Transactions of the ASME 129:242-247

Loh-Mousavi M., et al. (2008), Improvement of formability in T-shape hydroforming of tubes by pulsating pressure, Proc. IMechE Vol. 222 Part B: J. Engineering Manufacture, DOI: 10.1243/09544054JEM1143, pp1139-1146

Lophaven S. N., Nielsen H.B., Søndergaard J. (2002), DACE—a Matlab Kriging toolbox,Version 2.0, Technical Report IMM-REP-2002-12, Informatics and Mathematical Modelling, Technical University of Denmark

Lorenzo R. D., et al. (2004a), An integrated approach to the design of tube hydroforming processes: artificial intelligence, numerical analysis and

experimental investigation, Materials processing and design: Modeling, Simulation and Applications (NUMIFORM 2004), AIP Conference Proceedings, Vol. 712, pp. 1118-1123.

Lorenzo R. D., et al. (2004b), Optimal design of tube hydroforming processes: a fuzzy-logic-based approach,Proc. Instn Mech. Engrs Vol. 218 Part B: J. Engrg. Manuf., p599-606

Lorenzo R. D., Ingarao G., Micari F. (2006), Sensitivity analysis based preform die shape design for net-shape forging, IDDRG 2006 Conference: Drawing the things to come-Trends and advances in sheet metal forming, June 19-21, Porto, Portugal, 371-378.

Mac Donald B.J., Hashmi M.S.J. (2000), Finite element simulation of bulge forming of a cross-joint from a tubular blank, J. Mater. Process. Technol., 103: 333-342

Mathworks (2008), Matlab Model-Based Calibration Toolbox™ 3-CAGE User's Guide.

Manabe K., Miyamoto S., Koyama H. (2002), Application of Database- Assisted Fuzzy Adaptive Process Control System to Tube Hydroforming Process, Intelligence in a Materials World (Selected Papers from IPMM2001), CRC Press, pp. 537–543.

Manabe K.,et al. (2006), Hydroforming process optimization of aluminum alloy tube using intelligent control technique, International Journal of Machine Tools & Manufacture 46:1207–1211.

Manabe K., et al. (1984), Bulge forming of thin walled tubes by Micro-computer controlled hydraulic press, Advanced technology of plasticity, 1:279-284.

Manabe K., Amino M. (2002), Effects of process parameters and material properties on deformation process in tube hydroforming, J. Mater. Process. Technol., 123 :285–291

Marciniak Z., Kuczynski K. (1967), Limit strains in the processes of stretch-forming sheet metal. Int. J. Mech. Sci. 9, 609.

McKay M. D., Bechman R. J., and Conover W. J. (1979), A Comparison of Three Methods for Selecting Values of Input Variables in the Analysis of Output from a Computer Code, Technometrics, 21(2):239–245.

Mehnen J, Michelitsch T, Lasarczyk C, et al. (2007), Multi-objective evolutionary design of mold temperature control using DACE for parameter optimization, Intl. J. Applied Electromagnetics and Mechanics, 25:661–667

Mentella A., Strano M., Gemignani R. (2008), A new method for feasibility study and determination of the loading curves in the rotary draw-bending process, Int. J. Mater. Forming, Vol.1, Suppl.1, DOI: 10.1007/s12289-008-0017-0, P165-168

Miyamoto S., Koyama H. and Manabe K. (2001), Fuzzy adaptive control system for tube hydroforming process, The proceedings of the 52nd Japanese Joint conference for the technology of plasticity, pp.6.

Montgomery C. (1997), Design and Analysis of experiments, 4th ed. Wiley, NY.

Mori K., et al. (2007), Mechanism of improvement of formability in pulsating hydroforming of tubes, J. Machine Tools & Manufacture 47 978–984

Murata M., et al. (1989), The hydraulic tube bulging of a tube attached lining rubber membrane with axial compressive force, JSME Int. J. Series III, 32.

Myers R H, Montgomery D C (1995), Response Surface Methodology – Process and Product Optimization Using Designed Experiment, Wiley-Interscience.

Myers R. and Montgomery D. (2002), Response surface methodology: process and product optimization using designed experiments", 2nd edn. Wiley, New York

Nakazima K, Kikuma T., Hasuka K. (1971), Study on the formability of steel sheets. Yawata Tech. Rep. No. 284: 678-680

Oliveira D.A., Worswick M.J., Grantab R. (2005), Effect of lubricant in mandrel-rotary draw tube bending of steel and aluminum, Canadian Metallurgical Quart., 44(1), pp.71-78

Palumbo G., et al. (2004), Analysis Of Hydro Formed Complex Shape Parts Using A Ductile Fracture Criterion, AIP Conference Proceedings, June

Panos Seferlis, Michael C. Georgiadis (Editors) (2004), The Integration of Process Design and Control, Published by Elsevier, ISBN 0444515577, 9780444515575.

Park K.S., Kim B.J., Moon Y.H. (2005), Optimization of tube hydroforming process by using fuzzy expert system, The fifth pacific rim intl. conference on adv. mater. and process., pts 1-5 materials sci. forum, 475-479: 3283-3286, Part 1-5

Peñuelas I., et al. (2009), Inverse determination of the elastoplastic and damage parameters on small punch tests. Fatigue Fract Engrg Mater Struct 32: 872–885.

Ponthot J.P. and Kleinermann J.P. (2006), A cascade optimization methodology for automatic parameter identification and shape/process optimization in metal forming simulation. Comput. Methods Appl. Mech. Engrg. 195:5472–5508.

Rafiq M.Y., Bugmann G., Easterbrook D.J. (2001), Neural network design for engineering applications, *Comput Struct* 21(17): 1541–1552

Ray P. and Mac Donald B.J. (2004) , Determination of the optimal load path for tube hydroforming processes using a fuzzy load control algorithm and finite element analysis, *Finite Elements in Analysis and Design* 41:173–192

Rimkus W., Bauer H., Mihsein M.J.A. (2000), Design of load-curves for hydroforming applications, J. Mater. Process. Technol., 108: 97-105

Reid JV (2002) Twist compression evaluation of hydroforming lubricants. Private contract report submitted to DA Stuart Inc. by the Industrial Research & Development Institute (IRDI), Midland, ON, Canada

Rigoni E (2004) NBI-NLPQLP Scheduler, Technical Report 2004-003. http://www.kxcad.net/ESTECO/modeFRONTIER320/html/userman/files/ Schedulers/ NBI_NLPQLP.pdf

Ross PJ (1988), Taguchi Techniques for Quality Engineering: Loss Function, Orthogonal Experiment, Parameter and Tolerance Design. McGraw-Hill, pp.120–123.

Roy S., Ghosh S., and Shivpuri R. (1997), A new approach to optimal design of multi-stage metal forming processes with micro genetic algorithms, Int. J. Mach. Tools Manuf. Vol. 37, No. 1, pp. 29-44

Sacks J., et al. (1989), Design and Analysis of Computer experiments, Statistical Science, vol. 4, no. 4:409-435,

Seshadri A (2006), Multi-objective optimization using evolutionary algorithms (MOEA), Matlab website: http://www.mathworks.com/matlabcentral/file exchange/10429, by 19 Mar (Updated 27 Jan 2009), accessed on Mar. 8, 2009

Simha C.H.M., et al. (2007), Prediction of Necking in Tubular Hydroforming Using an Extended Stress-Based Forming Limit Curve. Transactions of the ASME, Vol. 129:36-47

Simpson T.W., et al. (1998), Comparison of Response Surface and Kriging Models for Multidisciplinary Design Optimization, Paper No. AIAA-98-4755,7th AIAA/USAF/NASA/ ISSMO Symposium on Multidisciplinary Analysis and Optimization, St. Louis, MO, September 2-4, 1998.

Simpson T.W., et al. (2001), Kriging Models for Global Approximation in Simulation-Based Multidisciplinary Design Optimization, AIAA JOURNAL, Vol. 39, No. 12, December, p2233-2241

Singh H. (2003), Fundamentals of hydroforming, the society of Manufacturing Engineers, p128.

Sorine M. (2007), Formability of advanced high strength steel tubes in tube bending and hydroforming, MASc. Thesis, University of Waterloo.

Stander N., et al. (2007), LS-OPT user's manual V3.2, Livermore Software Techn. Co.

Stander N., Roux W., Goel T., et al. (2009), LS-OPT® user's manual, April, LSTC

Storen, S., Rice, J.R. (1975), Localized necking in thin sheets. J. Mech. Phys. Solids 23, 421.

Stoughton TB. Stress-based forming limits in sheet-metal forming. J Eng Mater Technol 2001;123:417–22.

Stoughton T.B. (2000), A general forming limit criterion for sheet metal forming. Int. J. Mech. Sci. 42:1–27, Transactions on Evolutionary Computation, 6(2): 182-197.

Stoughton TB (2001). Stress-based forming limits in sheet-metal forming. J Eng Mater Technol. 123:417–22.

Stoughton TB, Yoon JW (2005), Sheet metal formability analysis for anisotropic materials under non-proportional loading. International Journal of Mechanical Sciences 47:1972-2002.

Stoughton T. B., Zhu Xinhai (2004), Review of theoretical models of the strain-based FLD and their relevance to the stress-based FLD, International Journal of Plasticity 20: 1463–1486

Strano M. (2006), Optimization under uncertainty of sheet-metalforming processes by the finite element method, Proc. IMechE Vol. 220 Part B: J. Engineering Manufacture. 1305-1315

Strano M., Jirathearant S. and Altan T. (2001), Adaptive FEM simulation for tube hydroforming: a geometry-based approach for winkle detection, Annals of the CIRP, Vol. 50, pp.185-190.

Strano M., Jirathearanat S., Shr S., Altan T. (2004), Virtual process development in tube hydroforming, J. Mater. Process. Technol., 146:130-136

Taguchi G (1981) System of Experimental Design. UNIPUB/ Kraus Intl. Publication

Thiruvarudchelvan S. and Lua A.C. (1991), Bulge forming of tubes with axial compressive force proportional to the hydraulic pressure, Mat. Shaping Tech.9.

Tjotta, S. (1992). Formability and the growth of damage. Wood, R.D., Zienkiewicz, O.C. (Eds), Numerical Methods in Industrial Forming Processes, Balkema, ISBN 9054100877, 187.

Trana K. (2002), Finite element simulation of the tube hydroforming process – bending, performing and hydroforming, Mater. Process. Technol.,127: 401-408

Todoroki A., Ishikawa T. (2004), Design of experiments for stacking sequence optimizations with genetic algorithm using response surface approximation, Composite Structures, 64:349–357

Wang J and Yin Z (2008), C-NSGA-II-MOPSO: An effective multi-objective optimizer for engineering design problems, Chapter 4 in Book: Global design to gain a competitive edge,519-528, Springer London. DOI: 10.1007/978-1-84800-239-5

Wu H.Z. (2003), Adaptive simulation for Tee-shape tube hydroforming processes, [Master thesis], National Sun Yat-Sen University, Kaohsiung, Taiwan,China

Xia Z.C. (2001), Failure analysis of tubular hydroforming, J. of Engineering Materials and Technology, 123, pp. 423-429

Yang J., Jeon B., Oh S. (2001), The tube bending technology of a hydroforming process for an automotive part, J. Mater. Process. Technol., 111:175-181

Yang JB, Jeon BH, Oh SI (2001), Design sensitivity analysis and optimization of the hydroforming process. J. Mater. Process. Technol. 113:666–672.

Yao, H., Cao, J. (2002), Prediction of forming limit curves using an anisotropic yield function with prestrain induced backstress. Int. J. Plasticity 18, 1013–1038.

Yoon J. W. , Chung K., Pourboghrat F. (2006), Design optimization of extruded preform for hydroforming processes based on ideal forming design theory, Intl. J. Mechanical Sciences 48: 1416–1428

Yuan S, Wang X, Liu G, Wang ZR (2007), Control and use of wrinkles in tube hydroforming. J. Mater. Process. Technol., 182:6–11.

Zhang S. (1999), Developments in hydroforming, J. Mater. Process. Tech., 91:236-244

Zhao L., Sowerby R. and Sklad M. P. (1996), A theoretical and experimental investigation of limit strains in sheet metal forming. Int. J. Mech. Sci. 38, 1307-1317

Zitzler Eckart and Thiele Lothar (1999), Multiobjective Evolutionary Algorithms: A Comparative Case Study and the Strength Pareto Approach, IEEE transactions on evolutionary computation, Vol. 3, No. 4:257

http://www.thomasnet.com/articles/custom-manufacturing-fabricating/hydroforming-auto-industry, accessed on Jan 10, 2010

http://nsmwww.eng.ohio-state.edu/Advances_in_Hydro.swf, accessed on Jan 6,2010

Appendix A: Two examples of the evolution with sorting by CV operation in constrained NSGA-IIa (the last two columns are the violation values and their ranks, respectively)

```
Command Window

Columns 10 through 15

  0.5844    0.4190    1.0000      Inf          0    1.0000
  0.5632    0.3724    1.0000    0.3742          0    1.0000
  0.5755    0.3968    1.0000    0.2165          0    1.0000
  0.5763    0.3589    1.0000    0.1681          0    1.0000
  0.5455    0.3767    1.0000    0.0832          0    1.0000
  0.5464    0.3928    1.0000    0.2603          0    1.0000
  0.5794    0.3700    1.0000    0.1218          0    1.0000
  0.5992    0.4181    2.0000    0.5982          0    1.0000
  0.5658    0.4567    2.0000    0.7687     0.0067    2.0000
  0.6107    0.3618    1.0000    0.3514     0.0107    3.0000
  0.5091    0.4700    1.0000    0.9524     0.0200    4.0000
  0.6237    0.3727    1.0000    0.3016     0.0237    5.0000
  0.6279    0.4211    1.0000    0.3943     0.0279    6.0000
  0.4914    0.4787    1.0000      Inf     0.0287    7.0000
  0.6292    0.3505    1.0000    0.1310     0.0292    8.0000
  0.6325    0.4172    2.0000    0.2591     0.0325    9.0000
  0.6362    0.3660    2.0000      Inf     0.0362   10.0000
  0.6390    0.3757    1.0000    0.1895     0.0390   11.0000
  0.6396    0.3635    1.0000    0.1539     0.0396   12.0000
  0.6457    0.3794    1.0000    0.2572     0.0457   13.0000
  0.6474    0.3771    1.0000    0.1566     0.0474   14.0000
  0.6573    0.3550    1.0000      Inf     0.0573   15.0000
  0.6601    0.3885    1.0000    0.1409     0.0601   16.0000
  0.6663    0.3625    1.0000    0.1427     0.0663   17.0000
  0.6689    0.3805    1.0000    0.0997     0.0689   18.0000
  0.6766    0.3696    1.0000    0.1516     0.0766   19.0000
  0.6804    0.3654    1.0000    0.1670     0.0804   20.0000
  0.6859    0.3941    2.0000    0.5492     0.0859   21.0000
  0.6887    0.3423    1.0000      Inf     0.0887   22.0000
  0.6899    0.3561    1.0000    0.2992     0.0899   23.0000
  0.6907    0.3715    2.0000      Inf     0.0907   24.0000
  0.6200    0.5235    3.0000      Inf     0.0985   25.0000
  0.7031    0.4067    2.0000    0.5109     0.1031   26.0000
  0.7186    0.3847    2.0000    0.6489     0.1186   27.0000
  0.7224    0.3636    1.0000      Inf     0.1224   28.0000
  0.7543    0.4788    2.0000      Inf     0.1831   29.0000
  0.7451    0.5010    2.0000      Inf     0.1961   30.0000
  0.5807    0.5628    3.0000    5.0000     0.2127   31.0000
  0.5515    0.5543    2.0000    0.4206     0.2191   32.0000
  0.5275    0.5659    2.0000    0.7948     0.2280   33.0000
  0.5410    0.5674    1.0000    1.3884     0.2321   34.0000
  0.5101    0.5394    2.0000    0.9650     0.2663   35.0000
```

Appendix B: The normalized dataset of DOE with LHS: input of 6 and output of 5 (Chapter 5)

0.66395	0.59625	0.35247	0.25549	0.60740	0.42283	0.45407	0.53078	0.20609	0.59925	0.41807
0.39064	0.42063	0.39298	0.57850	0.40203	0.44094	0.41827	0.62498	0.20313	0.64742	0.37713
0.39895	0.72036	0.38903	0.77600	0.48577	0.22547	0.71321	0.61993	0.61687	0.52444	0.57489
0.28397	0.76351	0.23605	0.65226	0.45083	0.69883	0.71519	0.45714	0.63472	0.55677	0.57457
0.52433	0.39931	0.60002	0.59071	0.20531	0.20922	0.38473	0.61646	0.20034	0.72238	0.36363
0.62584	0.30544	0.29082	0.68363	0.56553	0.39556	0.43693	0.45046	0.20111	0.63901	0.37573
0.57901	0.68652	0.49538	0.62240	0.52030	0.47564	0.66567	0.55544	0.39998	0.58069	0.56276
0.50394	0.56204	0.43107	0.47833	0.28702	0.39082	0.43315	0.59366	0.20671	0.70312	0.40669
0.53743	0.32628	0.26677	0.21162	0.34411	0.75425	0.43202	0.53717	0.20012	0.68987	0.35614
0.68743	0.27146	0.70497	0.31048	0.73305	0.73997	0.46354	0.47004	0.20020	0.57632	0.35895
0.32683	0.52431	0.65962	0.53412	0.71270	0.52891	0.68389	0.54220	0.41210	0.52752	0.56588
0.60587	0.38635	0.56777	0.54142	0.55930	0.29372	0.43450	0.42551	0.20134	0.62365	0.37271
0.35500	0.63241	0.74057	0.28807	0.77840	0.58456	0.56347	0.54719	0.47681	0.51015	0.53945
0.65334	0.66296	0.77835	0.67185	0.25131	0.62097	0.50181	0.46178	0.22349	0.75434	0.47876
0.30633	0.23587	0.55025	0.73312	0.22779	0.49425	0.40960	0.62518	0.20149	0.71862	0.38473
0.42139	0.61111	0.48135	0.78598	0.63366	0.34996	0.48393	0.53721	0.25005	0.56579	0.45675
0.26067	0.36573	0.33088	0.36438	0.31638	0.33611	0.40308	0.60589	0.20199	0.67662	0.36956
0.72832	0.21611	0.77326	0.40962	0.32172	0.65063	0.41832	0.59635	0.20000	0.68868	0.34233
0.79419	0.45949	0.45108	0.37681	0.76116	0.30487	0.45158	0.48005	0.22081	0.54635	0.39283
0.20279	0.55409	0.51233	0.49326	0.61689	0.54006	0.64678	0.53587	0.41479	0.55154	0.55429
0.22416	0.48863	0.64871	0.72450	0.43918	0.67229	0.57243	0.54259	0.30503	0.61999	0.52351
0.44036	0.29247	0.61537	0.44543	0.68771	0.26618	0.45501	0.38753	0.21440	0.58435	0.41899
0.71885	0.47232	0.69553	0.24189	0.49524	0.79693	0.43330	0.48825	0.20211	0.66894	0.38050
0.47729	0.73171	0.20702	0.43350	0.66138	0.70723	0.79568	0.48806	0.63247	0.49795	0.56899
0.75502	0.78288	0.31310	0.33737	0.37928	0.58291	0.61400	0.47423	0.43183	0.64093	0.54628
0.36355	0.25580	0.51471	0.56408	0.55925	0.30778	0.46075	0.39746	0.20682	0.62789	0.42110
0.55818	0.43948	0.20588	0.52672	0.76444	0.56423	0.51645	0.48651	0.26275	0.49143	0.47873
0.40558	0.69274	0.27556	0.68635	0.69217	0.28118	0.68735	0.57773	0.53273	0.51291	0.56733
0.21341	0.56935	0.22032	0.41861	0.57207	0.77565	0.76398	0.46111	0.57473	0.51075	0.56410
0.79928	0.49291	0.76215	0.59290	0.67260	0.41751	0.44461	0.52709	0.20137	0.57941	0.37003
0.73746	0.33176	0.62878	0.61137	0.39443	0.52786	0.42233	0.64710	0.20011	0.65731	0.35499
0.56434	0.37310	0.50605	0.32509	0.72350	0.29444	0.43633	0.39345	0.21037	0.57548	0.39677
0.51245	0.44497	0.66110	0.62335	0.70876	0.70672	0.54445	0.63237	0.26139	0.50910	0.47000
0.45492	0.51742	0.32246	0.41202	0.38631	0.68357	0.44255	0.51544	0.20745	0.68594	0.39405
0.51983	0.53714	0.35836	0.35534	0.45193	0.57812	0.42522	0.56123	0.20405	0.64567	0.37943
0.60787	0.24051	0.57810	0.62323	0.62860	0.77464	0.44171	0.52477	0.20030	0.61065	0.36178
0.75128	0.22095	0.21987	0.73507	0.57130	0.24190	0.43838	0.39385	0.20005	0.62924	0.35054
0.60196	0.50203	0.60499	0.25363	0.44585	0.38927	0.43161	0.58461	0.20100	0.63957	0.36351
0.47808	0.75664	0.44642	0.79895	0.23227	0.60363	0.52638	0.45650	0.29322	0.74515	0.50096
0.37983	0.31485	0.22167	0.79641	0.28017	0.54002	0.40837	0.65178	0.20068	0.69070	0.37155
0.78300	0.63837	0.76424	0.31972	0.53127	0.58411	0.46702	0.49264	0.21968	0.63250	0.41718
0.36480	0.48691	0.79037	0.73534	0.63575	0.21157	0.68671	0.48249	0.41475	0.54100	0.56737
0.65479	0.39782	0.35561	0.73060	0.37303	0.42513	0.40749	0.64450	0.20031	0.66631	0.36249
0.71759	0.44731	0.25303	0.62912	0.47643	0.67378	0.44020	0.58497	0.20043	0.63617	0.36601
0.26221	0.38390	0.53287	0.62078	0.36799	0.63560	0.42323	0.59507	0.20478	0.66009	0.38846
0.38172	0.39535	0.40324	0.33360	0.31520	0.23346	0.40172	0.58730	0.20120	0.68036	0.36539
0.27474	0.79932	0.40868	0.40528	0.20682	0.31653	0.66116	0.49542	0.62302	0.62307	0.56069
0.63552	0.73757	0.69646	0.63627	0.79513	0.51069	0.67807	0.54952	0.45178	0.51888	0.56704
0.45920	0.30529	0.76411	0.28409	0.79432	0.78357	0.48101	0.48834	0.20179	0.56317	0.37240
0.74276	0.36324	0.39169	0.27277	0.78482	0.63701	0.45211	0.59927	0.20738	0.54552	0.37666

APPENDIX C: CODE FOR OPTIMIZATION OF THF IN SQUARE-SHAPED DIE USING LS-DYNA

```
                              LS-DYNA file

$---+----1----+----2----+----3----+----4----+----5----+----6----+----
$ LS-DYNA(970) DECK WRITTEN BY : eta/FEMB-PC version 28.0
$    PROJECT : Prebent tube hydroforming by Kevin An
$      UNITS : MM,  KG,  SEC,  N
$       TIME : 12:50:25 AM
$       DATE : Monday, April 20, 2009
$---+----1----+----2----+----3----+----4----+----5----+----6----+----
*KEYWORD
*PARAMETER
rpa,14,rpb,35,rpc,60,rpd,90
rpe,125,rfend,25
$---+----1----+----2----+----3----+----4----+----5----+----6----+----
*TITLE
PREBENT TuBE HYDROFORMING (t=1.85)
$---+----1----+----2----+----3----+----4----+----5----+----6----+----
$
$                              CONTROL CARD
$
$
$---+----1----+----2----+----3----+----4----+----5----+----6----+----
*CONTROL_TERMINATION
$    ENDTIM    ENDCYC     DTMIN    ENDENG    ENDMAS
   0.00500         0       0.0       0.0       0.0
*CONTROL_TIMESTEP
$    DTINIT    TSSFAC      ISDO    TSLIMT     DT2MS      LCTM
      0.0       0.60         0
$    DT2MSF   DT2MSLC
*CONTROL_CONTACT
$    SLSFAC    RWPNAL    ISLCHK    SHLTHK    PENOPT    THKCHG
      0.10                             2         4         1
$    USRSTR    USRFRC     NSBCS    INTERM     XPENE     SSTHK
        0         0        10         0       4.0
$     SFRIC     DFRIC       EDC       VFC        TH     TH_SF
      0.0       0.0       0.0       0.0       0.0       0.0
$    IGNORE    FRCENG   SKIPRWG    OUTSEG   SPOTSTP   SPOTDEL
        0         0         0         0         0         0
*CONTROL_SHELL
$    WRPANG     ESORT     IRNXX    ISTUPD    THEORY       BWC
       20         0        -1         1         2         2
*CONTROL_ENERGY
$      HGEN      RWEN    SLNTEN     RYLEN
        2         2         2         2
*CONTROL_HOURGLASS
$      IHQ        QH
        1       0.10
$*HOURGLASS
$     HGID       IHQ        QM       IBQ        Q1        Q2
$        1         6       1.0
*CONTROL_OUTPUT
$    NPOPT    NEECHO    NREFUP    IACCOP     OPIFS    IPNINT
        1         3         0         0       0.0         0
$    IPRTF
        0
*DATABASE_NODOUT
$       dt    binary
```

```
      0.001        2
$---+----1----+----2----+----3----+----4----+----5----+----6----+----
$                          SPRINGBACK DYNAIN FILE
$---+----1----+----2----+----3----+----4----+----5----+----6----+----
*INTERFACE_SPRINGBACK_LSDYNA
$     psid
           1
$      nid    tcode    rcode
$---+----1----+----2----+----3----+----4----+----5----+----6----+----
$                          DATABASE CONTROL FOR ASCII
$---+----1----+----2----+----3----+----4----+----5----+----6----+----
*DATABASE_GLSTAT
$       DT    BINARY
   0.00020
*DATABASE_RCFORC
$       DT    BINARY
   0.00020
$---+----1----+----2----+----3----+----4----+----5----+----6----+----
$                          DATABASE CONTROL FOR BINARY
$---+----1----+----2----+----3----+----4----+----5----+----6----+----
*DATABASE_BINARY_D3PLOT
$ DT/CYCL      LCDT      BEAM     NPLTC
   0.00020
$    IOOPT
         0
*DATABASE_BINARY_D3THDT
$ DT/CYCL      LCDT
       0.0
$---+----1----+----2----+----3----+----4----+----5----+----6----+----
$                          DATABASE EXTENT CARDS
$---+----1----+----2----+----3----+----4----+----5----+----6----+----
*DATABASE_EXTENT_BINARY
$^
$    NEIPH     NEIPS    MAXINT    STRFLG    SIGFLG    EPSFLG
RLTFLG    ENGFLG
         0         0         7         1         1         1
1         1
$   CMPFLG    IEVERP    BEAMIP     DCOMP      SHGE     STSSZ
         0         0         0         0         0         0
$  NINTSLD
         1
*DATABASE_HISTORY_NODE
$      id1       id2       id3       id4       id5       id6
id7       id8
      2992      2790      2614      1613      1331      1161
2298      2290
$      id1       id2       id3       id4       id5       id6
id7       id8
       957
....................
...
....................
*LOAD_SHELL_SET
$^LOADED AT SHELL SET 1
$     ESID      LCID        SF        AT
         1         1   -1.0000       0.0
$---+----1----+----2----+----3----+----4----+----5----+----6----+----
$                          LOAD CURVE CARDS
$---+----1----+----2----+----3----+----4----+----5----+----6----+----
*DEFINE_CURVE_TITLE
LCur_2
```

185

```
$       LCID        SIDR        SFA        SFO       OFFA       OFFO
DATTYP
        2                       1.0        1.0        0.0        0.0
0
$                                A1         O1
                0.0                        0.0
            0.00001                        1.0
              0.050                        1.0
$
$ LOAD CURVES
$
*DEFINE_CURVE
4,0,0.000E+00,0.000E+00,0.000E+00,0.000E+00,0
0.0000000000000E+00,0.0000000000000E+00
5.0000000000000E-03,&fend
6.0000000000000E-03,&fend
$
*DEFINE_CURVE
1,0,1.000E+00,1.000E+03,0.000E+00,0.000E+00,0
0.0000000000000E+00,0.0000000000000E+00
1.0000000000000E-04,4.0000000000000E+00
2.0000000000000E-04,&pa
1.0000000000000E-03,&pb
2.5000000000000E-03,&pc
3.5000000000000E-03,&pd
5.0000000000000E-03,&pe
$
*DEFINE_CURVE
$ FLD curve
90
$
-0.57,1.9552
-0.5,1.5415
-0.4,1.1179
-0.3,0.8154
-0.2,0.5884
-0.1,0.4119
0,0.2707
0.1,0.331
0.2,0.3818
0.3,0.4168
0.4,0.434
0.42,0.4354
0.43,0.4358
```

APPENDIX D: CODE FOR OPTIMIZATION OF THF IN SQUARE-SHAPED DIE USING LS-OPT3.4

```
"Square Tube Hydroforming"
Author "An"
$ Created on Fri Jul 03 13:16:27 2009
$ NO HISTORIES ARE DEFINED
$
$ DESIGN VARIABLES
variables 6
 Variable 'pa' 14
  Lower bound variable 'pa' 10
  Upper bound variable 'pa' 19
 Variable 'pb' 25
  Lower bound variable 'pb' 19
  Upper bound variable 'pb' 28
 Variable 'pc' 28
  Lower bound variable 'pc' 26
  Upper bound variable 'pc' 28
 Variable 'fend' 10
  Lower bound variable 'fend' 10
  Upper bound variable 'fend' 14
 Variable 'pd' 30
  Lower bound variable 'pd' 30
  Upper bound variable 'pd' 35
 Variable 'pe' 60
  Lower bound variable 'pe' 40
  Upper bound variable 'pe' 85
$$$$$$$$$$$$$$$$$$$$$$$$$$$$$$$$$$
$       OPTIMIZATION METHOD
$$$$$$$$$$$$$$$$$$$$$$$$$$$$$$$$$$$
Optimization Method SRSM
$$$$$$$$$$$$$$$$$$$$$$$$$$$$$$$$$$$
$       SOLVER "1"
$ DEFINITION OF SOLVER "1"
  solver command "C:\temp\LS_OPT\test5\ls971_single.exe"
  solver input file "C:\temp\LS_OPT\test5\sqhydro1.dyn"
$ ------ Pre-processor --------
$   NO PREPROCESSOR SPECIFIED
$ ------ Post-processor --------
$   NO POSTPROCESSOR SPECIFIED
$ ------ Metamodeling ---------
  solver order RBF
  solver experiment design space_filling
   solver number experiments 12
   solver update doe
$ ------ Job information ------
  solver concurrent jobs 1
$
$ RESPONSES FOR SOLVER "1"
$
 response 'THICK2' 1 0 "DynaThick REDUCTION 1 MAX"
 response 'NODOUT_X1' 1 0 "BinoutResponse -res_type Nodout  -cmp
x_coordinate -id 1855 -select TIME "
 response 'NODOUT_Y1' 1 0 "BinoutResponse -res_type Nodout  -cmp
y_coordinate -id 1855 -select TIME "
 response 'NODOUT_Z1' 1 0 "BinoutResponse -res_type Nodout  -cmp
z_coordinate -id 1855 -select TIME "
 response 'NODOUT_X2' 1 0 "BinoutResponse -res_type Nodout  -cmp
x_coordinate -id 1967 -select TIME "
```

```
 response 'NODOUT_Y2' 1 0 "BinoutResponse -res_type Nodout  -cmp
y_coordinate -id 1967 -select TIME "
 response 'NODOUT_Z2' 1 0 "BinoutResponse -res_type Nodout  -cmp
z_coordinate -id 1967 -select TIME "
 response 'NODOUT_X3' 1 0 "BinoutResponse -res_type Nodout  -cmp
x_coordinate -id 1743 -select TIME "
 response 'NODOUT_Y3' 1 0 "BinoutResponse -res_type Nodout  -cmp
y_coordinate -id 1743 -select TIME "
 response 'NODOUT_Z3' 1 0 "BinoutResponse -res_type Nodout  -cmp
z_coordinate -id 1743 -select TIME "
 response 'FLD2' 1 0 "DynaFLDg LOWER 1 90"
$
$ COMPOSITE EXPRESSIONS    $
composite 'CE1' {(NODOUT_X2-NODOUT_X1)**2+(NODOUT_Y2-
NODOUT_Y1)**2+(NODOUT_Z2-NODOUT_Z1)**2}
 composite 'CE2' {(NODOUT_X3-NODOUT_X2)**2+(NODOUT_Y3-
NODOUT_Y2)**2+(NODOUT_Z3-NODOUT_Z2)**2}
 composite 'CE3' {(NODOUT_X3-NODOUT_X1)**2+(NODOUT_Y3-
NODOUT_Y1)**2+(NODOUT_Z3-NODOUT_Z1)**2}
 composite 'CE4' {(NODOUT_Y2-NODOUT_Y1)*(NODOUT_Z3-NODOUT_Z2)-
(NODOUT_Z2-NODOUT_Z1)*(NODOUT_Y3-NODOUT_Y2)}
 composite 'CE5' {(NODOUT_Z2-NODOUT_Z1)*(NODOUT_X3-NODOUT_X2)-
(NODOUT_X2-NODOUT_X1)*(NODOUT_Z3-NODOUT_Z2)}
 composite 'CE6' {(NODOUT_X2-NODOUT_X1)*(NODOUT_Y3-NODOUT_Y2)-
(NODOUT_Y2-NODOUT_Y1)*(NODOUT_X3-NODOUT_X2)}
 composite 'CE7' {CE4**2+CE5**2+CE6**2}
 composite 'CE8' {0.5*sqrt(CE1)*sqrt(CE2)*sqrt(CE3)/sqrt(CE7)}
$
$ OBJECTIVE FUNCTIONS  $
objectives 1
 objective 'CE8' 1
$
$ CONSTRAINT DEFINITIONS
$
 constraints 3
 constraint 'THICK2'
  lower bound constraint 'THICK2' 0
  upper bound constraint 'THICK2' 35
 constraint 'FLD2'
  strict
  upper bound constraint 'FLD2' 0
 constraint 'CE8'
  slack
  lower bound constraint 'CE8' 5
  upper bound constraint 'CE8' 12
$
$ PARAMETERS FOR METAMODEL OPTIMIZATION
$
 Metamodel Optimization Strategy SEQUENTIAL
$
  iterate param design 0.01
  iterate param objective 0.01
  iterate param stoppingtype and
$
$ OPTIMIZATION ALGORITHM
$
 Optimization Algorithm simulated annealing
$
$ JOB INFO  $
 iterate 3
STOP
```

APPENDIX E: Conversion between corner radius and corner fill expansion (CFE)

1. Calculate the corner radius through 3 points to get R_{in} and R_{out} (Assumption: the curve is tangent to die at the contact points)

2. Calculate the distance d1 and d2

$$a = \overline{AB} - \overline{NB} = R - \frac{R}{\sqrt{2}} = \frac{2 - \sqrt{2}}{2} R$$

$$d1 = \sqrt{2}a = (\sqrt{2} - 1)R$$

$$d2 = \sqrt{2}a' = (\sqrt{2} - 1)R'$$

$$d2_{in} = \sqrt{2}a' = (\sqrt{2} - 1)R_{in}$$

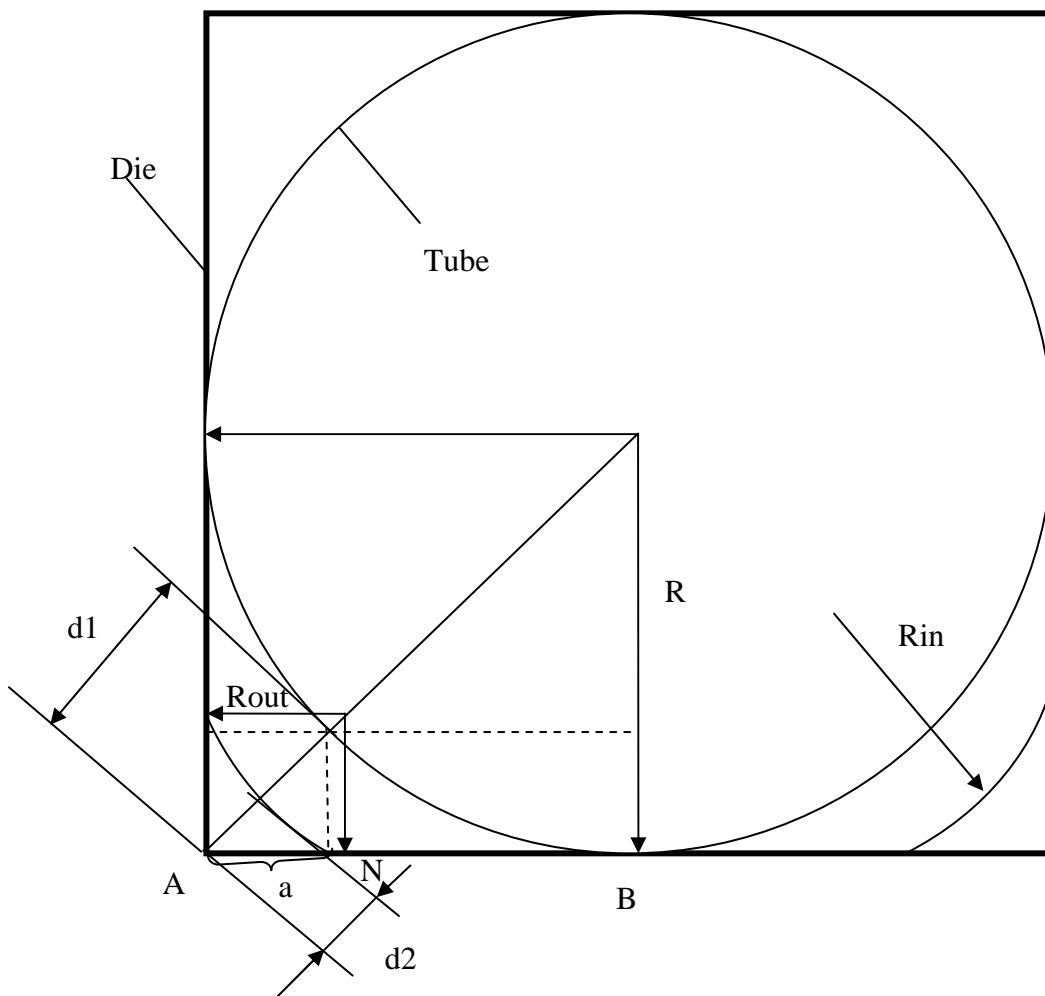$$d2_{out} = \sqrt{2}a' = (\sqrt{2} - 1)R_{out}$$

Fig.G1 Calculation of the distance measurement by LVDT

So, for R'=Rin and R'=Rout, the displacement δ measured by LVDT is d1-d2.
Therefore, the equations of LVDT movement and corner fill expansion ratio (CFE%)
for intrados and extrados are:

$$\delta_{in} = d1 - d2_{in}$$
$$CFE\%_{in} = (d1 - d2_{in})/d1$$

and,

$$\delta_{out} = d1 - d2_{out}$$
$$CFE\%_{out} = (d1 - d2_{out})/d1$$

Example (using Excel):

R_original	R-Inner	R-outer
38:1	8.55	11.19
	δ-Inner	δ-Outer
	11.14649	12.240011
	CFE%-In	CFE%-Out
	0.706299	0.7755906

PUBLICATIONS

Refereed Journal Publications

- **An, H.**, Green, D.E., Johrendt J., **Multi-objective optimization and sensitivity analysis of tube hydroforming simulations**, Int. J. Advanced Manufacturing Technology, 50: p67-84,DOI:10.1007/s00170-009-2505-x (2010)

- Turton, N., Jin, S.Y., Majumder, A., **An, H.**, Vijayan, V.,Altenhof, W., and Green, D. **Experimentally observed strain distributions near circular discontinuities of AA6061-T6 extrusions during axial crush,** Accepted by Experimental Mechanics (EXME763), in press (2010)

- **An Honggang,** Green, D.E., Johrendt J., **Optimal load path design for tube hydroforming using hybrid constrained MOGA and local search**, Advanced Engineering Informatics (Submitted)

Refereed Conference Publications

- **An, H.,** Green, D.E., and Johrendt J. **A global optimization of load path design for tube hydroforming applications using MOGA,** IDDRG, June, Golden, CO, USA, p307-318 (2009)

- **An, H.,** Green, D.E., and Johrendt J. **Optimization of tube hydroforming using pulsating internal pressure,** Proceedings of Materials Science & Technology (MS&T), October 25-29, 2009, Pittsburgh, Pennsylvania, USA, p2321-2332 (2009)

- **An, H.,** Green, D.E. **Optimization and sensitivity analysis of numerical simulation of tubular hydroforming,** 10th LS-DYNA® conf., June, Dearborn, MI, USA (2008)

- **Honggang An,** Green, D.E., Johrendt J. and K. Hertell, **Inverse Analysis in Hydroforming of a Refrigerator Door Handle Using MOGA**, Accepted by NUMIFORM2010, Pohang, Korea. June 2010.

- Turton, N., Majumder, A., Altenhof, W., Green, D., Vijayan, V., **An, H.**, and Jin, S. Y., **Numerical and Experimental Determination of Strains in the Vicinity of a Centrally Located Circular Discontinuity in AA6061-T6 Square Extrusions during Axial Crushing**,10th international LS-DYNA® users conf. June, Dearborn, MI, USA. p16.1-16.11 (2008)

Non-refereed contributions (Conference presentation)
- **Honggang An**, Daniel E. Green(2007) Study on load path optimization for tube hydroforming. North American Deep Drawing Research Group (NADDRG) spring 2007 symposium. May, Oakland University, Michigan, USA.

- **Honggang An**, Daniel E. Green(2008) Multi-objective optimization and sensitivity analysis of simulation of tubular hydroforming. NADDRG 2008. May, Windsor, ON, Canada.

- **Honggang An**, Daniel E. Green (2008) Multiobjective optimization of numerical simulation on formability of tube hydroforming with square die. Modeling and Optimization: Theory and Applications (MOPTA) 2008 conference. University of Guelph, Ontario, Canada.

VITA AUCTORIS

NAME: Honggang An

PLACE OF BIRTH: Hubei, China

YEAR OF BIRTH: 1975

EDUCATION: Hubei University of Technology, Hubei, China

Master of Mechanical Engineering, 1996-1999

Hubei University of Technology, Hubei, China

Bachelor of Mechanical Engineering, 1992-1996

University of Windsor, Windsor, ON, Canada

PhD candidate of Mechanical Engineering,

2006-2010